NASA CR-159832

NASA

National Aeronautics and
Space Administration

CF6 JET ENGINE PERFORMANCE IMPROVEMENT PROGRAM

HIGH PRESSURE TURBINE AERO-DYNAMIC PERFORMANCE IMPROVEMENT

by

W.A. Fasching

GENERAL ELECTRIC COMPANY

July 1980

Prepared For

National Aeronautics and Space Administration

NASA Lewis Research Center
NAS3-20629

1. Report No. NASA CR-159832	2. Government Accession No.	3. Recipient's Catalog No.
4. Title and Subtitle CF6 Jet Engine Performance Improvement Program High Pressure Turbine Aerodynamic Performance Improvement		5. Report Date July 1980
		6. Performing Organization Code
7. Author(s) W.A. Fasching		8. Performing Organization Report No
		10. Work Unit No.
9. Performing Organization Name and Address General Electric Company Aircraft Engine Group Cincinnati, Ohio 45215		11. Contract or Grant No. NAS3-20629
		13. Type of Report and Period Covered Contract or Report
12. Sponsoring Agency Name and Address National Aeronautics and Space Administration Washington, DC 20546		14. Sponsoring Agency Code

15. Supplementary Notes

Project Manager, J.A. Ziemianski, Engine Component   Project Engineer - R.J. Antl
Improvement Office -- NASA-Lewis Research Center
21000 Brookpark Road, Cleveland, Ohio 44135

16. Abstract

The improved single shank high pressure turbine design was evaluated in component tests consisting of performance, heat transfer and mechanical tests, and in core engine tests. The instrumented core engine test verified the thermal, mechanical, and aeromechanical characteristics of the improved turbine design. An endurance test subjected the improved single shank turbine to 1000 simulated flight cycles, the equivalent of approximately 3000 hours of typical airline service.

Initial back-to-back engine tests demonstrated an improvement in cruise sfc of 1.3% and a reduction in exhaust gas temperature (EGT) of 10° C. An additional improvement of 0.3% in cruise sfc and 6° C in EGT is projected for long service engines.

17. Key Words (Suggested by Author(s)) CF6-6 HP Turbine Performance Improvement	18. Distribution Statement Unclassified – Unlimited		
19. Security Classif. (of this report) Unclassified	20. Security Classif. (of this page) Unclassified	21. No. of Pages	22. Price*

* For sale by the National Technical Information Service, Springfield, Virginia 22161

NASA-C-168 (Rev. 10-75)

FOREWARD

The work was performed by the CF6 Engineering Department of General Electric's Aircraft Engine Group, Aircraft Engine Engineering Division, Cincinnati, Ohio. The Design Managers were J.B. Sidenstick, F.C. Herzner and C.A. Freck. The program was conducted for the National Aeronautics and Space Administration, Lewis Research Center, Cleveland, Ohio, under Subtask 2.3 of the CF6 Jet Engine Performance Improvement Program, Contract Number NAS3-20629. This report was prepared by W.A. Fasching, General Electric Program Manager, with the assistance of F.C. Herzner, C.A. Freck, and C. Fehl. The NASA Project Engineer for this program was R.J. Antl. The program was initiated in February 1978 and was completed in July 1979.

TABLE OF CONTENTS

SUMMARY

The purpose of the High Pressure Turbine Aerodynamic Performance Improvement Program was to develop the technology and to demonstrate the technical feasibility of the improved single shank turbine design on a CF6-6 core engine.

Performance, heat transfer, and mechanical component tests were conducted to evaluate the new turbine design. The thermal, mechanical, and aerothermal characteristics of the single shank turbine were verified in an instrumented core engine test. The turbine hardware successfully completed 1000 simulated flight cycles of endurance testing, equivalent to approximately 3000 hours of typical airline service.

Initial sea level static back-to-back engine tests carried out in March 1980 demonstrated an improvement in sfc of 0.85% and a reduction in exhaust gas temperature (EGT) of 10° C for the high pressure turbine aerodynamic improvements. A reduction in turbine inlet area will provide an additional sfc reduction of 0.72%. This amounts to a total improvement of 1.57% sfc at sea level which is equivalent to 1.06% at cruise. In addition, there is also an improvement in shroud roundness which was assessed to amount to an additional improvement of 0.24% sfc at cruise. The total cruise sfc improvement for a new engine amounts, therefore, to 1.3%.

An additional reduction of 0.3% in cruise sfc and about 6° C in exhaust gas temperature is projected for long service engines due to the elimination of the mateface shank cooling air leakage associated with the original twin shank blades. This sums to an improvement of 1.6% in cruise sfc and 16° C in EGT for long service engines.

An economic assessment of the improvement was made for new engines on the Douglas DC-10-10 aircraft. This assessment indicated that the CF6-6 improved high pressure turbine has a payback period of about 0.2 year. The acceptability of this concept is enhanced with the trend to higher fuel prices.

1

2.0 INTRODUCTION

National energy demand has outpaced domestic supply creating an increased U.S. dependence on foreign oil. This increased dependence was dramatized by the OPEC oil embargo in the winter of 1973 to 1974. In addition, the embargo triggered a rapid rise in the cost of fuel which, along with the potential of further increases, brought about a changing economic circumstance with regard to the use of energy. These events, of course, were felt in the air transport industry as well as other forms of transportation. As a result of these experiences, the Government, with the support of the aviation industry, has initiated programs aimed at both the supply and demand aspects of the problem. The supply problem is being investigated by looking at increasing fuel availability from such sources as coal and oil shale. Efforts are currently underway to develop engine combustor and fuel systems that will accept fuels with broader specifications.

Reduced fuel consumption is the other approach to deal with the overall problem. A long-range effort to reduce consumption is to evolve new technology which will permit development of a more energy efficient turbofan or the use of a different propulsive cycle such as a turboprop. Although studies have indicated large reductions in fuel usage are possible (e.g., 15 to 40%), the impact of this approach in any significant way would be 15 or more years away. In the short term, the only practical propulsion approach is to improve the fuel efficiency of current engines. Examination of this approach has indicated that a 5% fuel reduction goal starting in the 1980 to 1982 time period is feasible for the CF6 engine. This engine is, and will continue to be, a significant fuel user for the next 15 to 20 years.

Accordingly, NASA is sponsoring an overall Engine Component Improvement (ECI) Program to reduce the CF6 fuel consumption. This ECI program consists of two parts: Engine Diagnostics and Performance Improvement. The Engine Diagnostics effort is to provide information to identify the sources and causes of engine deterioration. The Performance Improvement effort is directed at developing engine performance improvement and retention components for new production and retrofit engines. The initial Performance Improvement effort consisted of a Task 1 Feasibility Analysis which was conducted in cooperation with the Boeing and Douglas aircraft companies and American and United airlines, and is reported in Reference 1. The study identified engine and component modifications which exhibited a fuel savings potential over current practice in CF6 engines; provided a technical and economic assessment of the modifications, including the impact on airline acceptability and the probability of production introduction of the concepts by the 1980 to 1982 time period as well as their retrofit potential; and assessed the fuel savings potential for the DC-10-10, DC-10-30, and the B747-200 aircraft.

The high pressure turbine (HPT) aerodynamic performance improvement concept was studied in the Performance Improvement Task 1 Feasibility Study and was selected for development and evaluation because of its fuel savings potential and high payback for the above-mentioned aircraft. The results of the

Feasibility Analysis are reported in Reference 1. This report presents the results of the development work on the concept.

The high pressure turbine of the CF6-6 engine is essentially the same turbine that was developed for the U.S. Air Force TF39 engine in the mid-1960's. The core of the TF39 engine subsequently became the core engine for the CF6-6 commercial turbofan engine and the LM2500 marine and industrial turboshaft engine. This turbine, which has been in airline service since 1971, has accumulated about 6,000,000 operating hours. During the ensuing period since initial development, design improvements have been limited to relatively modest changes directed at improved life and durability.

Design techniques and basic technology have made considerable advance-ments since the original turbine was conceived. In 1976, it was decided to initiate redesign studies directed at improved life and durability incorpo-rating many features employed in the second generation CF6-50 turbine. Much of this initial work has been sponsored by the U.S. Navy for the LM2500 engine which powers the Spruance class destroyers. Since significant mechanical de-sign changes were contemplated for this turbine, steps were also taken to im-prove basic performance and reduce operational performance deterioration.

Performance improvement studies indicated that up to 1.3% engine specific fuel consumption (sfc) improvement/retention could be achieved through reduced cooling air requirements, flowpath and basic aerodynamic refinements, and re-duced pressure losses in the turbine rear frame.

The objective of the NASA effort, which was initiated in early 1978, was to develop the technology of the improved high pressure turbine in component and engine tests. The HPT Aerodynamic Performance Improvement Concept was a 17-month effort. Testing included component performance, heat transfer, and mechanical tests along with an instrumented engine and engine endurance tests.

3.0 DESCRIPTION OF HIGH PRESSURE TURBINE AERODYNAMIC PERFORMANCE IMPROVEMENT CONCEPT

The program was initiated to provide aerodynamic and mechanical improvements for the CF6-6/LM2500 high pressure turbine. Objectives were aimed at significant reductions in specific fuel consumption, increased ruggedness, longer life, and reduced deterioration in service. The program has concentrated on:

- Improved aerodynamics

- Adoption of the single shank blade concept utilized on the CF6-50

- Improved cooling designs

- Improved clearance control.

The improved turbine has fewer, more rugged blades, and longer chord Stage 2 nozzle vanes, both of which provide better aerodynamic efficiency and reduced turbine exit losses.

3.1 DESCRIPTION OF PERFORMANCE IMPROVEMENTS ITEMS

The new turbine has a number of features which enhance overall engine performance. These features are:

- Modified Stage 2 vane aerodynamics

- Reduced Stage 2 exit swirl

- Better blade cooling effectiveness

- More effective wheel space seals

- Tighter tip clearance

- No mating face shank leakage

- Improved airfoil surface finish.

The following paragraphs describe these performance features:

Stage 2 Vane Aerodynamics - The new Stage 2 vane has increased solidity. This was accomplished by increasing the chord length as shown in Figure 1 while maintaining the same number of vanes. The inner and outer band shape was redefined, and the leading edge was reshaped to optimize the local pressure distribution.

Stage 2 Exit Swirl - The original design has a larger than desired exit swirl resulting in significant turbine midframe pressure losses. The new design reduces the exit swirl by 9° which reduces the turbine midframe pressure loss. This increases the efficiency by 0.57% as shown in Figure 2.

● Increased Solidity
● New Band Shape
● New Leading Edge Shape
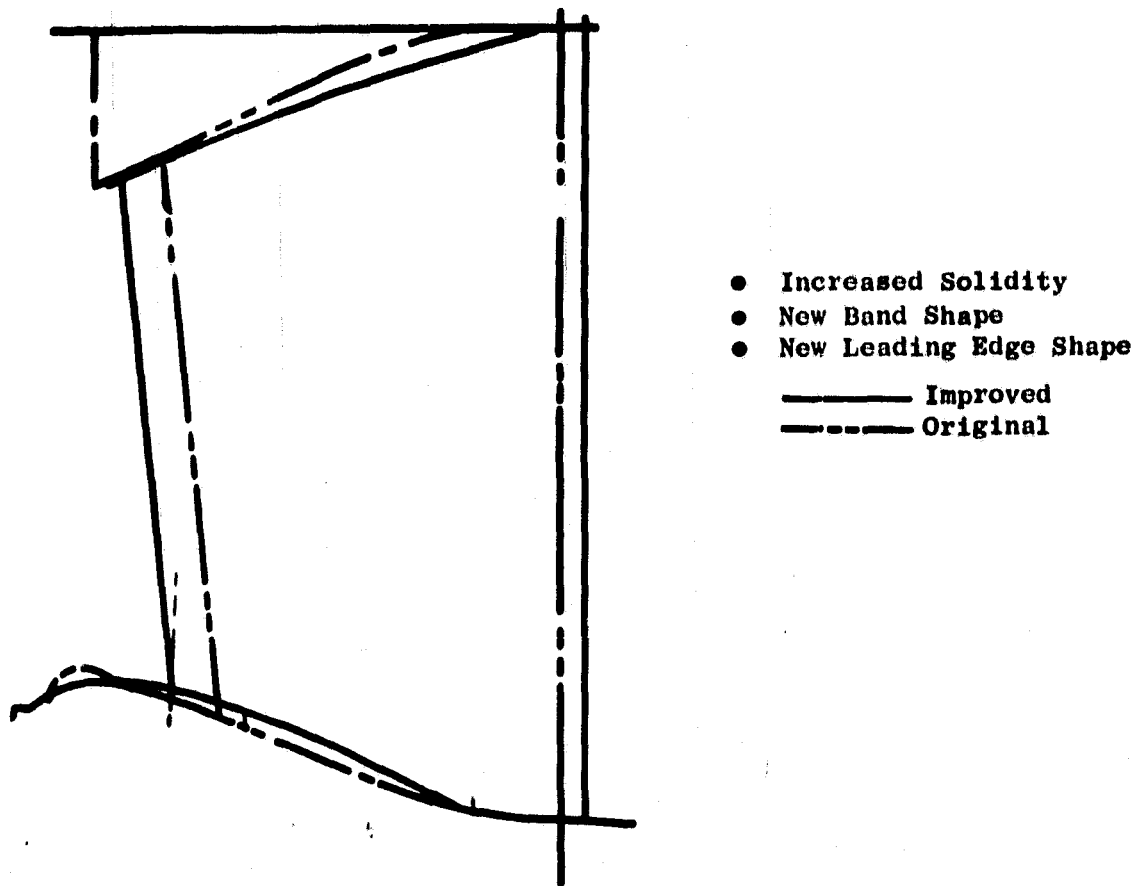
───────── Improved
──·──·── Original

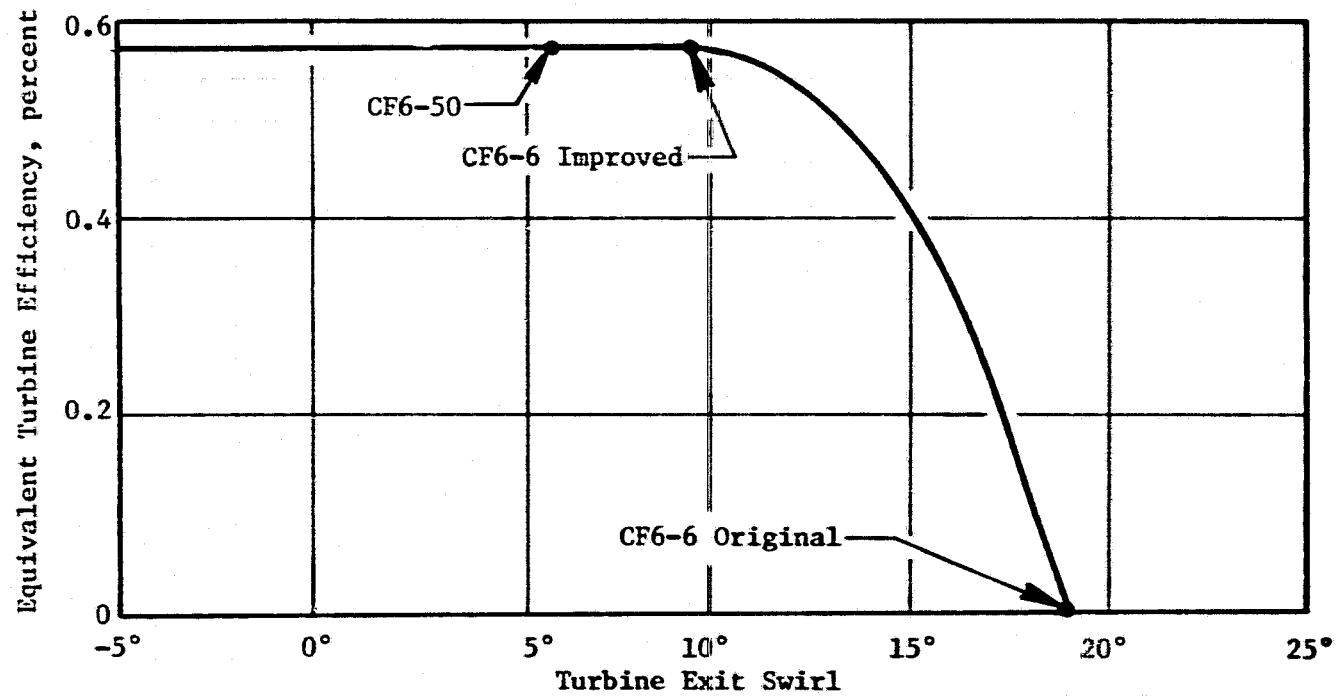Figure 1.   Improved Stage 2 Vane Aerodynamics.

Figure 2. Reduced Stage 2 Exit Swirl.

Blade Cooling Effectiveness - Modern casting technology allowed more flexibility in the design of the Stage 1 and 2 turbine blades. The original blades start with a solid casting which is then drilled to form the various cooling passages. By introducing precision cast cored airfoils, similar to the CF6-50, more effective cooling can be achieved. Features such as shaped passages, sidewall turbulence promoters, pin fin trailing edge passages, and smooth turnarounds in the serpentine passages are achieved. A comparison of the new design to the original blade in Figure 3 shows significant metal temperature reduction for the same amount of cooling flow. The better cooling effectiveness could have been used to reduce cooling flow while maintaining current temperature levels. To increase Stage 1 blade life, it was decided to lower the metal temperature instead. Stage 2 maintains current metal temperatures and reduces cooling flow, resulting in a performance improvement.

Wheelspace Seals - The new turbine incorporates better wheel seals as shown in Figure 4. By introducing seals over and under the blade "angel wings", adequate cavity purging is achieved with reduced airflow. These improved seals have been proven on the CF6-50 turbine. An improved Stage 1 blade retainer which reduces flow leakage across the Stage 1 wheel rim is another CF6-50 feature which is being incorporated to help achieve reductions in cavity temperature and purge flow. The reduction in purge flow results in improved overall performance.

Tip Clearance - The new turbine incorporates features in the stator system which improve clearance control in several ways as indicated in Figure 5. By increasing the cross-sectional mass of the clearance control ring and by better isolating it from the shroud cooling air, a slower thermal response is achieved. This will result in a better thermal match with the rotor blade tip during steady-state and transient operation. Also, the stiffer clearance control ring, in its controlled environment, will have a greater influence in resisting engine case distortion.

The shroud supports, with a stronger cross section, are less flexible. This makes the supports deflect less inwardly due to the high radially inward pressure at takeoff conditions. In turn, this reduces the tip rub at takeoff, resulting in improved tip clearance at the cruise conditions.

Mateface Shank Leakage - A source of turbine deterioration has been eliminated with the introduction of the single shank blade design (see Figure 6). With the twin shank blades, the two blades have a mating face which must be brazed together to seal in the cooling air. After a fairly short time, the braze cracks and cooling air leakage results in performance deterioration. With the new design, the cooling air passages are cast in with the cooling air being fed from underneath the dovetail. This entirely eliminates deterioration due to leakage of cooling air.

Airfoil Finish - The blade and vane surface finish requirements for the CF6-50 are presently more stringent than those for the CF6-6 twin shank design. Surface finish requirements for the single shank design have been brought in line with those used on the CF6-50.
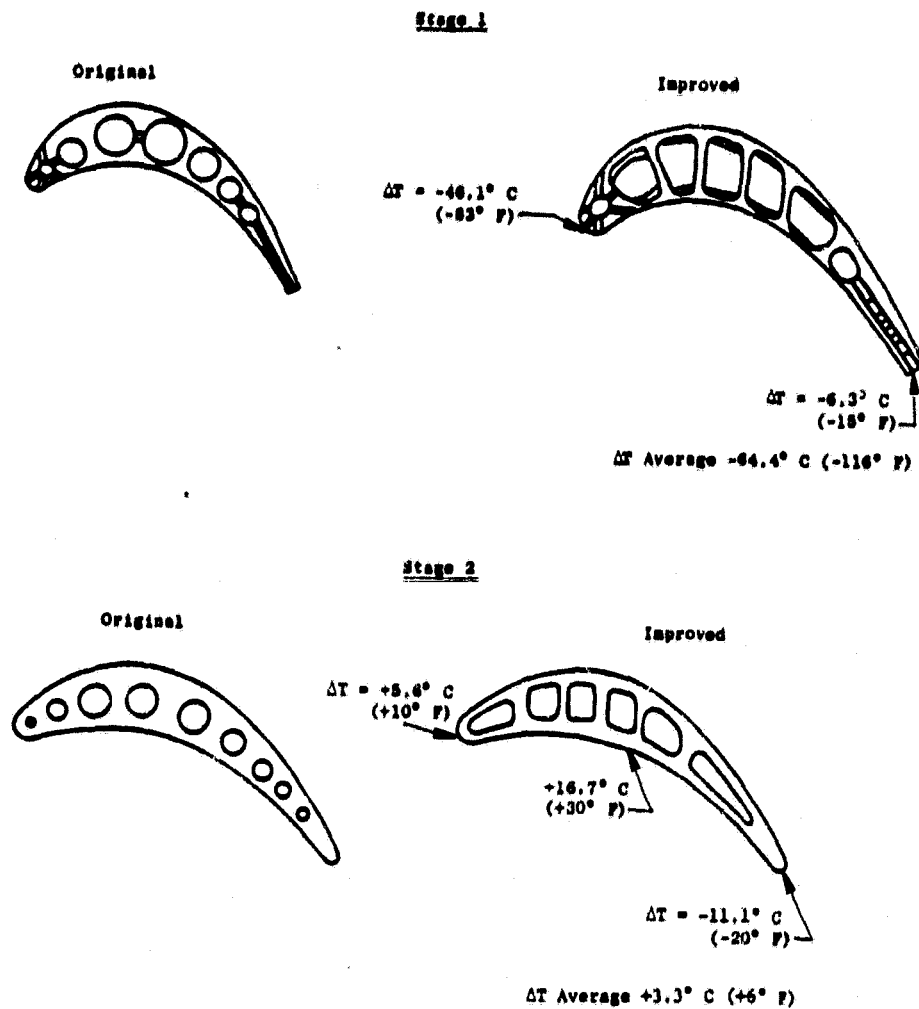
Stage 1

Original   Improved

$\Delta T = -46.1°$ C
$(-83°$ F)

$\Delta T = -6.3°$ C
$(-15°$ F)

ΔT Average $-64.4°$ C $(-116°$ F)

Stage 2

Original   Improved

$\Delta T = +5.6°$ C
$(+10°$ F)

$+16.7°$ C
$(+30°$ F)

$\Delta T = -11.1°$ C
$(-20°$ F)

ΔT Average $+3.3°$ C $(+6°$ F)

Figure 3.   Comparison of Original and Improved Blades
            Showing Improved Cooling.

8
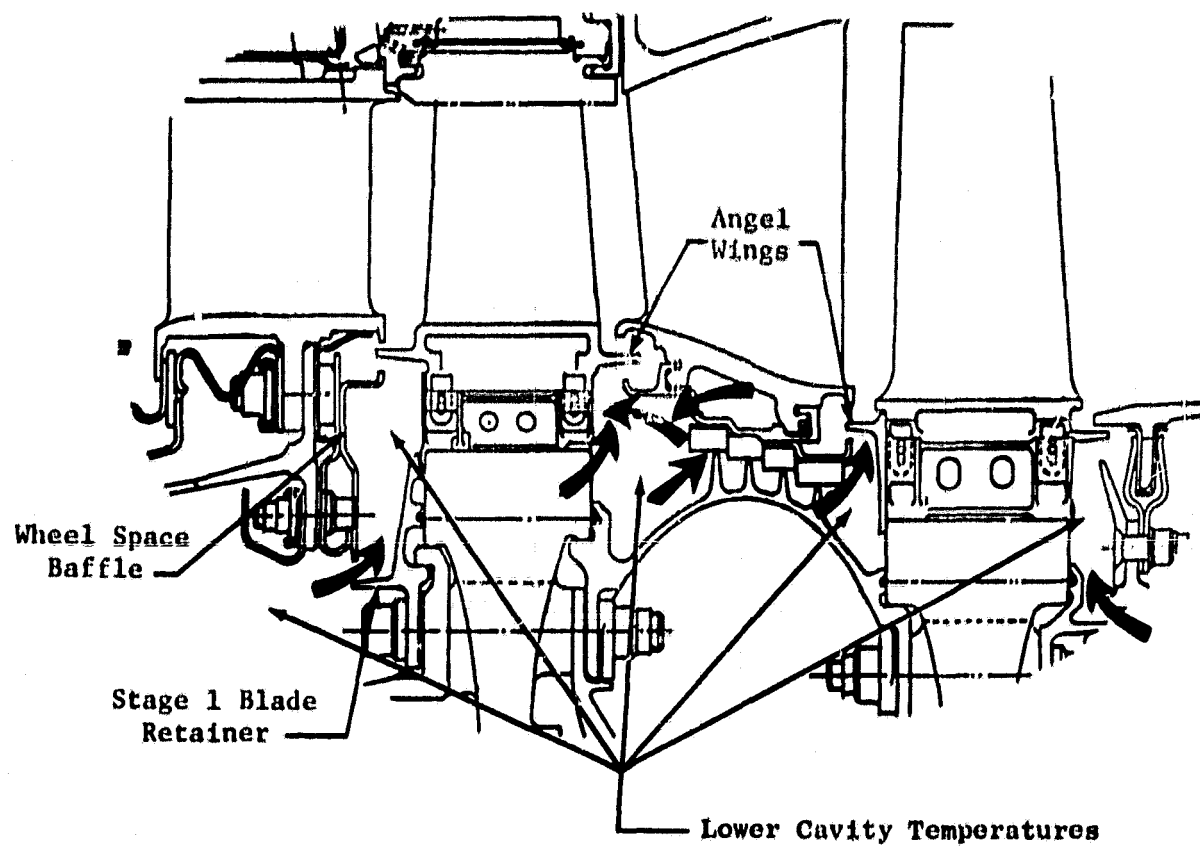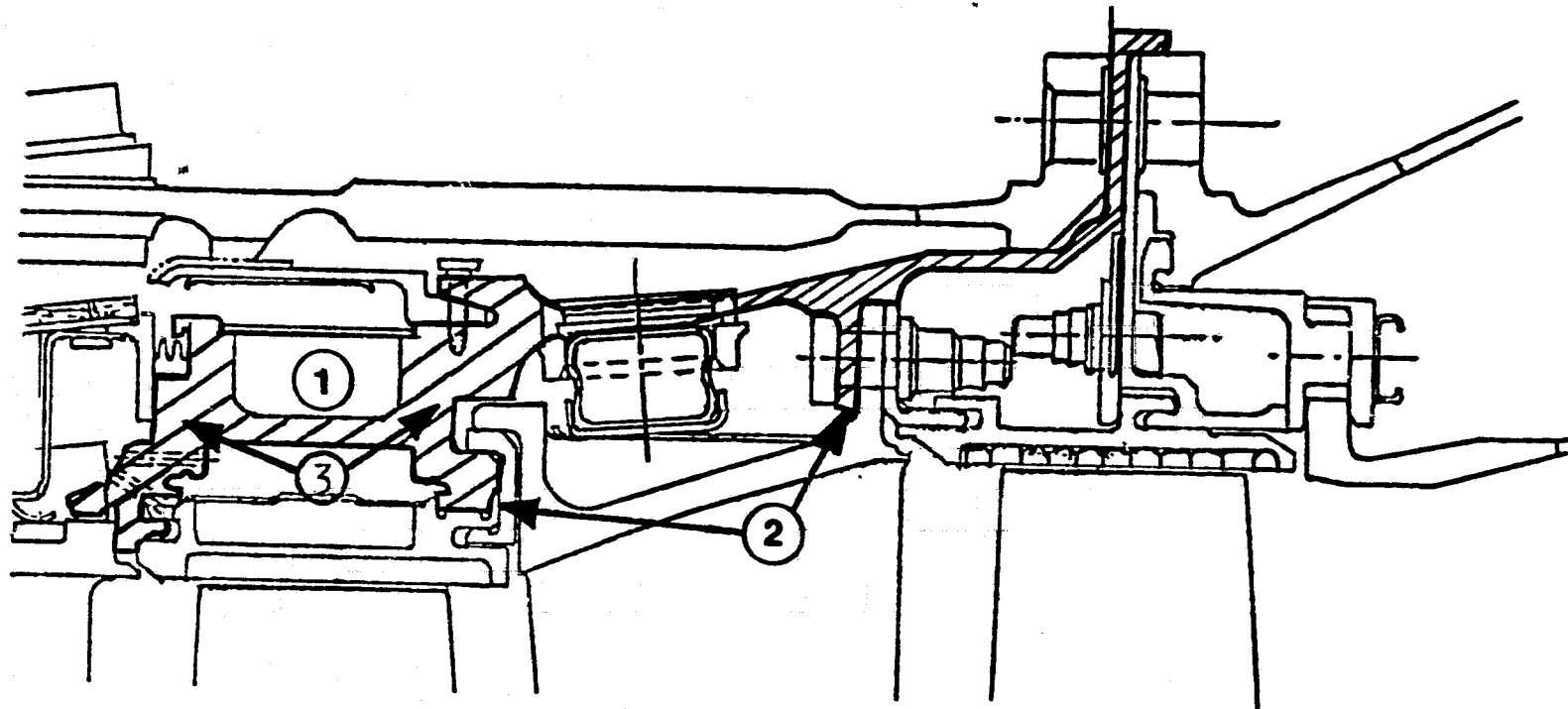
Figure 4. Improved Wheel Space Seals.

① Improved Stator to Rotor Thermal Match

② Basic Structure More Isolated from Gas Path

③ Stiffer Hoop
   - Roundness Improvement
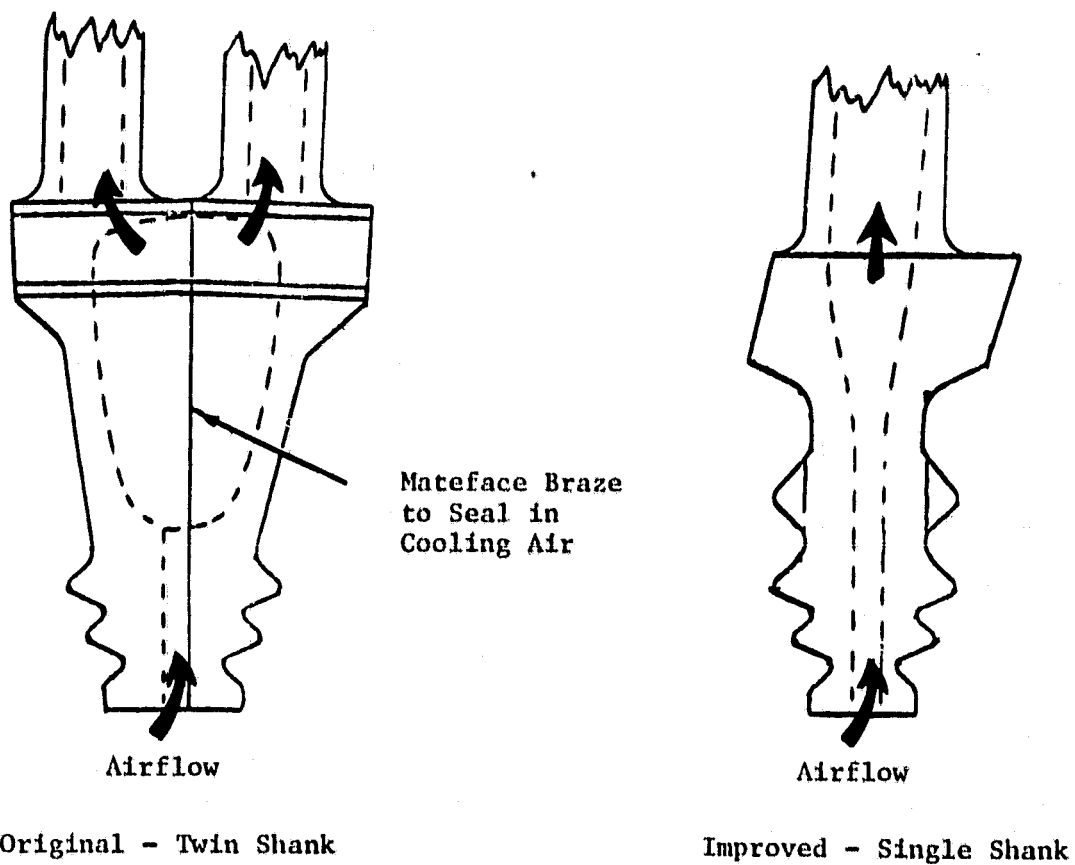   - Improved Cruise Match

Figure 5.   Tighter Tip Clearance.

Mateface Braze
to Seal in
Cooling Air

Airflow

Original – Twin Shank

Airflow

Improved – Single Shank

Figure 6.   Single Shank Turbine Deterioration Reduction – No
Mateface Shank Leakage.

11

3.2 PERFORMANCE

The predicted performance improvements of the individual items with respect to cooling air and turbine efficiency are summarized in Table I below:

Table I. Estimated Performance Improvements.

Improvement Item	% Δ Wc	% Δ η T
Stage 2 Vane Aero		+0.14
Stage 2 Exit Swirl		+0.57
Blade Cooling (Stage 2)	-0.20	+0.03
Wheel Space Seals	-0.55	+0.10
Tip Clearance		+0.45
Airfoil Finish		+0.20
Life Features (Thicker blade edges, longer chord, better cooling)	+0.19	-0.40
Net Total	-0.56	+1.09

The predicted net effect of these changes is estimated to reduce exhaust gas temperature (EGT) by 20.6° C (37° F) and sfc by approximately 1.3%.

The above estimates apply to new engines. For long service engines, the single shank turbine should provide an additional 0.3% sfc decrease and 5.6° C (10° F) reduction in EGT due to the elimination of the mateface shank leakage discussed above. This sums to a sfc benefit of 1.6% and an EGT reduction of 26.1° F (47° F) for long service engines.

3.3 OVERALL DESIGN APPROACH

The design approach chosen for the single shank turbine is based upon the proven successful CF6-50 turbine design. This design incorporates relatively large size airfoils in reduced numbers relative to the CF6-6 for improved ruggedness and lower cost. In addition, numerous design features of the CF6-50 turbine were incorporated such as:

- Lightweight blade dampers

- Over-under rotor stator cavity baffles

- Intrarotor centrifugal pump for cooling air delivery to
  Stage 1 blades.

These features offer the demonstrated reliability of the CF6-50 and also offer the potential for further performance improvements by reducing the cavity cooling air requirements.

Another aspect of the chosen design approach was to utilize technology to further enhance performance and reliability. This is particularly evident in the approach taken to blade cooling where highly sophisticated cast coring was used in both stages. This technology permitted the judicious reduction in cooling flows without the expected compromises in metal temperature levels. In addition, significant amounts of weight were saved in spite of overall reductions in component stress levels for enhanced life.

Further improvements in overall turbine performance were achieved by utilization of an improved shroud support system as described in Section 3.1. This support system was an integral part of the redesign and was executed in such a fashion as to achieve the desired clearance benefits along with improved cooling air screening capability and better containment capability. These features were incorporated without adversely affecting the good maintainability feature of the current design.

3.4   DESIGN DESCRIPTION

3.4.1   Rotor

In keeping with the overall design approach, the rotor design was done in a fashion which blended the proven features of the CF6-50 with current design and manufacturing technology. This design approach utilized the following key design features:

- Large blades/fewer in number

- Effective blade damping

- State-of-the-art cooling technology

- Conservative design thickness/stress

- Proven rotor structural concept.

The turbine blade design is cast-cored and has most of the cooling system cast-in as an integral feature. Wall thicknesses are relatively thick having been sized to meet the requirements of the LM2500 marine environment. However,

the key design feature is the use of the lightweight damper system which has proven so successful on the CF6-50 on the core engine instrumented test which measured blade vibratory response. Ruggedness is also enhanced by increasing airfoil size while reducing numbers of blades. This has the side benefit of reducing hardware costs. Blade suction sides are polished to achieve an additional benefit in overall turbine efficiency.

The rotor structure bears a strong family resemblence to the current CF6-6D turbine and to the CF6-50 turbine. All materials are the same in these rotors as are the methods used to manufacture them. The CF6-50 and the improved single shank rotors both have a spacer between the Stage 1 and 2 disks which have radial vanes and a cover over these vanes. This is done to deliver cooling air to the Stage 1 blade at a higher pressure and thus improve cooling efficiency. Interfaces with the compressor shaft and the aft bearing are unchanged. Only small modifications to the current midframe liner are required to make the single shank turbine interchangeable with the original design. This modification involves machining approximately 3.5 mm (0.14 in.) from the inner flowpath liner and adding a simple ring seal.

Design and analysis of the rotor structure have been ongoing throughout the program. This effort involved extensive computer analysis which investigated steady-state and transient effects. In addition, operational severity, commonly called "mission mix", has been included in the life analysis. In areas where it was appropriate, model and/or photoelastic testing has been conducted to verify analytical results. Results of this work will provide the basis for Shop Manual life limits for all rotating turbine hardware as required by Government regulation.

In summary, the turbine rotor design is based on the successful features of the CF6-50 and blending in proven manufacturing technology. The design is interchangeable when minor modifications are made to the turbine midframe.

3.4.2 Stator

The improved single shank turbine stator design was carried out with the objective of improved life and increased performance using components which used current state-of-the-art capabilities in both the design and fabrication of parts. The design of the stator includes:

- An improved cooling scheme for the Stage 1 vane

- An aerodynamically redesigned Stage 2 vane

- Improved wheelspace cavity baffling

- Stator structure designed for improved clearance control.

The Stage 1 vane has been designed using the same cast-cored cooling features normally used in blade design. Leading and trailing edge cooling

circuits have increased area for reduced losses in coolant flow pressure drop. The trailing edge has cast-in cooling slots with turbulence promoters in the slot walls. A cast pin fin array precedes the trailing edge slots. The vane wall thicknesses have been increased and cast-in ribs added to prevent ballooning of vane walls and to precisely locate impingement inserts. The large radius of the vane leading edge reduces local heat flux and allows the use of a greater concentration of film cooling holes.

The Stage 2 vane has an increased chord and minor flowpath changes required for better rotor-to-stator matching and reduced exit swirl. This vane also uses cast-in cooling features, along with casting changes made to provide a more rugged design.

Wheelspace baffles and interstage seals are designed as fabricated sheet metal components. The interstage seals have honeycomb surfaces for sealing at the rotor seal teeth and are designed so as to be positioned and retained without the use of a bolted joint. These baffles and seals provide the improved wheelspace cavity baffling through the use of a cylindrical surface which maintains a close clearance both radially and axially with the mating cylindrical surfaces on the blades.

The Stage 2 nozzle support also carries the shrouds for the Stage 1 and 2 blade tips. This support has been designed to provide stiffening rings over the Stage 1 shroud. These rings make the stator more resistant to both axisymmetric and asymmetric distortions induced by engine operation. The Stage 2 nozzle support has an improved cooling design and provides a better rotor-to-stator thermal match. The support is machined from a ring forging in much the same fashion as the original support.

Overall, the turbine stator design incorporates design features based on current manufacturing capability which are aimed at improved life and increased performance. The design is in keeping with the CF6-6 and CF6-50 design philosophy and closely resumbles both engines. The stator is interchangeable as an assembly when used with the twin shank turbine rotor.

3.4.3 Maintainability

Maintainability features of the improved turbine are very similar to the original production design. The biggest differences are in two areas:

1. The cooling air screen for the Stage 1 vanes is attached to the Stage 2 nozzle support in the original production design. On the single shank design, the screen is attached to the Stage 1 vane assembly. This allows the Stage 2 nozzle support to be removed without disturbing the screen assembly. This feature was built in at the request of the airlines.

2. The turbine rotor Stage 1 disk rim is bolted to the forward shaft and thermal shield by a bolt which is torqued from the head into a captive nut. This is as opposed to as bolt/stud arrangement in the original design. The overall rotor assembly is not grossly changed by this feature.

No other significant changes in maintainability features have been made.

3.4.4 Safety

Safety of the improved turbine is as good or better than the original design. Overall reliability should be significantly enhanced as previously discussed. Larger blades are used but the strength of the shroud support, and, therefore, containment capability is significantly increased for the Stage 1 blades. From an overall point of view, conservative design features throughout the turbine will provide a safe design to at least currently achieved levels.

4.0 COMPONENT PERFORMANCE TESTS

4.1 STAGE 1 VANE CASCADE TEST

High pressure Stage 1 vane designs are required to use a large quantity of cooling air to control the metal temperatures in a severe thermal environment. This cooling air is used to convection cool the inside of the airfoil and is then expelled through airfoil and band holes to film cool the gas-side metal surfaces. The addition of this cooling air to the gas stream causes a turbine performance penalty in the form of a flowpath total pressure loss. The objectives of this test program were to compare the aerodynamic efficiency of the original CF6-6 production Stage 1 vane and a new CF6-6 Stage 1 vane (single shank) design with full cooling air, and to determine the aerodynamic efficiency effect of various rows of airfoil and band cooling injection.

4.1.1 Test Setup

The cascade tests were set up using eight vanes (four vane pairs) welded together as shown in Figure 7. A schematic of the test setup is shown in Figure 8 while Figure 9 shows the test cell with the vane cascade and supply systems. Engine conditions in terms of flowpath and cooling air pressure and temperature ratios were simulated. Shop air at its normal supply temperature of 43° C (110° F) was used for cooling air, requiring the gas stream to be heated to 354° C (670° F) to attain the proper engine gas stream to coolant temperature ratio. The cascade exhausted to atmospheric pressure, requiring a gas stream pressure of 17.72 N/cm^2 (25.17 lb/in.^{2}) to match the design engine pressure ratio. To obtain the correct design cooling flow, the cooling air feed pressures were set at 18.04 N/cm^2 (26.17 lb/in.^{2}) at the outer band and 18.13 N/cm^2 (26.3 lb/in.^{2}) at the inner band. The data were recorded on two X-Y plotters which recorded the circumferential traces of upstream total pressure minus downstream total pressure and downstream total temperature.

4.1.2 Instrumentation

The instrumentation used in setting the above conditions consisted of a thermocouple and three total pressure probes installed ahead of the vane cascade and a thermocouple and static pressure probe in each of the inner and outer coolant feed plenums. The downstream data were taken with a total pressure probe and thermocouple which were attached to an actuator system that provided control of the angle, radial position, and circumferential travel speed of the probe. The actuator system is shown in Figure 10.
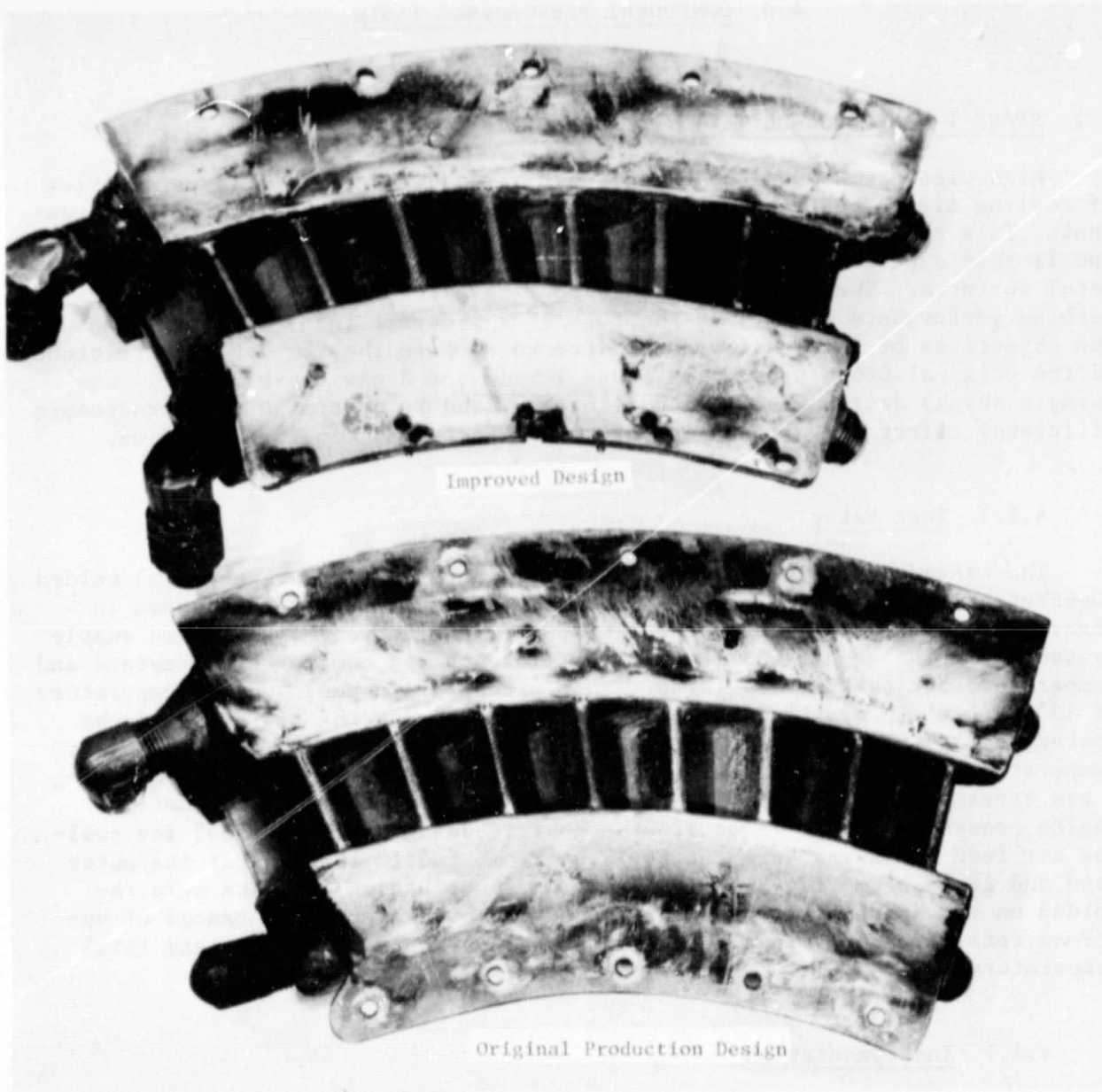
Improved Design

Original Production Design
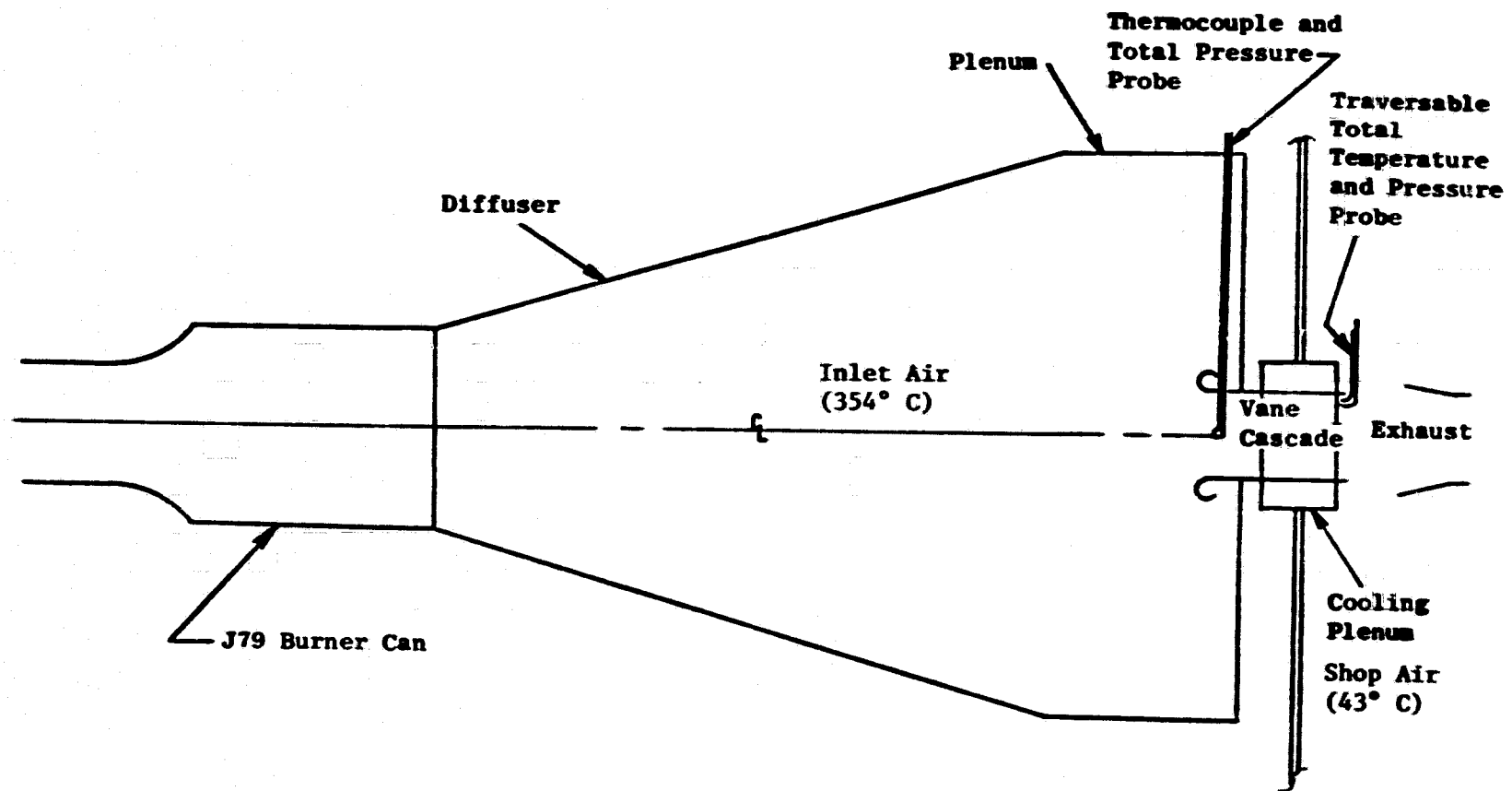
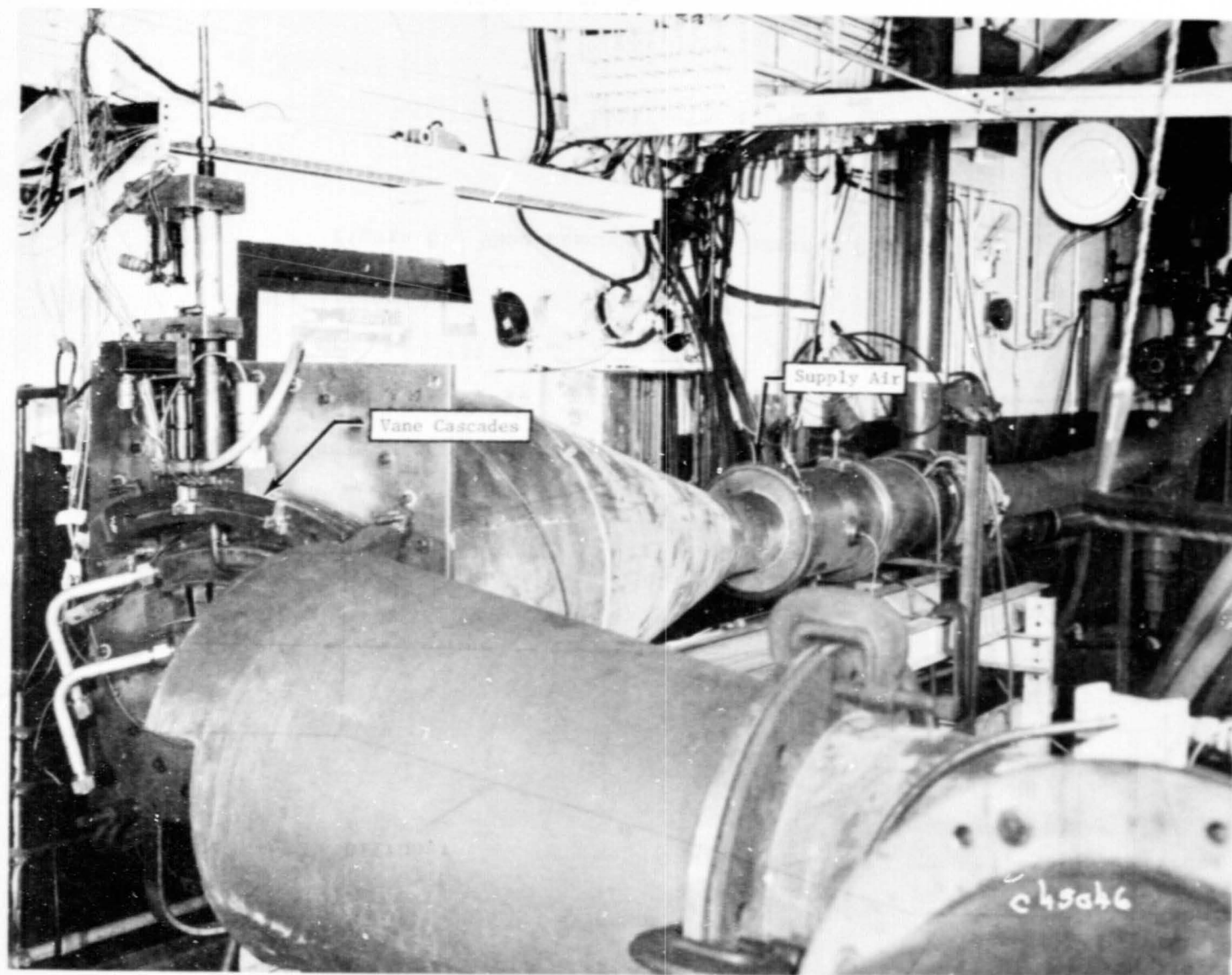Figure 7. Vane Cascade (Forward Looking Aft).

18

Figure 8. Vane Cascade Test Schematic Drawing.

Figure 9.   Vane Cascade Test Setup.

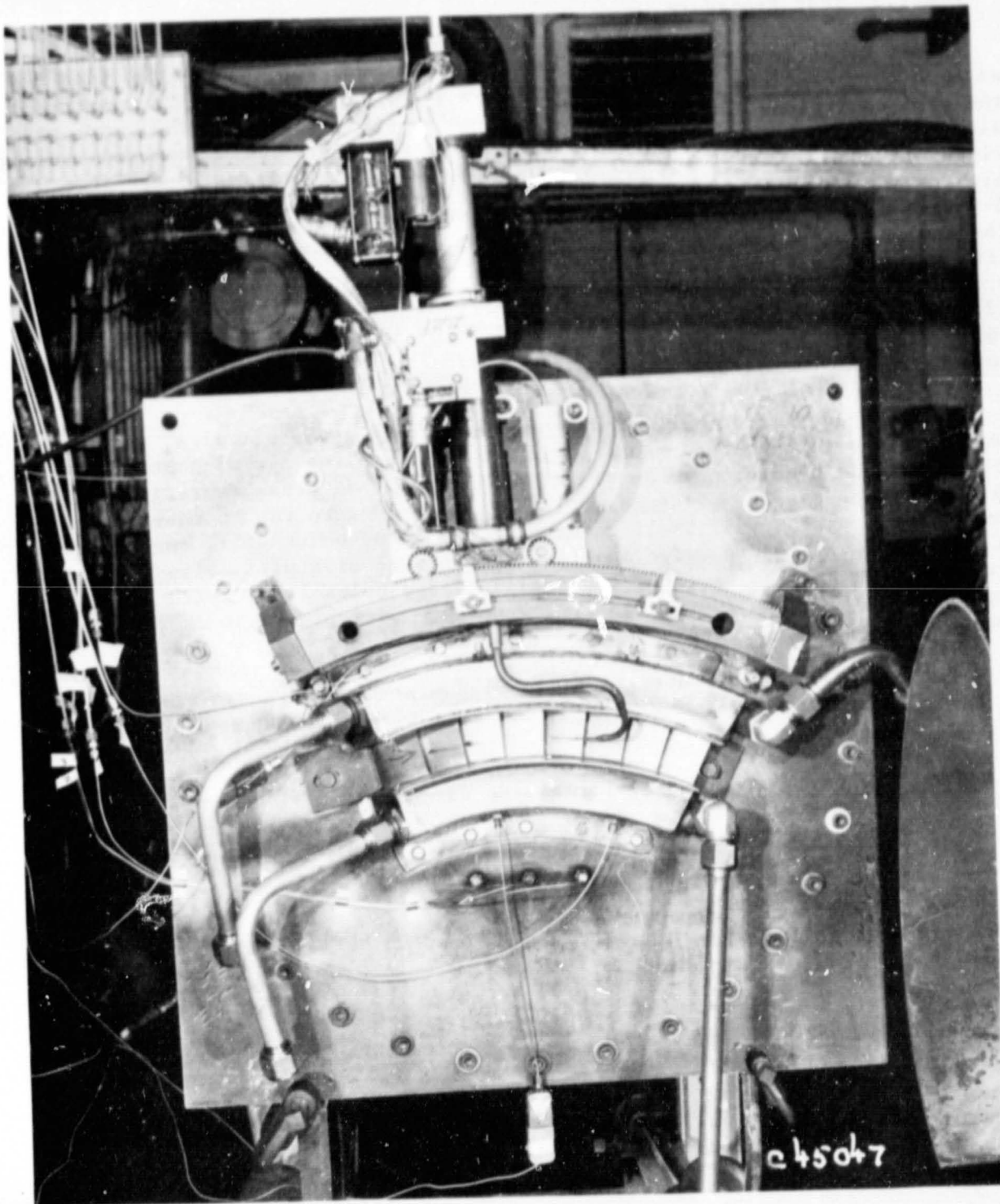Figure 10.   Total Pressure and Thermocouple Actuator System.

21

4.1.3 Test Procedure

Test Conditions - A total of 19 test points was run for the two vane designs with variations in the cooling flows and inlet condition. A summary of the test conditions for each point is given in Table II. Runs 2-11 were made with the original production vane. Run 2 was at design conditions and cooling flow while Run 3 was at a lower cascade pressure ratio and Run 4 was at a higher cascade pressure ratio. Design cascade conditions were used for Runs 6-9 with decreasing amounts of cooling air. This was accomplished by filling the cooling holes with a paste-like compound which hardens into a ceramic-like material and then sanding to a smooth contour. The cooling holes were progressively sealed as follows: band holes (6), suction side gill holes (7), leading edge and pressure side gill holes (8), and trailing edge holes (9). With all the cooling holes sealed, Run 10 was run at a low cascade pressure ratio and Run 11 was run at a high cascade pressure ratio.

The cascade hardware was then changed to the improved design, and the test points were repeated. Runs 12-14 had full cooling air with Run 12 at design cascade conditions. Run 13 at a lower cascade pressure ratio, and Run 14 at a higher cascade pressure ratio. Runs 15-19 were run at cascade design conditions progressively sealing these holes: band holes (15), suction side gill holes (16), leading edge and forward pressure side gill holes (17), aft pressure side gill holes (18), and trailing edge holes (19). With all cooling holes sealed, Run 20 was run at low cascade pressure ratio and Run 21 was run at high cascade pressure ratio.

For each test point, a total of 15 circumferential transverses was made at these radial locations: 2, 7, 10, 15, 20, 30, 40, 50, 60, 70, 80, 85, 90, 93, and 98% spans.

Data Analysis - Efficiency for a vane cascade is defined as:

$$\eta = \frac{\text{actual exit Kinetic energy}}{\text{ideal exit Kinetic energy}}$$

For the particular case where $P_{T, \text{coolant}} = P_{T, \text{mainstream}}$, the efficiency reduces to the classical cascade efficiency

$$\eta = 1 - \frac{\left(\frac{P_{S2}}{P_{T2}}\right)^{\frac{\gamma - 1}{\gamma}}}{\left(\frac{P_{S2}}{PTO}\right)^{\frac{\gamma - 1}{\gamma}}}$$

Where: P_{TO} = inlet total pressure

P_{T2} = exit average total pressure

P_{S2} = exit static pressure

22

Table II. Summary of Vane Cascade Test Conditions.

		Gas T_{IN}, 354° C; T_c, 43° C			Cooling Holes Flowing				
Run	Design	$T_{TIN, Gas}$ (N/cm²)	$P_{c, outer}$ (N/cm²)	$P_{c, inner}$ (N/cm²)	Band	Suction Side Gill	Leading Edge and Pressure Side Gill	Aft Pressure Side Gill	Trailing Edge
2	Original	17.72	18.04	18.13	X	X	X	---	X
3		16.20	16.50	16.58	X	X	X	---	X
4		20.27	20.64	20.75	X	X	X	---	X
6		17.72	18.04	18.13		X	X	---	X
7		17.72	18.04	18.13			X	---	X
8		17.72	18.04	18.13				---	X
9		17.72	18.04	18.13				---	
10		16.20	16.50	16.58				---	
11		20.27	20.64	20.75				---	
12	Improved	17.72	18.04	18.13	X	X	X	X	X
13		16.20	16.50	16.58	X	X	X	X	X
14		20.27	20.64	20.75	X	X	X	X	X
15		17.72	18.04	18.13		X	X	X	X
16		17.72	18.04	18.13			X	X	X
17		17.72	18.04	18.13				X	X
18		17.72	18.04	18.13					X
19		17.72	18.04	18.13					
20		16.20	16.50	16.58					
21		20.27	20.64	20.75					

The computer program "CADREX" was used to reduce the test data. This program uses a constant static pressure mixing assumption to integrate the exit pressure and temperature wake surveys.

4.1.4 Test Results

Typical pressure and temperature wake traverses are shown in Figure 11 for the original production airfoil and Figure 12 for the improved vane design. The pressure loss peaks correspond to the vane trailing edges. This total pressure loss is caused by airfoil boundary layer drag, trailing edge blockage, and cooling air injection. A total of 285 wake traverses was made for this test program.

A summary of the results of all tests is shown on Table III. The single value used to characterize each configuration was obtained by mass flow averaging the results at each of the radial traverse locations.

The fully cooled improved single shank vane has an aerodynamic efficiency equal to the fully cooled original production vane. Elimination of cooling flow caused an increase in efficiency in all cases, except when the trailing edge holes were plugged. Apparently, the roughness of the aerodynamic contour where the trailing edge slots were plugged caused more loss than was gained with elimination of the trailing edge flow.

Table III. Summary of Cascade Efficiency Results.

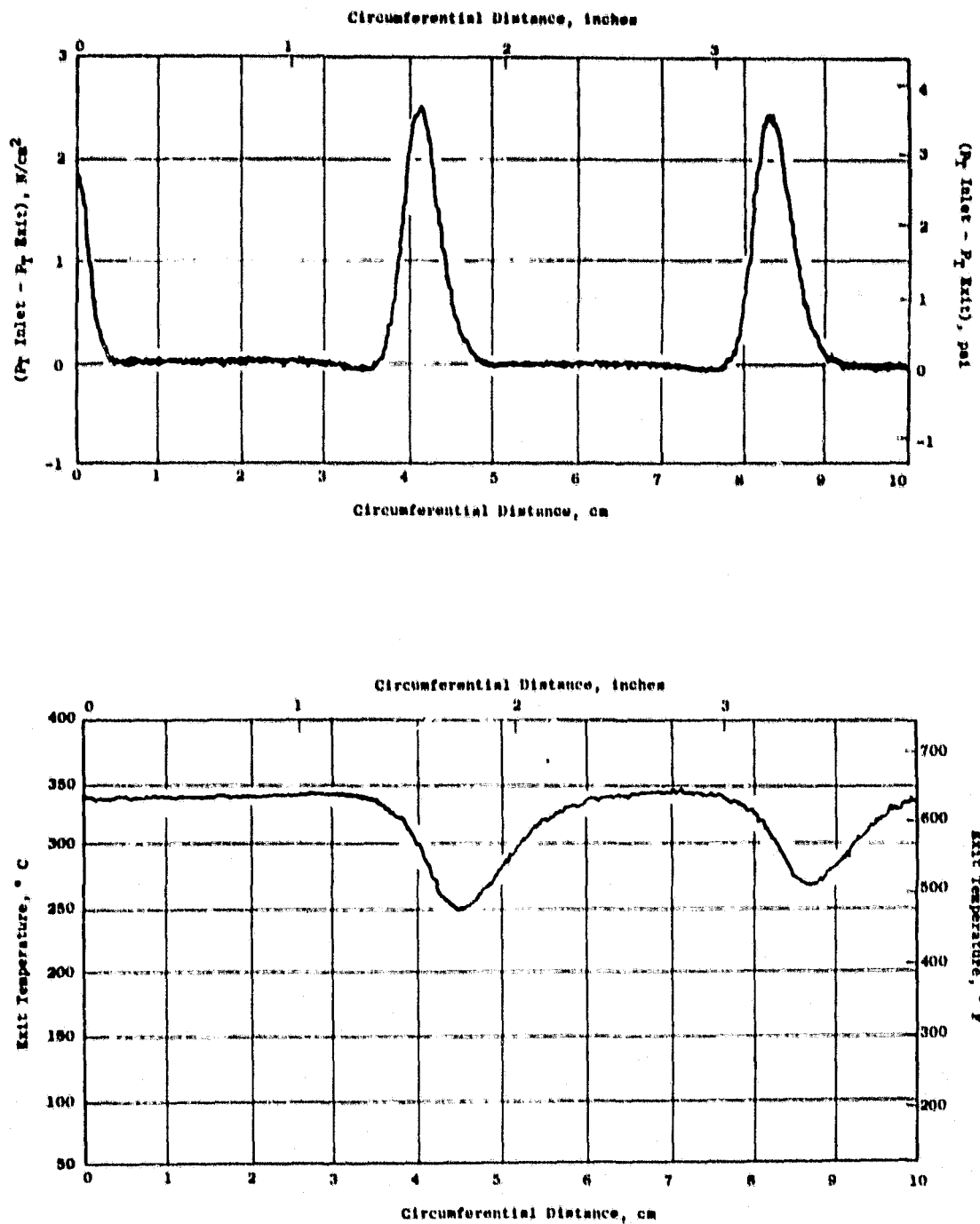| Vane Design | Cooling Holes Flowing | | | | | Percentage Points |
	Band	Suction Side Gill	Leading Edge and Pressure Side Gill	Aft Pressure Side Gill	Trailing Edge	
Original	X	X	X	---	X	0 (Base)
Original		X	X	---	X	+0.31
Original			X	---	X	+0.70
Original					X	+0.91
Original						+0.80
Improved	X	X	X	X	X	+0.04
Improved		X	X	X	X	+0.55
Improved			X	X	X	+0.95
Improved				X	X	+1.26
Improved					X	+0.96

Figure 11. CF6-6 Stage 1 Vane - Original Production Design, Full Cooling Air, 50% Span, Pressure and Temperature Traverse.
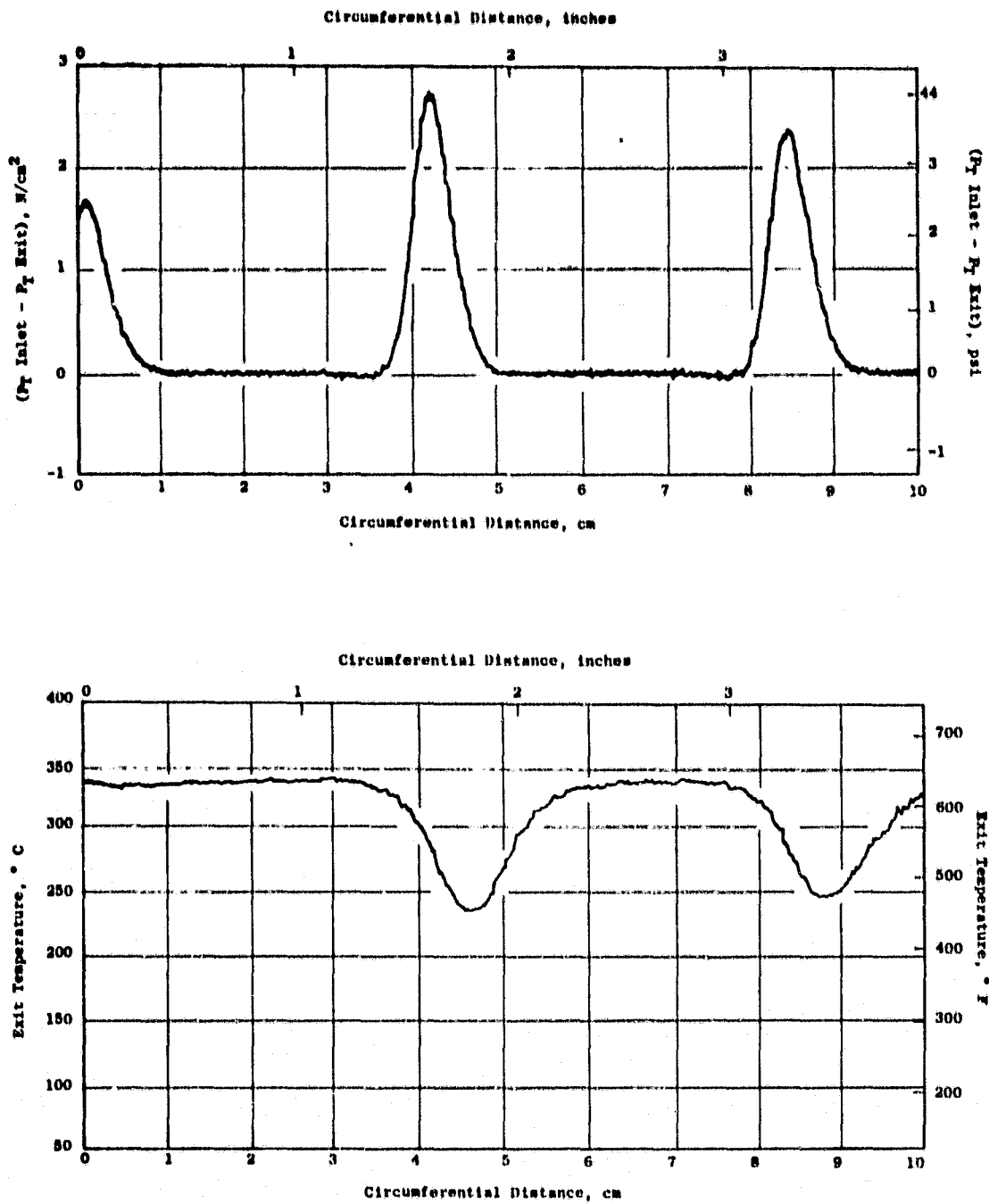
Figure 12. CF6-6 Stage 1 Vane - Improved Design, Full Cooling Air, 50% Span, Pressure and Temperature Traverse.

4.2 STAGE 2 VANE LEADING EDGE FLOW EVALUATION

The objective of this program was to obtain and compare flow character-istics between the vane shell and impingement insert, and radially within the insert for the original production and improved Stage 2 vane designs. This was accomplished by measuring the static pressure distribution between the vane shell and the insert, and radially within the insert cavity with con-trolled supply and discharge pressures.

4.2.1 Test Setup

The test models were actual vane segments and inserts having pressure taps attached to both the pressure and suction side walls. The basic differ-ence between the two designs as related to this test was the enlarged flow entrance area into the improved insert. The objective of this increase in inlet flow area was to reduce the static pressure drop through the inlet by lowering the velocity of the air in this region.

The test configuration shown in Figure 13 consisted of the vane to be tested having the insert of the vane attached to a supply plenum at the outer band and another plenum attached to the inner band discharge. The inner band plenum was designed to allow back pressuring of the fluid circuit to simulate engine pressure ratios.

4.2.2 Instrumentation

In order to determine the vane flow distribution between the vane shell and the impingement insert, pressure taps were installed through the shell on both the pressure and suction sides. Pressure tap locations used for both the original and improved designs are shown in Figure 14. The locations were selected to allow measuring the pressure between the insert holes to avoid sensing total pressure contributions from an impinging jet. A total of 58 pressure taps was installed in the original design vane and 63 pressure taps were installed in the improved vane.

Pressures were recorded using both mercury and water-filled manometers. Airflows were measured with a rotometer and orifice measuring devices.

The radial pressure distribution inside the inset was determined by tra-versing the insert cavity with a static pressure probe at five selected radial positions. These radial positions are shown by the dashed lines in Figure 14.

4.2.3 Test Procedure

The test procedure consisted of supplying air to the model and then back-pressuring the plenum attached to the inner band to the desired pressure ratio. The vane trailing edge holes discharged to ambient pressure. The
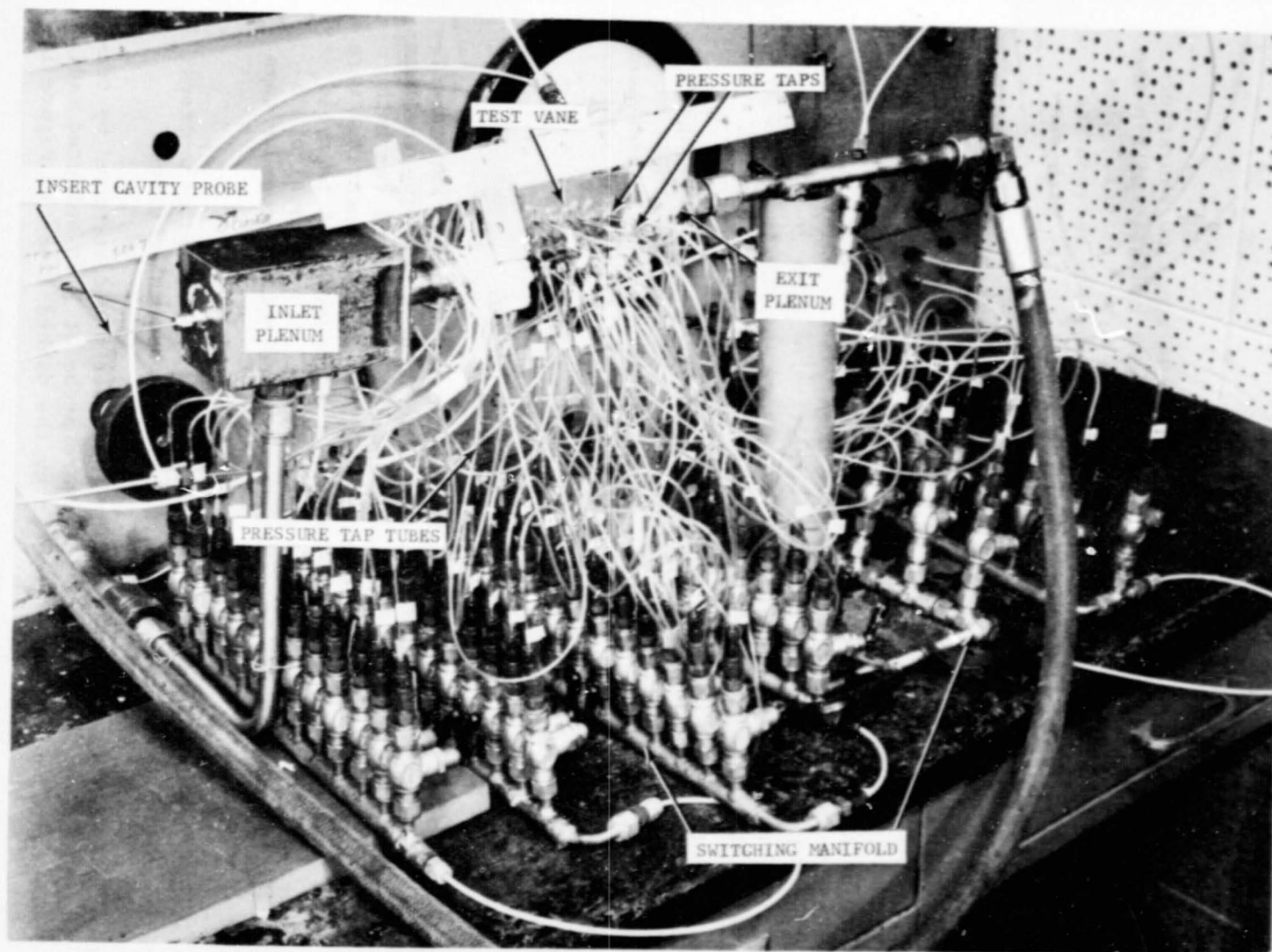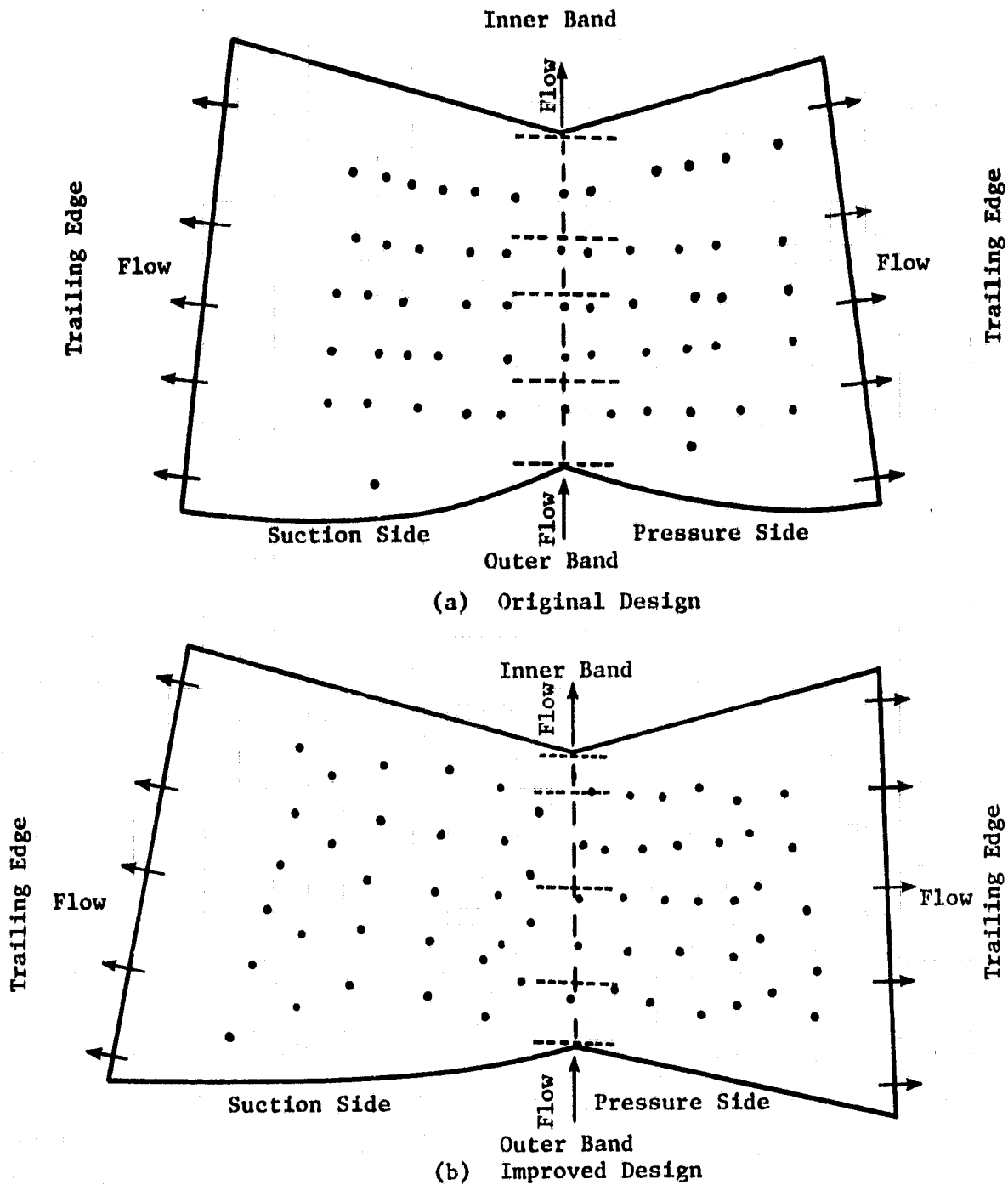
Figure 13. Test Setup for Stage 2 Vane Flow Evaluation Tests.

Inner Band

Trailing Edge

Flow

Flow

Trailing Edge

Flow

Suction Side   Pressure Side

Outer Band

(a) Original Design

Inner Band

Trailing Edge

Flow

Flow

Trailing Edge

Flow

Suction Side   Pressure Side

Outer Band

(b) Improved Design

● Denotes Pressure Tap Location   ----- Denotes Probe Locations

Figure 14.   Schematics Showing Surface Pressure Tap Locations on
             Original and Improved Design Vanes.

29

pressure ratios from the supply plenum to the inner band plenum and to ambient at the trailing edge were set to match engine design point conditions. Once a test point was established, pressure and airflow readings were recorded. Each pressure tap was monitored individually using either water or mercury manometers as the pressure levels dictated. Coolant flow rates were measured at the inlet plenum (outer band) and at the inner band exit. The trailing edge flow was determined to be the difference of the measured flows. Pressure measurements at the inlet and exit plenums were recorded as well as at the pressure tap locations. Five radial locations in the insert cavity were measured using the pressure probe.

4.2.4 Test Results

At design point conditions, pressure drop measurement through the insert impingement holes showed a 20% variation from the average for the original design. Similar data for the improved design resulted in a 6% variation from the average. These percentages are indicative of local flow variations for the respective designs. Spanwise pressure measurements within the original design inserts showed a 4% loss at the insert inlet (outer band) with an average loss in the insert of 1% of the inlet pressure. Correspondingly, the improved design had a 1% pressure loss through the insert inlet (outer band) and no detectable loss radially within the insert. Enlargement of the improved design insert inlet area has reduced the static pressure loss resulting in a reduction of the radial pressure gradient within the insert. This has eliminated the low impingement ΔP condition at the outer band.

The pressure and flow data revealed that when extrapolated to engine conditions, the flow split between the trailing edge holes and the inner band exit is different than the calculated design intent as illustrated in Figure 15. The difference is due to the trailing edge holes being undersized in both the current and improved vanes. The trailing edge holes would have to be enlarged in order to achieve the design flow split.
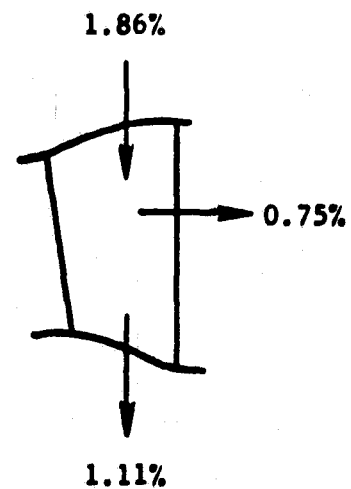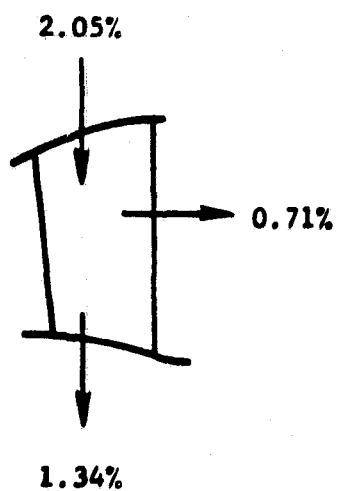
Original   Improved

Engine Design Point Conditions

2.05%   1.85%

1.15%   1.25%

0.90%   0.60%
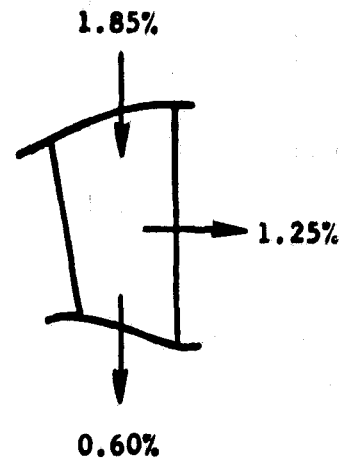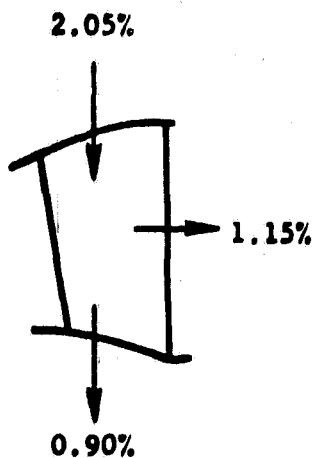
Bench Test Results

2.05%   1.86%

0.71%   0.75%

1.34%   1.11%

Note: All Flows are Percent of Compressor Inlet Flow

Figure 15.   Design Point Comparison of Flow Splits at Engine
             Design Point and Bench Test Conditions for Original
             and Improved Stage 2 Vanes.

5.0 COMPONENT HEAT TRANSFER TESTS

5.1 STAGE 1 VANE TRAILING EDGE TEST

The objective of this test was to experimentally determine the heat transfer and pressure loss characteristics of the Stage 1 vane trailing edge flow passages. In particular, the effect of rib-type turbulence promotors was investigated. Comparisons were made between a smooth duct and three turbulence promoting configurations.

5.1.1 Test Setup

A 10X scale model simulating a single trailing edge flow passage of the improved turbine design shown in Figure 16 was utilized. Four configurations of passage geometry and rib type were investigated and are shown in Figure 17. The first configuration was a smooth duct to establish baseline heat transfer coefficient levels. The second configuration had 2.5 mm square ribs directly opposite on opposing endwalls. The third configuration had the 2.5 mm square ribs, as described previously, with the addition of 2.5 mm radiused ribs mounted on the remaining partition walls spaced between the square ribs. The fourth configuration was the design configuration which had 2.5 mm square ribs on the two opposing endwalls; however, the ribs were not directly opposite one another but were arranged in a staggered array. The test model is shown schematically in Figure 18.

Photographs of the test configurations and the assembled model are presented in Figures 19 through 22. Configuration 2 is not shown because it is the same as Configuration 3 without the partition wall ribs.

5.1.2 Instrumentation

The turbulence promotor section (Figure 18) contained the data heaters. Eight individual data heaters were located on the four sides of the passage and split the passage into two axial segments. Data heaters are heated copper plates whose heat loss due to assigned mass flow rates was used to determine corresponding heat transfer coefficients. The endwall ribs were simulated as 2.5 mm square cross sections. Guard heaters to minimize axial heat losses were located on each end of the data heater section. At the exit end of the turbulence promotor section, the passage converged and discharged to ambient pressure.

The data heaters were fabricated from copper plate. Electrical heaters and two thermocouples were silver-soldered to the plate backs. This allowed soft soldering of ribs to the test surfaces of the plates. In assembly, asbestos insulation was placed on the heater ends to minimize contact between heaters. The heaters were bonded to the Textolite housing sides with RTV adhesive.
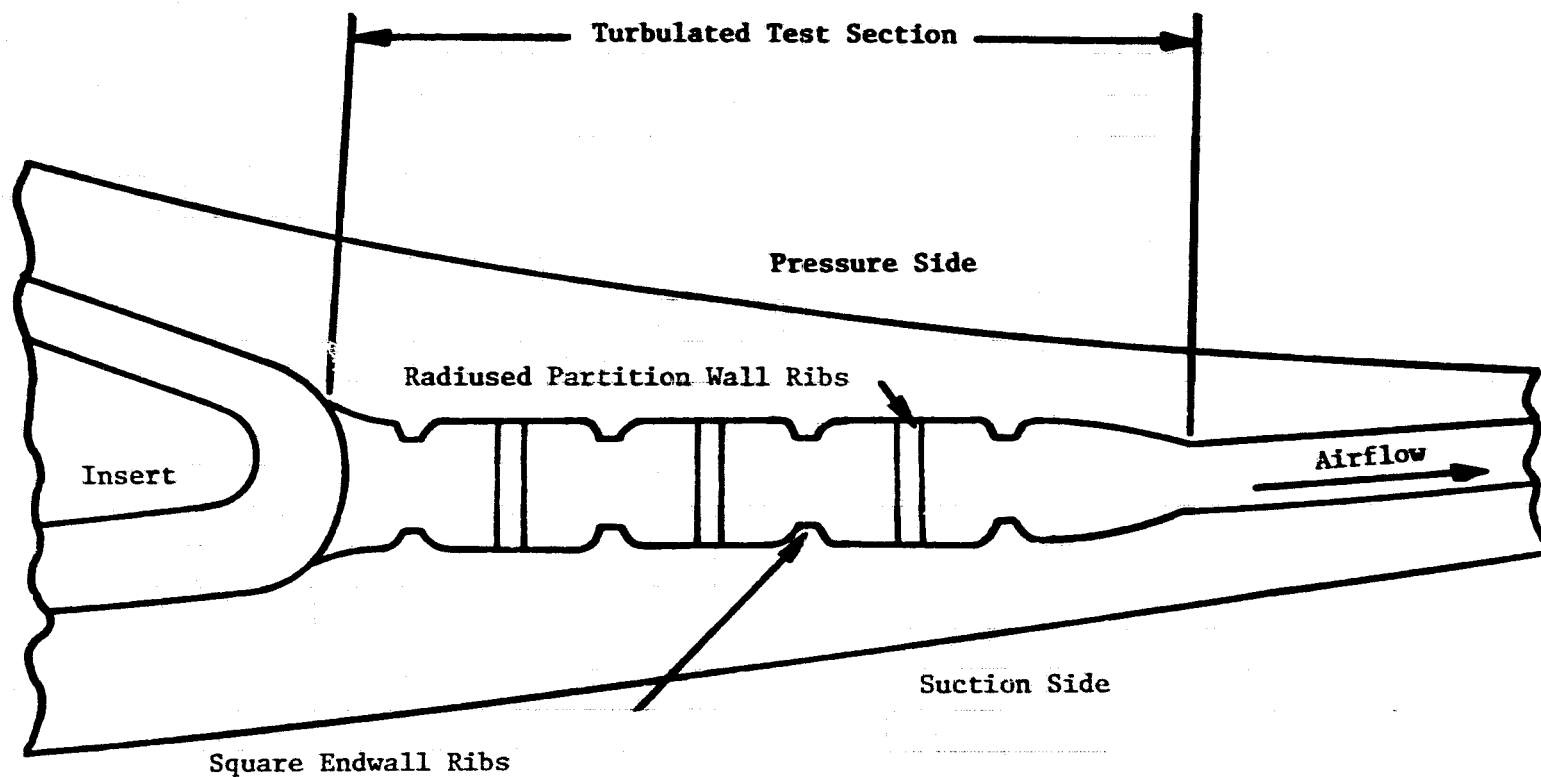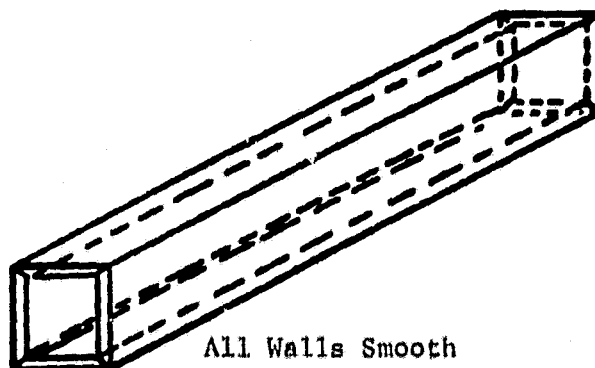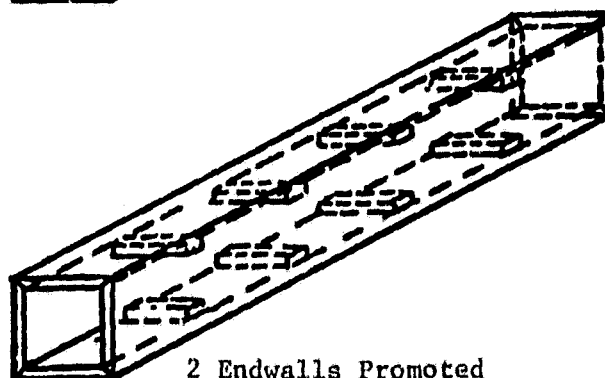
Figure 16. Pitchline - Stage 1 Vane Trailing Edge Cross Section.
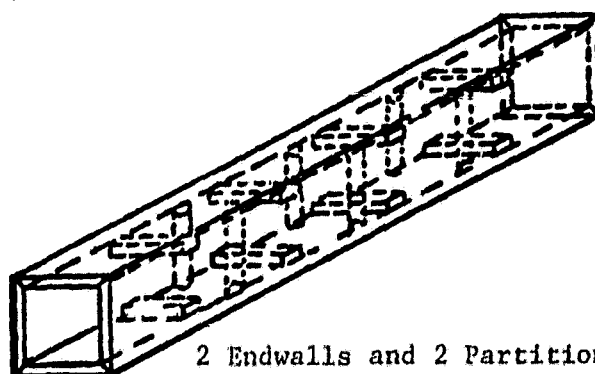
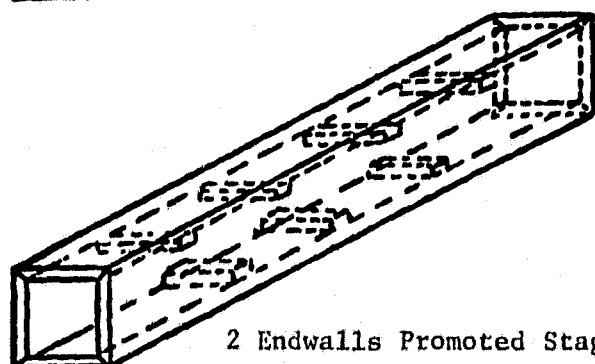Configuration 1 — All Walls Smooth

Configuration 2 — 2 Endwalls Promoted

Configuration 3 — 2 Endwalls and 2 Partition Walls Promoted

Configuration 4 — 2 Endwalls Promoted Staggered
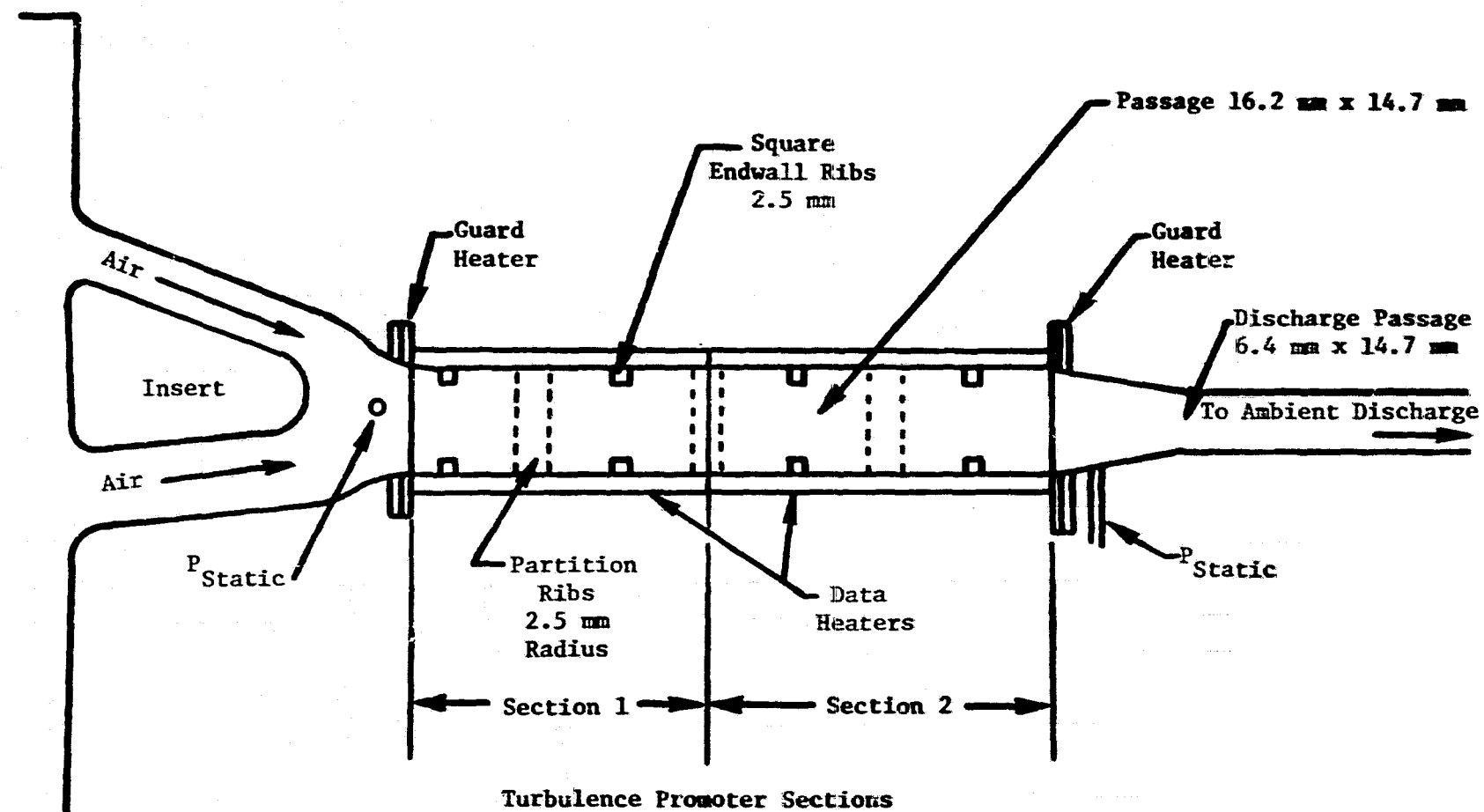
Figure 17.   Test Configuration Geometries.

34

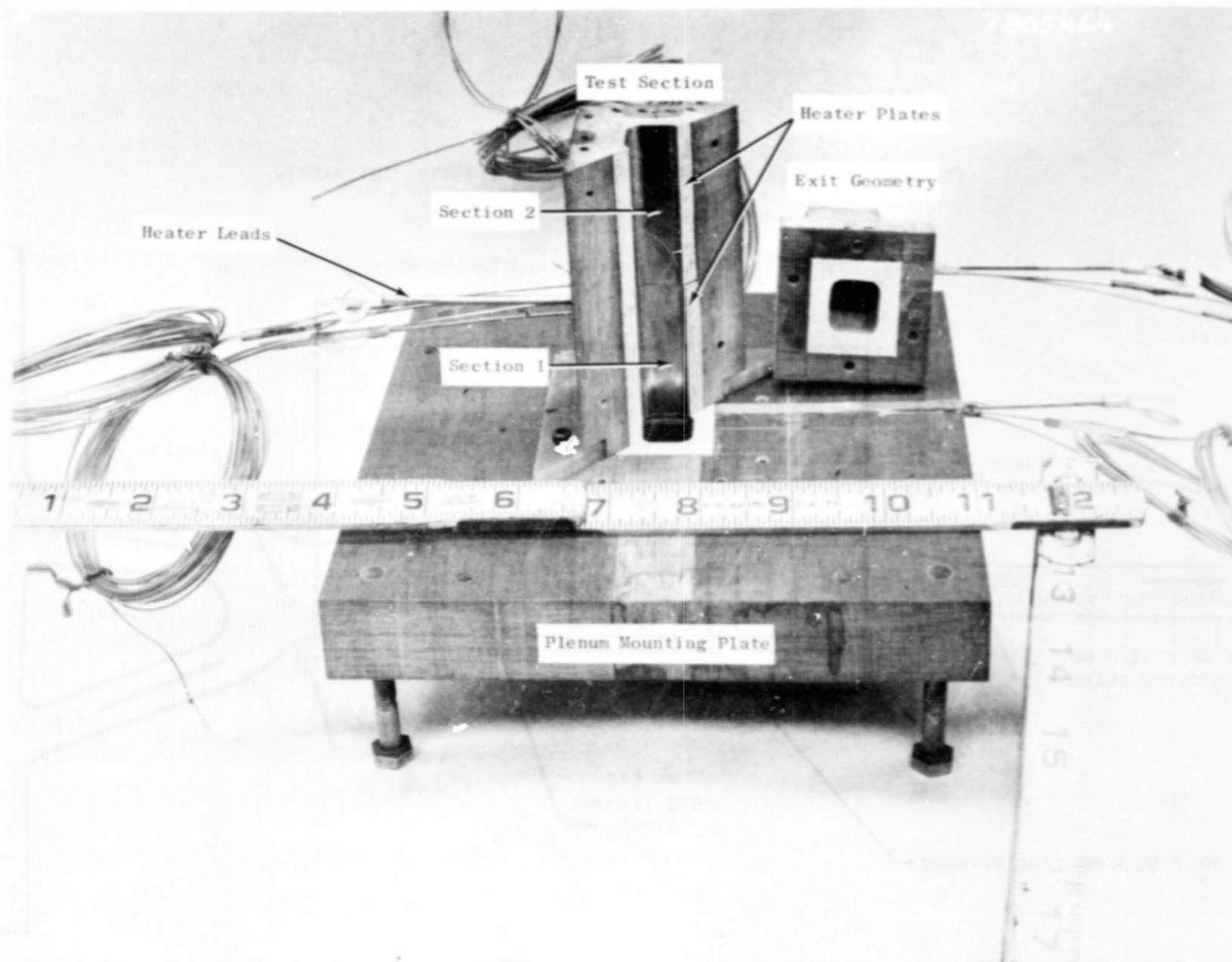Figure 18. Stage 1 Vane Trailing Edge Heat Transfer Model.

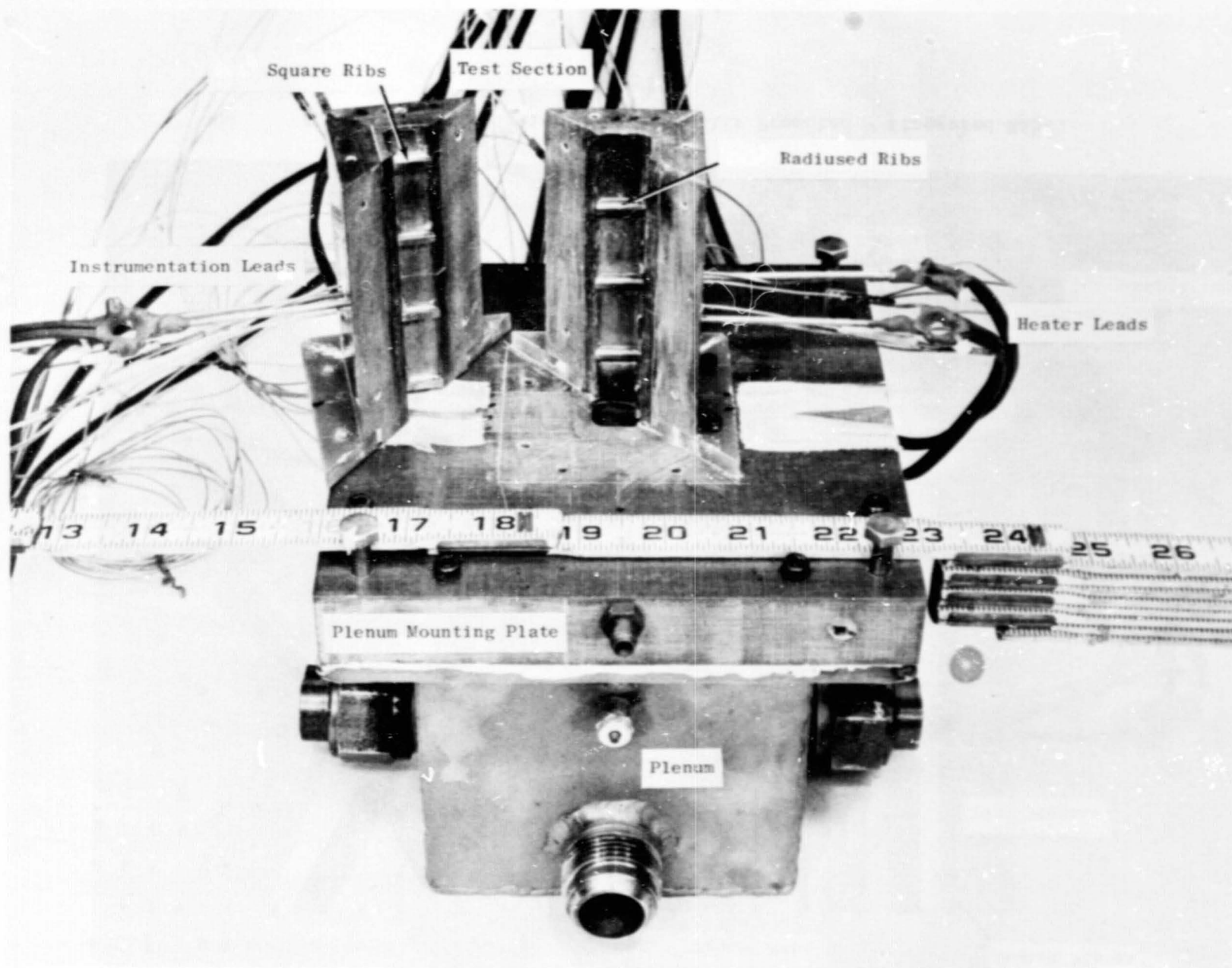Figure 19. Configuration 1, Smooth End and Partition Walls.

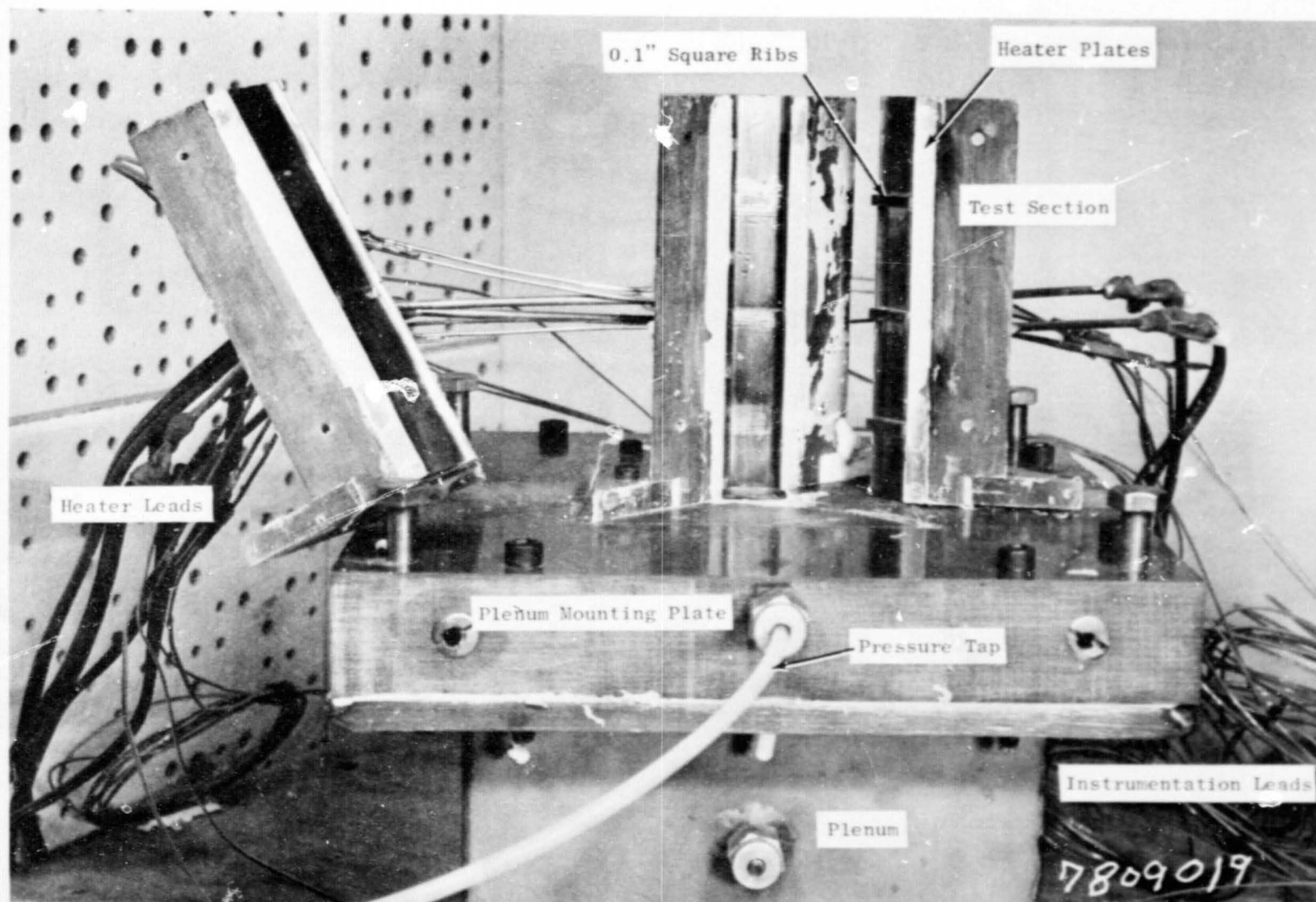Figure 20. Configuration 3, Two Endwalls Promoted and Two Partition Walls Promoted.

Figure 21. Configuration 4, Endwalls Promoted - Staggered Ribs.
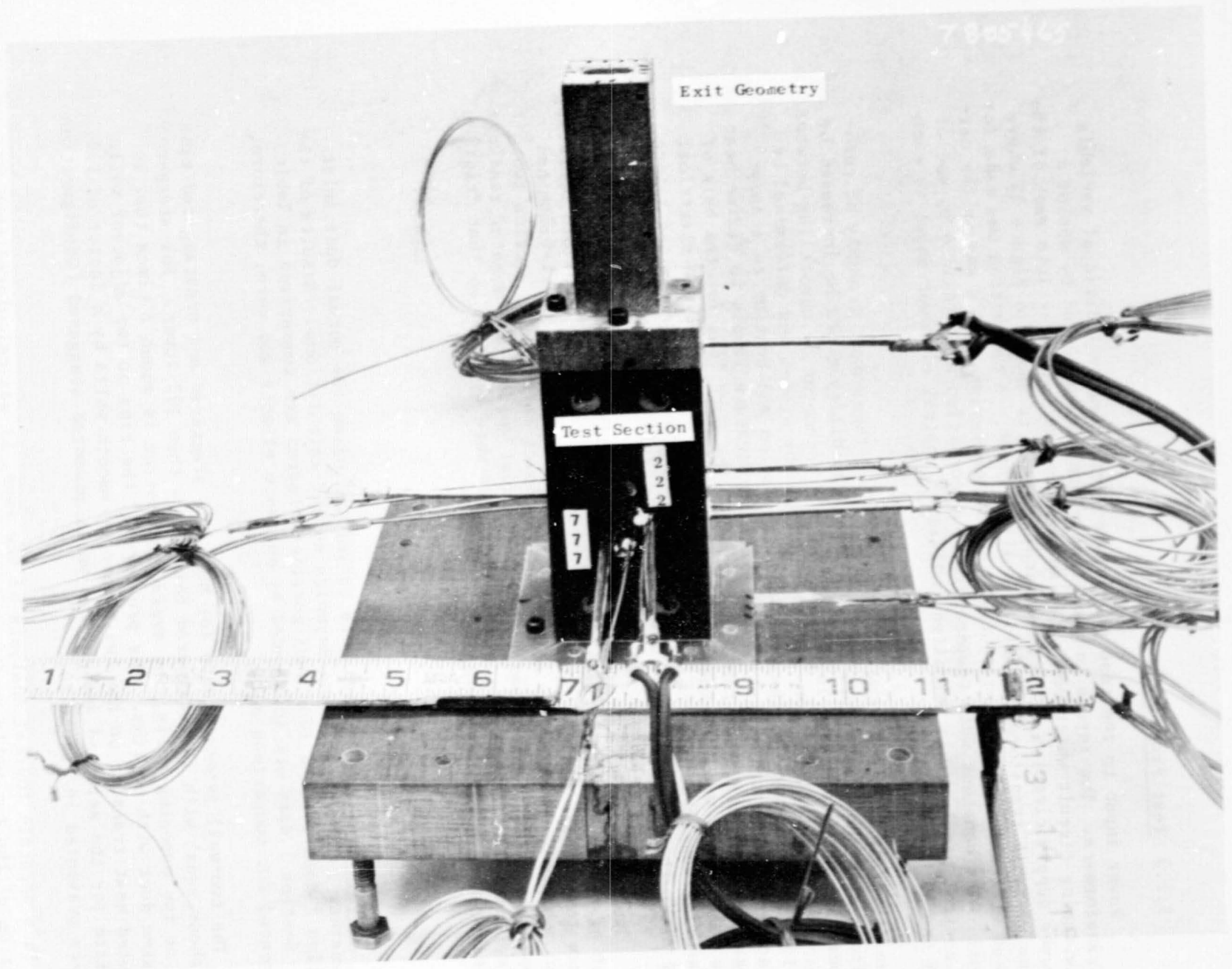
Figure 22. Assembled Model.

5.1.3 Test Procedure

Power input to the test plates was controlled by individual variable transformers. The inputs to each test plate were measured by use of a switching circuit which connected an ammeter and voltmeter into each of the power supply circuits. The electrical circuit is shown in Figure 23 where one variable transformer circuit is illustrated. A correction was made for lead wire and ammeter resistances when the measuring system was in the circuit. The constant wall temperature test condition was obtained by use of a control panel. This permitted individual control of power input to each of the 10 heaters.

The flow rate to the system was measured by a three-bank assembly of rotometers also shown in Figure 23. The flow capability could be increased by operating above atmospheric pressure at the rotometer by throttling between rotometer and test section. Heat loss from the system was determined by filling the interior of the duct with insulation and heating to steady-state conditions at several heater plate temperature levels to define heat loss from each heater in the test section. The heat loss for the bulk of the test points was less than 10%. Calibration curves for the electrical measuring equipment and the flow measuring equipment were obtained before and after the test to make acurate corrections for test readings.

The test operation consisted of setting a flow level and then adjusting each of the 10 individual variable transformers to obtain a uniform operating plate temperature of 96° C (205° F). After assuring that equilibrium had been achieved, the data for all 16 thermocouples in the test section two supply air thermocouples, and the 10 individual voltage and ammeter readings were recorded. In addition, plenum pressures were recorded so that friction pressure drop could be determined.

5.1.4 Test Results

Heat Transfer - The data were correlated using the actual duct inlet dimensions in the Nusselt and Reynolds number calculations. Results of the Section 2 data for the four configurations tested are summarized in Table IV. Section 1 data are influenced by entrance effects and were, therefore, presented for comparison only.

The two-wall promoted data for both the staggered and nonstaggered ribs are about equal with the staggered being less than 10% lower. For staggered ribs on two opposing walls, the average promotion is about 2 times that in the same duct with no ribs. The presence of the ribs on two adjacent walls promoted heat transfer on the two alternate smooth walls by a factor of 1.4. The data for the selected design, two walls promoted staggered (Configuration 4), are presented in Figure 24.

In a separate thermal analysis of the vane, it was calculated that the selection of the two walls promoted in the staggered matrix rather than the four walls promoted as the design configuration results in temperature increases of only 5.6° C in the promoted region and reduces the trailing edge temperature by 16.7° C.
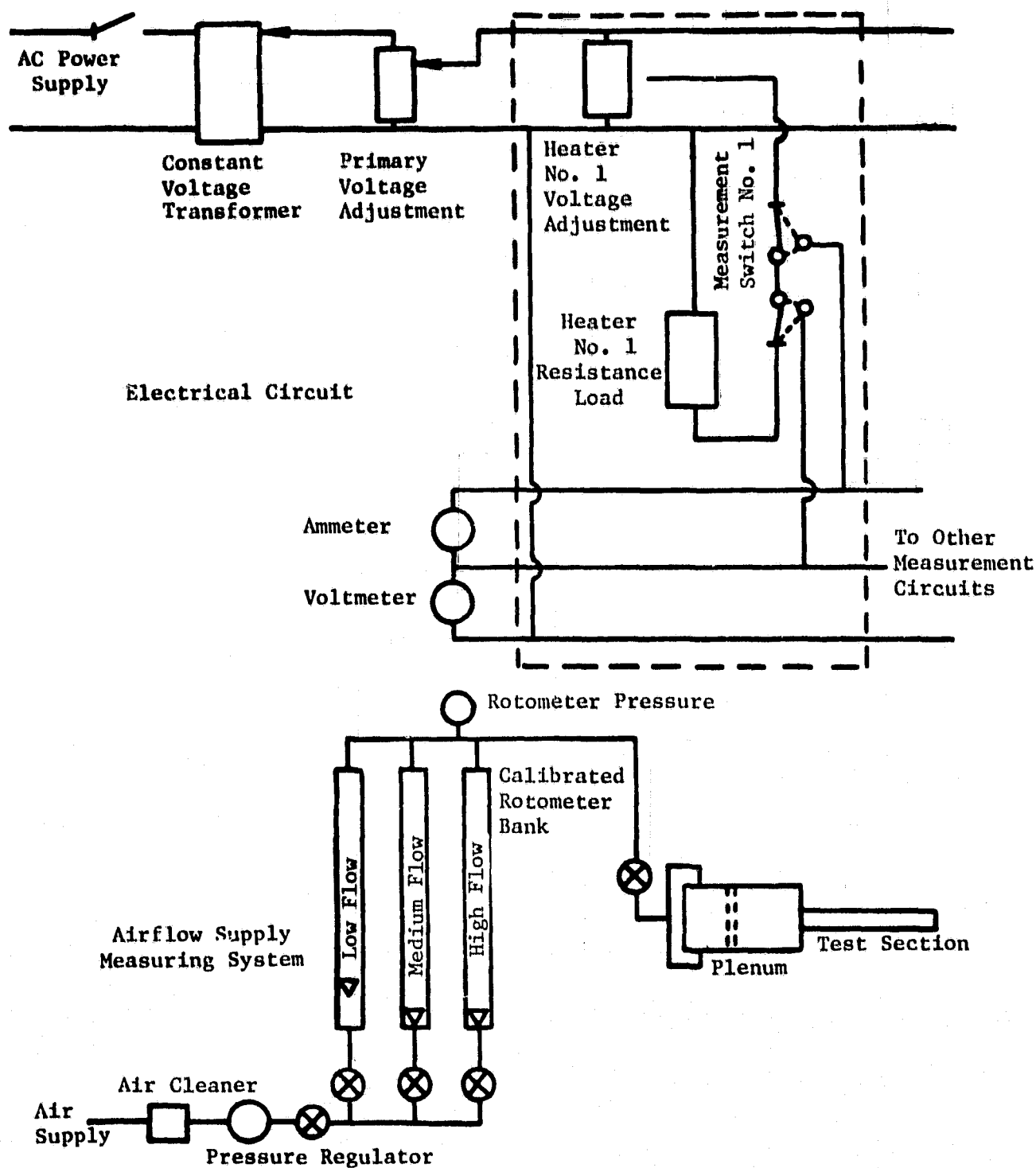
40

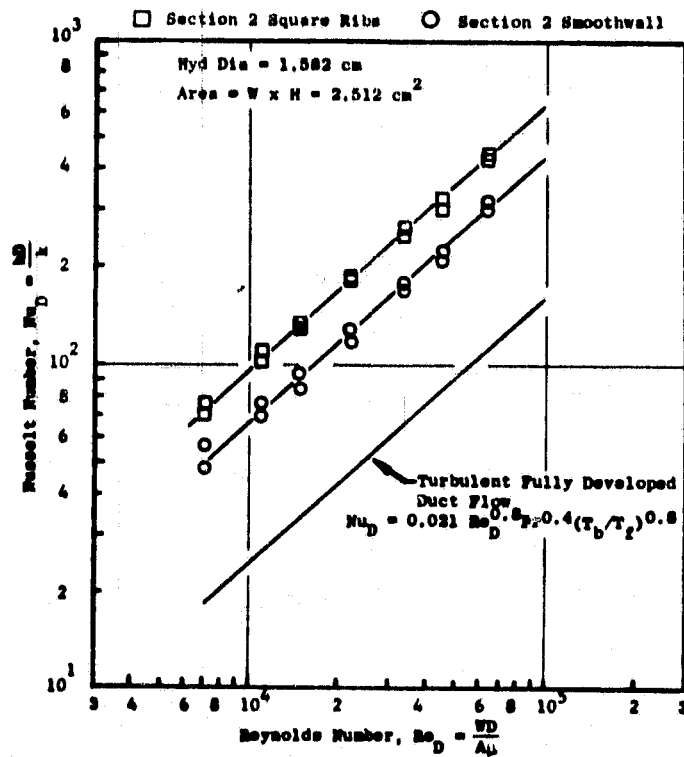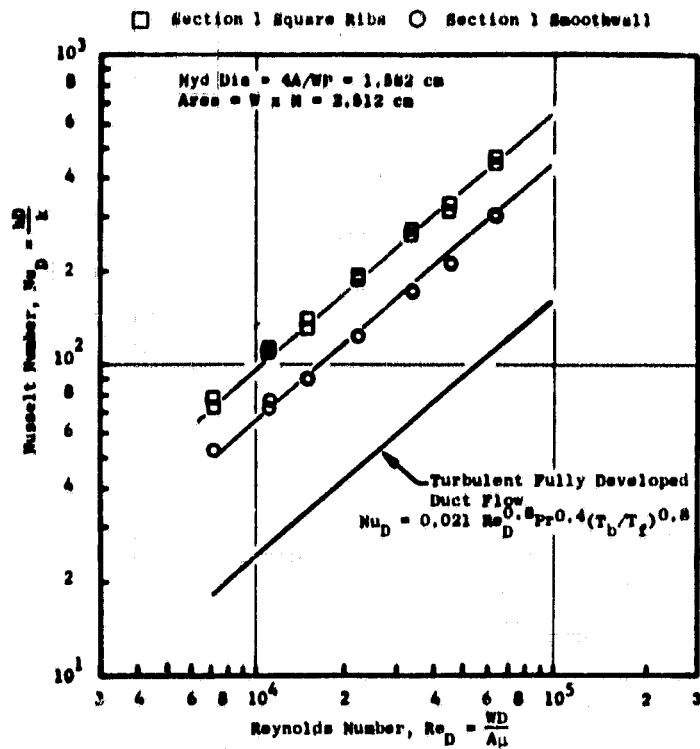Figure 23. Schematic of Electrical and Airflow Supply Measuring Systems.

Figure 24.   Stage 1 Vane Turbulence Promoter –
Two Walls Promoted Staggered.

Table IV. Heat Transfer Test Results.

No.	Configuration	Turbulence Promotion
1	All Walls Smooth	1.0 (Base)
2	Two Walls Promoted	
	• Smooth Partition Walls	1.67
	• Ribbed Endwalls	2.79
3	Four Walls Promoted	
	• Ribbed Partition Walls	2.47
	• Ribbed Endwalls	3.21
4	Two Walls Promoted Staggered	
	• Smooth Partition Walls	1.70
	• Ribbed Endwalls	2.44

Pressure Drop - Friction factors were determined from the pressure data. These calculations were based on maximum velocity and equivalent diameter dictated by the individual geometries. The data were correlated from experiments having the inlet and exit geometries removed. When the inlet and exit geometries were in place, realistic friction factors could not be calculated due to the indeterminable geometrical influence on the pressure measurements.

A comparison of the friction factor data correlations is shown in Figure 25. The friction factor of the four-wall promoted data is significantly higher (by approximately a factor of 2) than the two-wall nonstaggered data. The two-wall staggered rib data are at approximately the same level as the two-wall nonstaggered data. Smooth wall friction shows a descending trend as Reynolds number increases and is higher than the predicted level shown by the dashed line.

Friction factor data for the smooth passage of this model configuration were 2.1 times that for a straight smooth duct without entrance effects. This difference is attributed to entrance effects in the model data. The effects of two or four walls having turbulence promotor ribs increased the friction factor levels respectively to about 7.9 and 17.5 times that for a straight smooth duct.

5.2 STAGE 2 VANE LEADING EDGE TEST

The objective of this test was to investigate the Stage 2 vane leading edge region impingement heat transfer characteristics. Scale models of both the original production and the improved vane inserts were used.
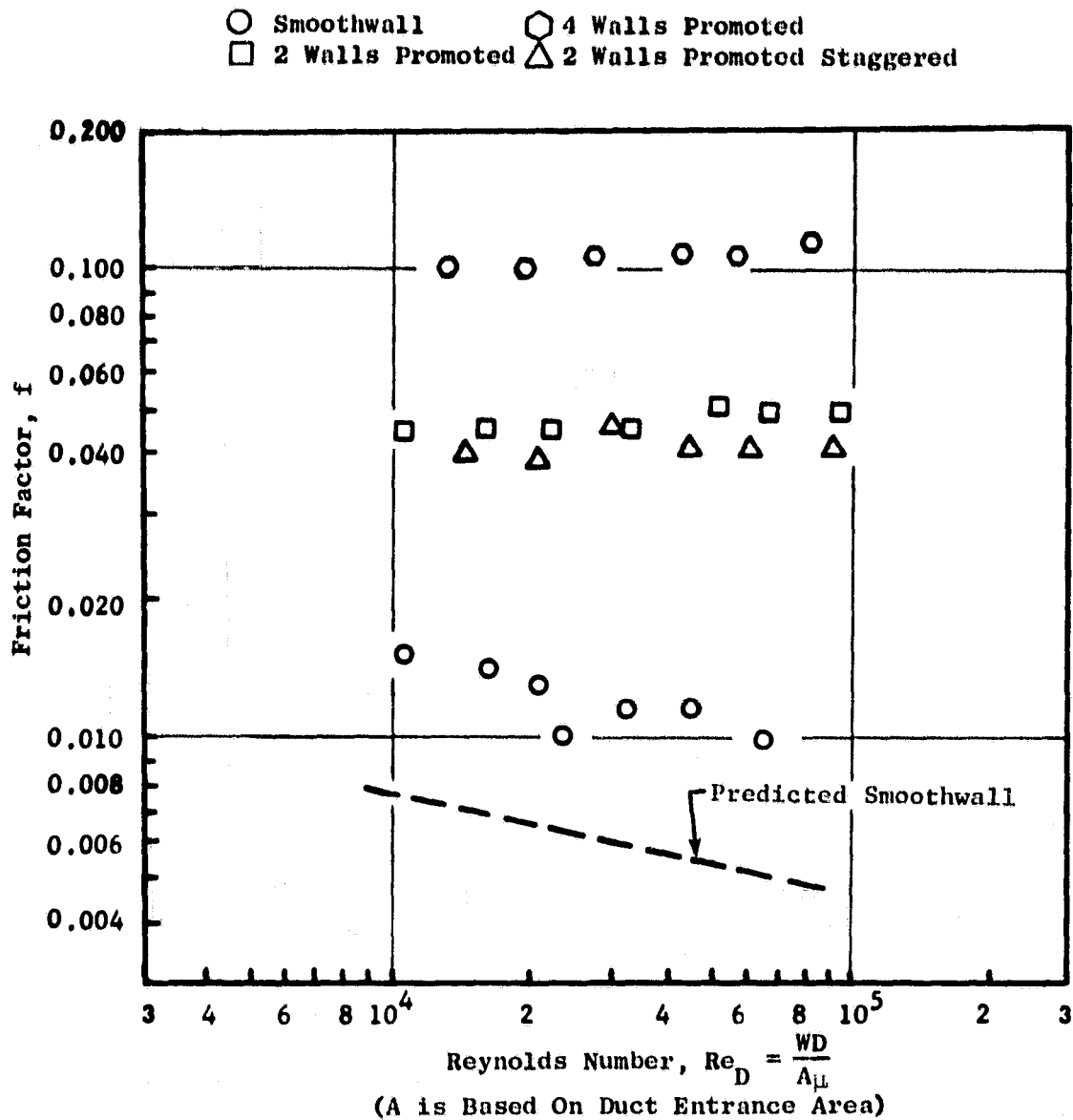
43

Figure 25. Comparison of Friction Factor Results.

5.2.1 Test Setup

The model scaling criteria used for this test allowed testing of both the original and improved insert configurations by using the new vane inner contour. A geometric comparison resulted in a 7X scale model of the improved insert and vane inner contour as the base. Using the improved vane inner contour to evaluate the original insert resulted in a 11.5X scale model. Figure 26 shows the superpositioning of the original and improved vane scale contours noting the region of interest.

Cross-sectional profiles of the two model configurations tested are shown in Figures 27 and 28. These figures show the insert position relative to the heated inner vane contour and impingement flow axes for Rows 1, 2, and 17.

The improved insert differed from the original insert in that it was closer to the vane inner surface. The design intention of the improved insert is to pass the same coolant flow through the three rows of leading edge holes (1, 2, and 17) while using a larger number of smaller diameter metering holes in the stagnation region (Row 1).

5.2.2 Instrumentation

Model instrumentation consisted of plenum pressure gages on both inserts. The simulated inner vane contour walls were composed of copper heater plates. Each heater plate was instrumented with two thermocouples to monitor the plate temperature.

5.2.3 Test Procedure

The test conditions were determined by calculating the Reynolds numbers for both inserts at takeoff engine operations conditions. The diameter of the leading edge impingement holes was used as the characteristic dimension in the Reynolds equation. Model airflow, pressure, temperature, and power input were measured. The Mach numbers were not matched, since in the compressible regime the effects were negligible.

The test points were selected by using the Reynolds number criterion:

$$Re_{D1} = \frac{\rho V D_1}{\mu} = \frac{W D_1}{A \mu}$$

where

D_1 = Diameter of the Row 1 impingement holes

μ = Viscosity evaluated at the coolant plenum temperature

W = Coolant mass flow

A = Total area of impingement holes present

Original (11.5 X Scale)
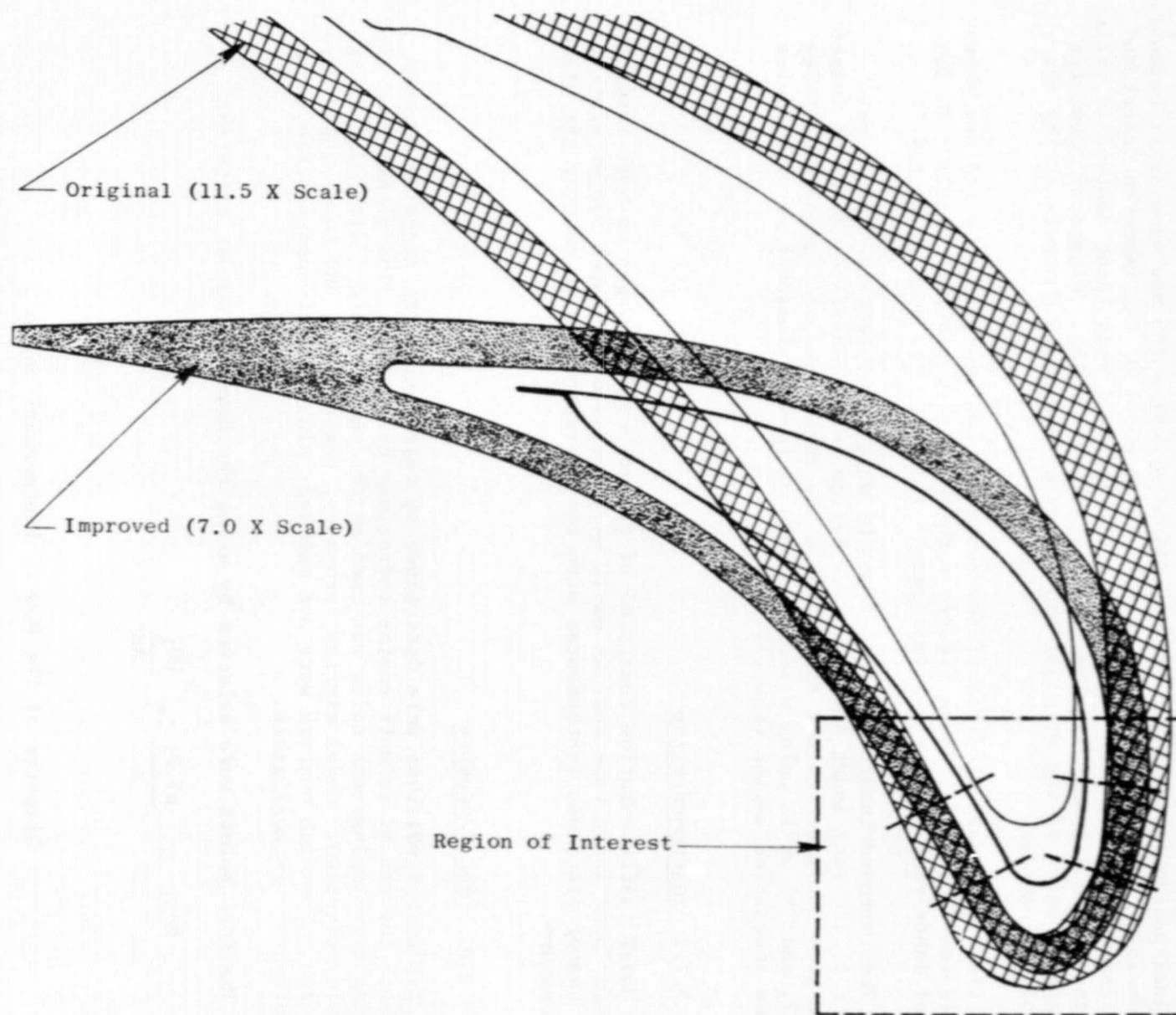
Improved (7.0 X Scale)

Region of Interest

Figure 26. Superpositioning of Original and Improved Vane Design.
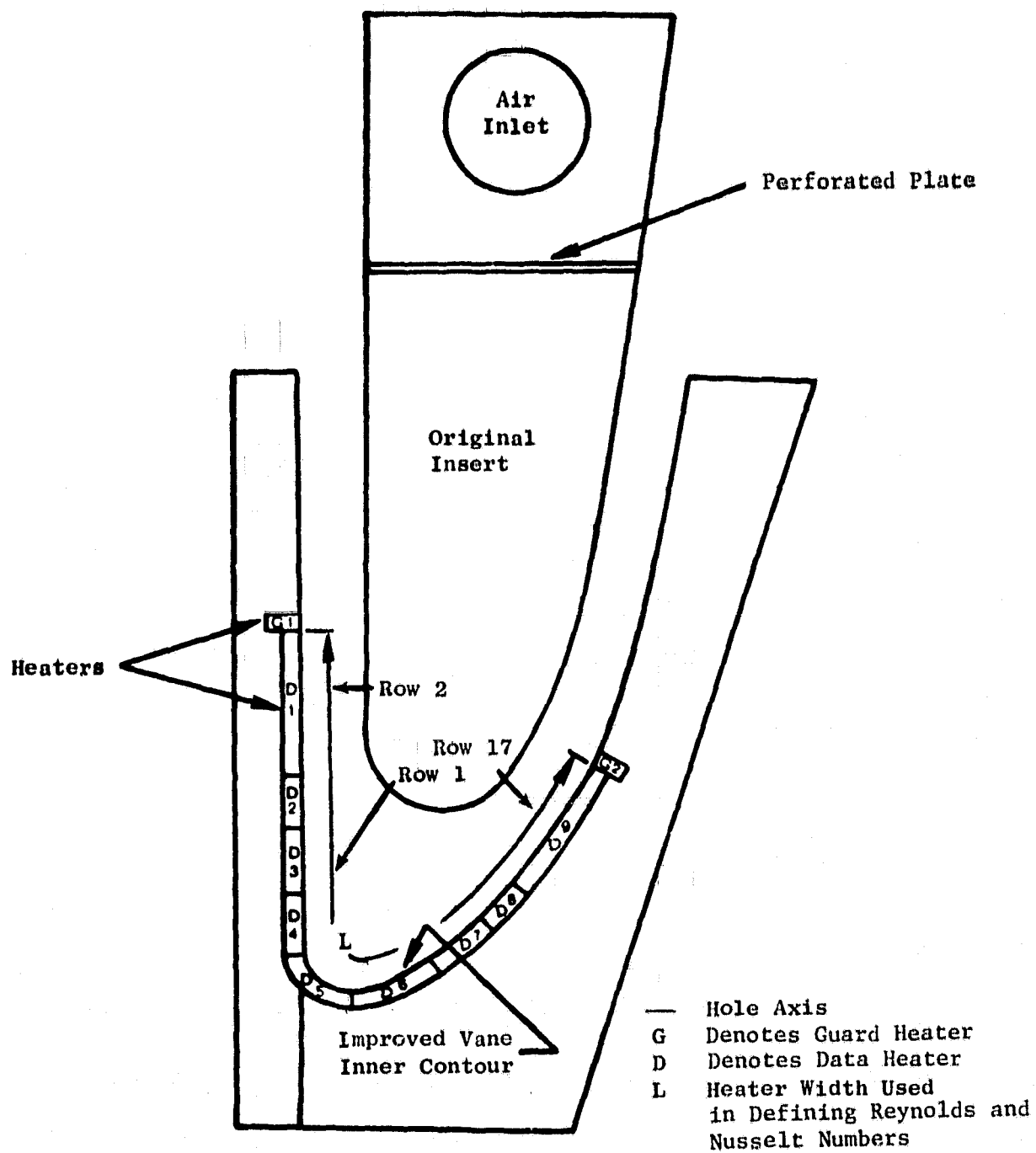
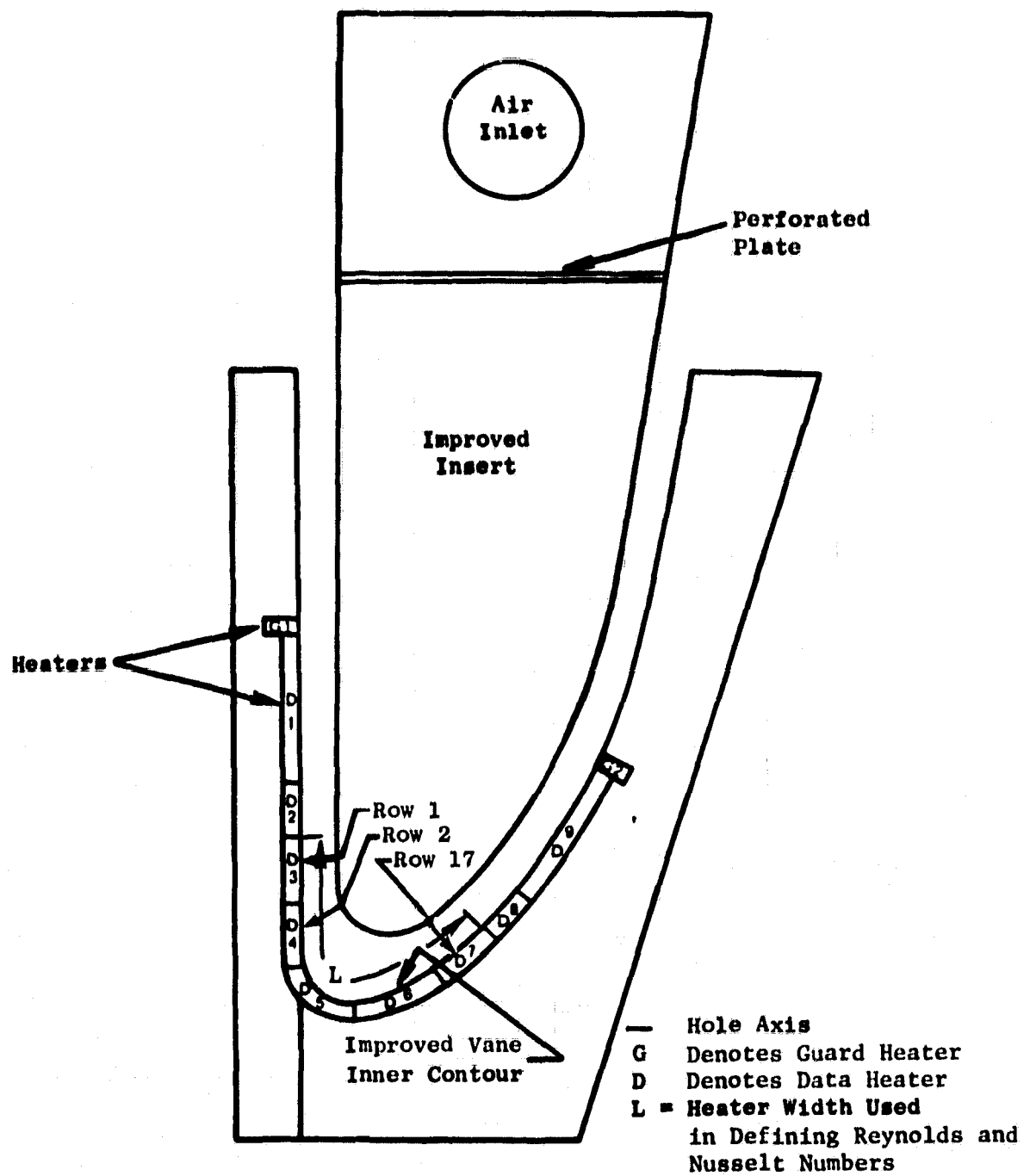Figure 27. Original Stage 2 Vane Insert Cross Section.

Figure 28. Improved Stage 2 Vane Insert Model Cross Section.

Test points were set by first setting the flow rate to the model. Electrical input was then adjusted to each heater plate to give a constant temperature surface. Time was allowed for transient response of the system and for adjusting the power supplies to provide a constant temperature; then airflow, temperature, and electrical inputs were recorded. To determine backside heat losses, an additional test was run with the insert removed and the heater plates heavily insulated on the front surface.

5.2.4 Test Results

A comparison of test results at engine conditions for the original and improved designs is shown in Figure 29. The characteristic dimension used in defining Nusselt number and Reynolds number in this figure is the equivalent heated width for each model. This is necessitated by the fact that the models had different scale factors.

For a given Reynolds number based on the width of the impinged surface, the average Nusselt number over that surface is about 20% higher for the improved new insert configuration than for the original insert configuration.

Compared at the respective design Reynolds numbers, the improved design vane insert shows a 10% increase in Nusselt number in the leading edge region.

5.3 STAGE 2 VANE TRAILING EDGE PIN FIN TEST

Pin fin turbulence generators are commonly used to augment convective cooling in high heat transfer applications. The objective of this program was to determine the benefits of pin fins in the unimpinged region ahead of the trailing edge holes of the Stage 2 vane trailing edge. The testing utilized a 10X scale model of the vane trailing edge and configurations having no pins, pins of low conductivity (Textolite), and pins of high conductivity (copper).

5.3.1 Test Setup

A cross-sectional view of the vane area modeled is shown in Figure 30. Based on this configuration, a 10X engine size model was designed and fabricated which simulated a radial height of 15.2 mm at the pitchline. This provided six 12.7 mm diameter pins per row. Two pin materials were utilized as mentioned previously: copper and Textolite. The Textolite pins were used to determine the effect of the pin created turbulence on the sidewall heat transfer by the low conductivity of Textolite. Correspondingly, the copper pins having a much higher conductivity than Textolite were designed to determine the contribution of the pins on the sidewall heat transfer. These pins were hand-fitted at each location and attached to the plates mechanically by machine screws. Highly conductive grease was used at the pin and plate interfaces when copper pins were used to reduce heat losses at this location. Pin locations are shown in Figure 31.
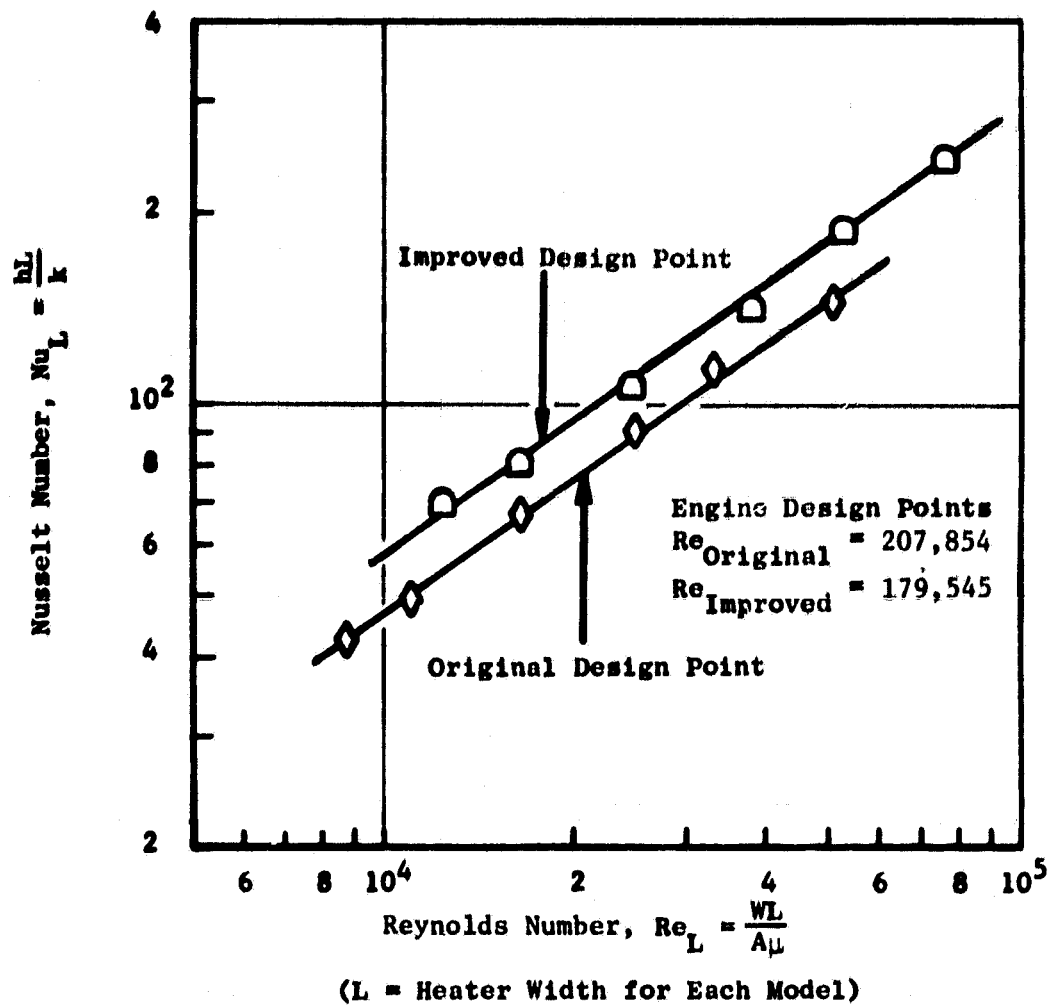
Figure 29. Comparison of Heat Transfer Results for Original
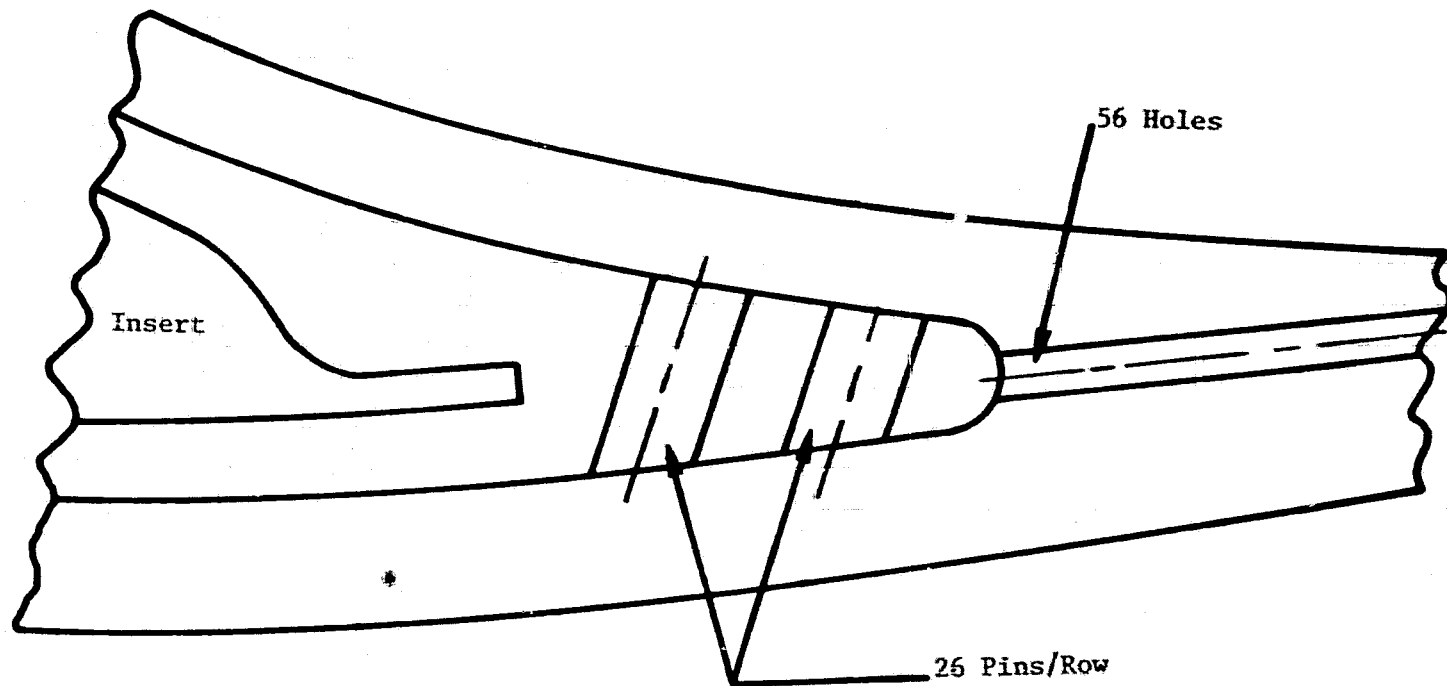and Improved Design Impingement Inserts.

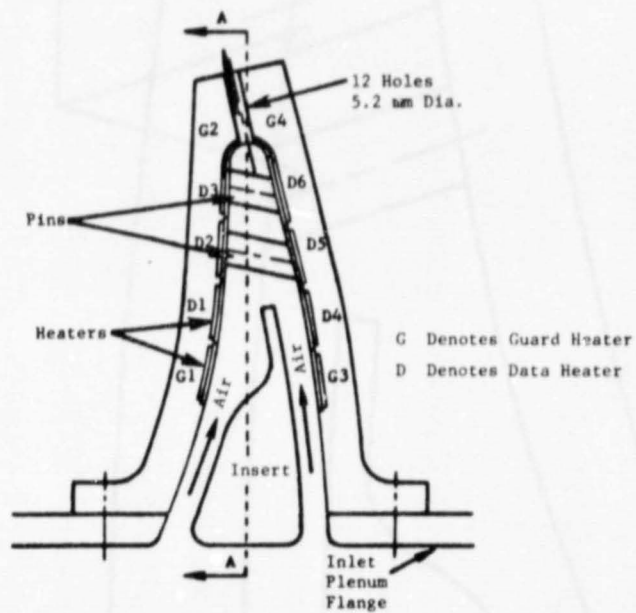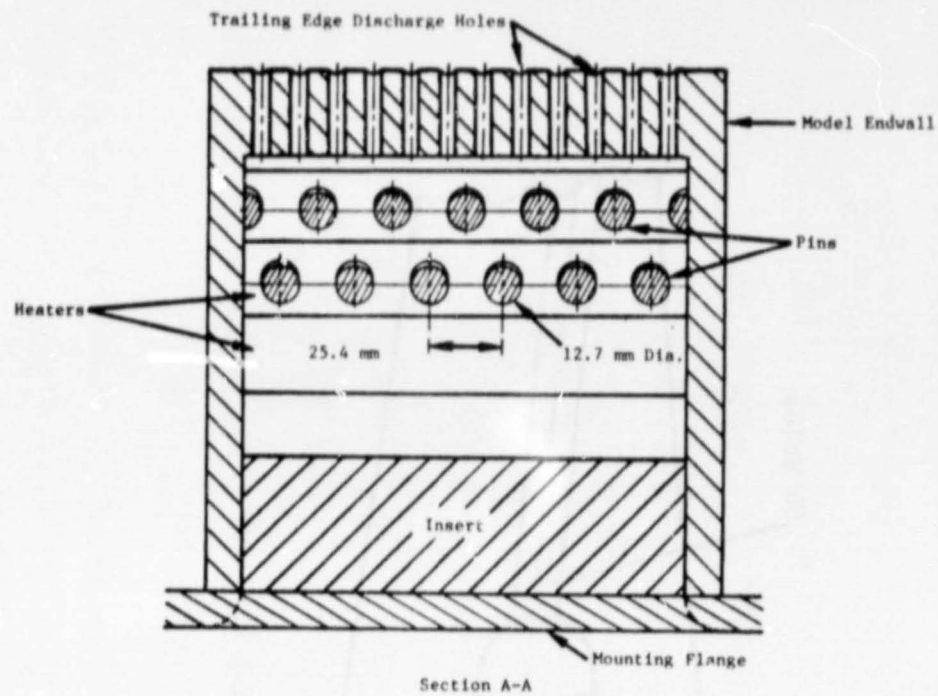Figure 30. Stage 2 Vane Trailing Edge.

Figure 31. Stage 2 Vane Trailing Edge Pin Fin Heat Transfer Model.

The model was fabricated such that it could be split axially to allow for installation/removal of the pins as required by the test configuration. The configurations tested were:

Number	Configuration
1	No Pins
2	Textolite Pins
3	Copper Pins

Photographs of the assembled model and the test setup are shown in Figures 32 and 33.

5.3.2 Instrumentation

Three data heaters were located on each side of the passage sidewall as shown on Figure 31 to obtain data for each pin row as well as immediately ahead of the pin rows. Guard heaters were located upstream and downstream of the data heaters to reduce heat losses and to provide upstream boundary layer heating. These heater plates were nominally 25.4 mm wide and 152.4 mm in length utilizing 1.6 mm thick copper. Heating elements were soldered to the back of the copper plates along the full length of the plates. Three thermocouples were attached to the plates to record the plate temperatures during test.

5.3.3 Test Procedure

The test procedure consisted of first setting the desired airflow and then electrical power was supplied to the heater plates. Variable transformers controlling each heater were adjusted such that each heater plate was at approximately 93° C (200° F). When the heater plate temperatures were stabilized, volts, ampere, flow rates, plate temperatures, and plenum pressures were recorded.

A time-share computer program was used to reduce the data. The program is divided into two parts: the first is handling the heat transer data while the second part converts the results to dimensionless parameters such as Stanton number, Reynolds number, and Nusselt number. As previously mentioned, three model configurations were tested. The geometry without pins was used as a basis to determine the increase in heat transfer resulting form the addition of pins. The heat transfer part of the program input consists of volts, ampere, plate temperatures, and heater resistance.

Total power input to each heater plate is calculated as
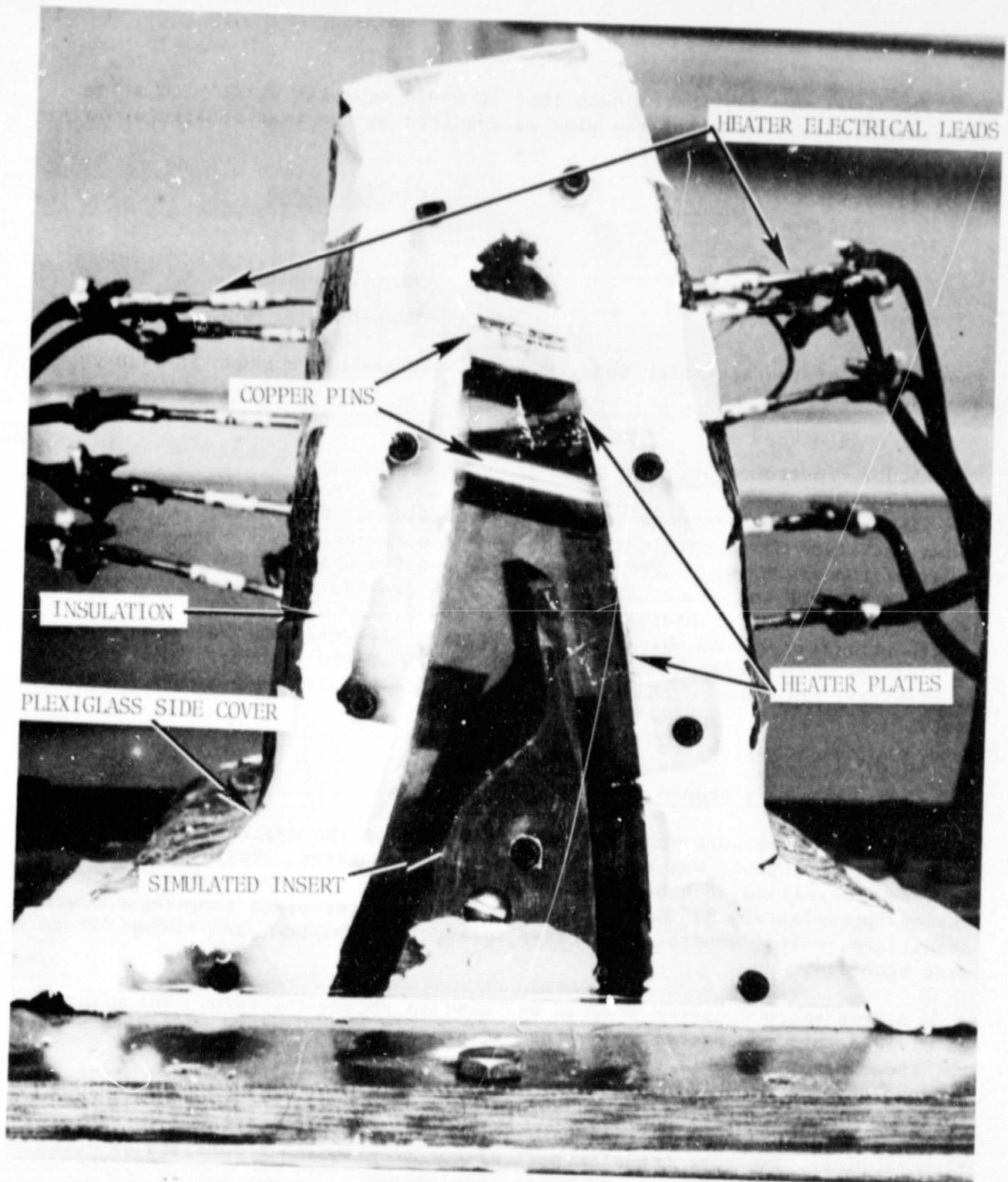
$$P = I^2R - \text{Losses}$$
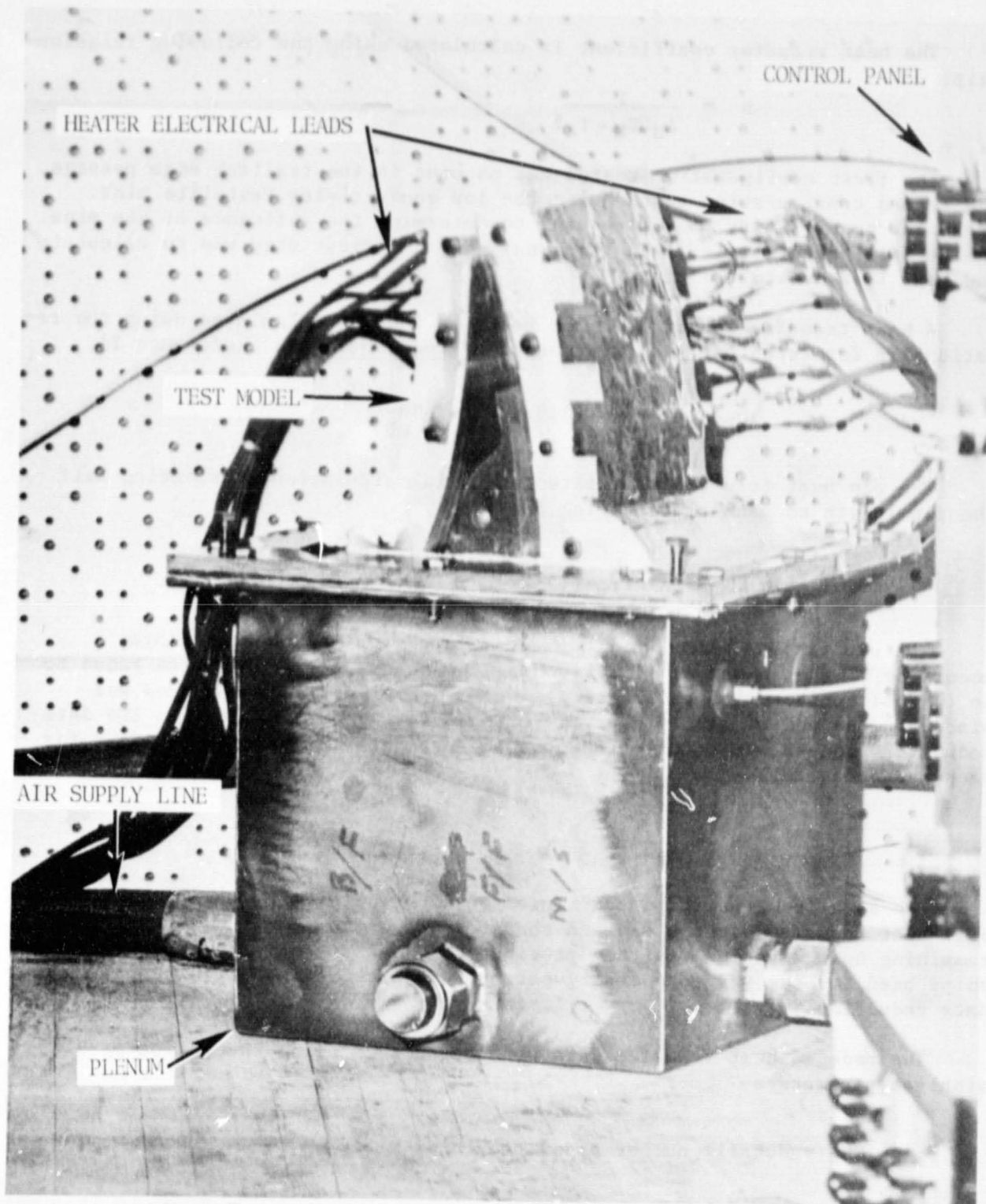
Figure 32. Photograph of Pin Fin Model.

54

Figure 33. Overall Model Test Setup.

55

The heat transfer coefficient is calculated using the following relationship:

$$h = \frac{P}{A_H(T_H - T_A)}$$

The first configuration tested had no pins in the trailing edge passage. The second configuration tested used the low conductivity Textolite pins. These low conductivity pins were used to determine the influence of the pins on the wall heat transfer. In this analysis, the first step was to calculate the heat loss due to the pins.

A heat transfer coefficient for each pin row was calculated using the relationship for turbulent flow over banks of tubes or pipes (Reference 2).

$$h_p = \frac{k}{D_{pin}} (0.33) \, Pr^{1/3} \, Re_D^{0.6}$$

The pin heat loss was calculated as a fin calculation attributing half the pin length to each plate having pins.

$$Q_p = \sqrt{h_{pin} \, P k_p A} \; (T_p - T_A) \, \tanh \left(L \sqrt{\frac{h_p \, P}{k_p \, A}} \right)$$

The pin fin heat loss was then accumulated for each heater plate according to the number of pins touching the heater. The pins were known to be in good contact with the heaters since a dab of silicone compound was placed on the end of each pin prior to assembly. The final step in the data reduction process was to calculate the average heat transfer coefficient for each heater as follows:

$$h = \frac{P - Q_p}{A_H \, (T_H - T_A)}$$

The data from the third configuration were analyzed by assuming that the wall heat transfer was the same as that resulting from Configuration 2. The remaining heat transfer was then attributed to the copper pins. The relationships used for the previous configurations were used for the Configuration 3 data reduction.

The reduced heat transfer data were correlated using the following dimensionless parameters:

$$Nu_D = \text{Nusselt number based on pin diameter} = \frac{hD}{k}$$

$$Re_D = \text{Reynolds number based on pin diameter} = \frac{\rho \, V_e \, D}{\mu}$$

5.3.4 Test Results

The data were correlated based on pin diameter for all three configurations. It should be noted that the Reynolds numbers are based on local velocity with no increase in velocity due to presence of pins which allows a direct comparison of three configurations.

A review of Figure 34 shows the average of the smoothwall data to be about 1.40 times the turbulent duct prediction and is attributed to the inlet effects resulting from the model configuration. Shown also in this figure are the wall heat transfer data from Configuration 2 showing an increase of 3.0 times the smoothwall data.

A comparison of the Configuration 3 data as an average of the walls and pins is shown in Figure 35 with the smoothwall results and the turbulent duct prediction. These data show a 2.8 times increase in heat transfer over the soothwall data which is slightly less than the increase shown by Configuration 2. This slight reduction is due to the averaging of the Configuration 3 pin and plate data. A comparison of heat transfer coefficient of the wall and of the pin of Configuration 3 is shown in Figure 36. This figure shows the pin heat transfer coefficient to be 25% to 35% lower than the walls.
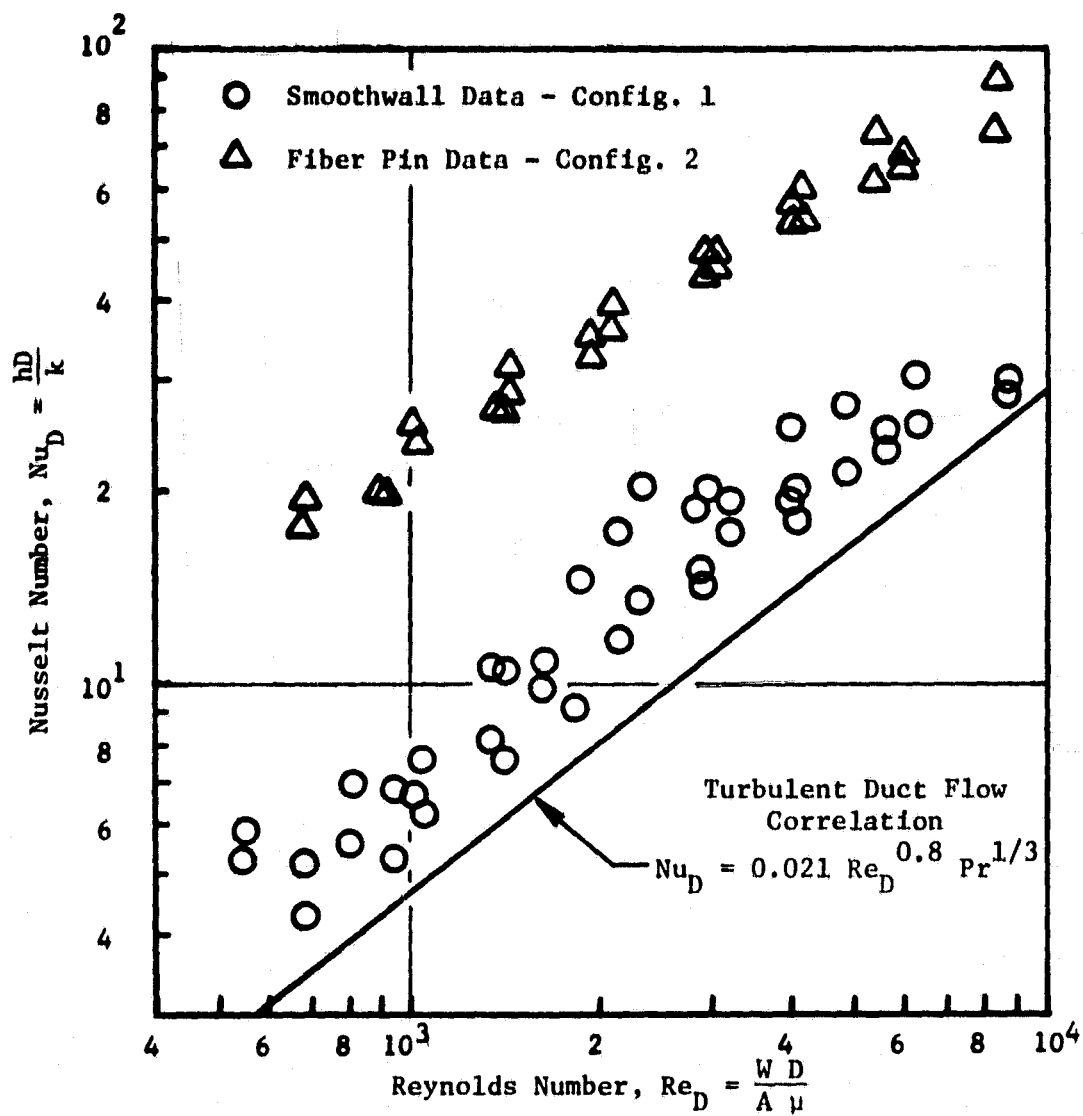
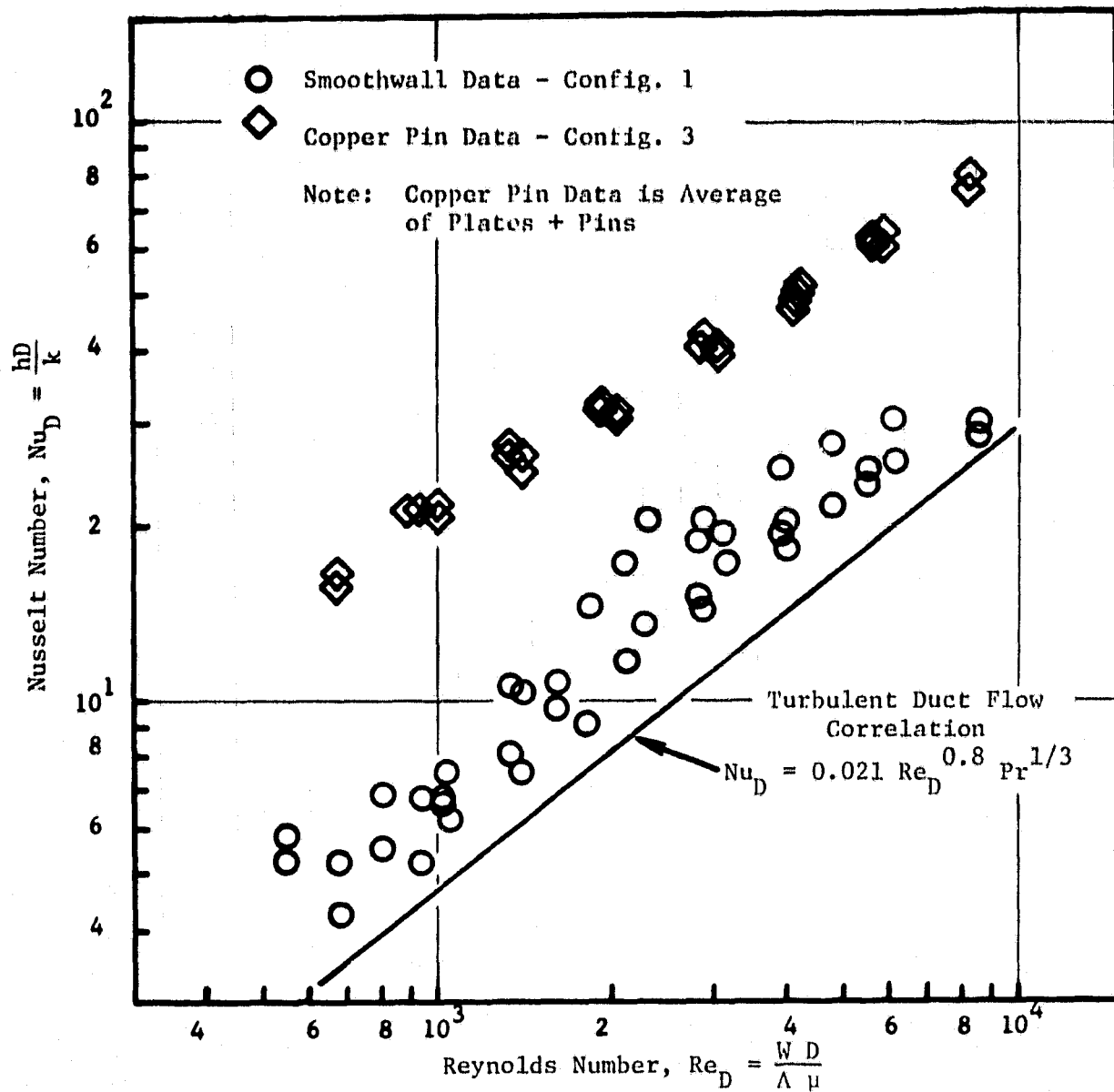Figure 34. Comparison of Fiber Pin Wall Data with Smoothwall Data.

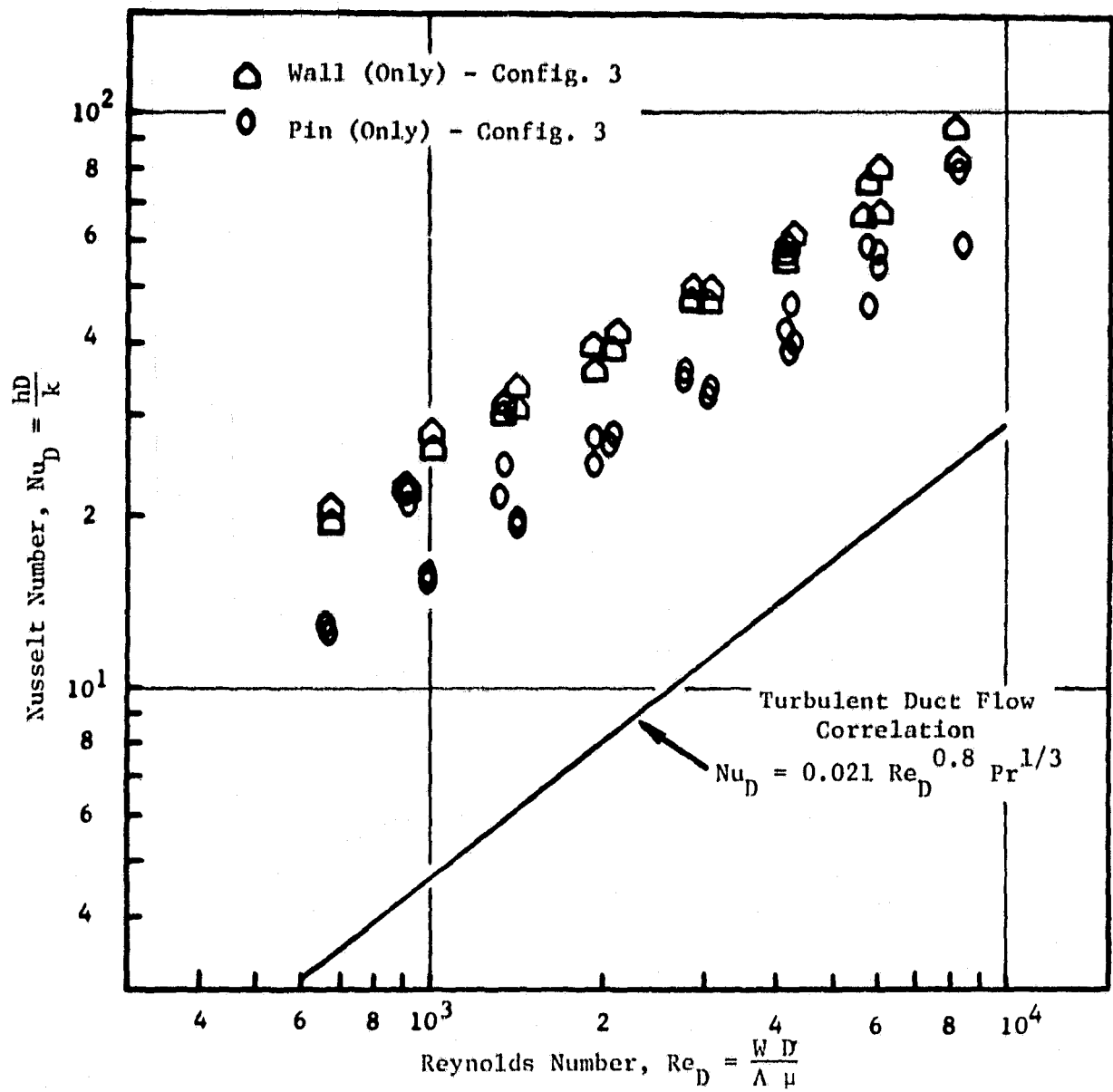Figure 35. Comparison of Average Copper Pin Data with Smoothwall Data.

Figure 36. Separation of Wall and Copper Pin Data for
Configuration 3.

6.0 COMPONENT MECHANICAL TESTS

6.1 BLADE DYNAMIC AND STEADY-STATE STRAIN DISTRIBUTION

In order to adequately determine the dynamic characteristics of a turbine blade operating in a gas turbine engine, it is necessary to conduct an instrumented engine test in which vibratory stress data can be measured. However, to properly collect and analyze such data, it is first necessary to perform a series of tests to determine the resonant frequencies of the blade and the relative distribution of strain throughout the blade while it is vibrating in each resonant mode. These data permit the construction of a Campbell diagram for the blade operating in the engine. Additionally, the data are needed to select optimum locations for engine test instrumentation (i.e., locations which will provide a large relative response in modes of interest) and to determine safe operational limits in each mode of vibration. The steady-state strain distributions are desirable on new blade designs in order to insure that the load transition through the airfoil root is relatively uniform and free from "hard spots". The objectives of these tests are to provide the required dynamic and steady-state strain distribution.

6.1.1 Test Description

The test hardware consisted of the Stage 1 and Stage 2 turbine blades of the improved (single shank) turbine. The test consisted of three parts: the determination of resonant frquencies and nodal patterns, the relative strain distribution tests, and the steady-state strain distribution test.

Resonant Frequencies and Nodal Patterns – In order to determine resonant frequencies and nodal patterns, the blades were cut off at the middle of the dovetail top tang pressure face and then brazed to blocks. The blades were driven electromagnetically at resonance and a crystal pickup was used to determine nodal patterns. Resonant frequencies from 0-24 KHz were recorded. The test setup for this test is shown in Figure 37.

Relative Strain Distribution – Relative strain distributions were obtained by clamping highly strain-gaged blades in dovetail coupons and driving the blades at each natural frequency with pressure pulses created by a siren. The effect of the damper loads on the relative distribution was determined by using a fulcrum-type fixture to apply a load at each damper pad which can be seen in Figures 38 and 39. Distributions were determined for three different conditions: (1) clamped at dovetail only, (2) clamped at dovetail with damper load equal to that experienced in the engine, and (3) clamped at the dovetail with a load approximately four times the engine load at the damper pads to simulate a limiting condition. An example of the strain gage instrumentation is shown in Figure 40.
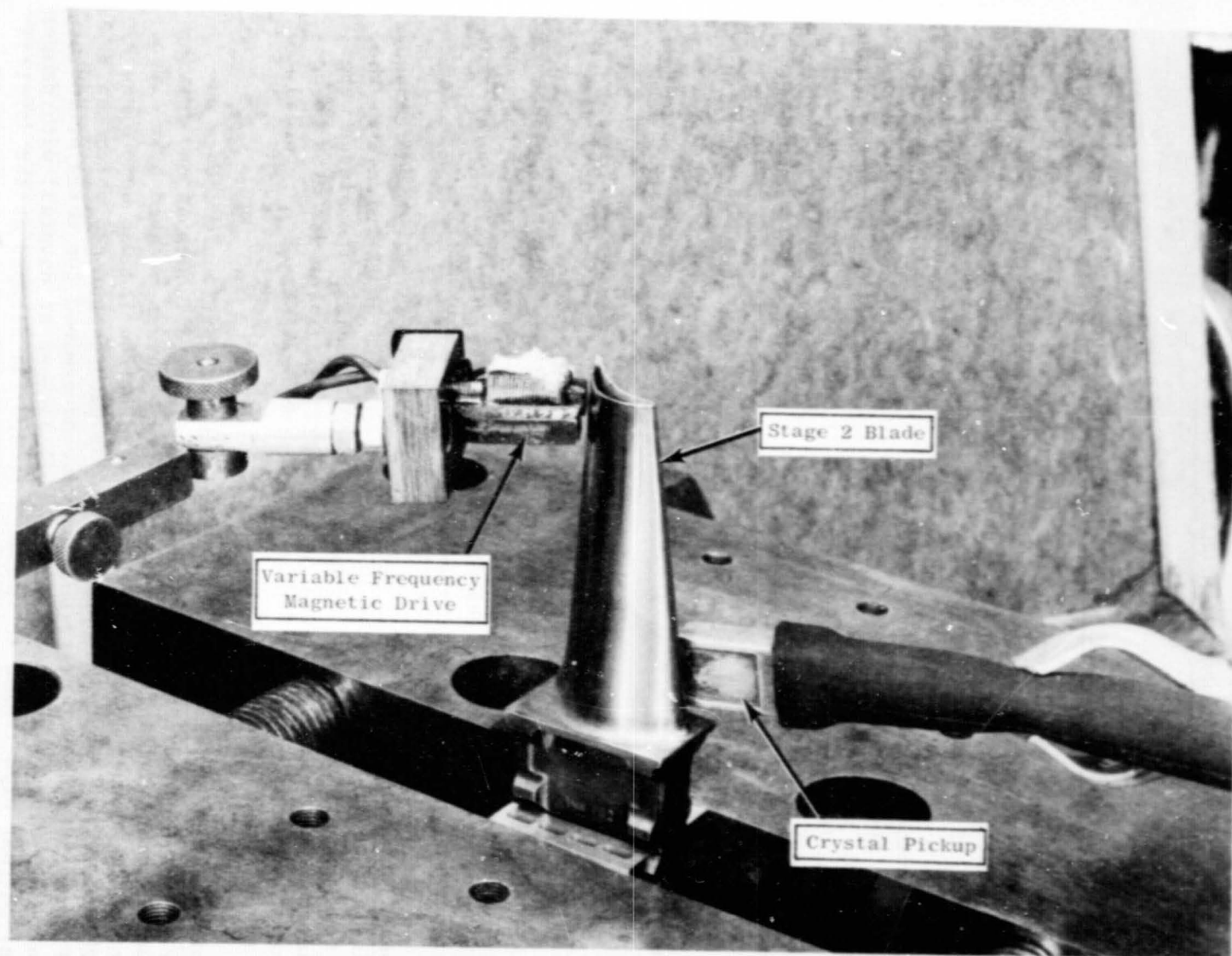
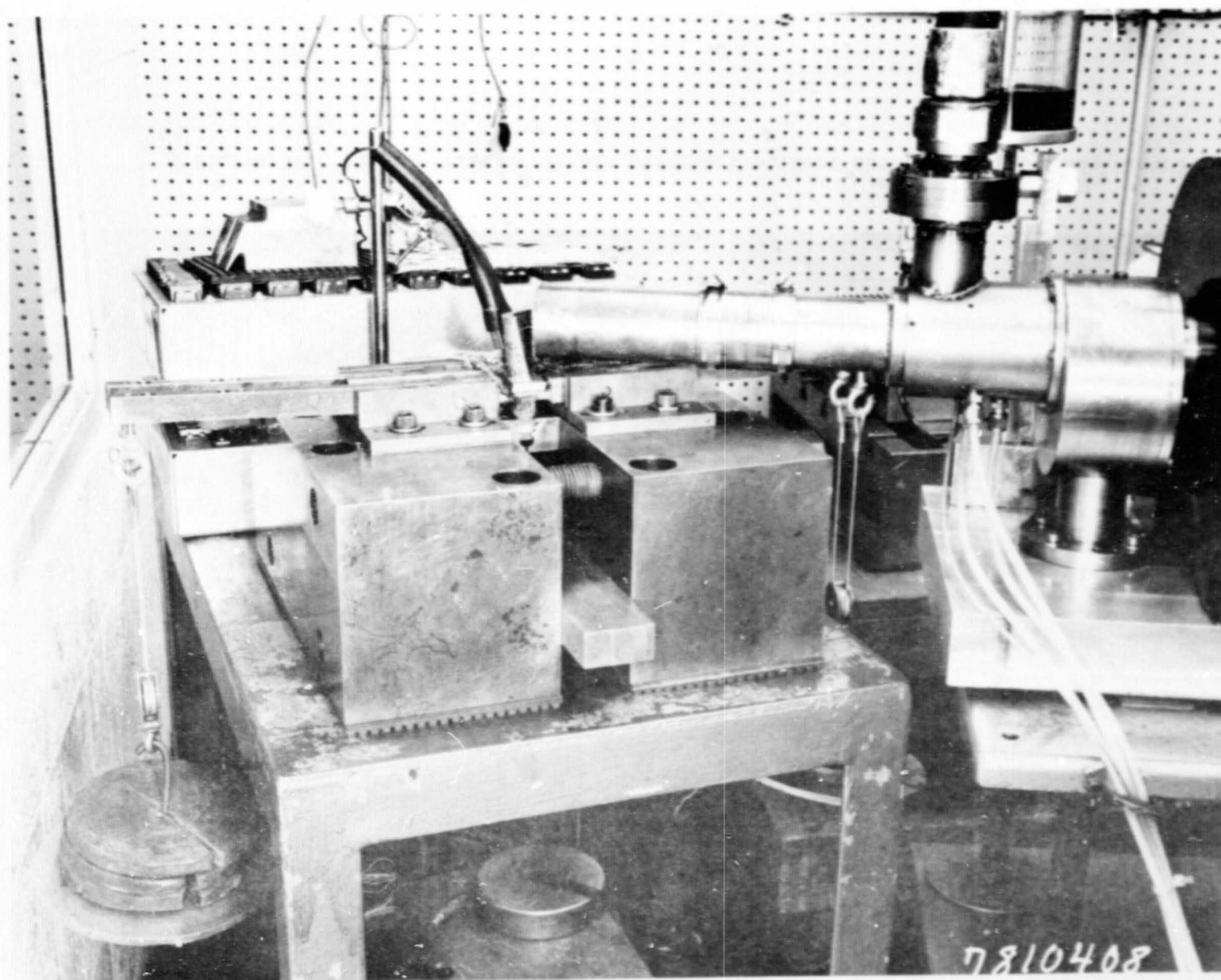Figure 37. Reasonant Frequency and Nodal Patterns Test Setup.

Figure 38. Strain Distribution Test Setup (Stage 1 Blade Shown).

Figure 39.   Closeup View of Strain Distribution Test Setup (Stage 1 Blade Shown).

Figure 40.   Example of Strain Gage Instrumentation (Stage 2
             Concave Side).

Steady-State Strain Distributions - The test setup for these tests are
shown in Figure 41. In order to conduct steady-state strain distributions,
an epoxy block was cast on the tip of each instrumented airfoil to provide a
means of loading the airfoil without causing distortion during testing. The
blade dovetail was clamped in coupons, as in the vibratory strain distribution
testing. Both positive and negative moments were applied about all three
axes, and 8,900 N (2,000 lb) and 17,800 N (4,000 lb) tensile loads were applied.
Results were recorded for each loading condition. The coordinate system used
was loading X in the direction of rotation, Y axially forward, and Z radial.

6.1.2 Test Results

Resonant Frequencies and Nodal Patterns - The resonant frequencies and
nodal patterns obtained for the Stage 1 and Stage 2 blades are presented in
Figures 42 and 43. These data are used to construct the Campbel[1] diagrams
shown in Figures 44 and 45 to determine which, if any, resonances with known
per revs could be potential problems. Also indicated are known engine excita-
tions and engine operating range.

As can be seen in the figures, several crossings occur in the range of
operation of the engine. However data taken from instrumented core engine
testing (see Section 7) demonstrates that all resonant vibratory responses were
within acceptable limits. The peak resonant response levels were lower for both
stages than the corresponding levels on the original blade design.

Relative Strain Distributions - Relative strain distributions were de-
termined for all modes which give the detailed distribution of stress in the
blades for these modes. These data are then used to insure that the most
limiting area of the blade is known and that this critical point strain can
be related to strains measured during engine testing.

Steady-State Strain Distribution - For the Stage 1 blade, positive and
negative moments of 79.1 N/m (700 in.-lb) were applied about the X and Y axes,
56.5 N/m (500 in.-lb) about the Z axis and tensile loads of 8,896 N (2,000 lb)
as well as 17,793 N (4,000 lb) in the Z axis. For the Stage 2 blade, positive
and negative moments of 56.5 N/m were applied about the X, Y, and Z axes and
tensile loads of 8,896 N and 17,793 N. Results of beam theory analyses were
compared with the measured values for both Stage 1 and Stage 2 blades at each
loading. Examples of the analytical results and the comparison are shown in
Figures 46 and 47.

The results for both blades are similar in that they tend to unload on
the leading and trailing edges and load up over the relatively stiff rail
areas. The Stage 1 blade also has a tendency to unload at the maximum curva-
ture on the convex side where the blade overhangs the shank.

The steady-state results did not show any unusual end effects for either
Stage 1 or 2. The magnitude of the end effects is within the realm of current
experience for blading of this type. Testing revealed no adverse steady-state
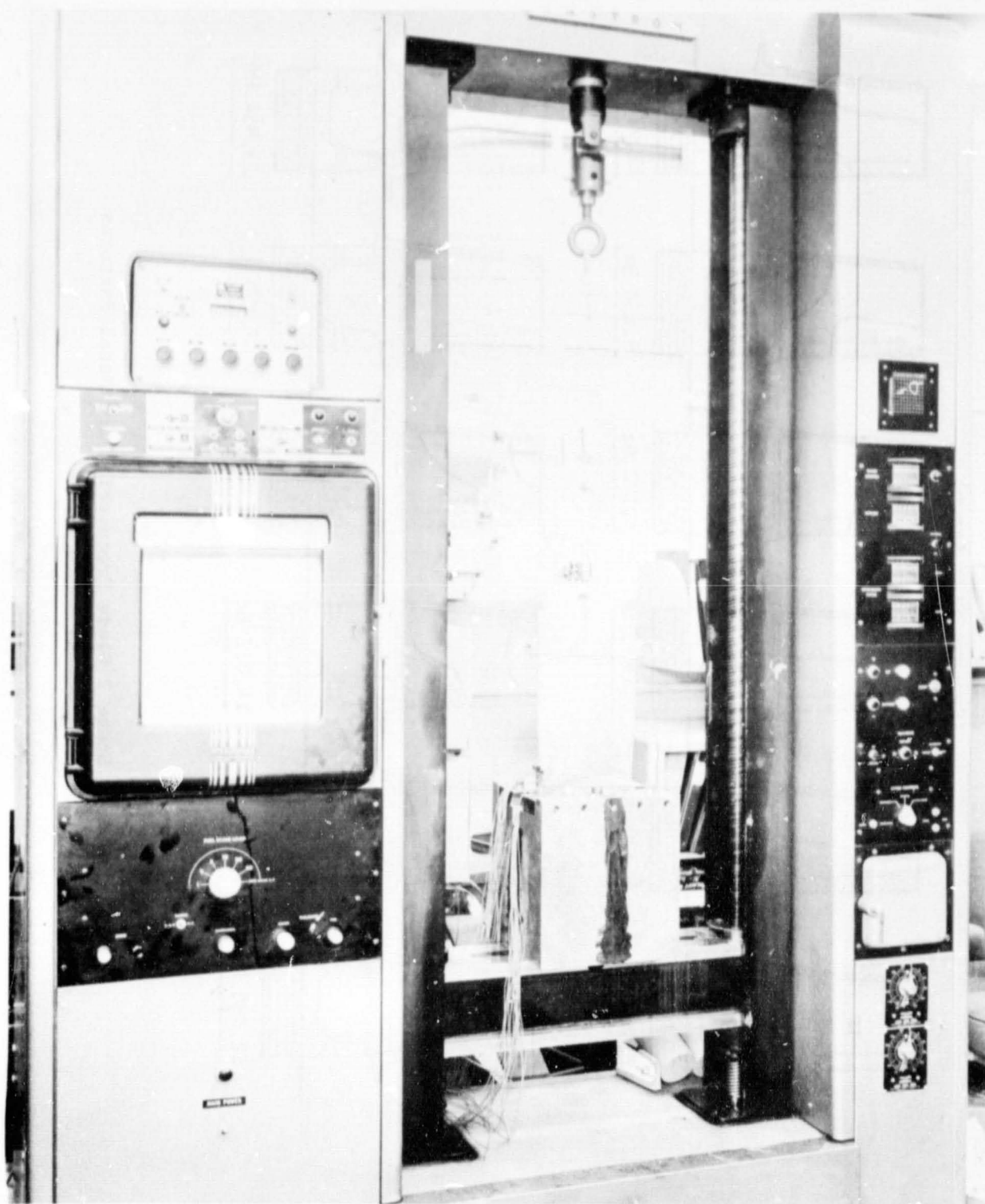end effects/stresses.

Figure 41.   Steady-State Strain Distribution Test Setup.

(Concave Side Shown)

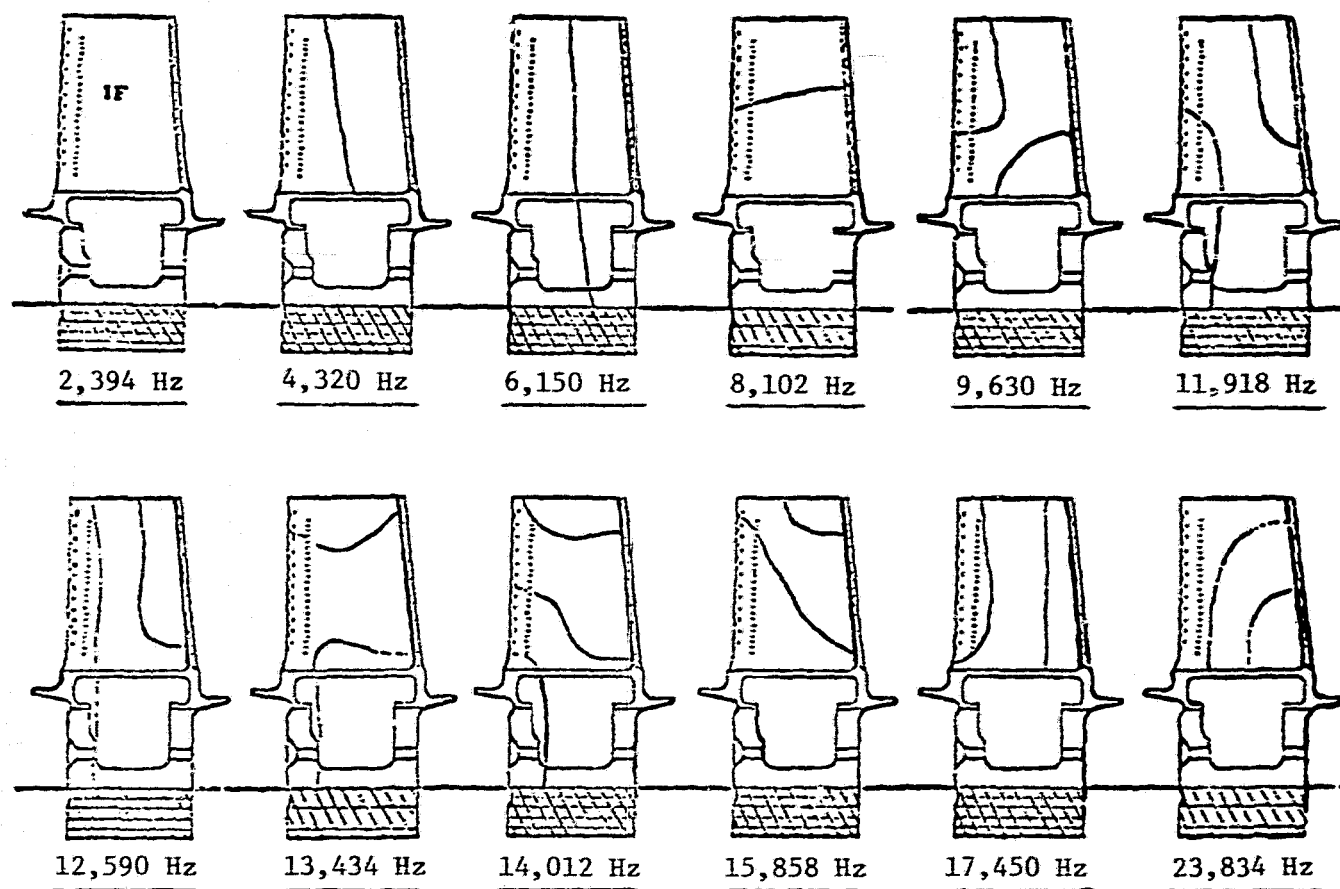|					
1F					
2,394 Hz	4,320 Hz	6,150 Hz	8,102 Hz	9,630 Hz	11,918 Hz

12,590 Hz	13,434 Hz	14,012 Hz	15,858 Hz	17,450 Hz	23,834 Hz

Figure 42. Stage 1 Blade Frequencies and Nodal Patterns.

(Concave Side Shown)

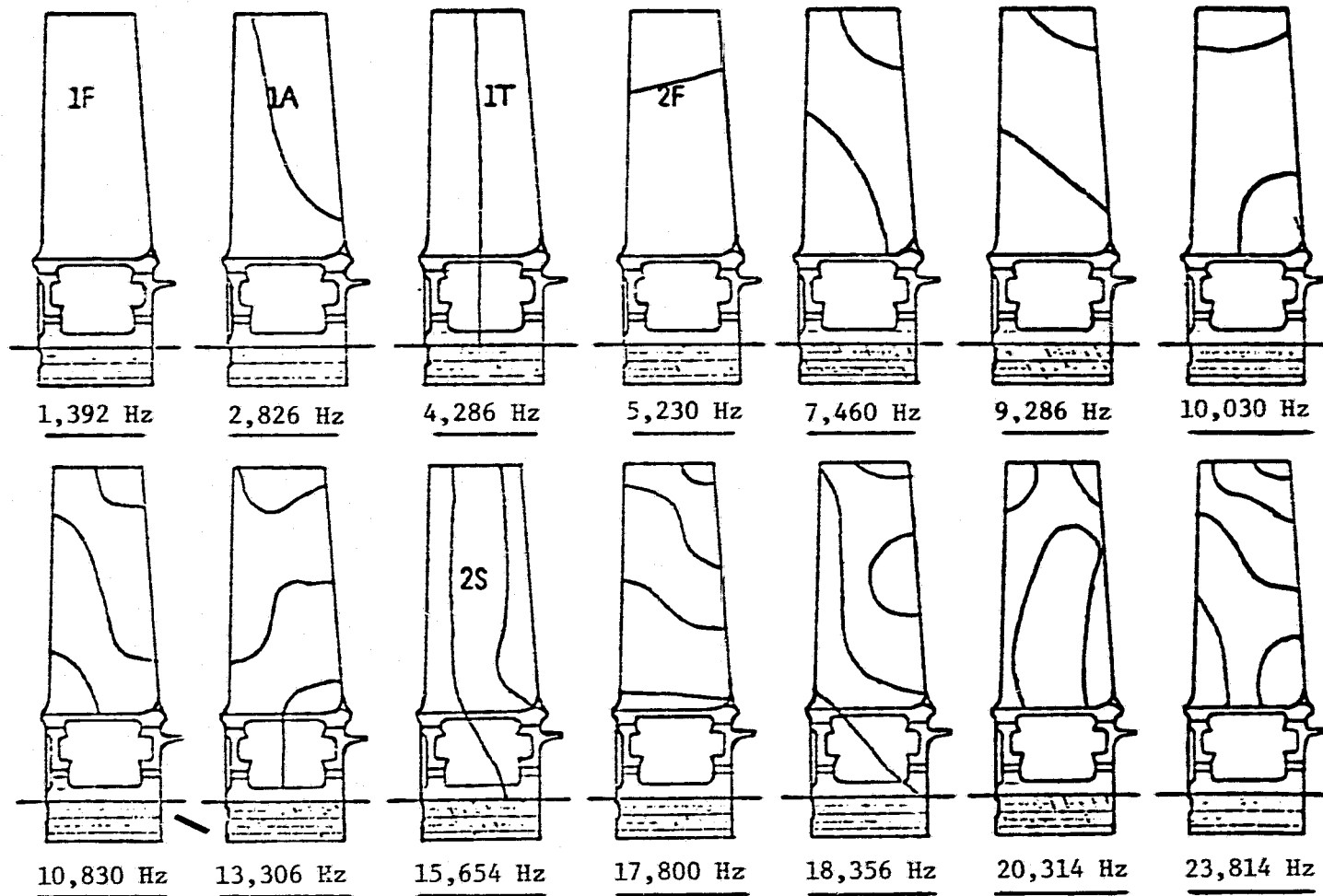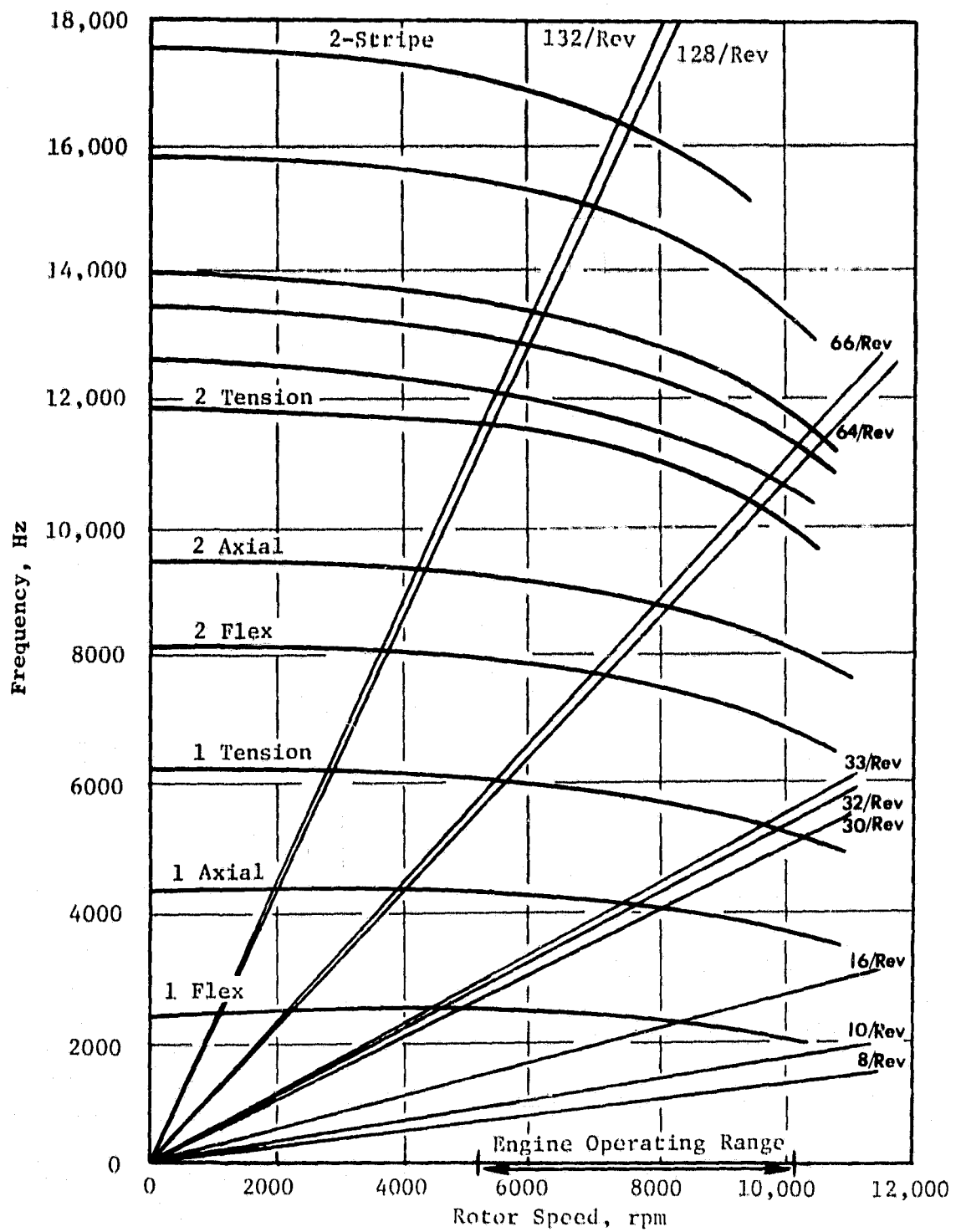|						
1F	1A	1T	2F			
1,392 Hz	2,826 Hz	4,286 Hz	5,230 Hz	7,460 Hz	9,286 Hz	10,030 Hz
		2S				
10,830 Hz	13,306 Hz	15,654 Hz	17,800 Hz	18,356 Hz	20,314 Hz	23,814 Hz

Figure 43.   Stage 2 Blade Frequencies and Nodal Patterns.

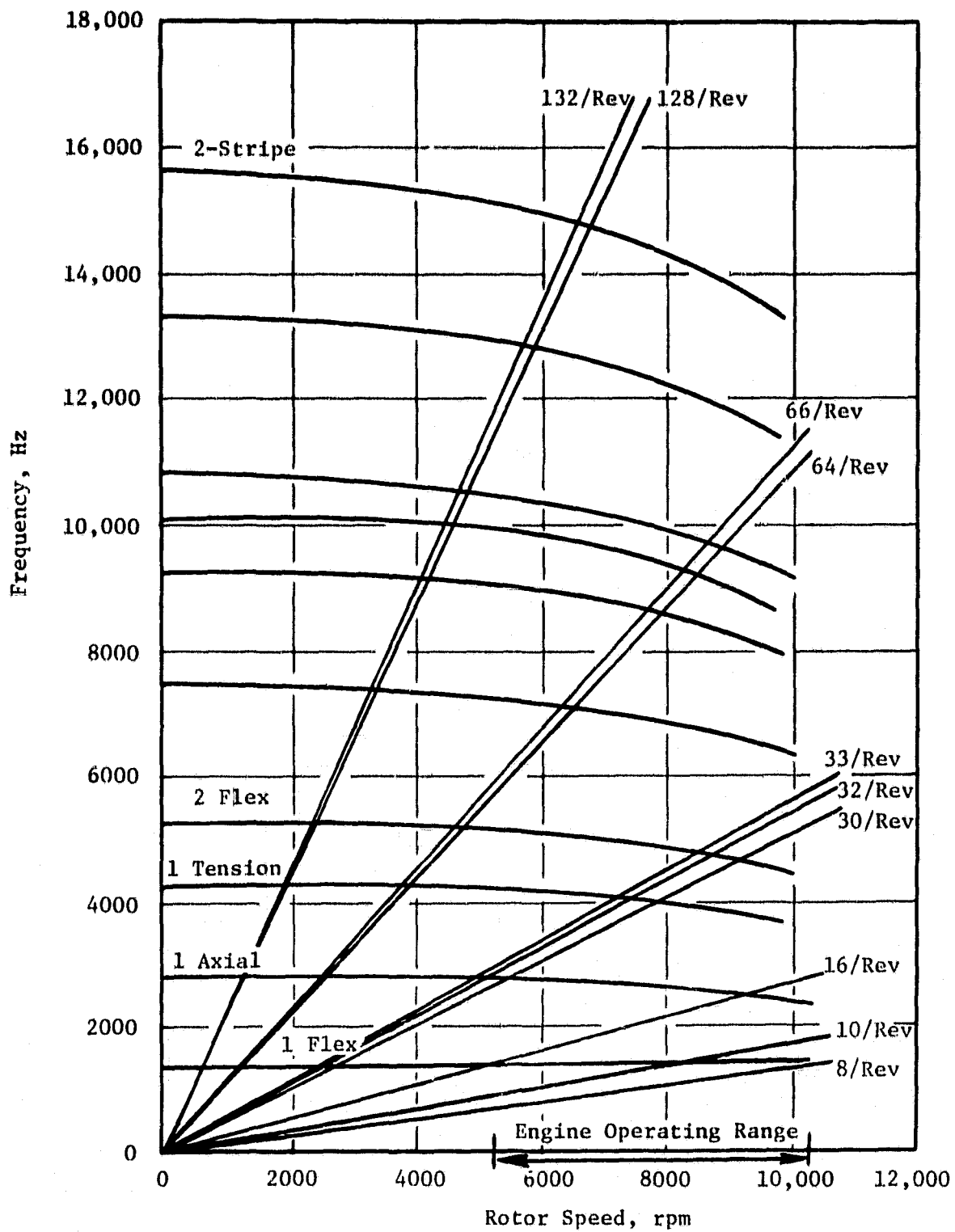Figure 44. Campbell Diagram for Stage 1 Blade.
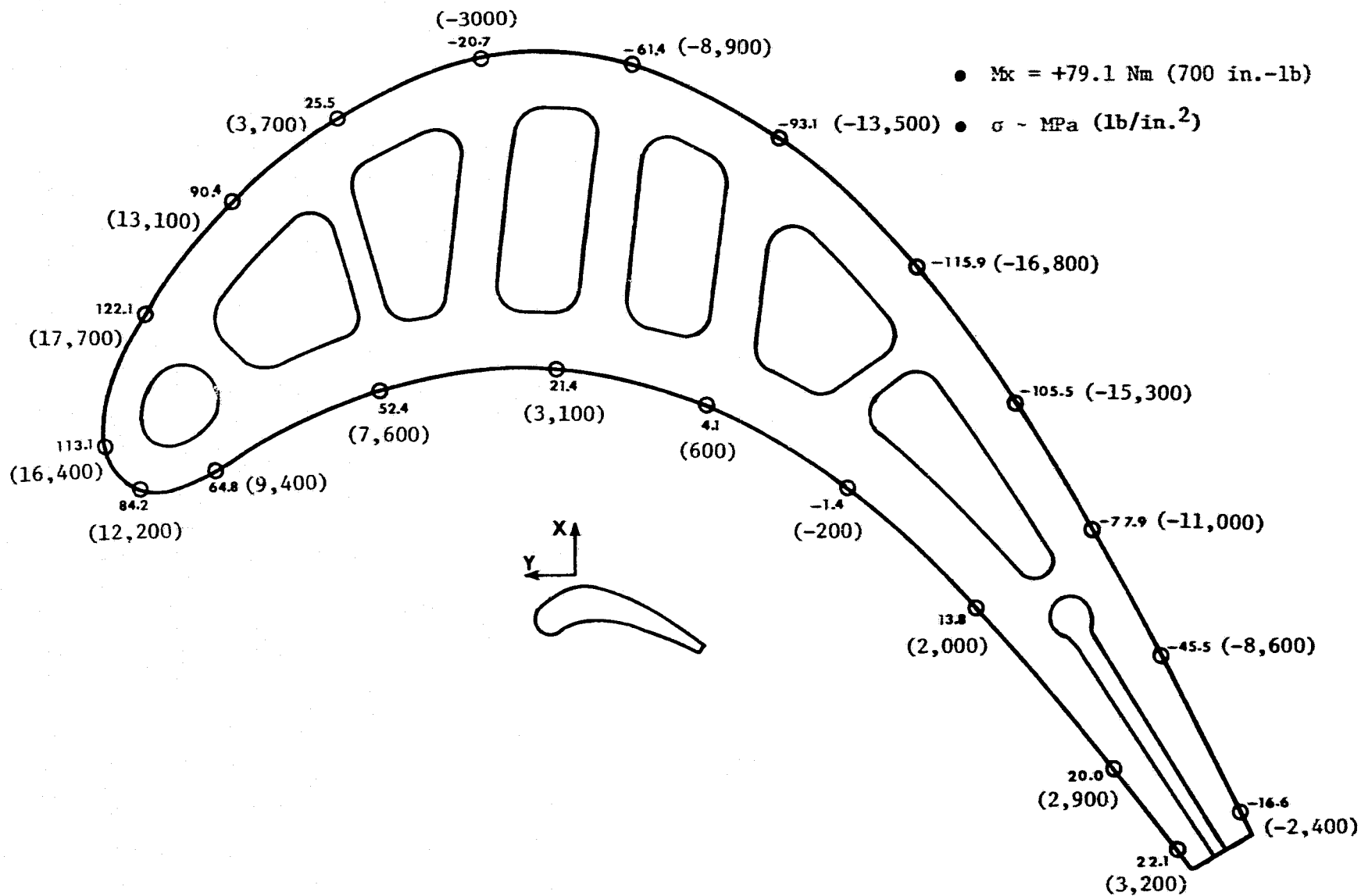
Figure 45. Campbell Diagram for Stage 2 Blade.

Figure 46. Typical Results of Beam Theory Analytical Steady-State Strain
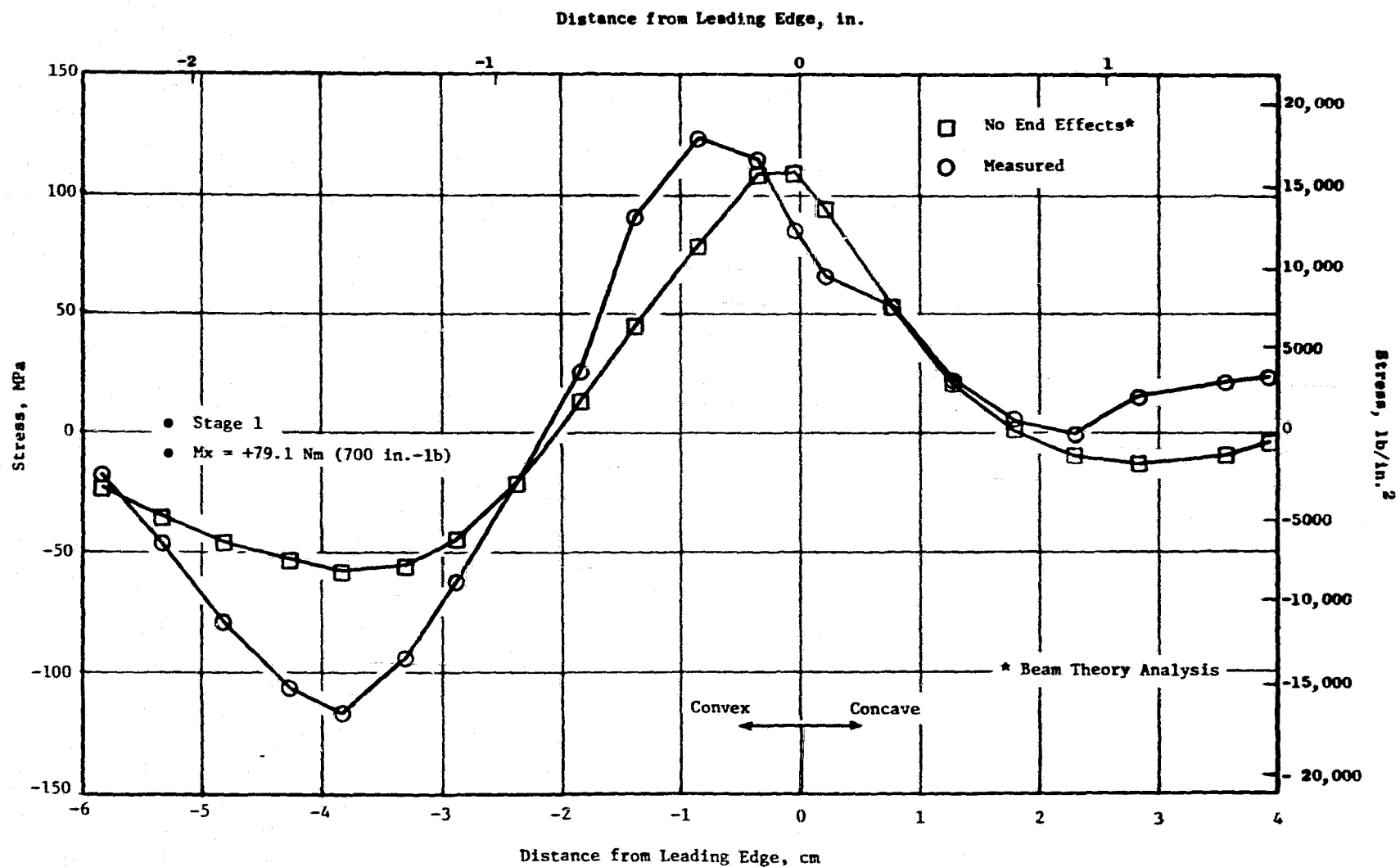Distribution (Stage 1 Root Section Shown).

Distance from Leading Edge, in.

Figure 47. Comparison of Analytical and Measured Steady-State Strain Distribution (Stage 1 Root Section Shown).

6.2 BLADE FREQUENCY AND AMPLITUDE AS A FUNCTION OF DAMPER FORCE

Frictional dampers have been used to reduce turbine blade vibratory stresses for a number of years and have been the subject of several investigations in the past years. Similar testing was used in the development of lightweight dampers for the CF6-50 HPT blade. The purpose of bench damping tests is to determine if the engine damper load will provide the desired combination of first flex frequency increase and stress reduction.

6.2.1 Test Description

The improved Stage 1 and Stage 2 blades to be tested where modified as shown in Figure 48. The blades were cut off at the middle of the dovetail top tang pressure face and brazed to a block. In addition, the damper pads were machined perpendicular to the dovetail centerline in an effort to maintain friction loading by the dampers. A strain gage was also applied to the airfoil root leading edge.

The blade was clamped between two large blocks and loading was applied to the damper pads with a fulcrum-type fixture (Figure 38). A load of 6 to 7 times the engine load was applied to the damper pads and the blade was then driven in the first flex vibratory mode with a siren. Holding the siren pressure excitation constant, the damper load was removed incrementally down to a minimum of 329 N (74 lb). At each load, the first flex frequency, tip deflection, and root leading edge stress were measured and recorded.

6.2.2 Test Results

Results are presented in terms of blade frequency, tip deflection, and root leading edge stress as a function of total damper load. The Stage 1 and Stage 2 frequency results are shown in Figure 49. The first flex frequency increases of about 11% for both blades were as expected.

The tip deflection and root leading edge stress results are shown for the Stage 2 blade in Figures 50 and 51. Tip deflection and stress data for the Stage 1 blade could not be obtained because of the extreme difficulty in driving this blade. The inability to drive the Stage 1 blade to high amplitudes has been observed in the past on other low aspect ratio turbine blading. With maximum damper load and full siren pressure, the tip deflection was less than 25 microns (0.001 in.) and the stress at the root leading edge was only 14 MPa (2000 lb/in.^{2}). The magnitude of the stress reduction on the Stage 2 blade is similar to that seen on other blades of this type, such as the CF6-50 Stage 2 blade.

Because the damper effectiveness appeared to be very large, further testing attempts were not conducted. In conclusion, the results indicate that the dampers will provide the desired effects relating to frequency gain and stress reduction.
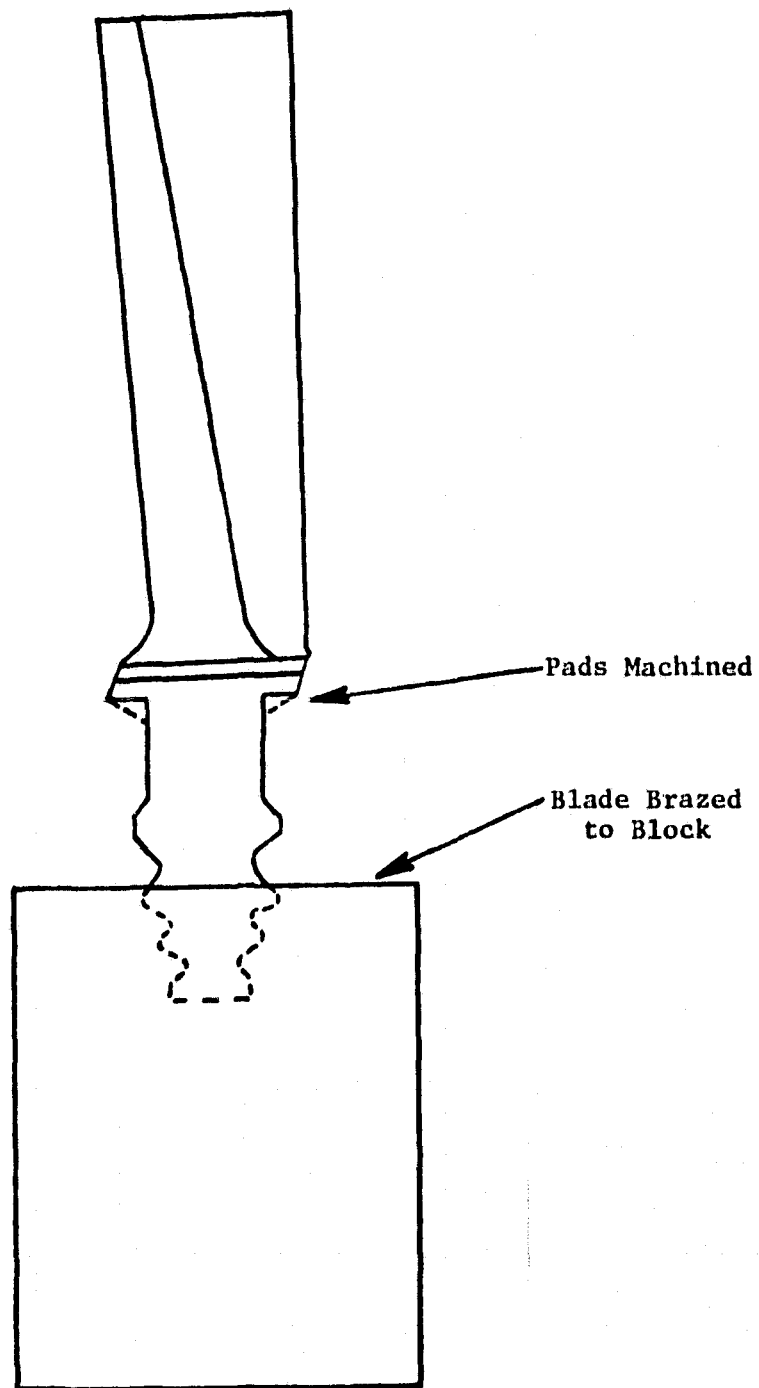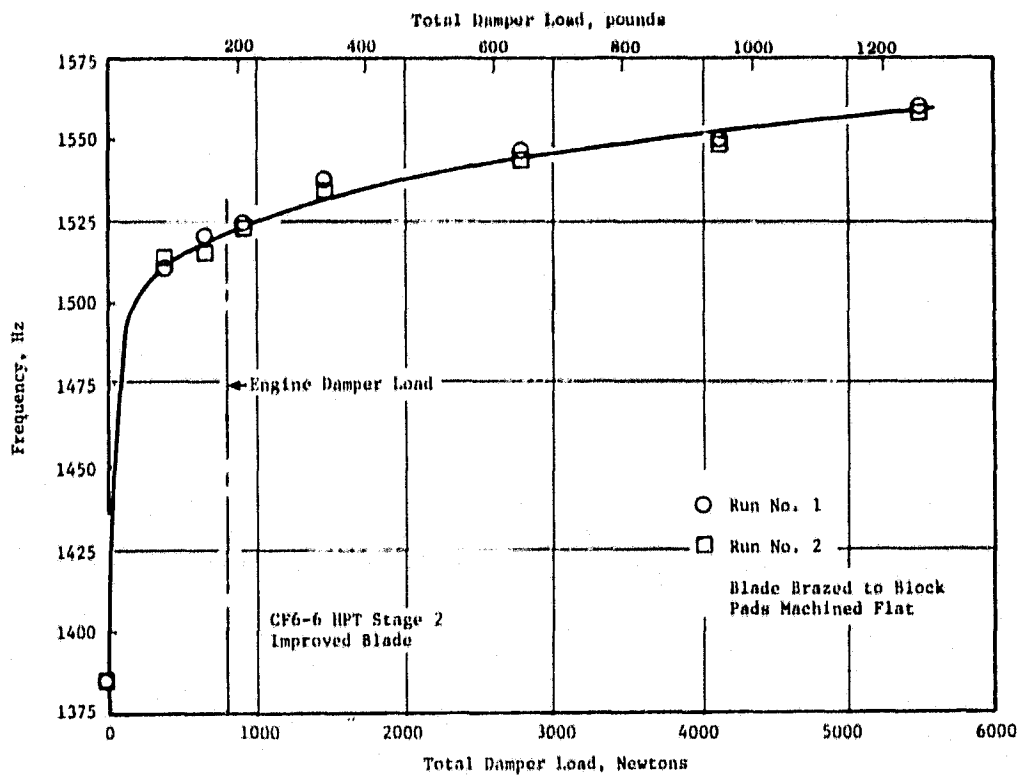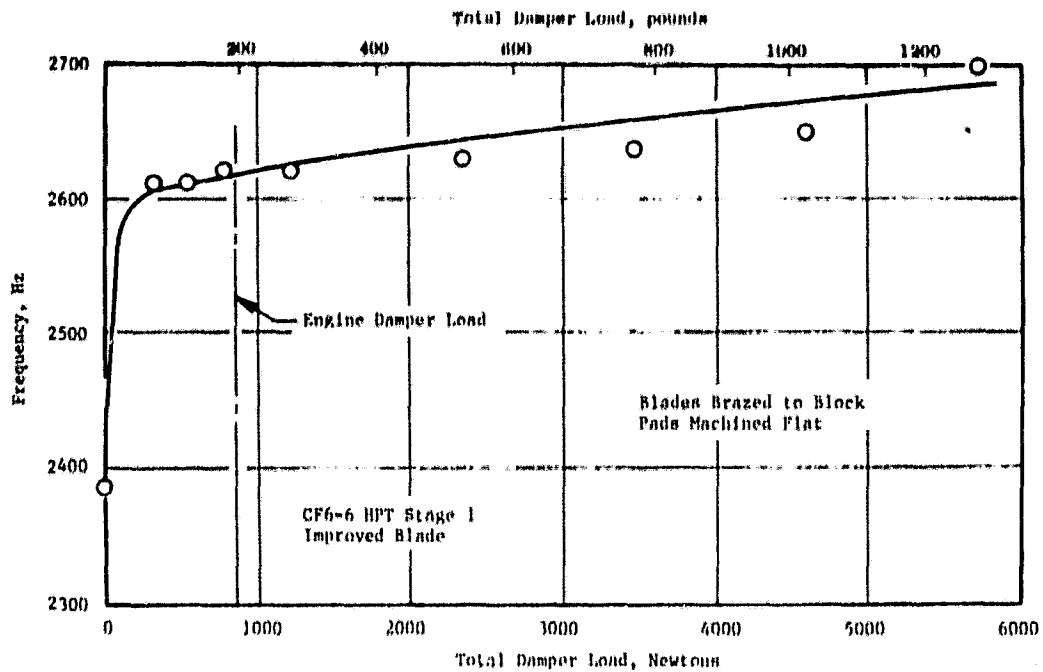
Figure 48.   Blade Modifications.

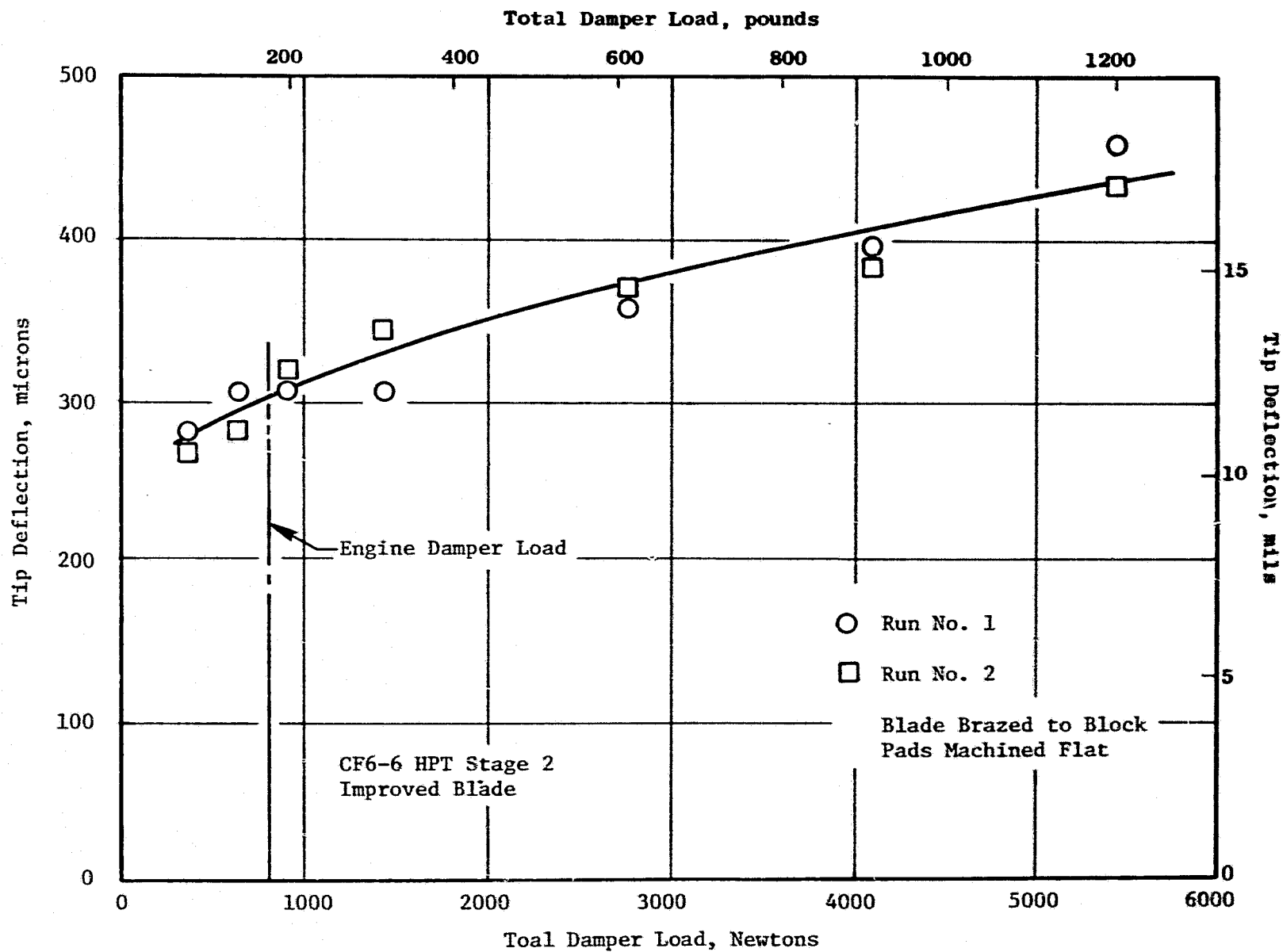**Figure 49.** Frequency Versus Damper Load for the Stage 1 and Stage 2 Blades.

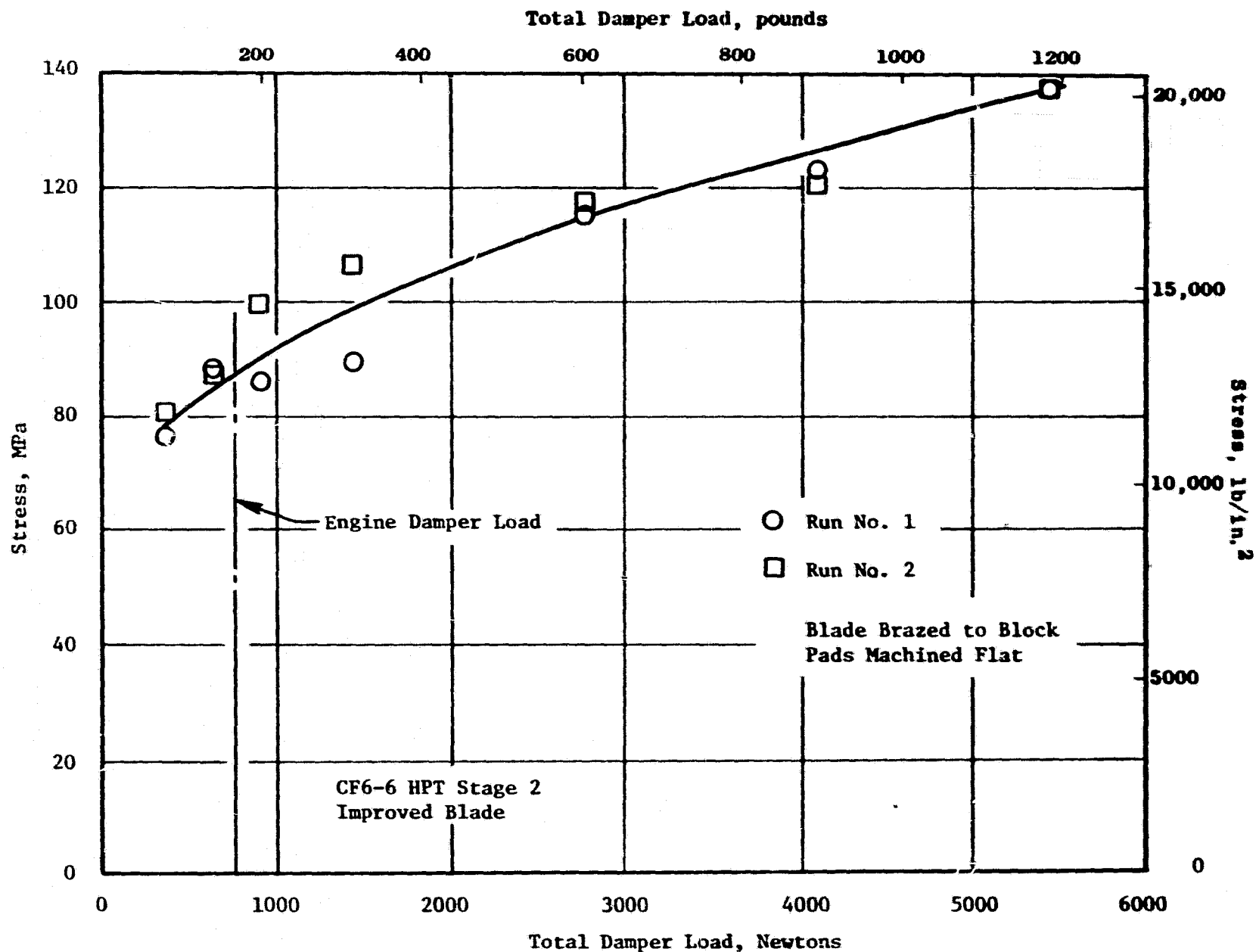Figure 50. Tip Deflection Versus Damper Load for Stage 2 Blade.

Figure 51. Root Leading Edge Stress Versus Damper Load for Stage 2 Blade.

6.3 DISK RIM STRESS DISTRIBUTION TEST

The objective of these tests was to determine the state of the surface stress in the rim area of the Stage 1 and Stage 2 disks. Models 3 times full size were utilized.

6.3.1 Test Description

Single dovetail post and bolt hole/embossment sections of the Stage 1 and Stage 2 disks were modeled. The models, shown in Figure 52, were 3 times full size and were formed from a photoelastic material which has approximately the same Poisson's ratio as the turbine disk material. The Young's modulus of the photoelastic material produced approximately half the strain as the disks experience in service at test loads within the capacity of the load test machine. Approximately 270 strain gages were applied with rosettes in areas with relatively uncertain principal stress directions.

The dovetail tangs of the models were tested in a Universal Load Test machine. Direct rim radial loads were applied independently to each of the three dovetail tang pairs. This was done to obtain the effects of tang-to-tang load splitting on the net strain distribution because tangs usually do not carry equal parts of the blade loads. The test setup is shown in Figures 53 and 54. The rabbet loading was tested in the setup shown in Figures 55 and 56. Each rabbet was loaded independently and a combined stress was then calculated using the principle of superposition.

6.3.2 Test Results

The final products of this three-dimensional (3D) rim stress distribution test are the stress concentration factors (K_T) of the forward and aft rabbet fillets. This result was arrived at by combining the tang and rabbet loading proportionally for a specific engine load case in the flight cycle. The dovetail tang load split was determined from a previous two-dimensional (2D) photoelastic test of the dovetails for both the Stage 1 and 2 disks. The value of rabbet loading was calculated using a complete computer shell model of the entire HPT rotor.

These K_T data were generated for each of the four radial strips of strain gages illustrated in Figure 57, a closeup photograph of the Stage 1 rim model. The four radial strips of gages were primarily uniaxial but had rosettes applied in key areas to permit determining the principal stress. The gages were radially spaced approximately 0.05 inch apart to assure that the peak stress was detected. The close positioning of the gages limited the number of rosettes that could be used because of the two additional leads required for each rosette. The results of this test revealed that the instrumentation was adequate.
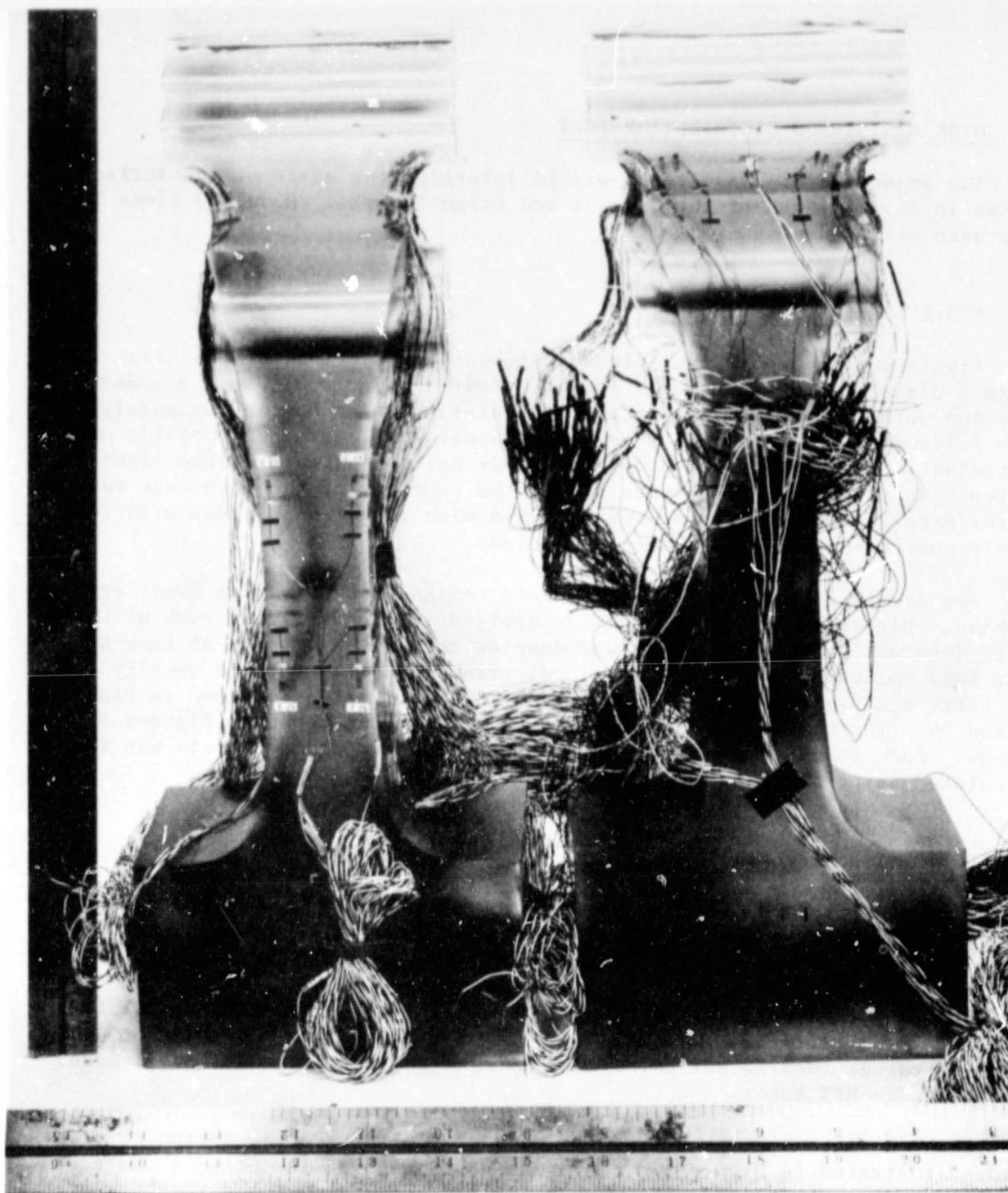
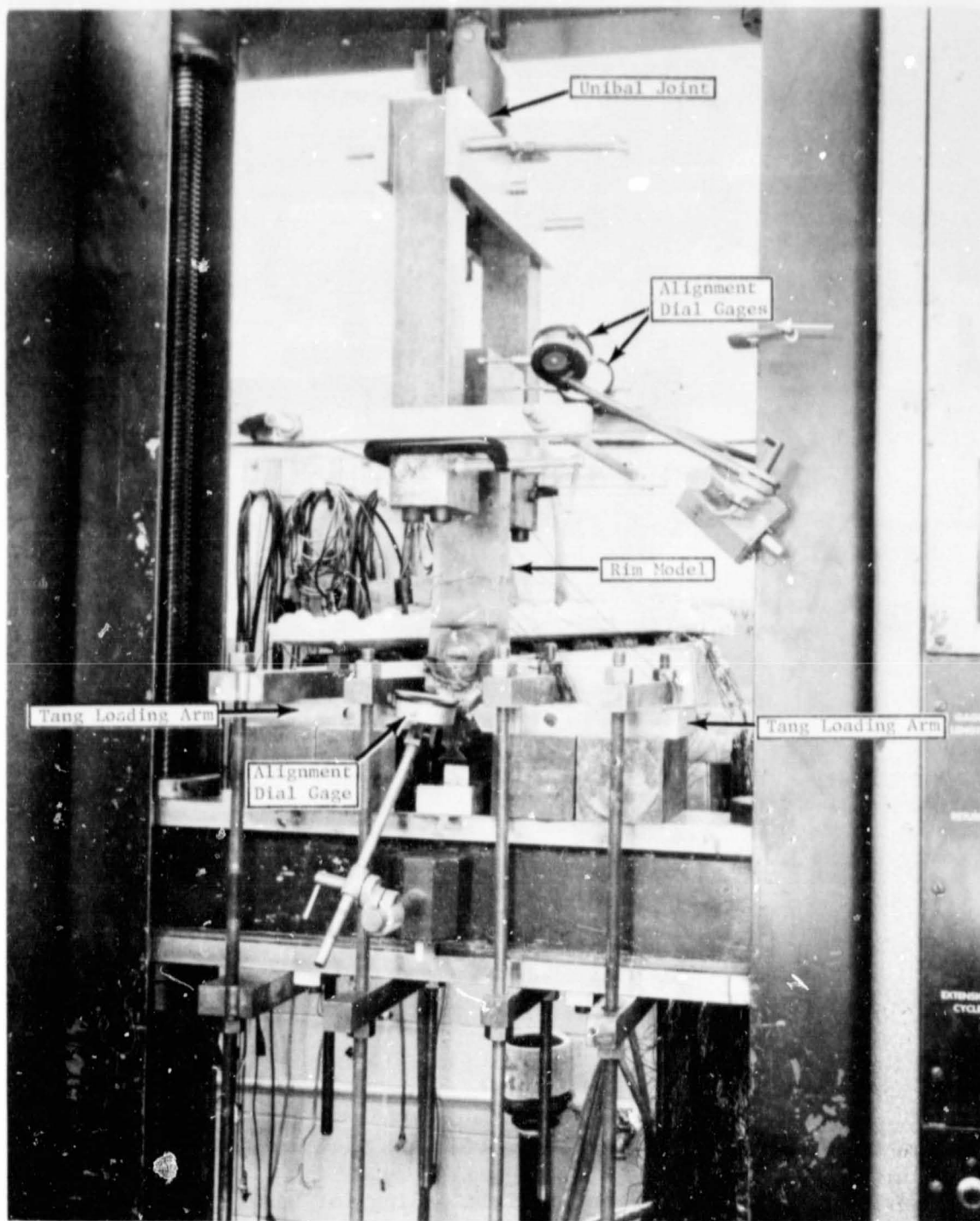Figure 52. Instrumented Stage 1 and 2 Disk Rim Stress Test Models.

80

Figure 53. Direct Radial Loading for Disk Rim Stress Tests
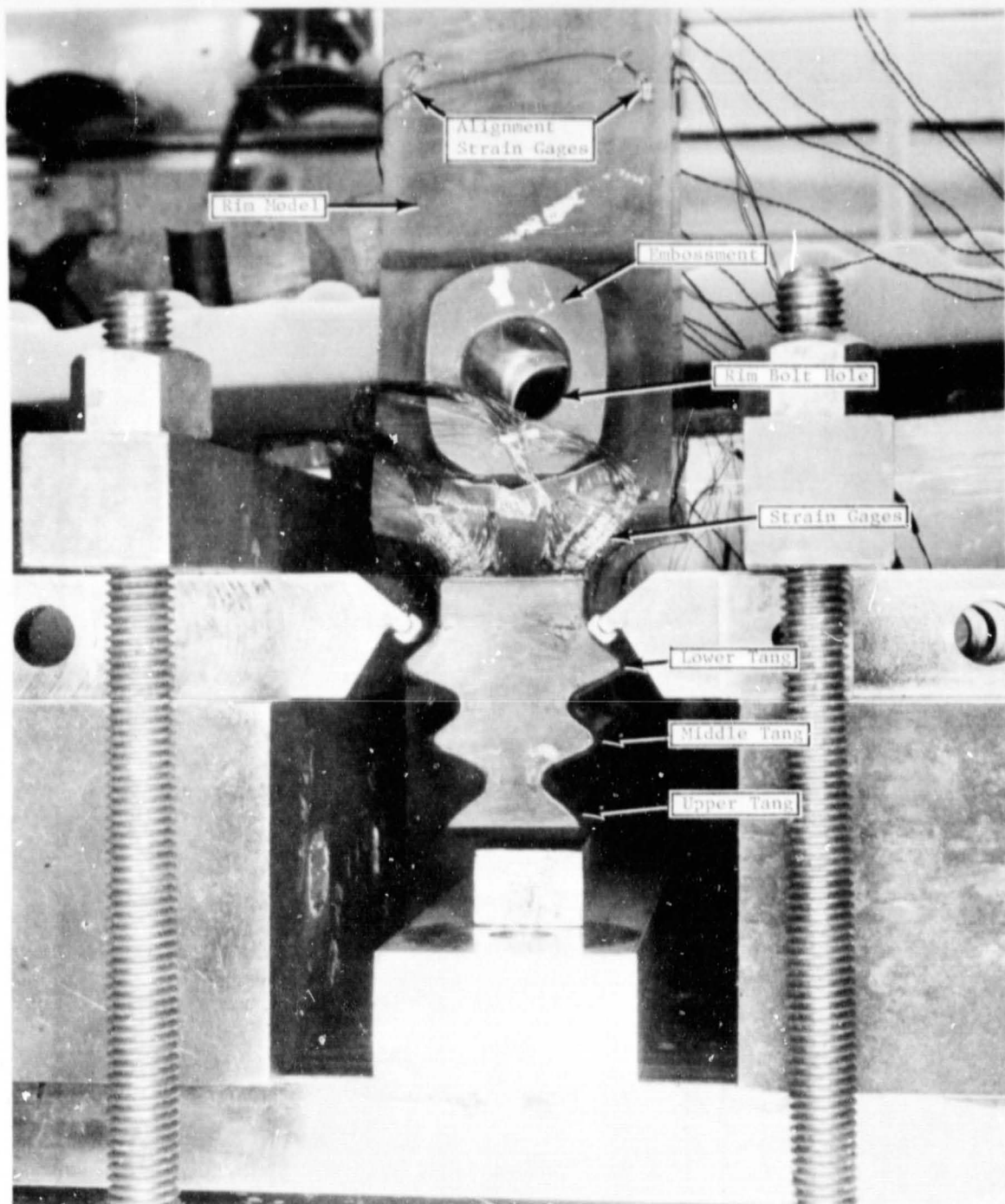(Lower Tang Loading).

81

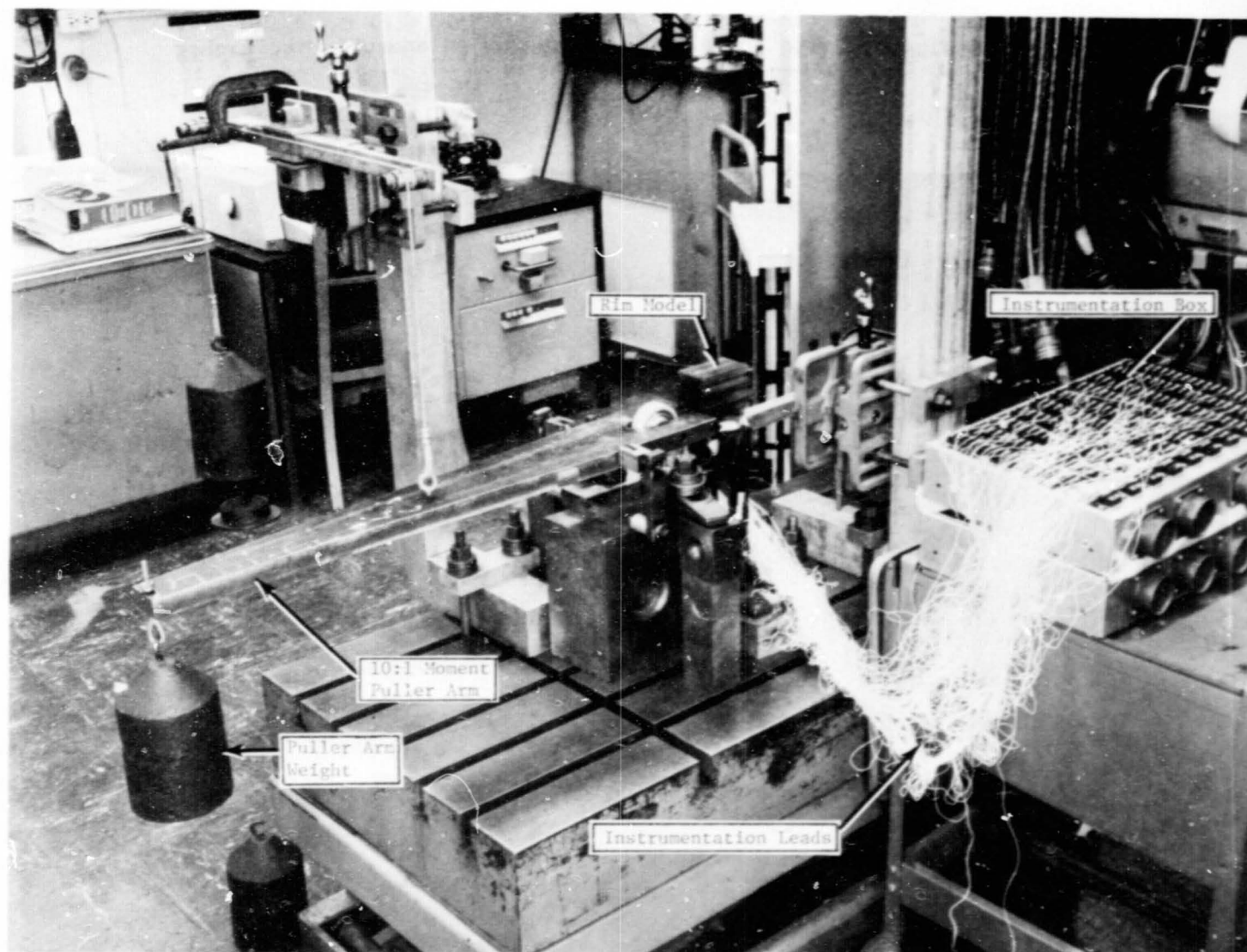Figure 54. Closeup of Direct Radial Loading for Disk Rim Stress Tests (Lower Tang Loading).
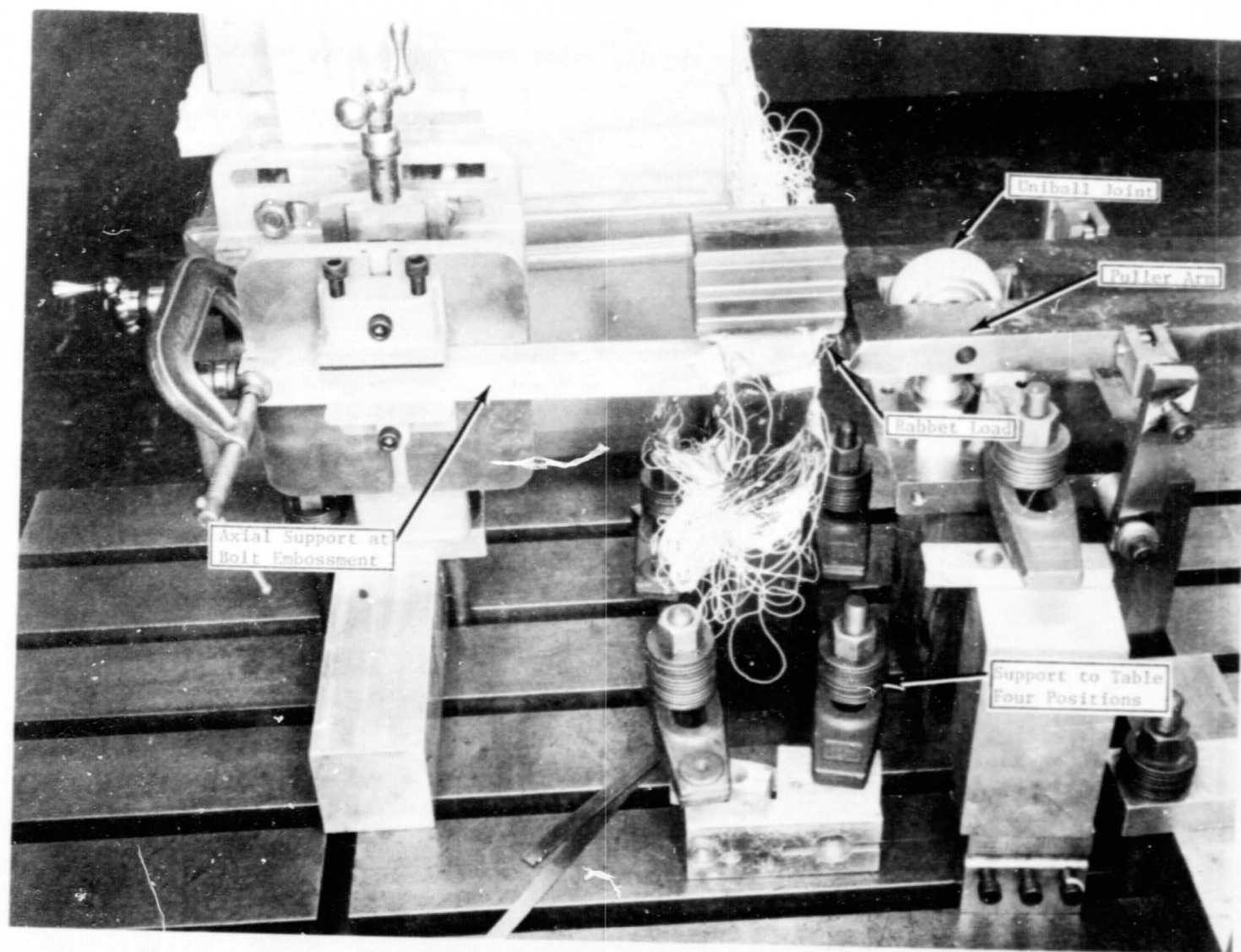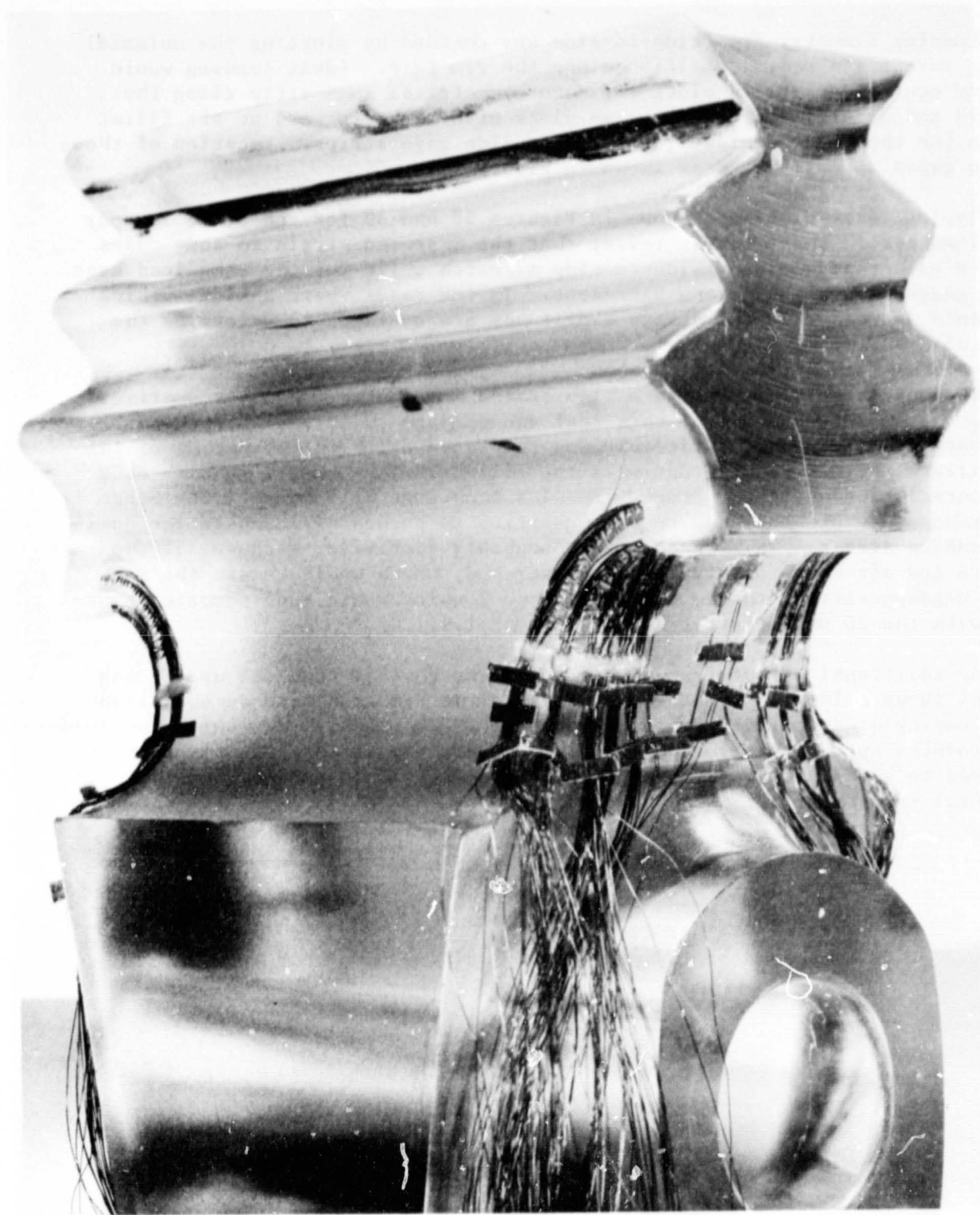
Figure 55. Rabbet Load Setup for Disk Rim Stress Tests.

Figure 56. Closeup of Rabbet Load Setup for Disk Rim Stress Tests.

Figure 57. Rim Model Instrumentation.

85

Loading symmetry from side-to-side was checked by plotting the uniaxial strain versus its radial position along the rim face. Ideal loading would produce equivalent strain plots for each symmetrical gage strip along the forward and aft fillets. Each curve plots either the forward or aft fillet strain for the corner, middle, inner, and side gage strips. Location of these strain gages is delineated as shown in Figure 57.

Typical data plots are shown in Figures 58 and 59 for the Stage 1 upper tang load case. These curves reveal that the measured strain in some cases shows a rather significant side-to-side mismatch while for the same load case other gages show a very close agreement. In the cases where a side-to-side imbalance is measured, the strain amplitudes are averaged to determine the value of K_T.

The results of this test are illustrated in Figure 60 which summarizes the K_T values determined from this test and compared with the 2D photoelastic test. The 2D photoelastic test was completed prior to the design of the rim fillets and was used to optimize the fillets. The Stage 2 results show good correlation while the Stage 1 results show some difference. The Stage 1 differences are probably due to the inability to accurately compute the nominal bending stress. This reasoning is probably justified; because, if the forward and aft K_T's for Stage 1 were averaged, which would negate the unknown bending stress, the K_T would be about 2 which would then compare favorably with the 2D photoelastic test result of 1.9.

An additional output from this stress test reveals that the upper tang loading shows a lower concentrated stress in the rim area than an equivalent tang loading at the middle or lower tang pair. The middle and lower tang loading produces approximately the same rim concentrated stress. This result is believed to be a function of the dovetail geometry and cannot be concluded as a general result for all parts.
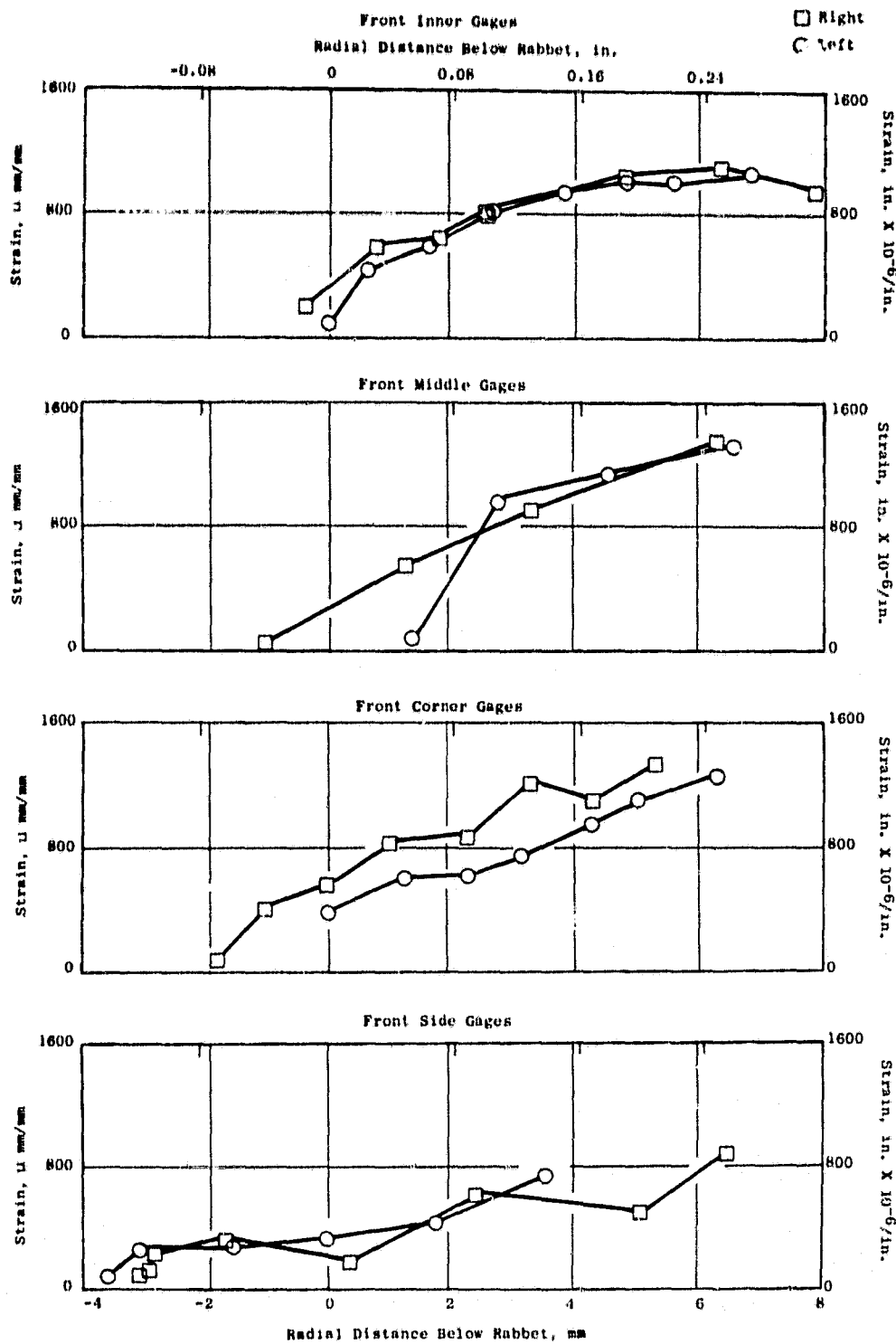
Figure 58.   Strain Versus Radial Distance from Rabbet -
Front Gages.
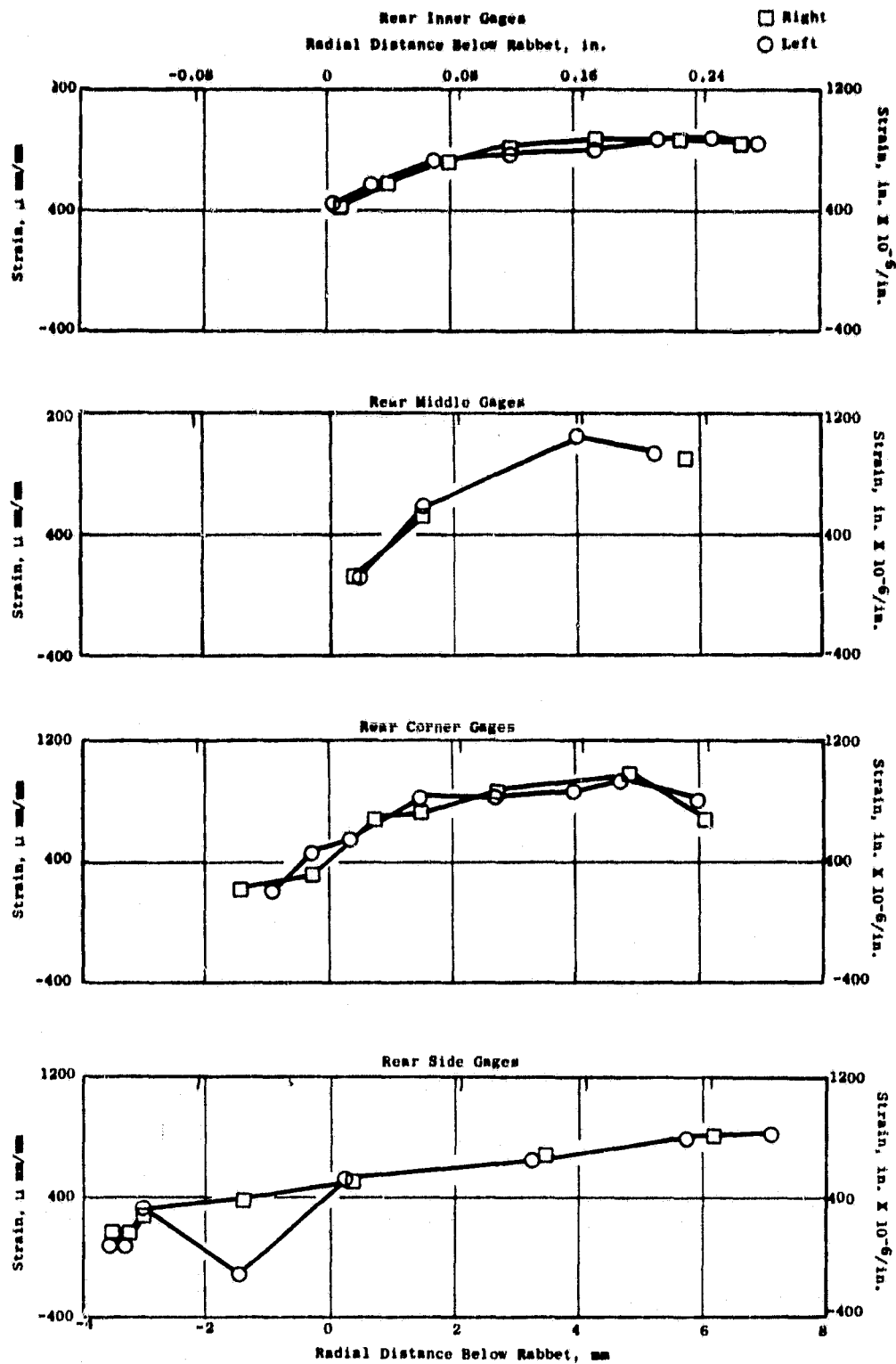
Figure 59. Strain Versus Radial Distance from Rabbet –
Rear Gages.
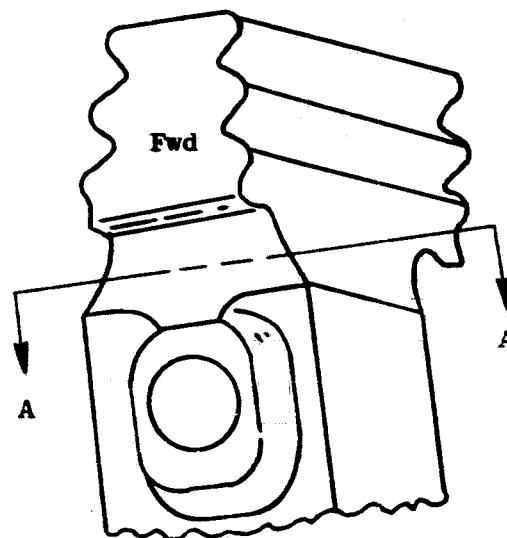
Stage 1 K_T's

Stage 2 K_T's

2D Photoelastic Test	3D Test		3D Test	2D Photoelastic Test
1.91	(inner) 1.70		1.74 (inner)	1.74
	(middle) 1.64		1.89 (middle)	
	(corner) 1.78		1.67 (Corner)	
	(side) 1.47	Rear	1.85 (side)	
	(side) 1.92	Forward	2.28 (side)	
1.90	(corner) 2.29		2.02 (corner)	2.25
	(middle) 2.49		2.16 (middle)	
	(inner) 2.25		2.20 (inner)	

Figure 60.   Summary of Rim Test Results.

7.0 INSTRUMENTED ENGINE TEST

The objectives of the instrumented engine tests were to evaluate the thermal, mechanical, and aeromechanical characteristics of the improved design turbine rotor and stator hardware. Pressure, temperature, cooling flow, and stress data obtained were also used to conduct additional life and design analyses. Testing at sea level included transient and steady-state conditions from minimum to maximum engine power level.

7.1 TEST SETUP

The test vehicle used was a TF39 core engine, which is the high pressure system, fitted with an exhaust gas recirculation system which provided heated air to the inlet as shown in Figure 61. This system was designed to deliver the inlet air at whatever temperature is required to set "redline" cycle parameters. Exhaust gas is "scooped" out of the exhaust stream and supplied to the front of the engine by an insulated pipe. At the front of the engine, the air splits into a Y-shaped pipe and is delivered to a manifold which distributes the air uniformly to the inlet of the engine.

The TF39 core is the same as a CF6-6 core with the exception that selected rotor spool joints are of doweled design versus the rabbets used on CF6-6. A standard turbine midframe was used to support the No. 5 bearing. The slave exhaust nozzle which simulated the low pressure turbine effective area was variable via bolt-on tabs to produce the proper turbine pressure ratio.

Rotor spool instrumentation was read out via a 100 point slip ring mounted to the hub of the turbine midframe. Provision was made during rotor buildup and instrumentation application to facilitate rapid reprogramming of the slip ring so as to permit three slip rings full of rotor instrumentation to be read out during one build of the main engine. Slip ring changeover was accomplished by removing the turbine midframe, reprogramming the leads, and reinstalling the turbine midframe. Figures 62 through 65 show the actual test hardware along with typical instrumentation applied.

7.2 INSTRUMENTATION

The test instrumentation used to measure engine performance, turbine stress and temperatures and to monitor engine operation is broken down into three groups: general instrumentation, aerodynamic instrumentation, and turbine instrumentation. Instumentation in each group is given below and is indicated on Figure 66.
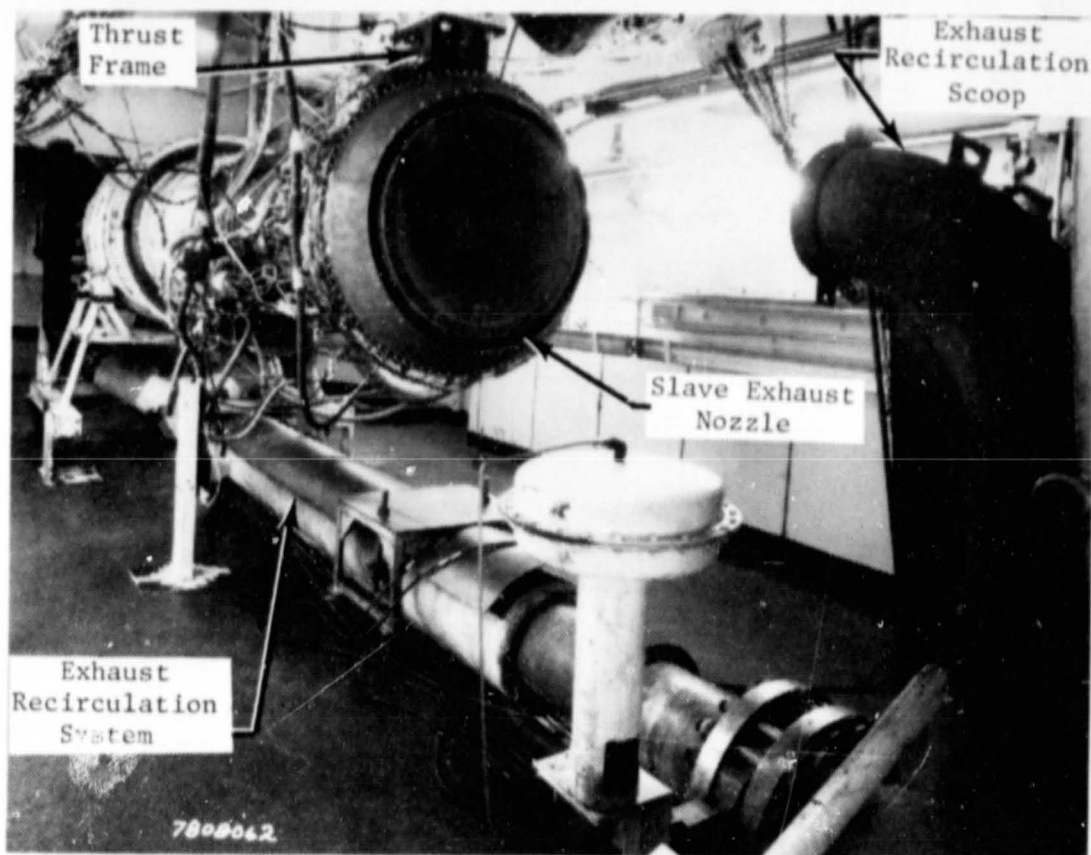
Figure 61.   TF39 Core Engine Installed in Test Cell.
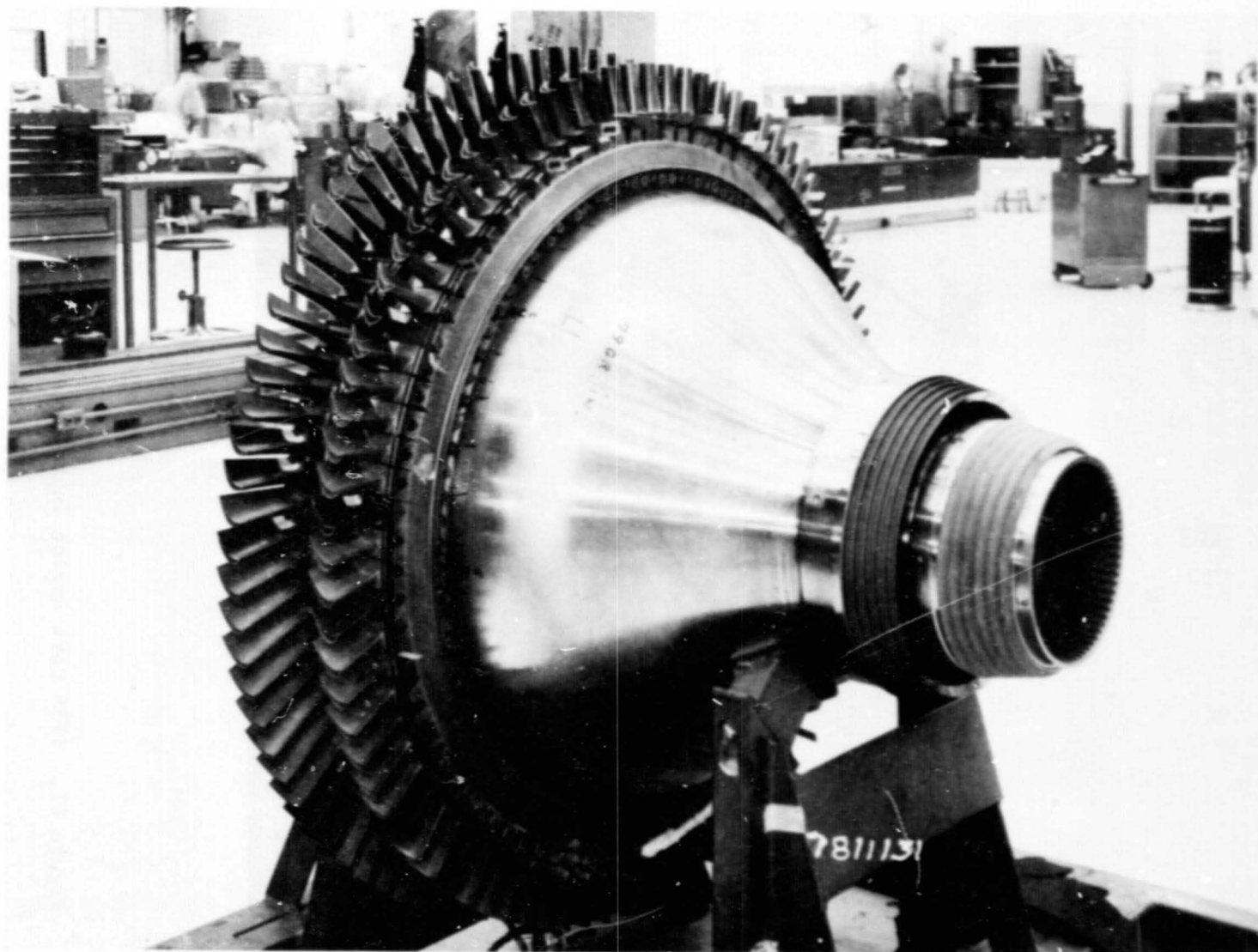
Figure 62.   Improved Turbine Rotor Front End View.
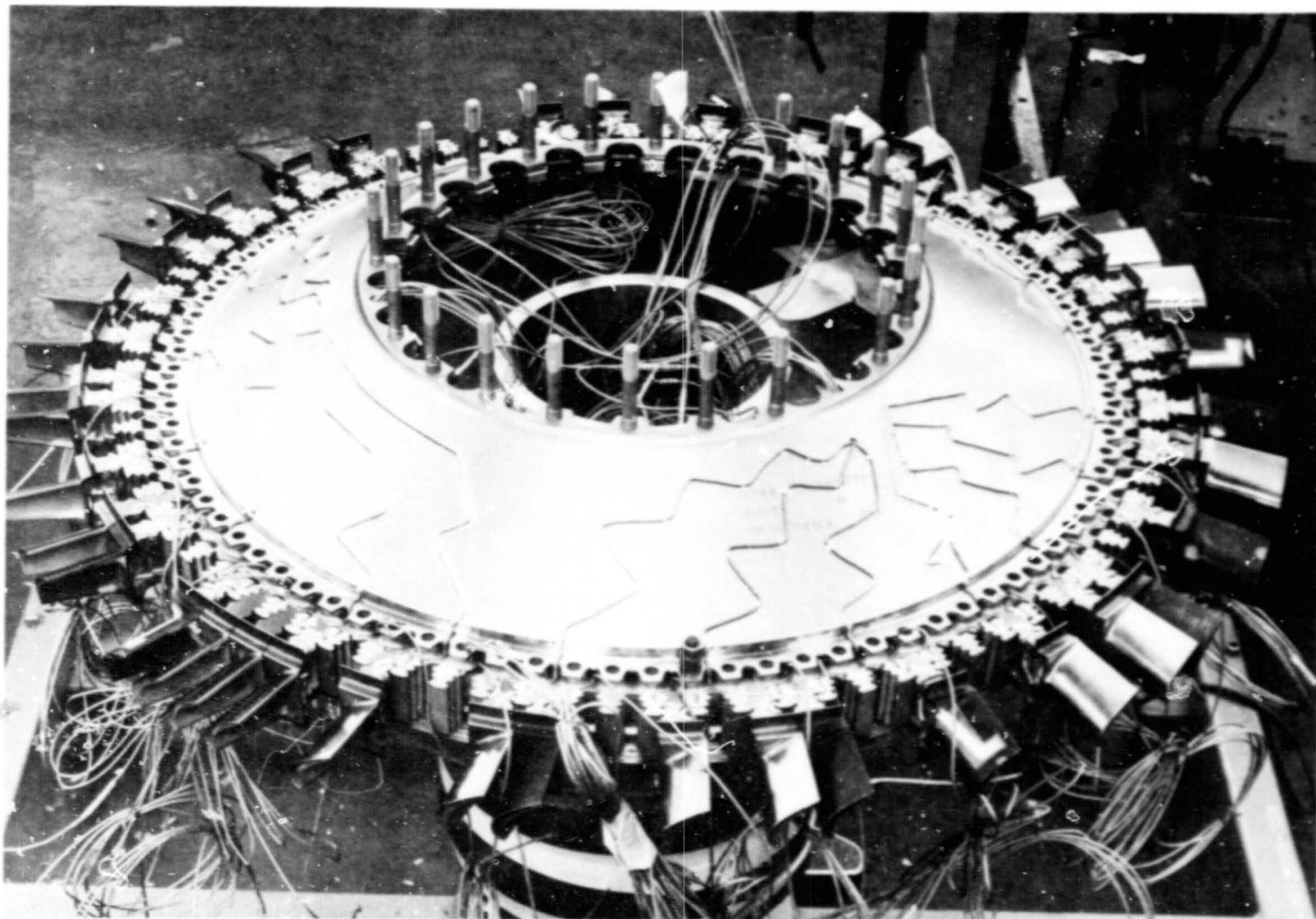
Figure 63.   Instrumented Stage 1 Rotor Showing Thermocouple and Strain
Gage Leadouts.
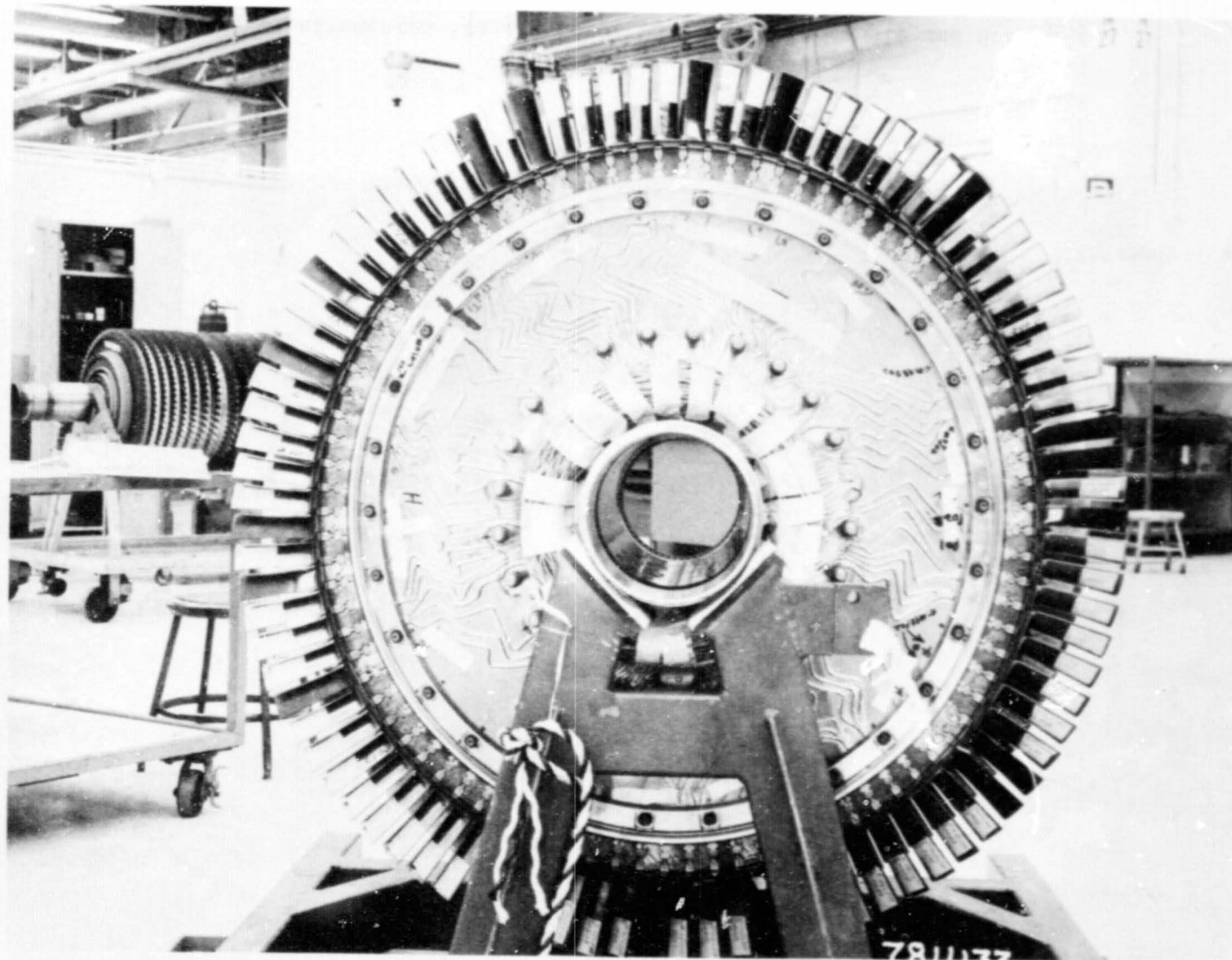
Figure 64.   Instrumented Stage 2 Rotor (Aft View) Showing Thermocouple and
Strain Gage Leadouts.
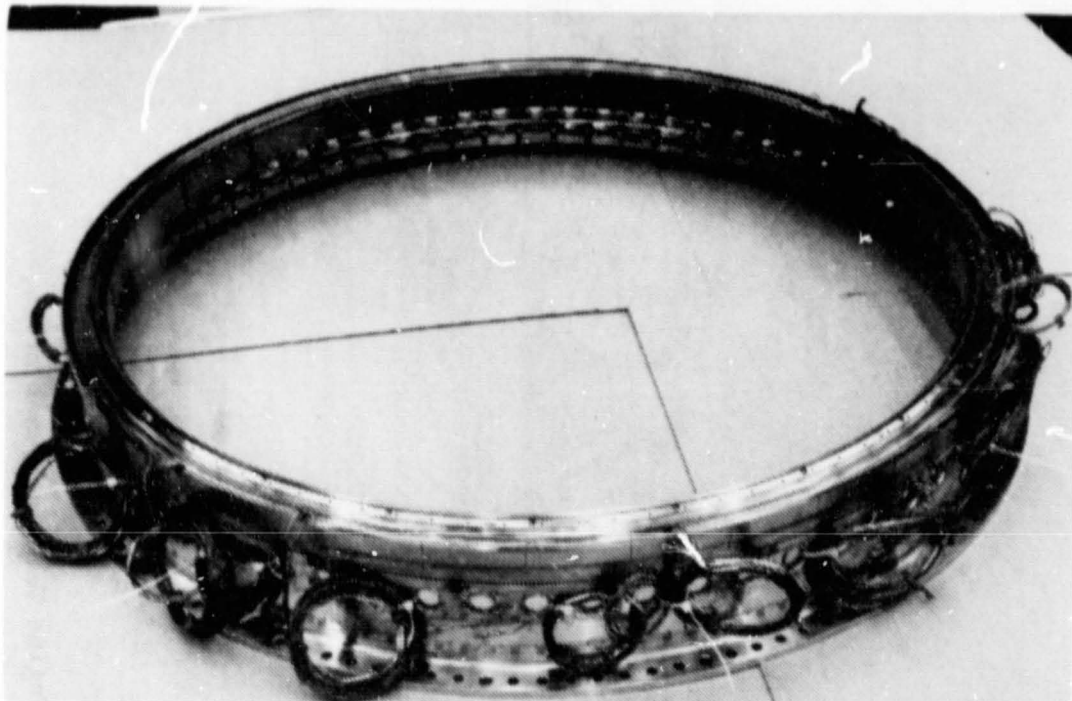
Figure 65. Instrumented Stage 2 Nozzle Support.

Aero
Plane 25 Core Inlet
3 Temperature Probes
5 Wall Static Pressures

Aero
Plane 44 Turbine Midframe Discharge
11 Temperature Probes
5 Pressure Probes

Aero
Inlet Bellmouth
Screen
20 Temperature
Probes

Aero
Plane 3 Compressor Discharge
4 Wall Static Pressures
1 5-Element Temperature Probe

Turbine
Turbine Stators
148 Metal T/C'S
52 Air T/C'S
23 Static Pressures

Aero Flows

9th Stage
Flow

13th Stage
Flow

EP Recoup
Flow

General
Barometric Pressure
Humidity
Cell Static Pressure
Core Speed
Main Fuel Flow
Verification Fuel Flow
Fuel Temperature
Fuel Sample Specific Gravity
Fuel Sample Temperature
Variable Stator Vane Position

Turbine
4B Bearing Housing
4 Thrust Bridges

Turbine
Turbine Rotor
Stage 1 Blades 23 S/G'S and 29 T/C'S
Stage 2 Blades 23 S/G'S and 23 T/C'S
Rotor Structures 8 S/G'S and 42 T/C'S

Figure 66.   Engine Test Instrumentation.

General Instrumentation

- Barometer Pressure
- Humidity
- Cell Static Pressure
- Core Speed
- Main Fuel Slow
- Verification Fuel Flow
- Fuel Temperature
- Fuel Sample Specific Gravity
- Fuel Sample Temperature
- Variable Stator Vane Position.

Aerodynamic Instrumentation

- Inlet Temperature
- Core Inlet Static Pressure
- Core Inlet Temperature
- Compressor Discharge Pressure
- Compressor Discharge Temperature
- Turbine Midframe Discharge Temperature
- Turbine Midframe Discharge Pressure
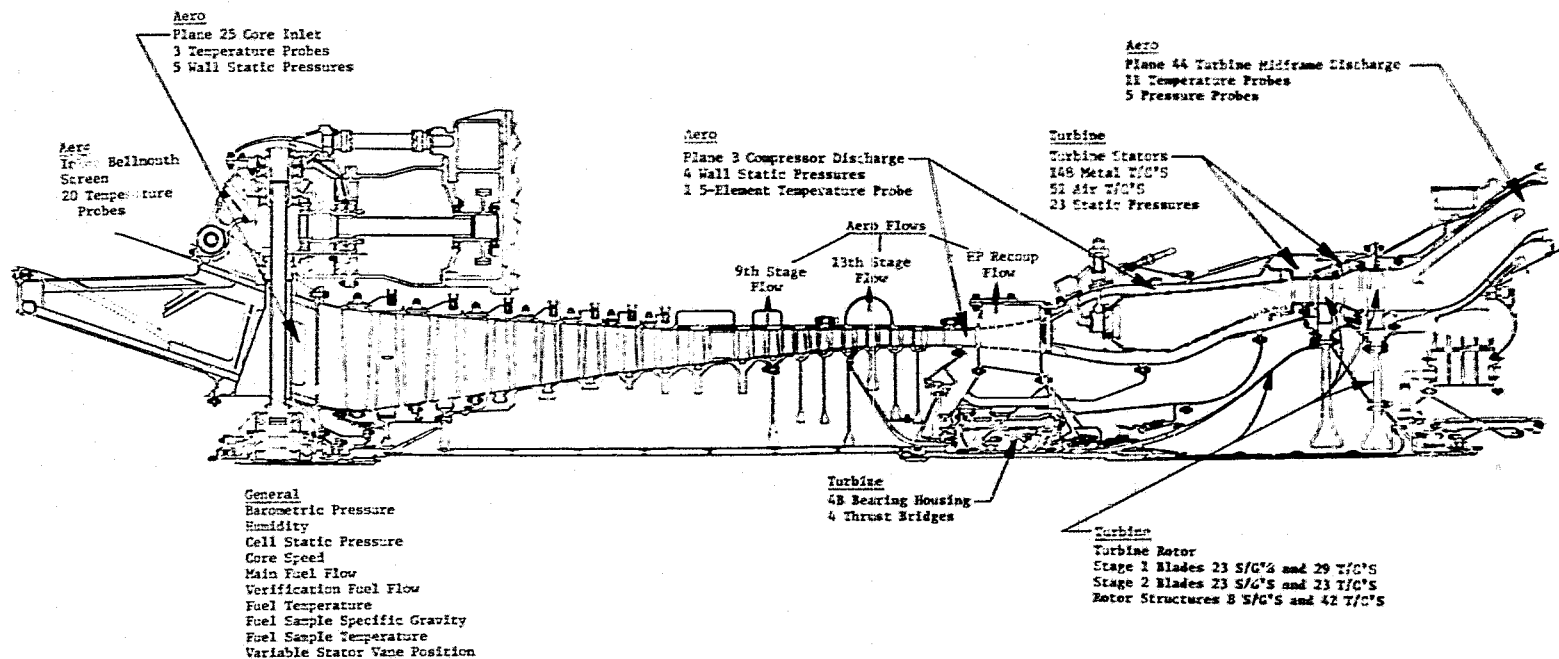- Instrumentation was installed and flow calibrated to measure compressor ninth stage flow to turbine midframe, thirteenth stage compressor flow to Stage 2 HP turbine nozzle, high pressure recoup to turbine midframe and cooling flow to high pressure turbine rotor.

Turbine Instrumentation

- Turbine Rotor Strain Gages -- Twenty-three dynamic strain gages on Stage 1 blades, 23 dynamic gages on Stage 2 blades, and 8 dynamic gages on nonairfoil components.

- Turbine Rotor Thermocouples - Twenty-nine chromel-alumel thermocouples on Stage 1 blades, 23 on the Stage 2 blades, and 42 on nonairfoil components.

- Turbine Stator Thermocouples - A total of 148 skin thermocouples and 51 air thermocouples (all chromel-alumel).

- Turbine Pressure Instrumentation - Twenty-three static pressures.

- 4B Bearing Thrust Bridges - Four static strain gain bridges on the 4B bearing housing.

7.3 TEST PROCEDURE

Instrumented testing of the improved turbine was divided into three distinct tests. This was required due to the quantity of sensors on the rotor and the capacity of the slip ring.

Test 1 - This test concentrated on accumulating the blade vibratory data throughout the engine speed range. A few "safety" thermocouples were read on the Stage 1 turbine blades. Simultaneously, turbine stator temperatures and pressures were recorded.

Test 2 - Reprogramming the slip ring provided data on Stage 1 blade temperatures, rotor spool strain gages, and selected spool temperatures. Numerous transients were run to determine heating/cooling rates. Steady-state data were obtained at a variety of power settings and inlet conditions.

Test 3 - Rerouting of rotor instrumentation was done with the rotor remaining in the engine. All remaining rotor spool thermocouples were read on this test along with Stage 2 blade metal temperatures. Essentially, the same test plan as Test 2 was followed to gather steady-state and transient data.

7.4 TEST RESULTS

The instrumented core engine tests were designed to provide vibratory response, temperature, pressure, and cooling flow data. Tests included a range of steady-state and transient engine operating conditions. Results presented are divided into three groups: rotor, stator, and cooling.

7.4.1 Rotor

Stage 1 Blade Vibratory Response - Blade strain gages were applied to the blades at three locations: shank with radial orientation, root trailing edge pressure side with radial orientation, and pitchline with axial orientation. The three locations chosen were enough to provide sensitive gages for all expected modes of vibration. Typical results of Stage 1 blade vibratory response are shown in Figure 67. Examination of this figure shows that primary Stage 1 blade response was in the first flex mode as expected. However, it is significant to note that no resonant response was observed. The blade responded in a force-driven fashion to very low levels. Maximum blade response
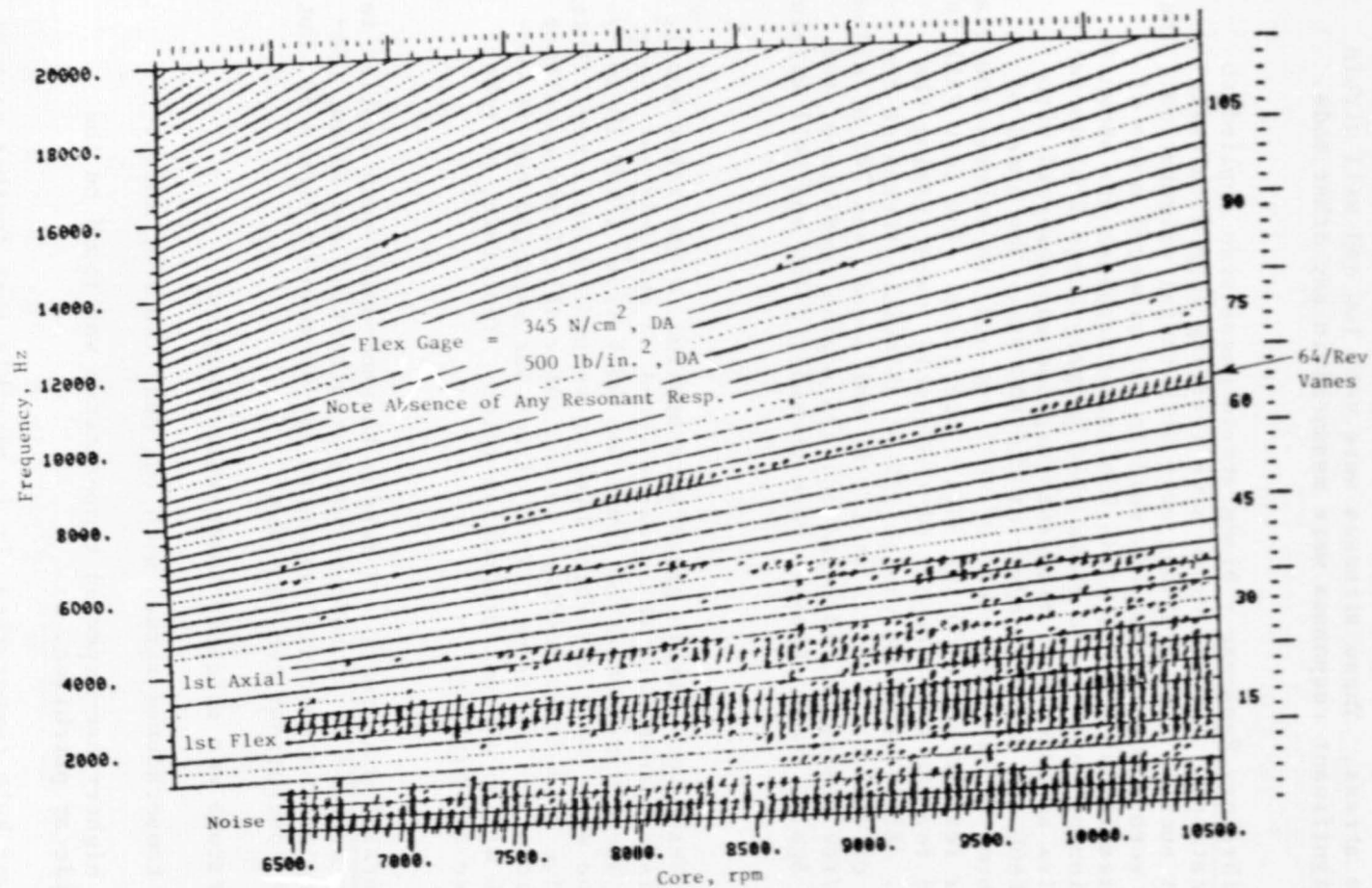
Figure 67.   Typical Stage 1 Blade Response.

was 19% of allowable stress, extrapolated to fan engine conditions and accounting for the +3σ blade stress. These stresses were very low and well within design limits. No significant responses were measured in any other mode.

Stage 2 Blade Vibratory Response - Blade strain gages were applied to the blades in two locations: root pressure side trailing edge with radial orientation, and root suction side trailing edge with radial orientation. The two locations chosen were enough to respond well to all expected modes of vibration. Typical results of Stage 2 blade vibratory response are shown in Figure 68. Examination of this figure shows that primary Stage 2 blade response is in first flex as expected. Resonant response was observed with 10/rev crossing at ≈8600 rpm and with 8/rev at ≈10,400 rpm. The speed of 10,400 rpm is well above CF6-6D core speed of 9827 rpm and, therefore, the blade will not see 8/rev or respond to it during engine operation. The test vehicle was run to this speed for the sole purpose of thoroughly investigating the 8/rev blade response. Blade response was to 11% of allowable stress at the 10/rev crossing, 19% of allowable stress at CF6-6D max speed, and 38% of allowable stress at the 8/rev resonance, adjusted for fan engine conditions, and +3σ blade response. Again, these stresses were considered low and well within design limits.

Rotor Vibratory Response - Strain gages were applied to the rotor spool. Response was to levels comparable to those experienced on the original (twin shank) CF6-6 rotor. The maximum observed level was 4826 N/cm^2 (7000 lb/in.^{2}) double amplitude. The mode shape was rotor bending responding to 2/rev. This 2/rev excitation is due to a frame feedback to the rotor of a 1/rev unbalance load applied by the rotor to the frame. This effect was expected and is consistent with response of the current production rotor. Therefore, no rotor vibratory problems are anticipated.

Stage 1 Blade Metal Temperatures - Numerous thermocouples were applied to the Stage 1 blades to measure metal temperatures at pitchline and below. Results varied depending on the specific region as can be seen on Figure 69, but the following general conclusions can be drawn:

● Bulk temperature was slightly lower than predicted.

● Most local temperatures agrees with the heat transfer model.

● An area of higher-than-expected temperatures was found on the pressure side at pitchline.

Based on the lower bulk temperature, it is possible that further performance benefits can be achieved with reduced cooling. This will be studied in conjunction with cooling pattern changes to reduce local areas of higher-than-projected temperatures.

100
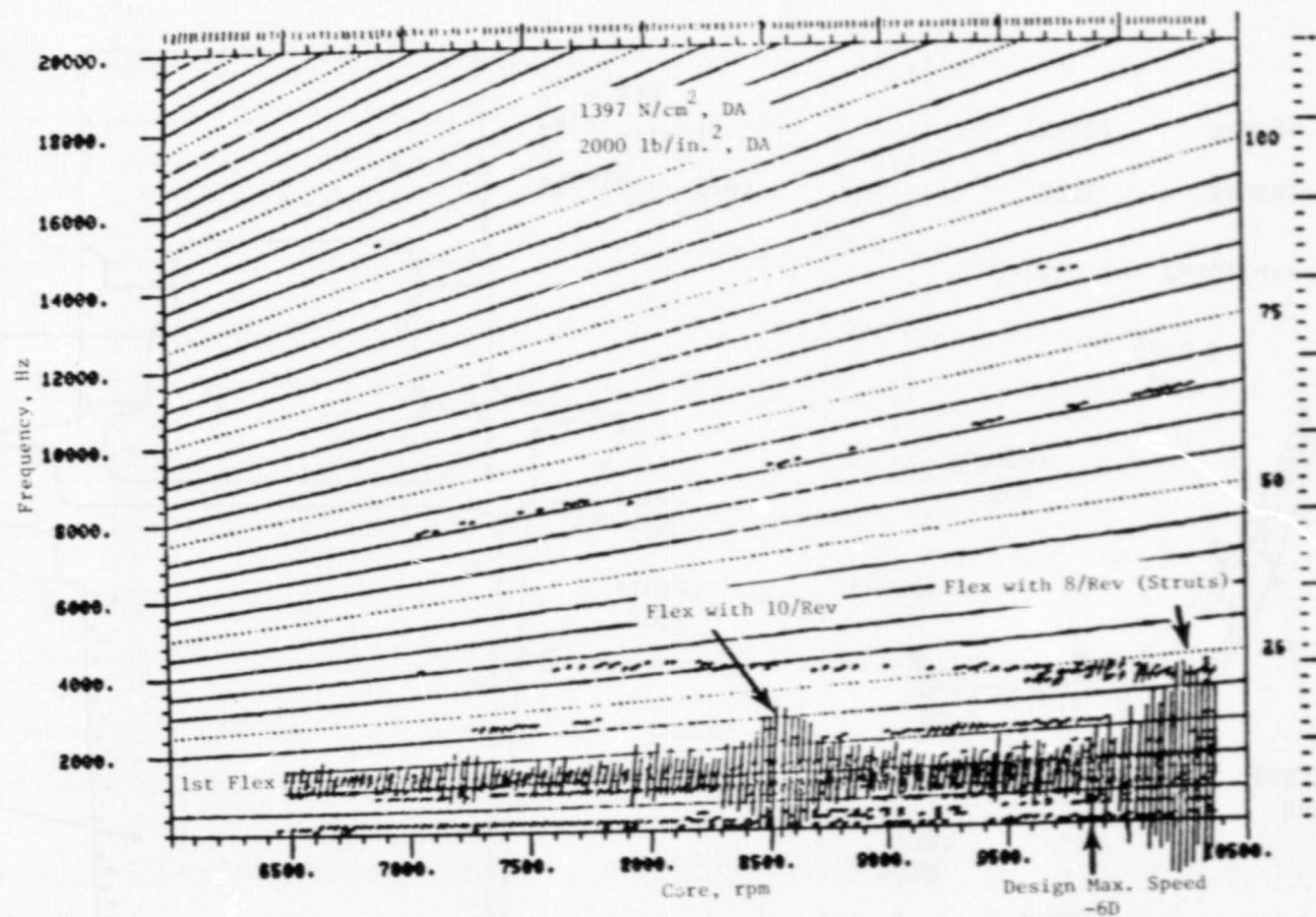
Figure 68. Typical Stage 2 Blade Response.

964
(1018)

1075
(1032)

1025
(1018)

919
(954)

958
(999)

682

(T$_{bulk}$ = 916)

T$_{4.1}$ = 1401

T$_3$ = 543

1028
(1022)

(960)

941
(983)

(1037)

904
(952)

1088
(1021)

(1052)
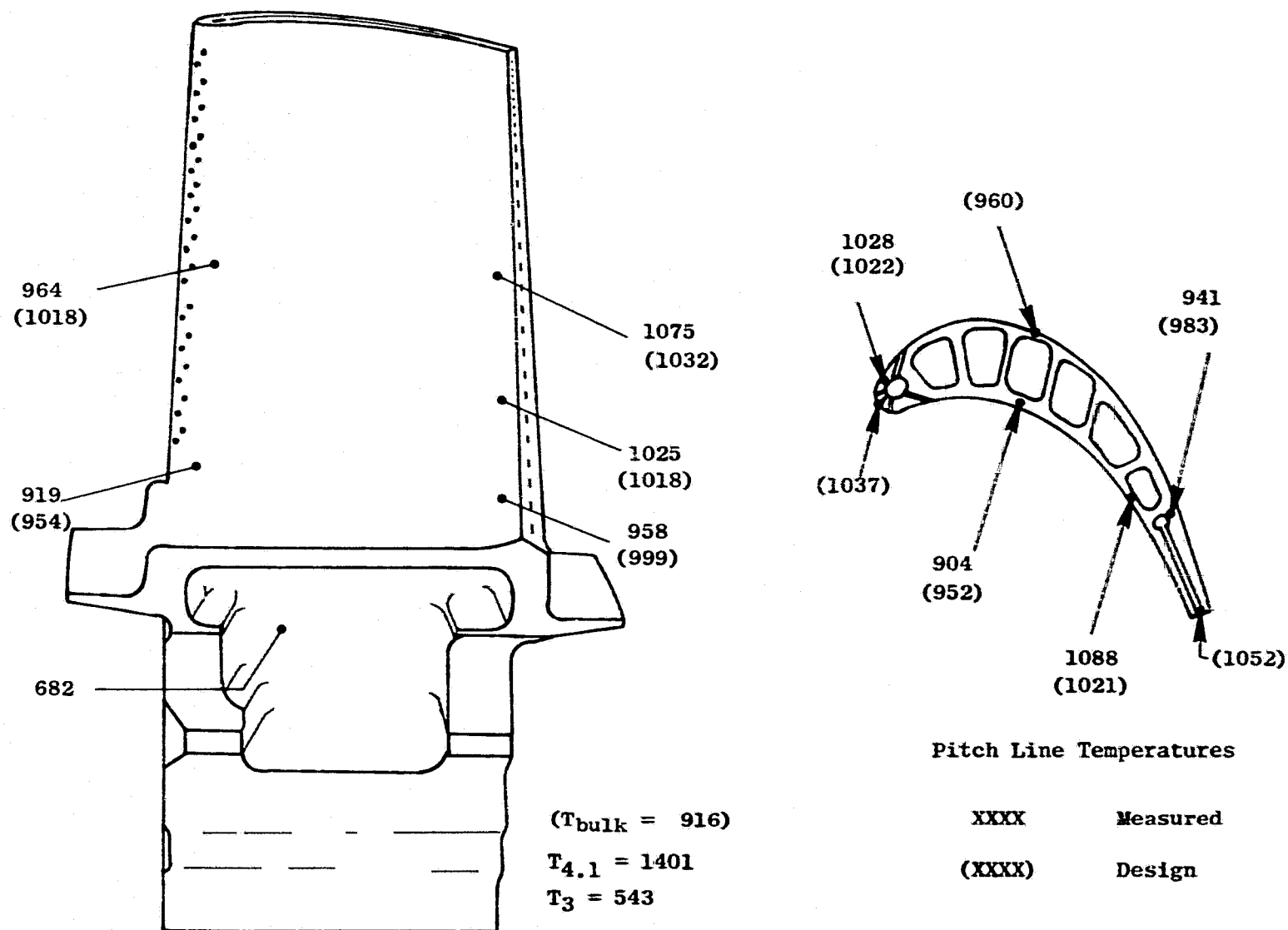
Pitch Line Temperatures

XXXX   Measured

(XXXX)   Design

Figure 69. Stage 1 Blade Metal Temperature (° C).

Stage 2 Blade Metal Temperatures - As shown on Figure 70, measured Stage 2 blade metal temperatures were close to the expected values with some discrepancies in the midchord and trailing edge regions of the blade. The temperature of the midchord region of the blade pressure side pitchline was somewhat higher than predicted, while the trailing edge was substantially cooler. This results in a net reduction in the blade bulk metal temperature. Posttest analysis has confirmed that there is a life/performance benefit potential due to this lower bulk temperature. Appropriate design changes for cooling flow reduction have been incorporated to achieve further performance benefits.

Rotor Spool Metal Temperatures - Numerous rotor spool temperatures were measured at steady-state and transient conditions throughout the engine operating range. The instrumentation was applied to key areas of the rotor to determine an overall rotor temperature distribution. Controlled transient tests were run to carefully determine the response rates of the rotor spool. Results for steady-state design conditions are shown in Figure 71.

With one exception, all rotor temperatures were in good agreement with pretest predictions. The exception was in the area of the front shaft which was about 28° C (50° F) warmer than expected at design conditions. The effect on stress and life has been analyzed and found to be acceptable, i.e., the life of the part meets requirements at the higher temperature.

7.4.2 Stator

Stator Temperatures - The Stage 2 nozzle support and surrounding structure were heavily instrumented to measure metal and air temperatures and static pressures. Figure 72 shows the difference between measured and predicted temperatures on the shroud support structure, extrapolated to redline turbine inlet temperature (T_4) conditions. Note that predictions were in good agreement with measured data except in two areas. The first of these areas is in the region near the Stage 1 shroud leading edge where the support temperature was measured to be about 83° C (150° F) cooler than predicted. It is suspected that the boundary conditions in the analytical model were in error, causing somewhat excessive predicted temperatures. The second area of disagreement between predicted and measured temperatures is in the area of the compressor rear frame and turbine midframe flange. In this test, this flange ran substantially cooler than predicted. It is believed that this difference is due to the difference between a fan engine and a core engine. In the core engine configuration, cold ambient air is free to flow onto this flange. In a fan engine, the flange is surrounded by the core cowl and air inside the cowl space is warmer and has little velocity. Predictions were made for the fan engine and measurements made on a core engine; hence, the measured data is colder than predicted. This is apparently reflected in the structure immediately inboard of this flange, which also ran cooler than predicted.

Figure 73 indicates the degree of success which has been achieved in terms of isolating the shroud hooks form the hot gas stream. Note that the Stage 1 hooks are 16.7° to 41.7° C (25° to 75° F) cooler, even at a relatively

952 (889)

965 (929)

939 (943)

961 (929)

934 (936)

903 (896)

960 (967)

948 (999)

951 (1005)

(1009)

893 (878)

889 (879)

897 (893)

922 (979)

(902)

973 (921)

900 (898)

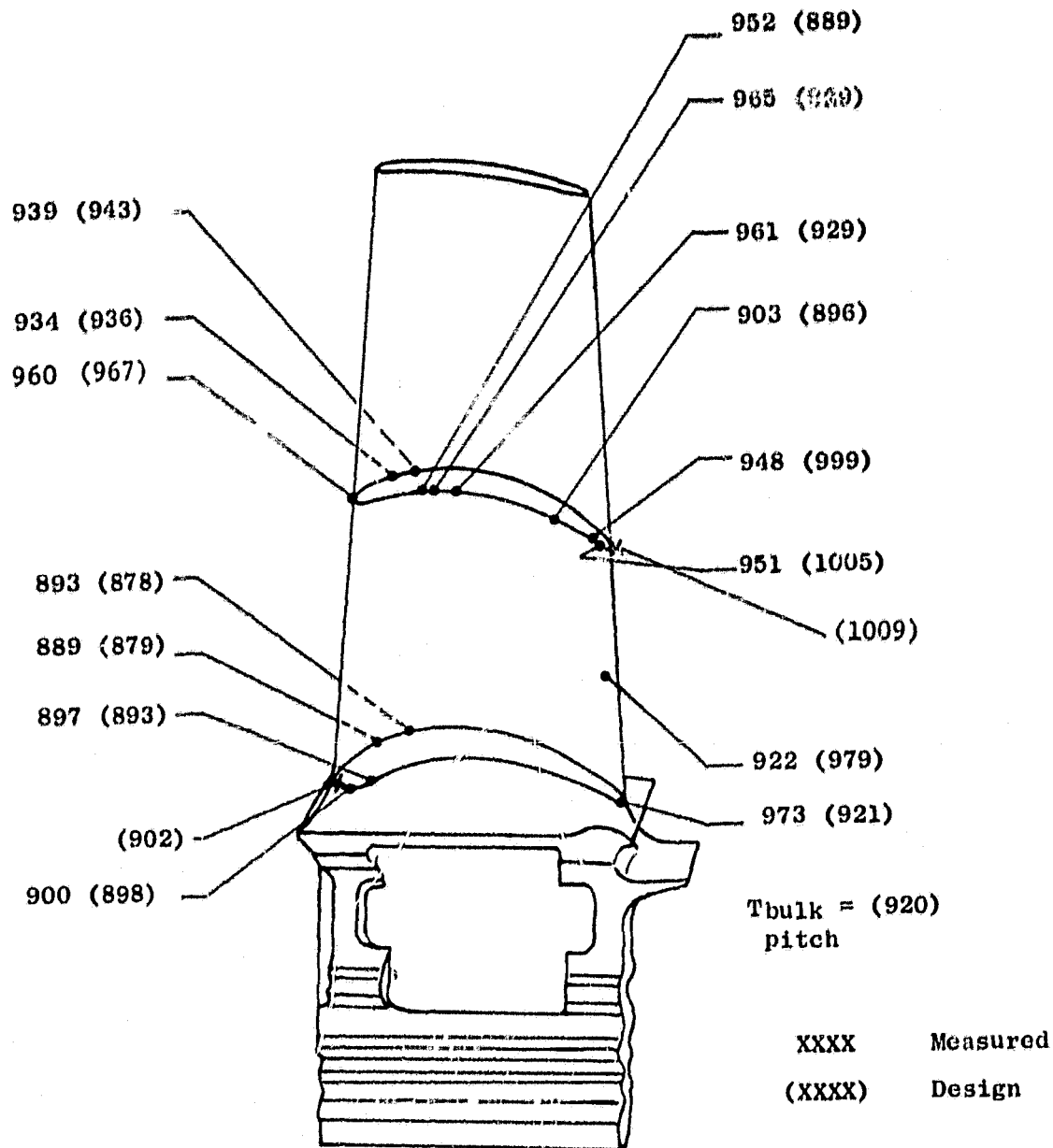Tbulk = (920)
pitch

XXXX   Measured

(XXXX)   Design

Figure 70.   Stage 2 Blade Metal Temperatures (° C).
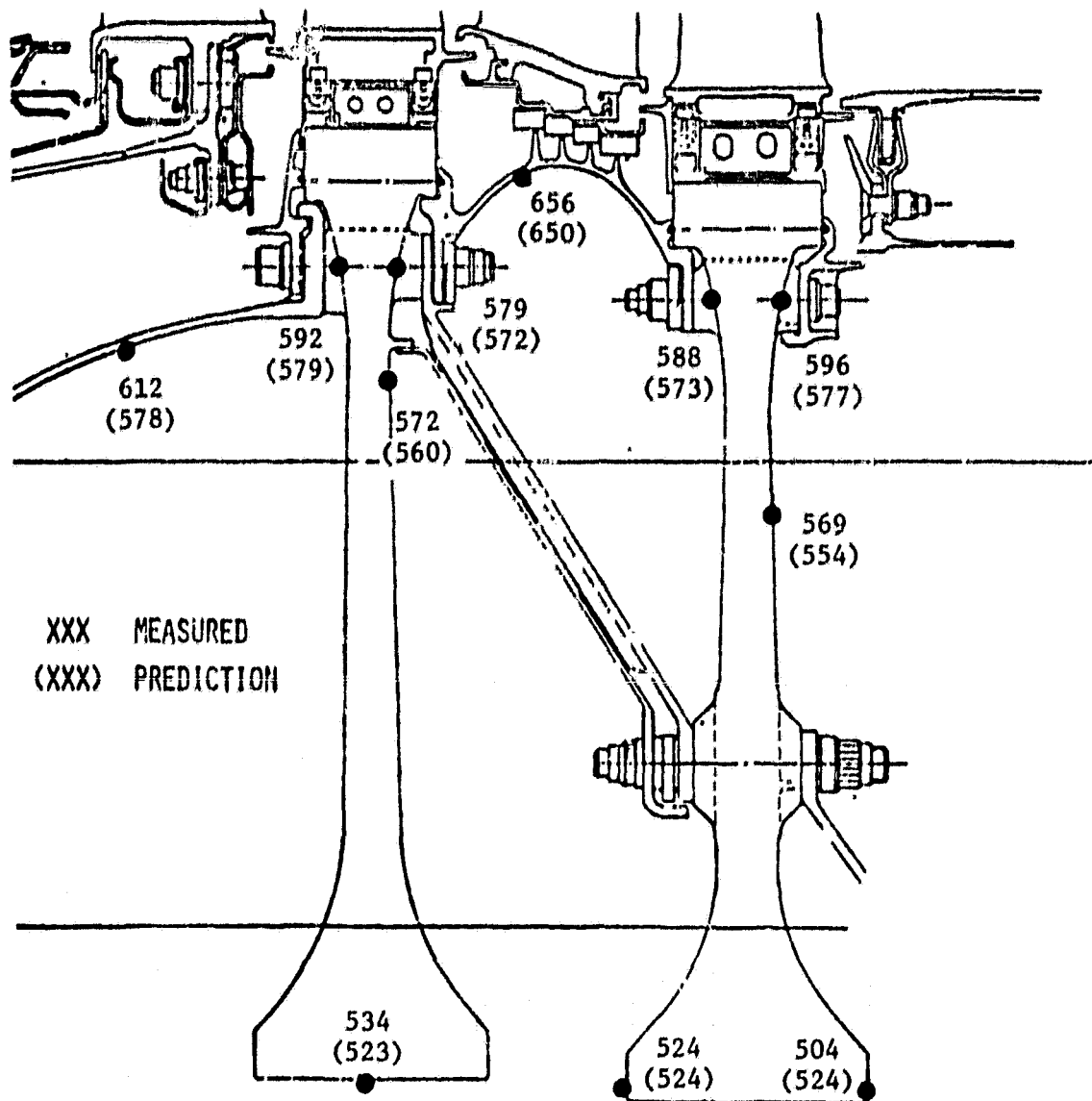
104

Figure 71. Steady-State Rotor Spool Temperatures (° C) for Design Conditions.
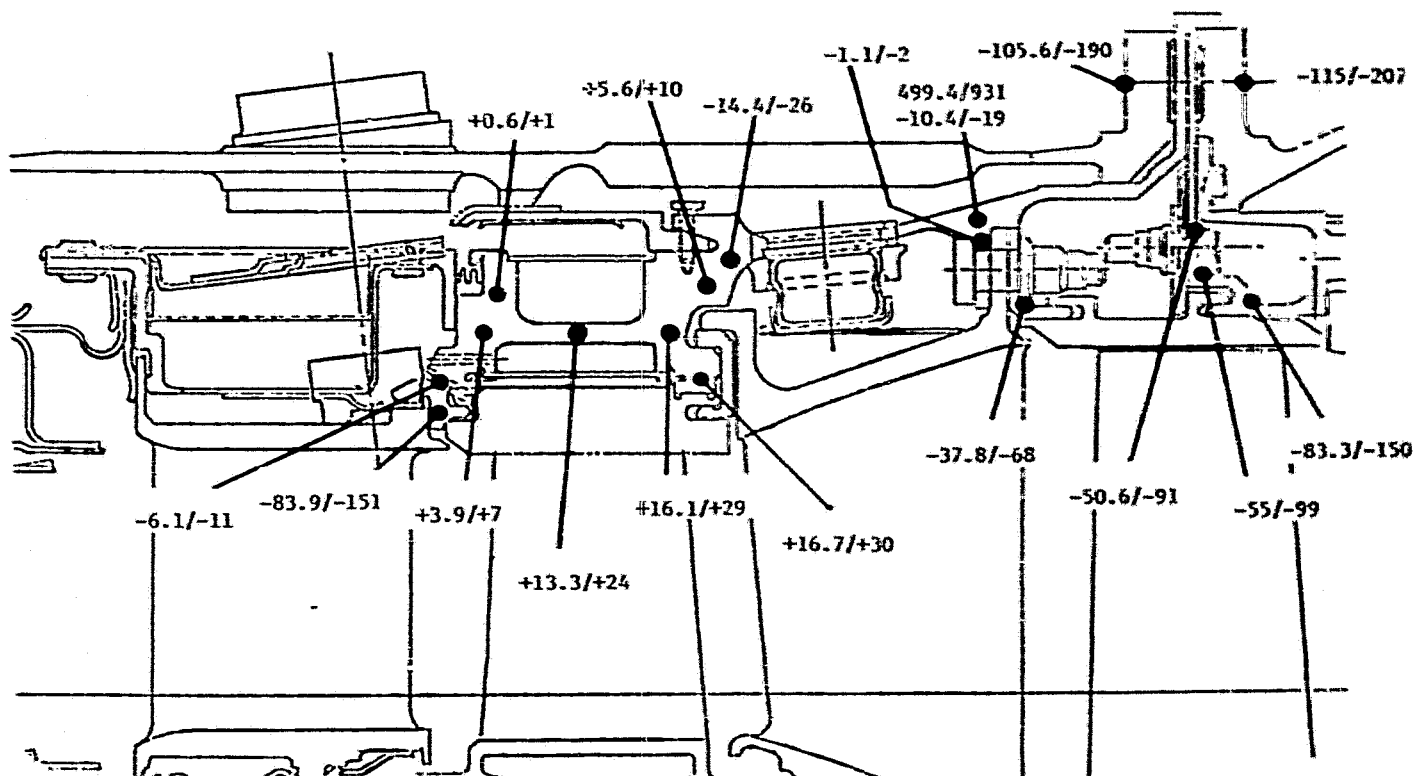
Figure 72. Measured Stator Temperature Deviations from Predictions (Δ° C/Δ° F).

Original

448.9/840   401.7/755   396.1/745

Temperatures in ° C/° F

396.1/750

Improved

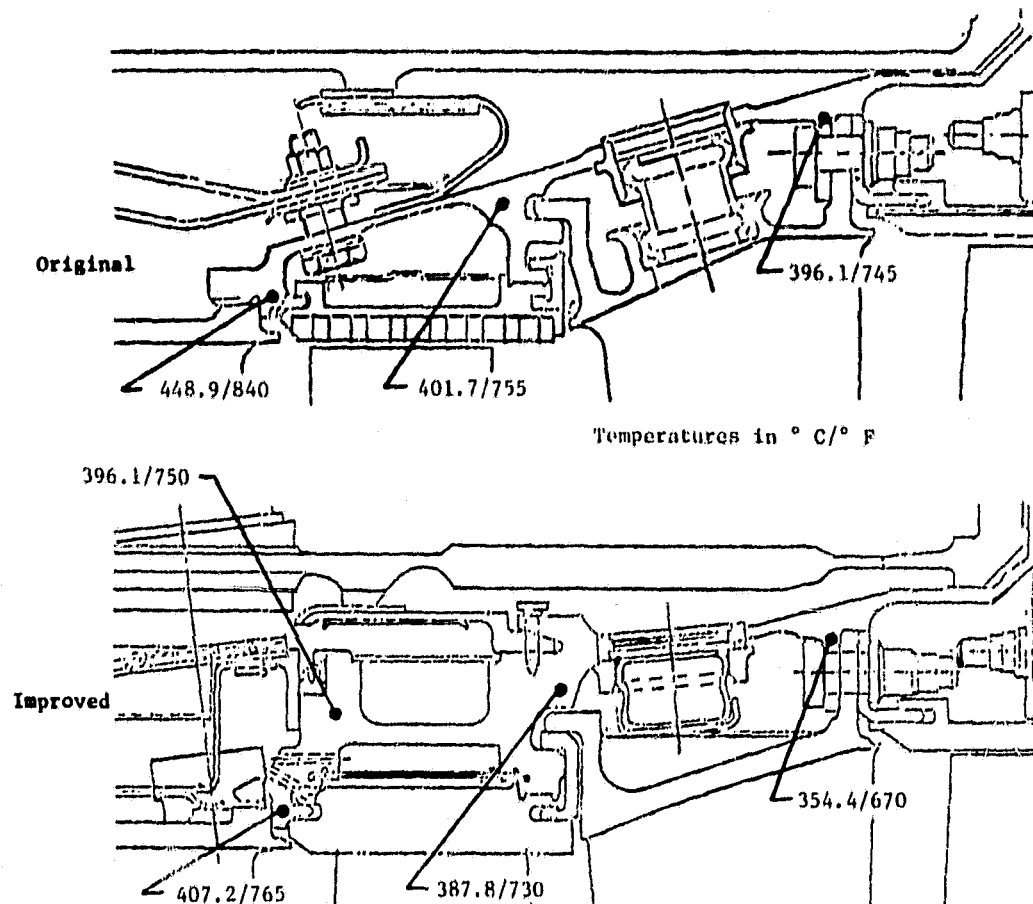407.2/765   387.8/730   354.4/670

Figure 73.   Isolation of Shroud Hooks from Hot Gas Ingestion for
             Improved Long-Time Dimensional Stability.

low compressor discharge temperature (T_3) of 398.9° C (750° F). The Stage 2 nozzle vane flange is 41.7° C (75° F) cooler. This should improve the long term dimensional stability of the support and reduce engine deterioration caused by out-of-roundness of the nozzle support.

Shroud support hook radial gradients have also been reduced, as shown in Figure 74. In this figure, the steeper sloped curves indicate a slower rate of change of temperature as a function of radius. On the aft-most flange, a lower overall gradient had been achieved by scalloping the flange. These lower gradients should improve both long term dimensional stability and reduce the potential cracking of the Stage 2 vane flange.

Figure 75 shows the circumferential thermal gradients at two selected points on the nozzle support. Note that the gradient is small in the forward ring, while a 45° C (81° F) gradient exists in the aft ring. The cause of the higher gradient in the aft ring is the impingement of 13th stage compressor air, which provides cooling air for the Stage 2 nozzle directly on the Stage 2 nozzle support. The thermocouples which are indicating the lower temperatures are directly under the 13th stage air pads.

Stator Transient Response – The response of the improved turbine rotor and stator during an accel is shown in Figure 76 based on radial growth calculations. The data shown reflect fan engine condition predictions which have been made based on the correlation of the analytical models using the core engine test data. The improved turbine was calculated not to rub. The sequence of testing on the engine was such that the amount of blade tip rub experienced during slow rollups to maximum speed during blade vibratory stress determination exceeded the amount of tip rub normally seen, and no additional tip rub was measured during subsequent rapid accels and decels. However, during testing on subsequent improved turbines, it has been established that the blade tips do not rub during a rapid accel.

The transient response during a decel is shown in Figure 77. The combined rotor/stator response leads to the hot rotor reburst predictions for tip rubs shown in Figure 78. Note that the improved turbine has substantially lower tip rubs incurred as a result of hot rotor reburst than the current twin shank turbine.

In summary, stator temperature measurements made during engine testing of the improved turbine show several trends relative to the current production design. In general, bulk temperatures have been reduced 13.9° to 47.2° C (25° to 85° F). Radial temperature gradients are at least 11.1° C (20° F) lower, and circumferential gradients are very low. The transient response of the stator shows that it responds slower than the current stator on both accels and decels. This indicates potential improvement in the amount of blade tip rub during both an accel and a hot rotor reburst.
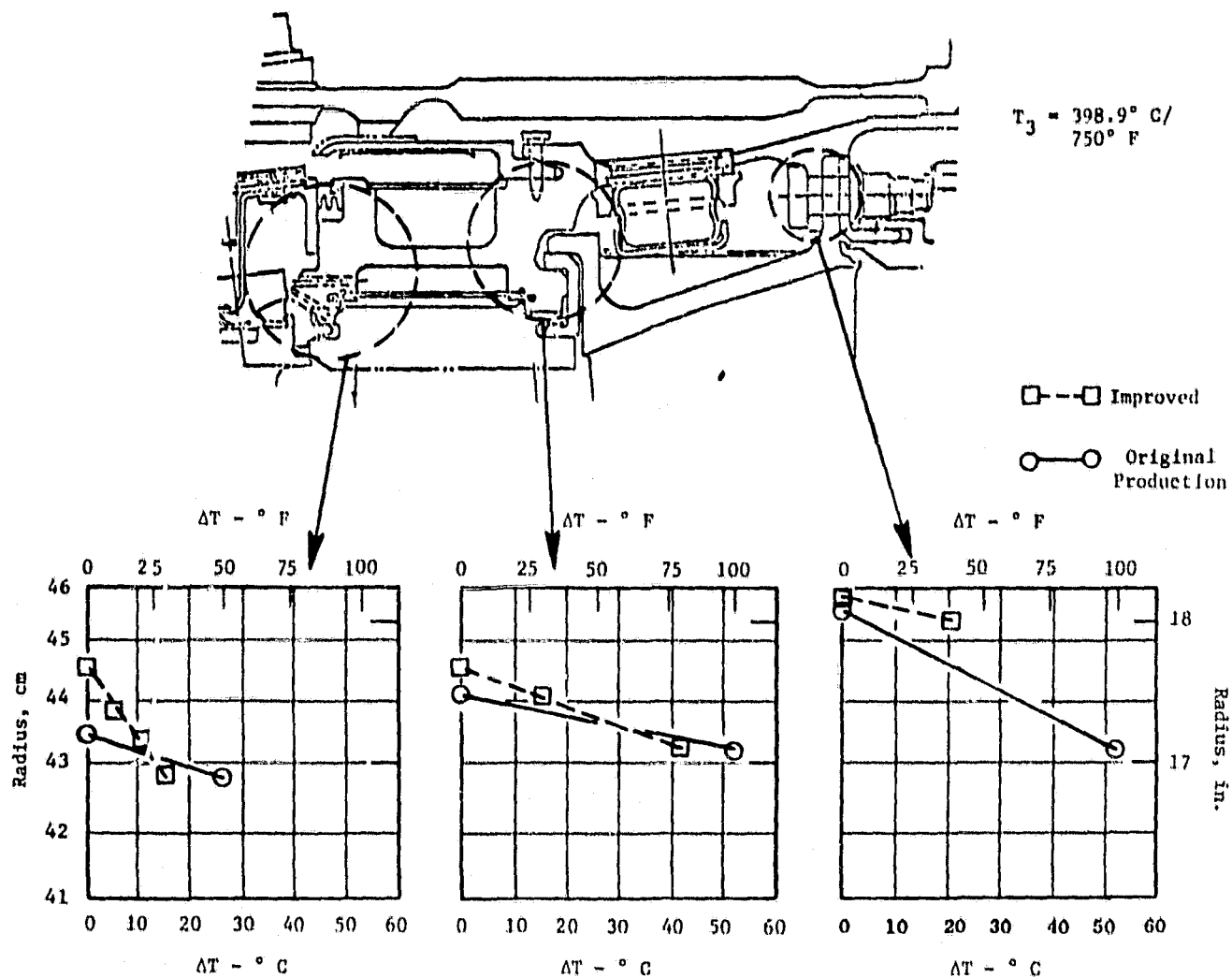
108

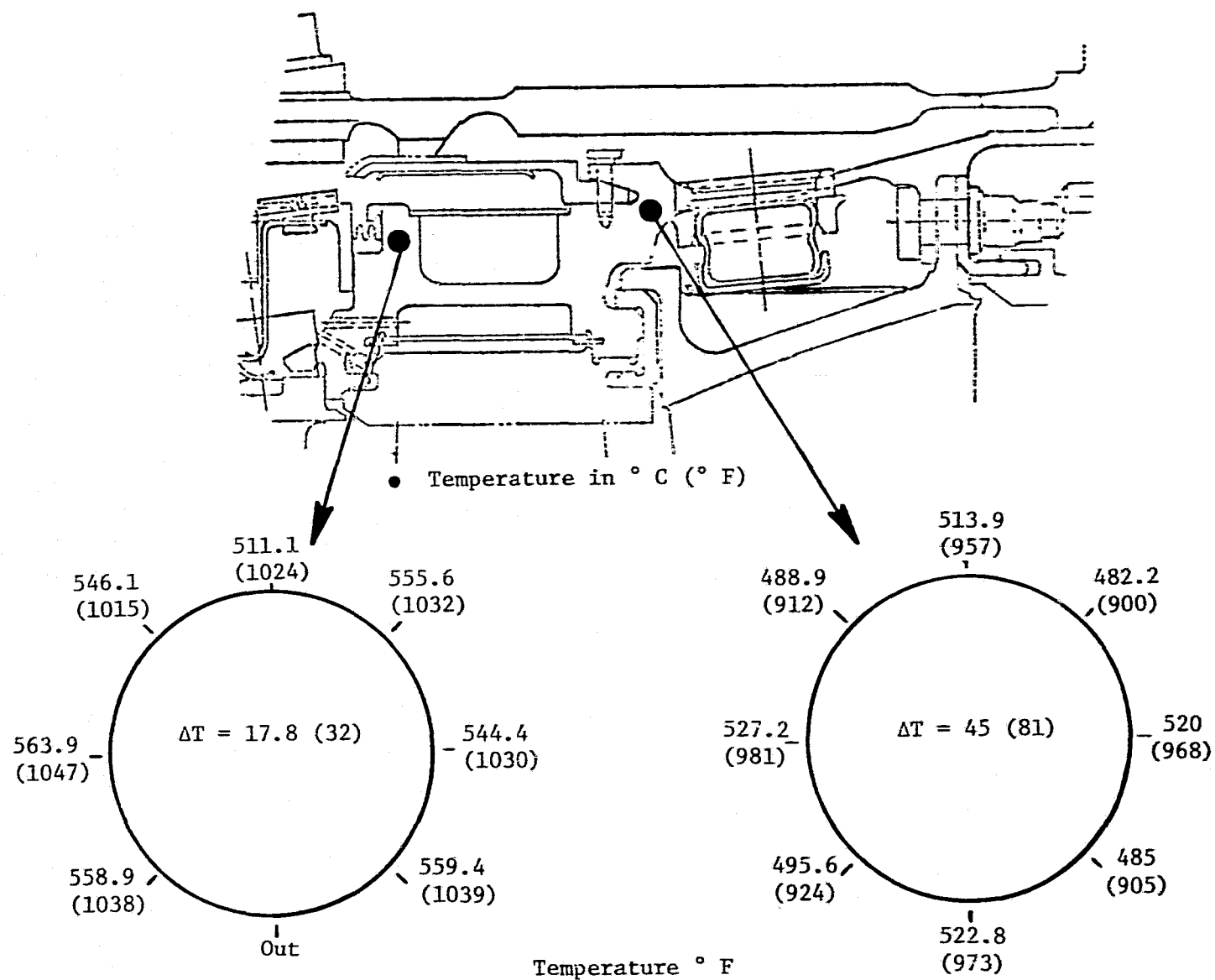Figure 74.   Shroud Support Radial Temperature Gradients.

Figure 75. Stage 2 Nozzle Support Circumferential Temperature Distribution.
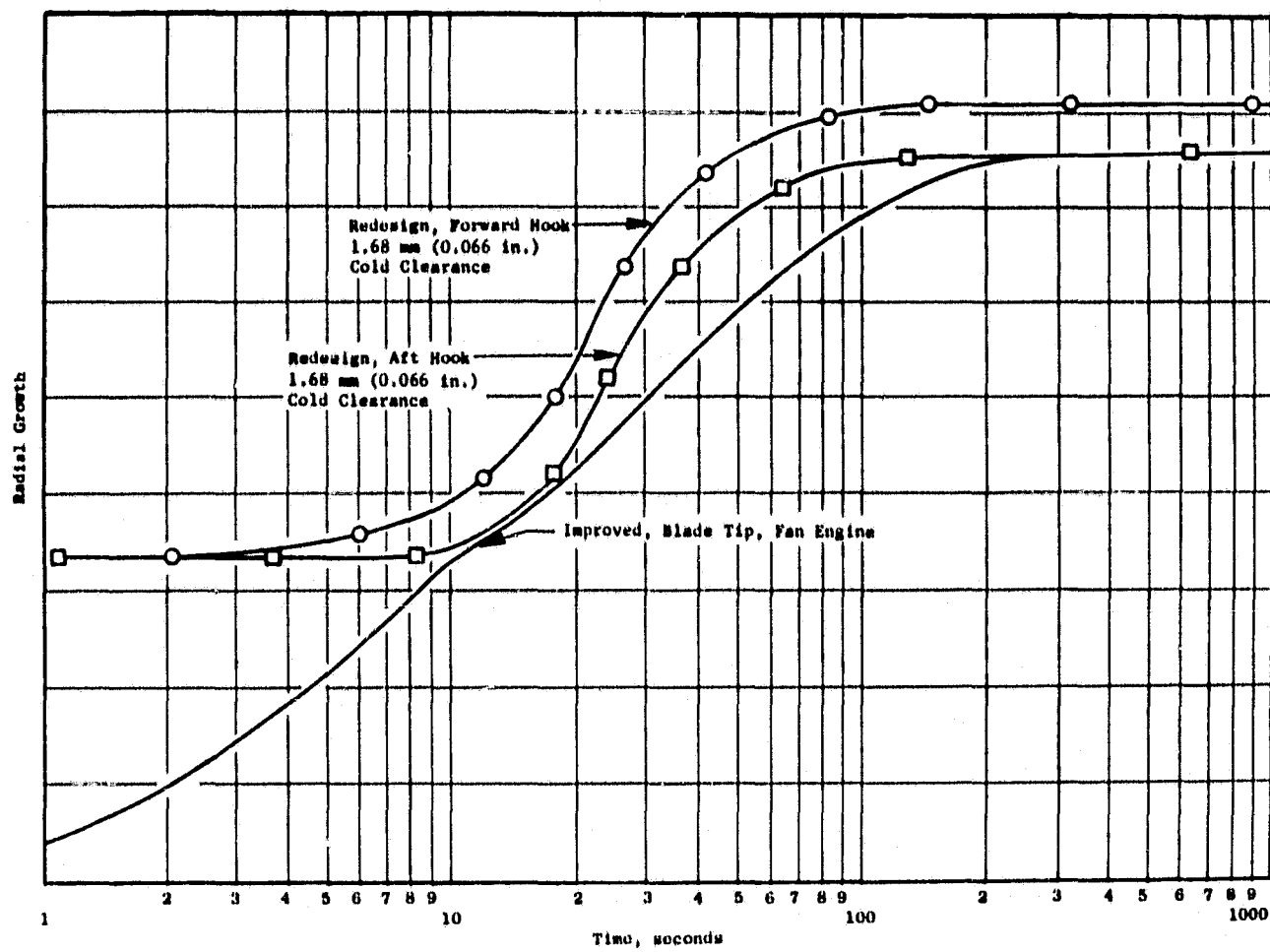
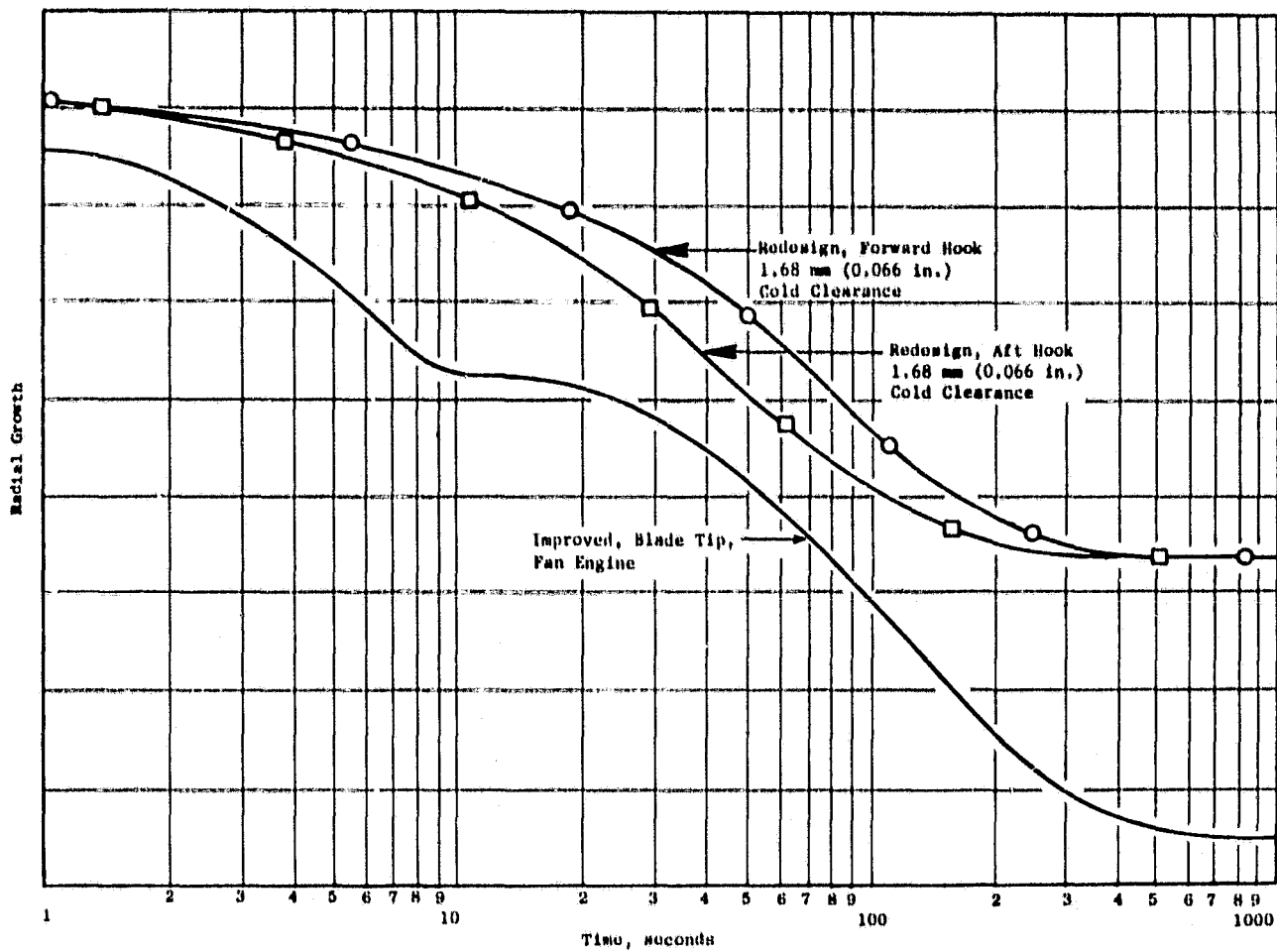Figure 76. CF6-6 Fan Engine Accel Response for Stage 1 HPT.

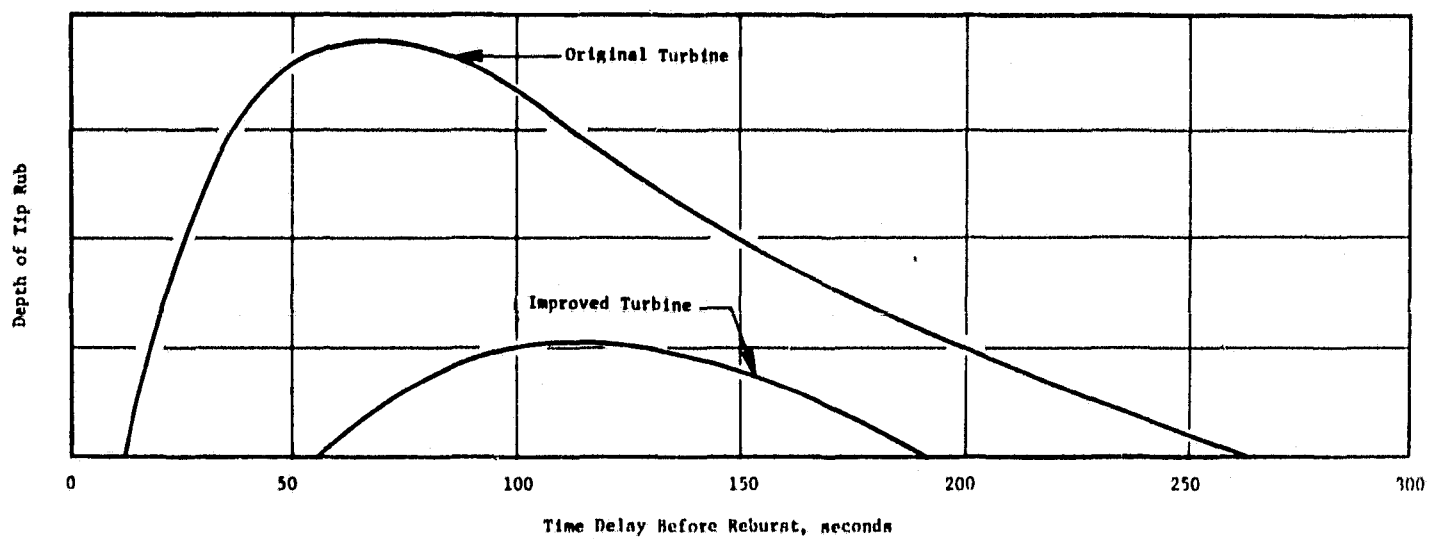Figure 77. CF6-6 Fan Engine Decel Response for Stage 1 HPT.

Figure 78. CF6-6 Average Stage 1 HPT Rub During Hot Rotor Rebursts.

7.4.3 Cooling

Rotor Cooling Flow - Measured cooling flows were about 1% higher than designed. This was probably due to leakage throught the multiplicity of slots in the rotor for instrumentation leadout. Subsequent noninstrumented tests have indicated flows to be about 0.2% above intent, possibly still due to rotor leakage. Mechanical design improvements are being incorporated into the production rotor design in the areas of suspected leakage.

Stage 2 Nozzle Cooling Flow - The thirteenth stage cooling flow rate to the Stage 2 vane was intended to be reduced by 0.2% for the improved single shank design. The test results showed flow increases of 0.2% to 0.4% above design intent. This increase in flow appeared to be caused by leakage around the insert where it rests against the nozzle as indicated in Figure 79. This potential leakage area will be sealed and evaluated in a subsequent engine test. A design change will be implemented to reduce this leakage.

Interstage Cavity Temperatures - Design changes were made in the rotor-stator cavity areas to improve the sealing from the hot gas flowpath, thus reducing hot gas inflow and permitting a reduction in cooling flow. As shown on Figure 80, measured temperatues were lower than predicted on both cavities aft of the rotor, but somewhat higher than predicted on the rotor forward cavities. In both regions, the cavity temperatures were still lower than those currently experienced on the CF6-50 engine. Effects of these temperatures are being evaluated and, if necessary, design changes will be implemented.

Rotor and Stator Transient Temperatures - Measured temperature transients on the rotor showed good agreement with predictions in the bore region for both Stages 1 and 2. The Stage 1 rotor responded slower than predicted in the web and rim region. This is due to the change in the Stage 1 blade cooling supply circuit to bring the air through the impeller attached to the rotor spacer rather than allowing it to flow along the disk as on the original production design.

Transient response of the stator agreed well with predictions and confirmed the desired slower response of the new Stage 1 shroud support.

114
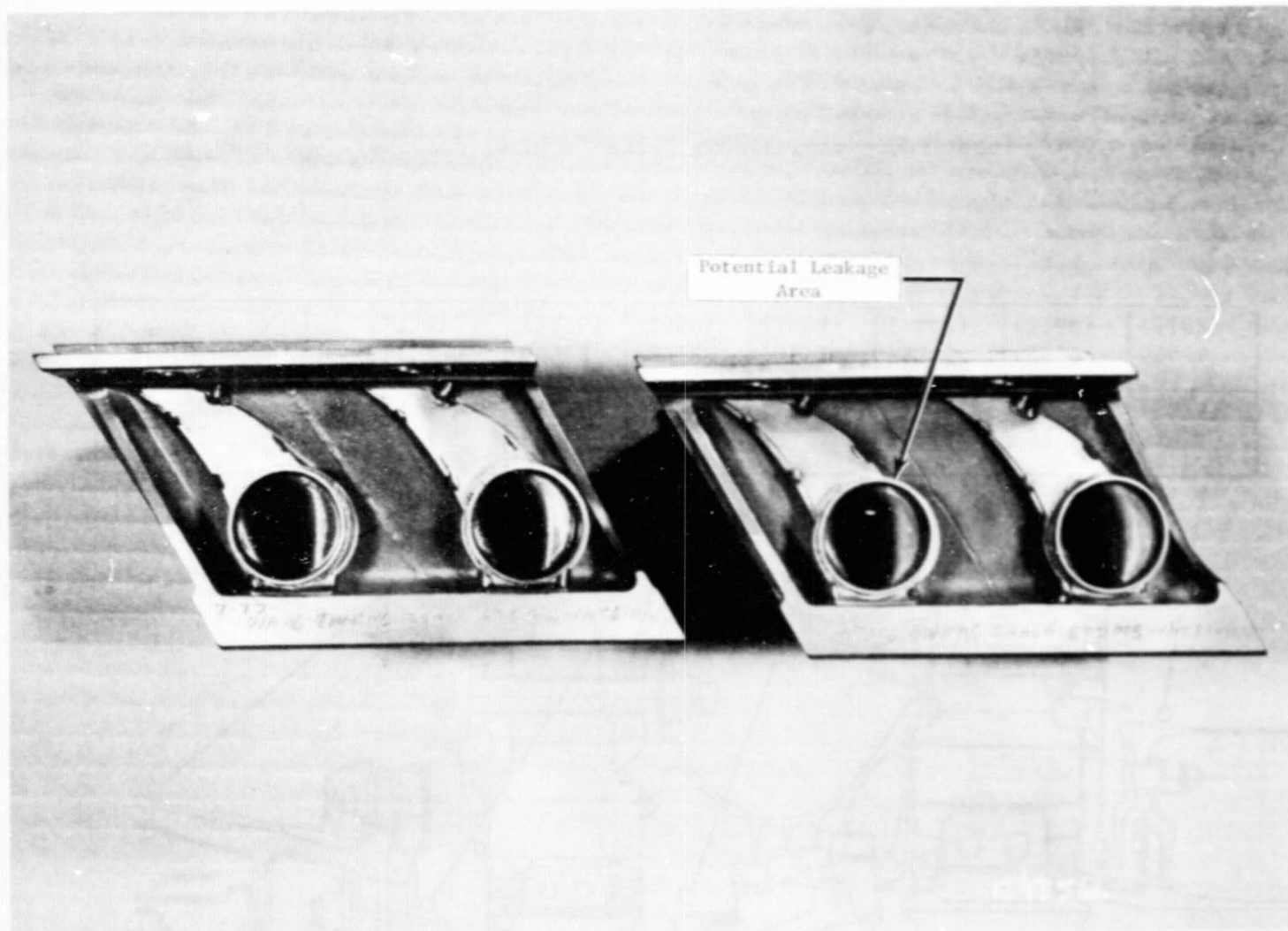
Figure 79. Stage 2 Nozzle Vanes.

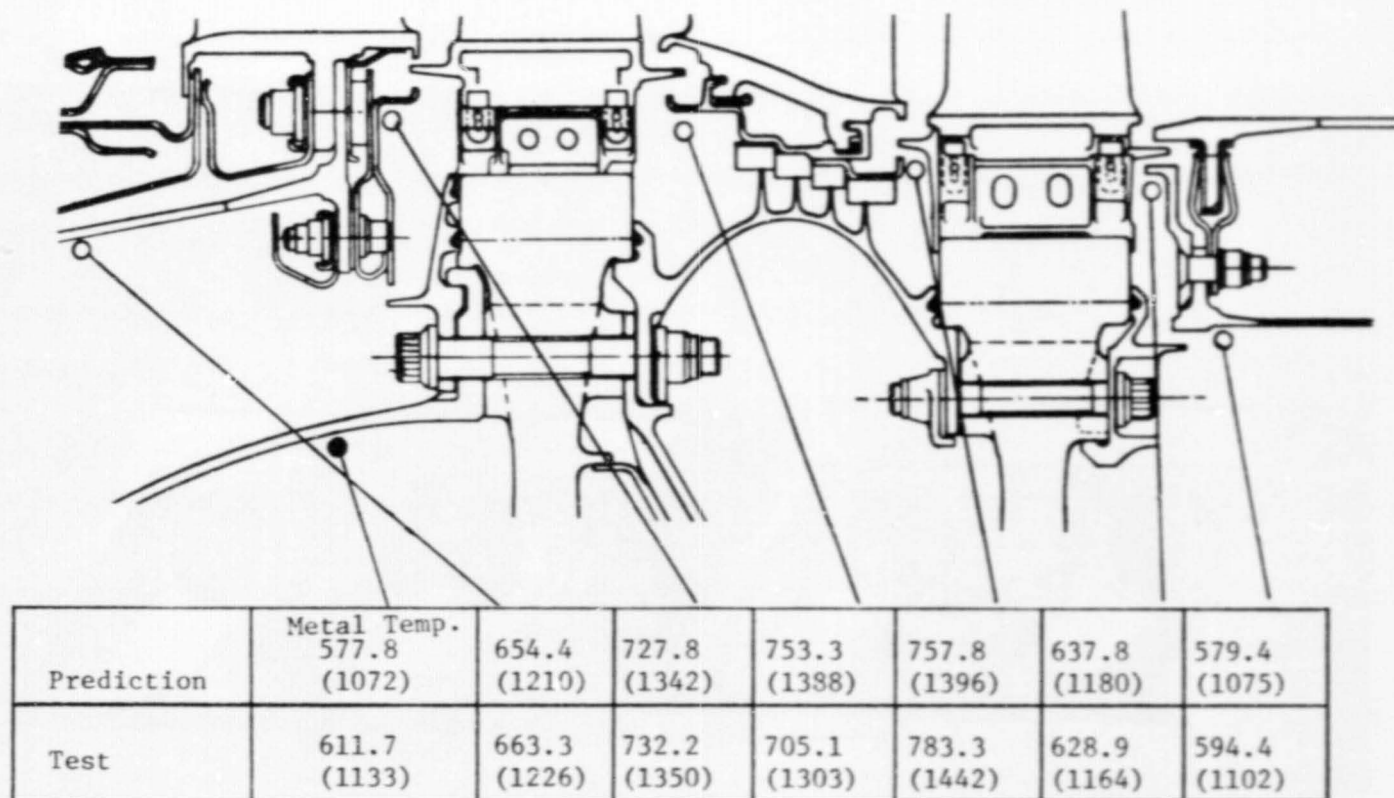|	Metal Temp. 577.8 (1072)	654.4 (1210)	727.8 (1342)	753.3 (1388)	757.8 (1396)	637.8 (1180)	579.4 (1075)
Prediction							
Test	611.7 (1133)	663.3 (1226)	732.2 (1350)	705.1 (1303)	783.3 (1442)	628.9 (1164)	594.4 (1102)

Figure 80. Improved Turbine Cavity Temperature Comparison, ° C (° F).

8.0 ENGINE ENDURANCE TEST

The objective of the endurance testing was to subject the improved high pressure turbine to an environment representative of approximately 3000 hours of typical airline service. Hardware condition at the end of the testing was evaluated and compared to current production hardware having comparable on the wing service.

8.1 TEST SETUP

The test vehicle used was the same as for the instrumented engine test, a TF39 core engine which is the high pressure system. A slave air supply was used as required to pressurize the sumps and a bellmouth and centerbody, designed and fabrictaed specifically for a TF39 core engine, was installed. In place of the low pressure turbine, a slave exhaust nozzle was installed to give an effective area similar to the inlet of the low pressure turbine.

Figure 61 shows the engine installation and the exhaust recirculation system used to simulate fan discharge temperatures at the compressor inlet. Instrumentation used for endurance testing included that required to measure engine performance and to monitor engine operation.

8.2 TEST PROCEDURE

The engine endurance test consisted of running 1000 cycles of the type shown in Figure 81. This cycle includes a maximum rate transient to the red-line exhaust gas temperature (EGT). The engine was held at this maximum temperature with periodic throttle adjustments to maintain temperatures for 5 minutes. At the end of 5 minutes, the throttle was chopped to flight idle (7700 rpm) for 30 seconds and then to ground idle (5630 rpm) for 30 seconds to cool the rotor spool components. After the 30 seconds at ground idle, the engine was shut down to maximize the stress range on the rotor spool parts. The rotor was caught by the starter at between 1000 and 500 rpm and restarted. Eight minutes was then spent at ground idle to complete the rotor cooling. At the end of the 8-minute ground idle period, a throttle burst was again made to begin the next cycle.

As previously stated, the intent of the test was to subject the improved turbine to an environment which simulates approximately 3000 hours of typical airline service. Judgment as to a given test cycle severity varies with each component and, in fact, each point on each component. However, an indicator of the test cycle severity can be gained by consideration of the rupture life consumed by the Stage 2 turbine blade. This calculation indicates that 1000 endurance cycles simulate approximately 9600 hours of airline service when consideration is given to derated takeoffs. Other components (like the HP turbine shrouds), when inspected after the test, appeared to be in a condition representative of 2500 flight hours in airline service. This judgment was confirmed by airline representatives when they made a posttest inspection of the hardware.
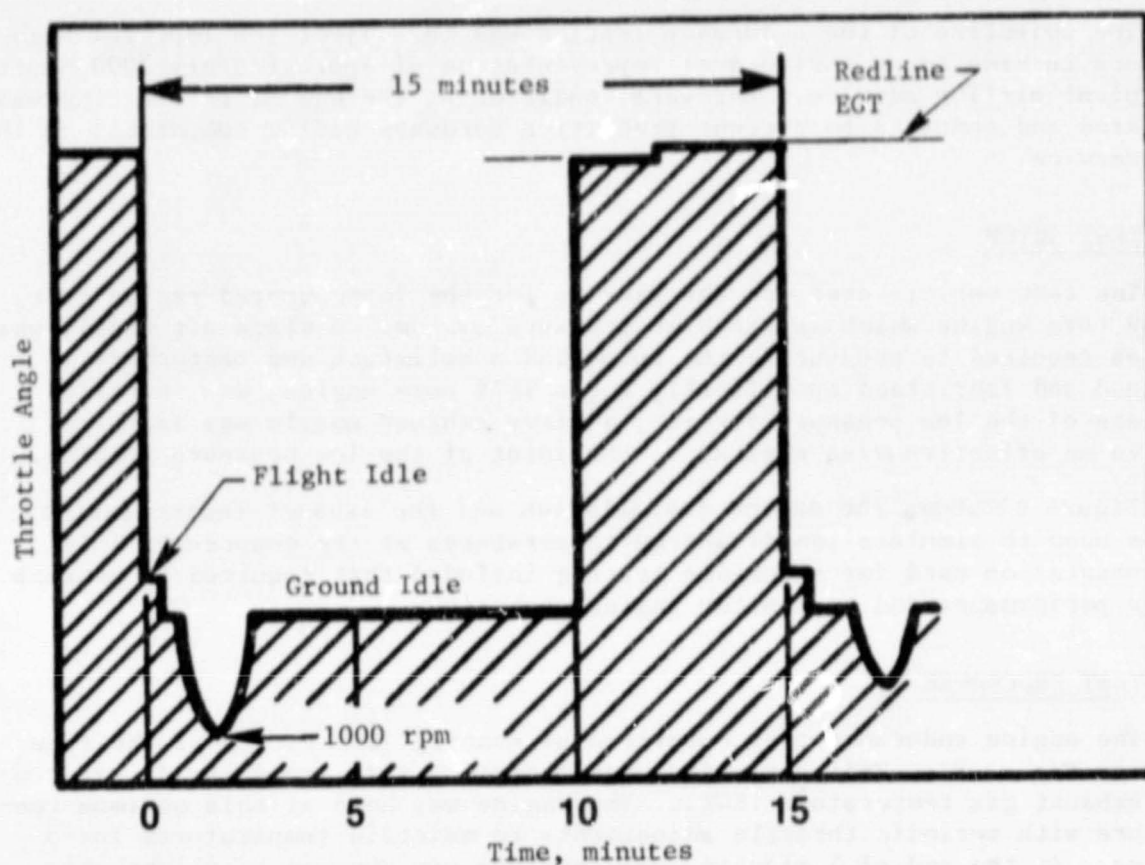
Figure 81. Endurance Test Cycle.

The "extra severity" cycle was chosen in order to quickly determine design weaknesses. It was also done to permit timely solution to revealed weaknesses prior to field service evaluation of the turbine. In order to do this, the test may have been overly severe in some respects.

8.3 TEST RESULTS

The test engine accumulated 255.37 hours of total running time with 84:14 hours at EGT's greater than 857° C (1575° F). During the test, 1000 endurance cycles were run with 1022 transients between speeds below 7700 rpm and above 8800 rpm. A total of 347 steady-state data points was obtained.

After completion of the 1000 cycle test, the engine was disassembled and the turbine torn down for inspection. This procedure included a "dirty" layout and visual inspection, cleaning, clean inspection, zyglo inspection, and appropriate dimensional checks. In addition, flow checks were made on sample airfoils to determine flow reduction due to surface debris buildup. The individual rotor and stator parts discussed are indicated in the improved turbine cross section shown in Figure 82.

8.3.1 Rotor Hardware

Posttest condition of the turbine rotor was excellent. Photographs of the rotor after the 1000 cycle endurance test are shown in Figures 83 and 84.

Stage 1 and 2 Blades - The Stage 1 blades were in excellent condition after 1000 cycles. Typical leading edge condition can be seen in Figure 84, and, the pressure side and trailing edge condition are shown in Figure 85. Each blade in the set was inspected under a microscope (up to 60X) in the dirty condition. The findings were as follows:

- Almost all blades had suction-side gill hole cracks up to 0.63 mm (0.025 in.) long. These cracks were predominantly around the pitchline but were observed to be as low as the fourth hole up from the root.

- Squealer tips were in good condition with no cracking. Some oxidation/erosion of the base René 80 was noted on the rubbed surface at the extreme tip of the blades.

- All other holes, including the trailing edge slots, appear to be uncracked.

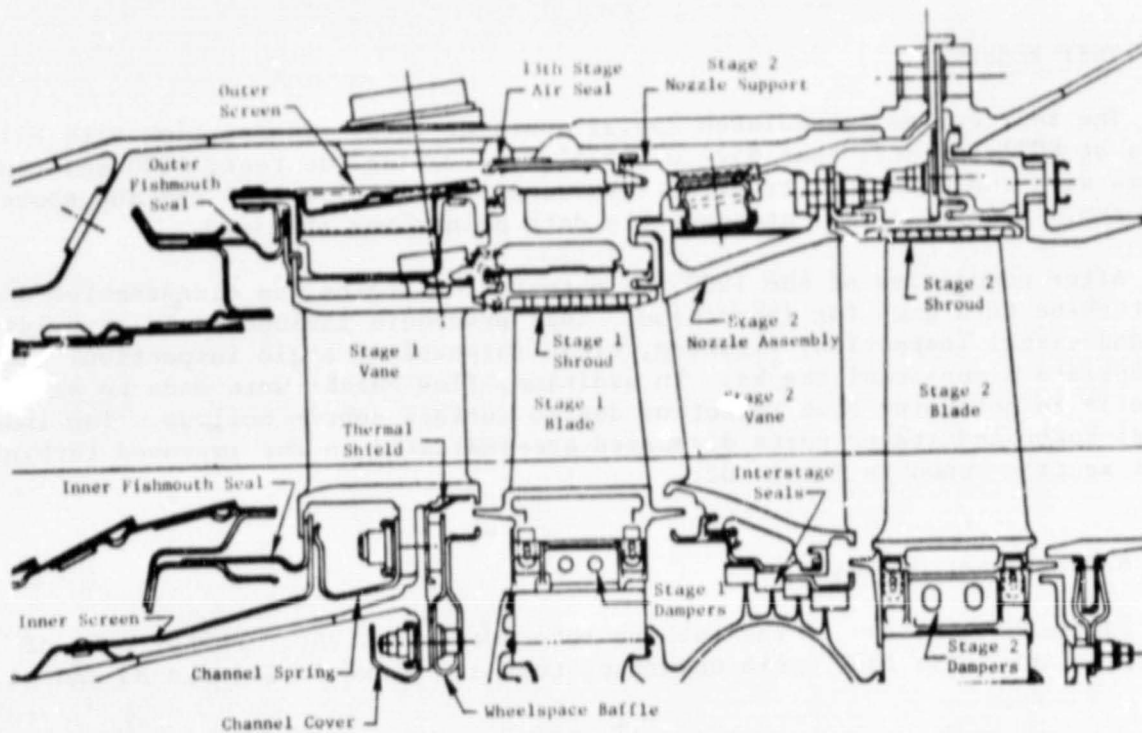Figure 82. Improved Turbine Cross Section.
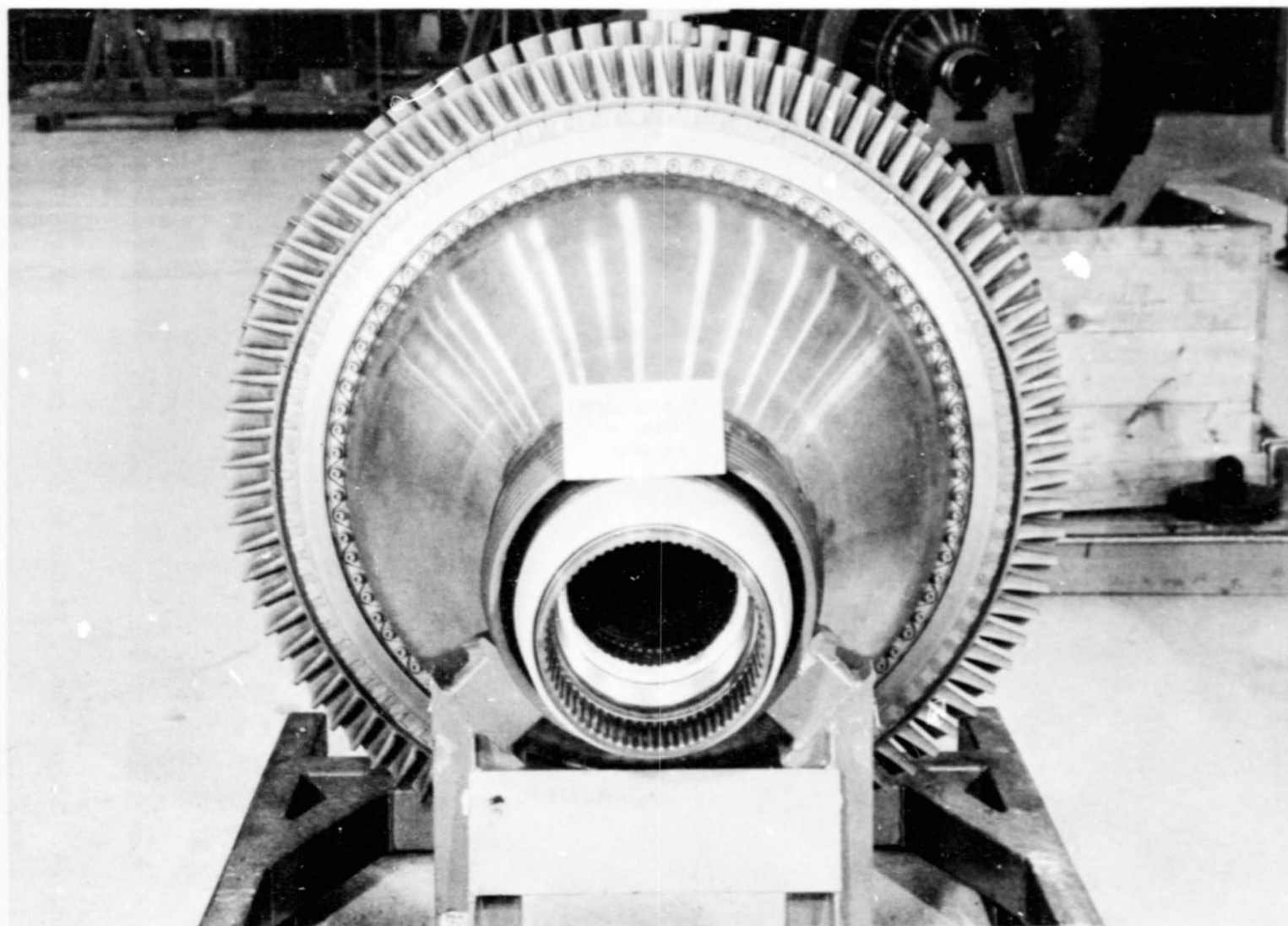
Figure 83. Turbine Rotor After 1000 Cycles (Forward Looking Aft).
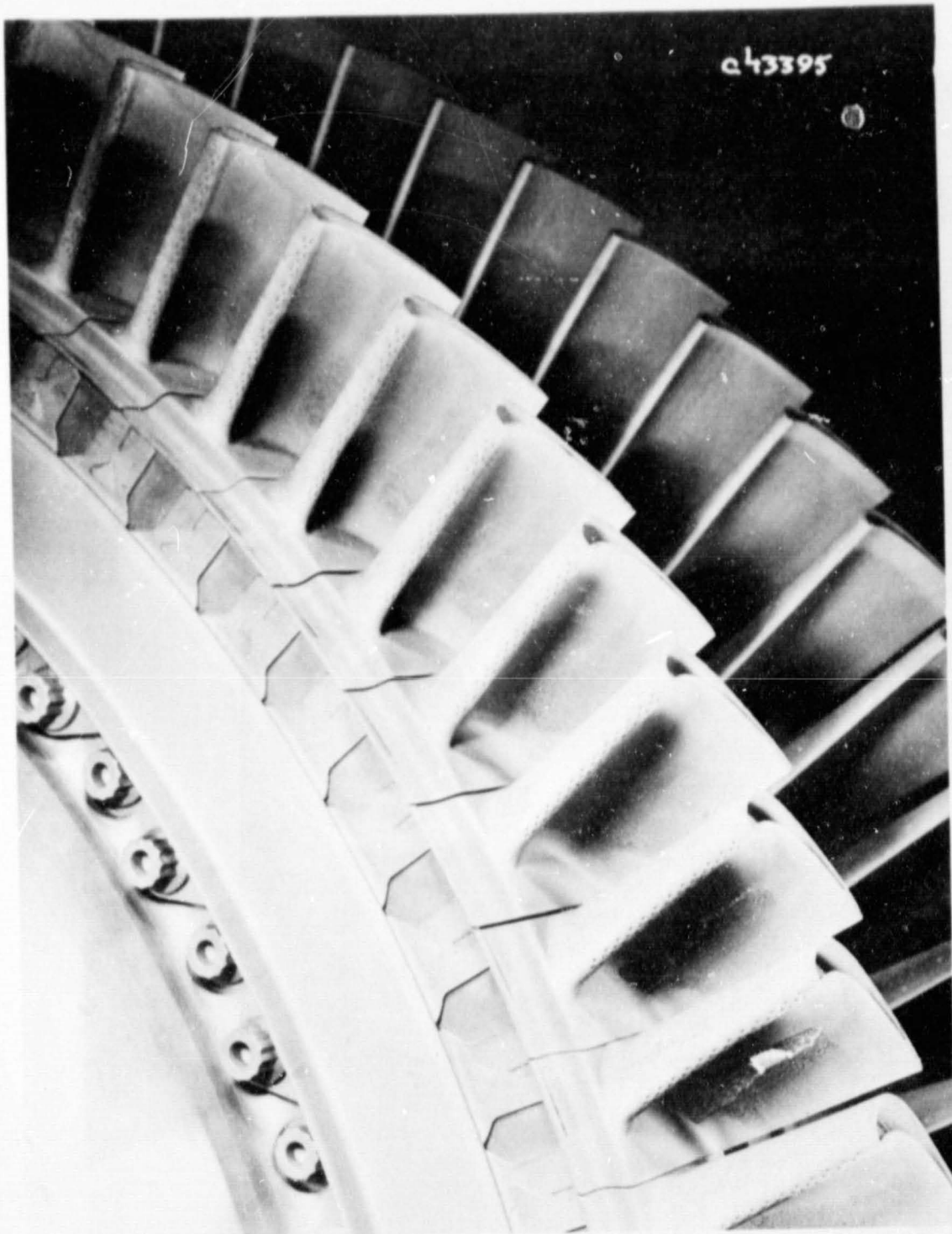
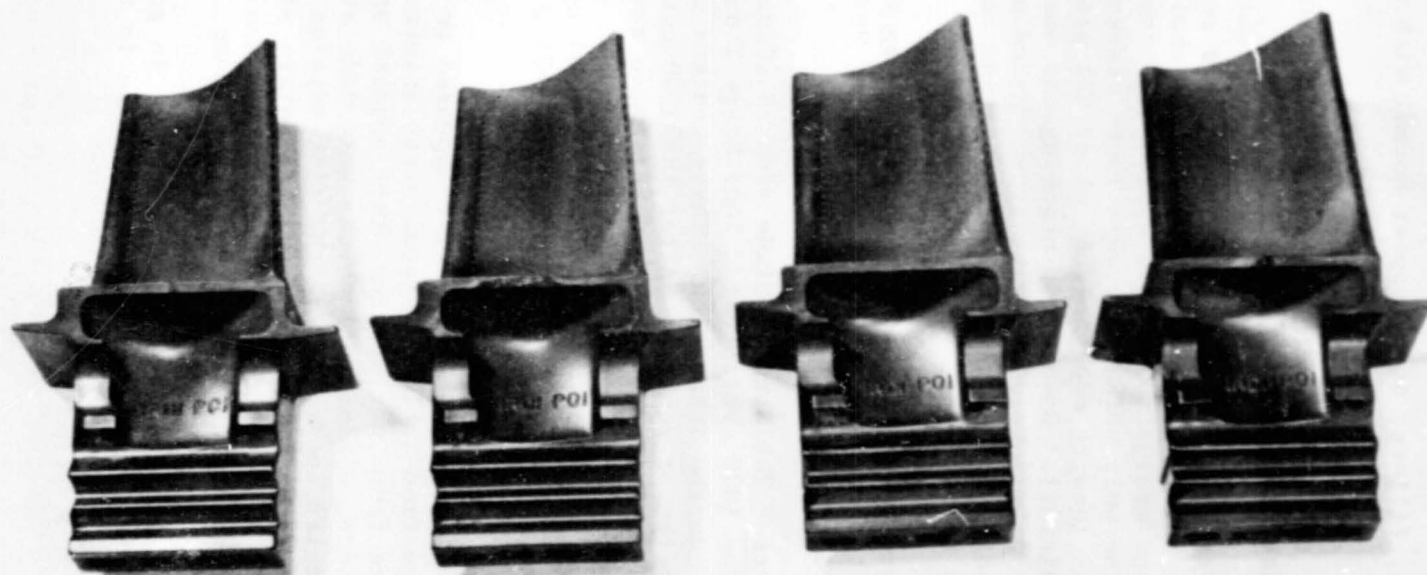Figure 84. Stage 1 and 2 Blades in Rotor Assembly After 1000 Cycles.

Figure 85. Typical Condition of Stage 1 Blades After 1000 Cycles (Pressure Side).

- The pressure sides of the blades were carefully examined (an area where other blades have shown distress) and no cracking was found.

- Dovetails, platforms, fillets, etc., appear normal with no unusual wear or cracking.

In addition to the above, two blades were vapor-blast cleaned and reinspected. No additional distress was seen.

All blades were judged serviceable, and all but three were returned for additional endurance running. The three blades removed were submitted for detailed metallurgical cutup and evaluation. This evaluation basically confirmed the visual findings. The only holes that were found cracked were the suction side gill holes and one leading edge hole at about 80% span. No other distress was observed in the airfoil. Some minor cracking was observed in the tip cap to squealer tip fillet at midchord pressure side. Based on these results, the Stage 1 blade is judged to be in excellent condition considering the severity of the 1000 cycle test.

All the Stage 2 blades were inspected under a microscope up to 60X. The blades were in excellent condition with no unusual distress or wear. Typical condition of the Stage 2 blades are shown in Figure 86.

Stage 1 and 2 Blade Dampers - The Stage 1 blade dampers (Figure 82) were in excellent condition after the 1000 cycle test. Four Stage 2 dampers were found cracked at the 500 cycle engine inspection. These cracked dampers were replaced for the second 500 cycles of running. After the 1000 cycle test, 33 dampers were found cracked. These damper cracks did not cause any functional problems. All the Stage 2 dampers which were tested were judged unserviceable and were replaced with new modified dampers for additional endurance testing. The damper design has been modified to eliminate this cracking problem.

Rotor Spool and Disks - All rotor spool hardware appeared to be in excellent condition. Posttest inspection included visual dirty examination, cleaning, and zyglo. No cracks were found nor was any other unusual or unserviceable distress found. In addition, dimensional checks were made at key locations on the rotor. Of particular interest were the disk outside diameters, blade retainer axial drop dimensions, and bolt circle diameters of the components dowelled at the Stage 2 disk inner bolted joint. No significant permanent distortions were disclosed by the dimensional inspections.

In summary, rotor spool components were all found to be in good serviceable condition. These parts were reassembled and reinstalled in the engine for additional endurance testing.

8.3.2 Stator Hardware

The condition of the turbine stator following the test was very good. Figure 87 shows the Stage 1 nozzle assembly as removed from the engine.
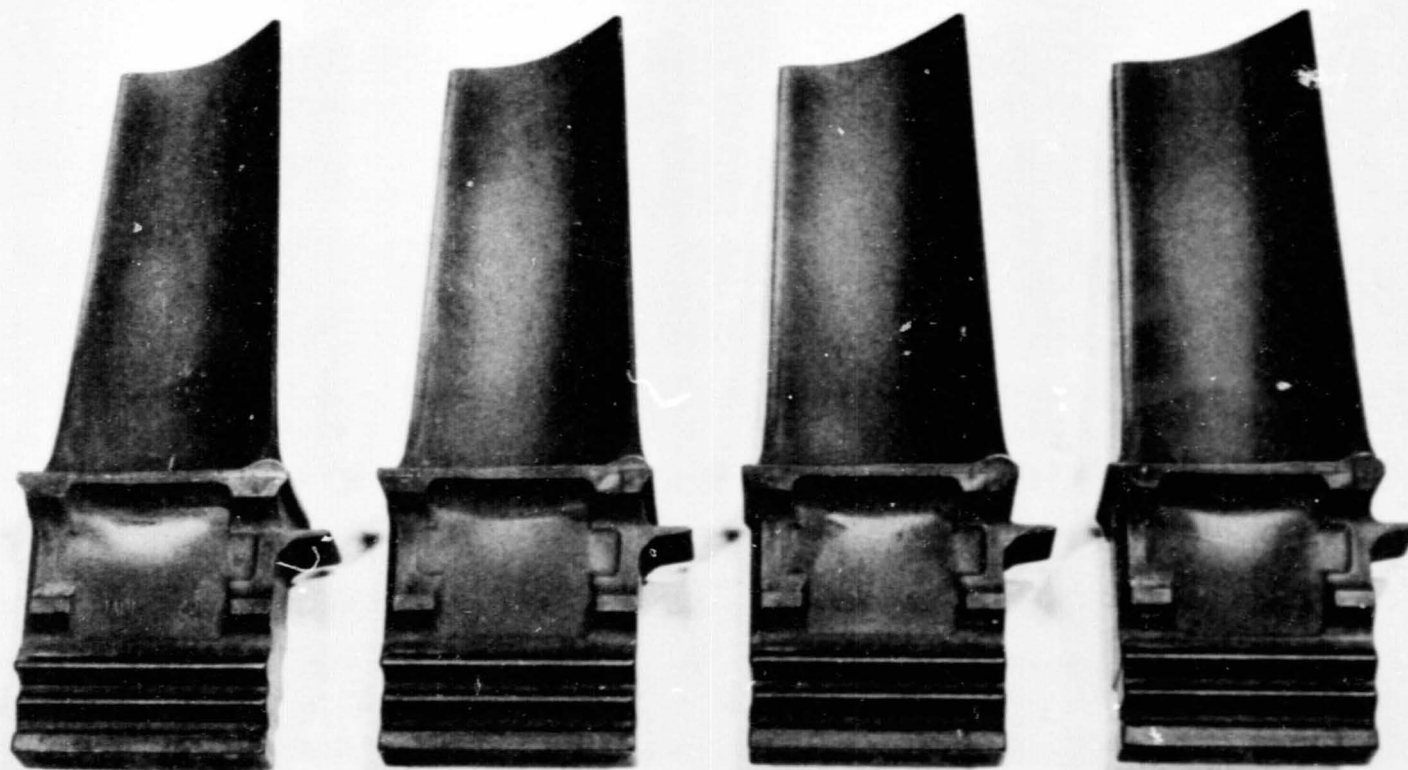
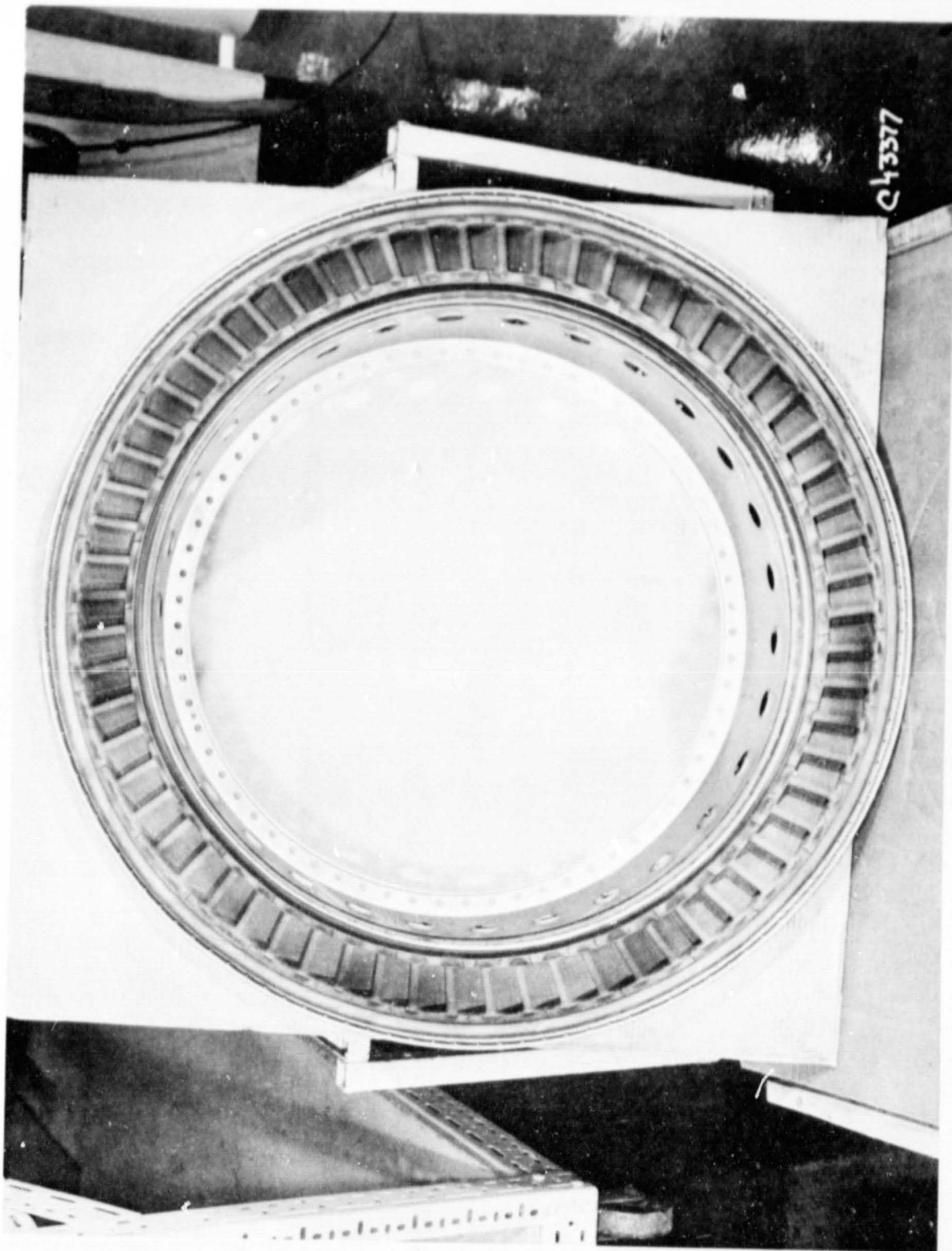Figure 86. Typical Condition of Stage 2 Blades After 1000 Cycles (Pressure Side).

Figure 87. Stage 1 HPT Nozzle Assembly After 1000 Cycles (Forward Looking Aft).

126

Stage 1 Vanes - Typical Stage 1 vane segments are shown in Figures 88 and 89. Twenty-two vane segments exhibited varying degrees of cracking. Ten segments showed no cracking when inspected in the as-run condition. Vane suction sides were clean while the pressure sides exhibited buildup of iron oxide scale and were extremely rough. Even though leading edge film holes showed considerable plugging and clogging, no leading edge cracking was observed. Elimination of leading edge cracks was a major objective of this redesigned vane. All parts were judged serviceable.

The cracking on the pressure side of the Stage 1 vanes is thought to be caused by pressure side temperatures which are too high. Design modifications have been made and subsequently tested. The vane cooling system has been modified to shift air from the suction side to the pressure side by adding film cooling holes to the pressure side.

Subsequent testing consisting of 1000 endurance cycles was conducted with the Stage 1 vane configuration as follows:

7 vane segments - Best from previous test (as-is)

7 vane segments - Worst from previous test (as-is)

6 vane segments - New vanes with inserts modified to put more cooling air to pressure side

6 vane segments - New vanes with modified inserts plus pressure side film cooling holes

6 vane segments - New vanes unmodified (to act as a control)

Results of this additional testing have shown that the addition of pressure side film holes provides substantial reduction in the pressure side cracking.

Stage 2 Vanes - Prior to disassembly of the Stage 2 nozzle assembly, an inspection of the vane inserts through the spoolie ports revealed significant deposits of aluminum, plugging the impingement holes of the inserts. This was particularly heavy in a 90° sector centered about the top vertical centerline. The source of this aluminum was the gap in the thirteenth stage seal located at the top vertical centerline. Plugging of Vane 2 resulted in a burned and bulged leading edge which is shown in Figure 90.

Examination of individual vane segments revealed that the two axial cracks found in the outer-band-to-suction-side fillet radius of the trailing vanes of Segments 4 and 18 during the 500 cycle inspection has grown to a length exceeding 2.54 cm (1 in.). A closeup view of the vane is shown in Figure 91. These two segments were directly behind areas of Stage 1 shroud distress (missing Bradelloy). Nine other vane segments also had axial cracks in this area, but they were much smaller and tighter. Low cycle fatigue is suspected as the cause of this problem.
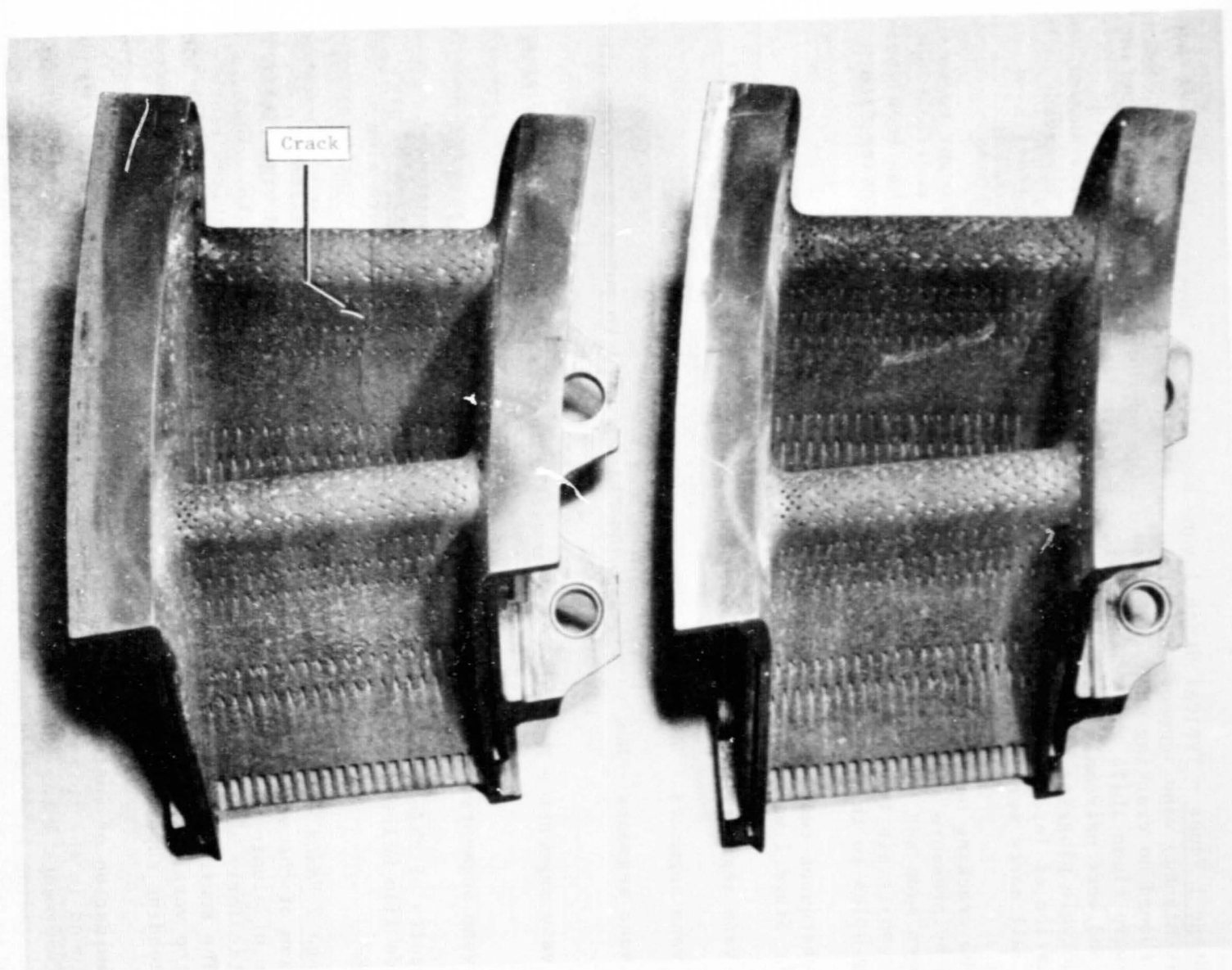
Figure 88. Typical Condition of Stage 1 Vane After 1000 Cycles (Pressure Side).
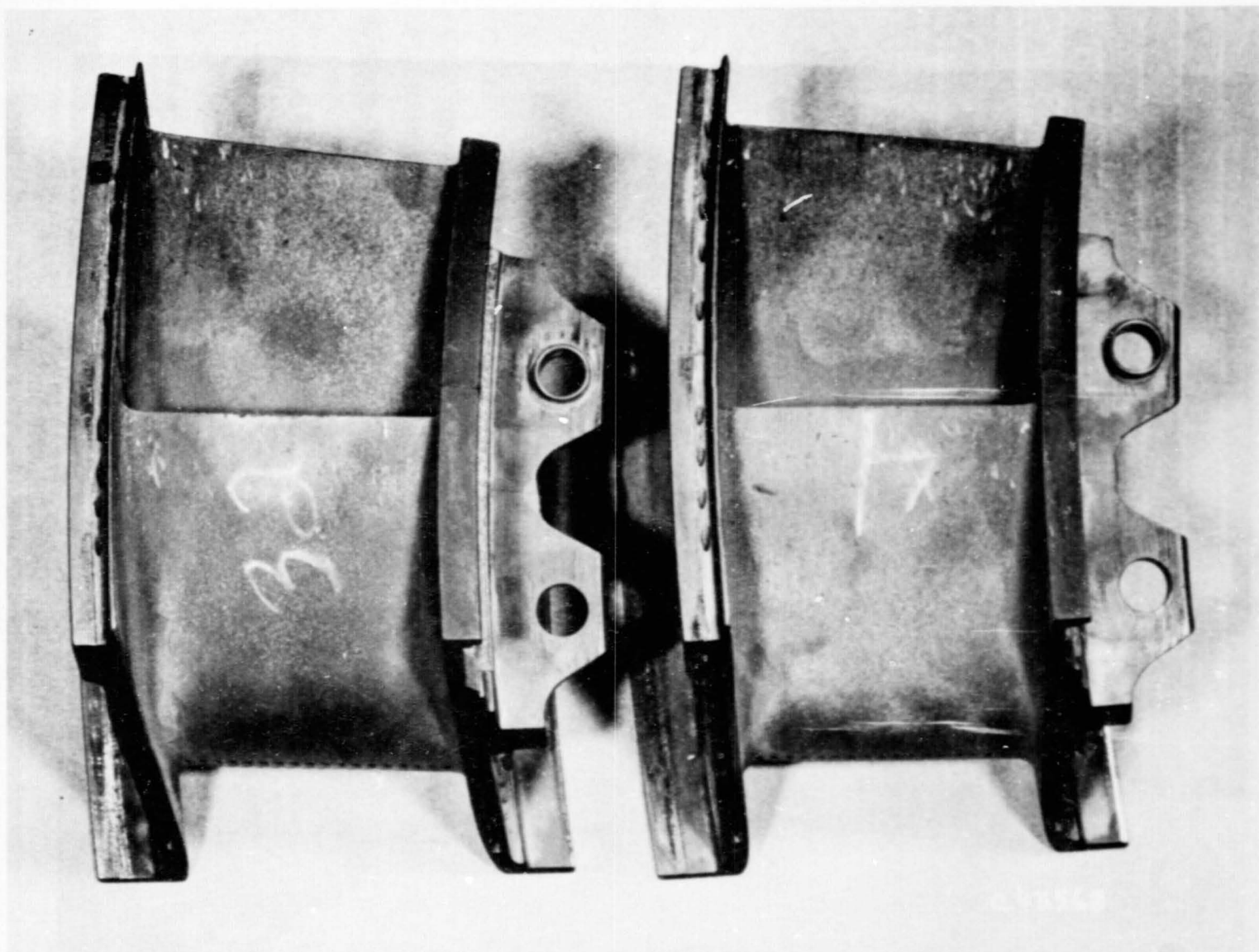
Figure 89. Typical Condition of Stage 1 Vane After 1000 Cycles (Suction Side).
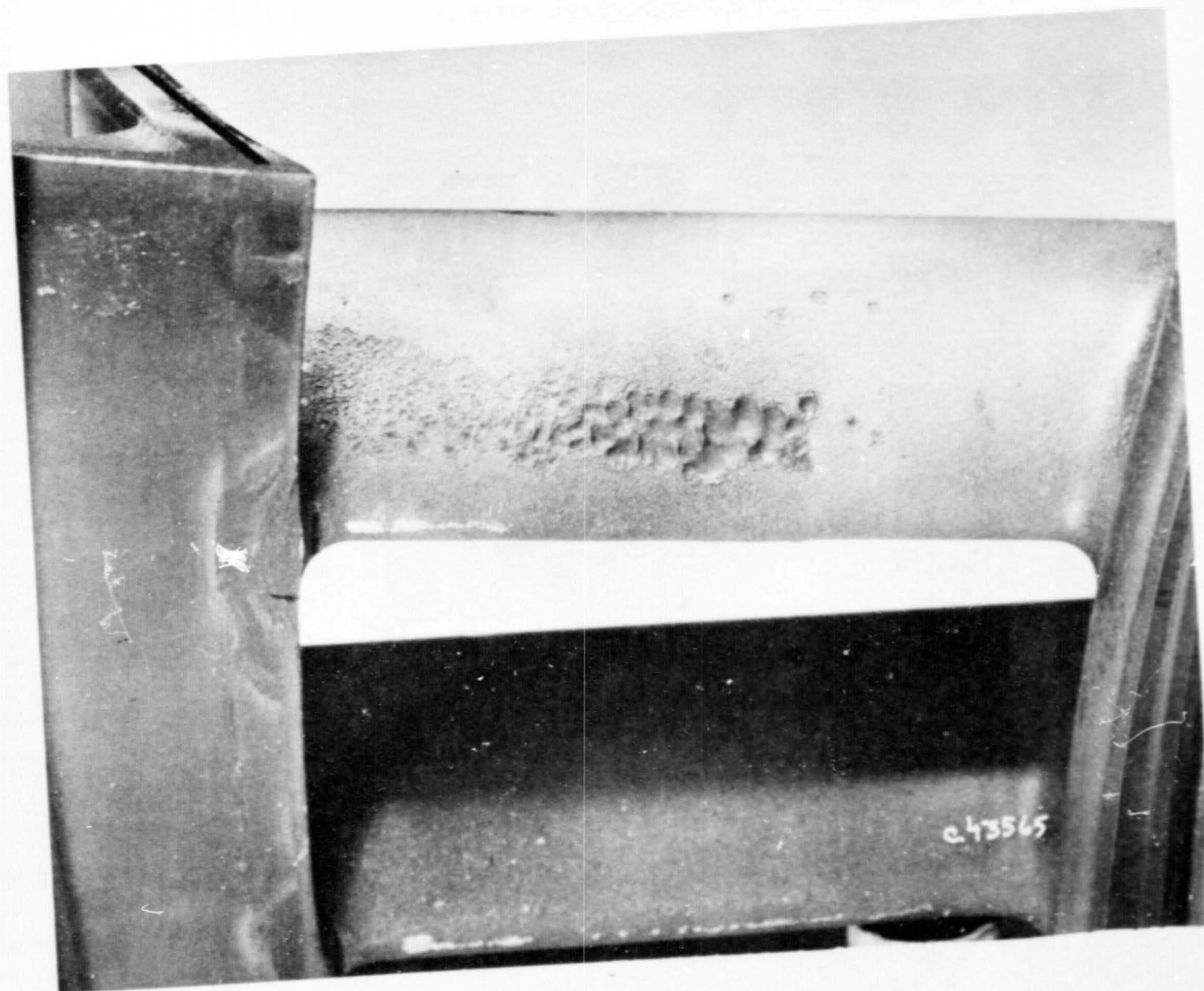
Figure 90. Stage 2 Vane Leading Edge Damage After 1000 Cycles.

Figure 91. Stage 2 Vane Suction Side Crack After 1000 Cycles.

Typical Stage 2 vane segments are shown in Figure 92. Eleven vane segments had outer band cracks between vanes. These cracks run roughly perpendicular to the gas flow direction between vanes. Sixteen vane segments had axial cracks in the inner band trailing edge. Sixteen vanes had small axial cracks in the trailing edge of the airfoil.

During machining of the shrouds, the leading edges of the Stage 2 vanes were notched inadvertently. These notches are indicated in Figure 92. This is an area where cracking occurs in the original production vane. None of these notches in the vane leading edges progressed into cracks, indicating that the improved single shank Stage 2 vane design has successfully solved the leading edge cracking problem. All of the Stage 2 vane segments are considered serviceable and will be returned to test.

Stage 2 Nozzle Assembly and Shrouds - Overall views of the Stage 2 nozzle assembly (Figure 82) showing the posttest condition of the Stage 1 and 2 shrouds are presented in Figures 93 and 94. While neither shroud was redesigned for the improved (single shank) turbine, the condition of the shrouds was significant.

The shroud distress observed after 1000 accelerated endurance cycles in the core engine, with the single shank turbine, indicates the severity of the test. These shrouds are identical to original production parts. According to Service Engineering personnel and to airline powerplant engineers who examined the single shank turbine parts following the test, original production shrouds would be in a similar condition after 2500 to 3000 hours of typical airline operation.

Stage 2 Nozzle Support - All cooling holes in the Stage 2 nozzle support (shown in Figure 82) were open and clean. The thirteenth stage air seal showed some inward distortion at 12 o'clock. No hot spots were observed. The thirteenth stage seal, which fits around the nozzle support, is not a full hoop, since it must be slit to be assembled to the support. This slit, even though it has a seal underneath it, allowed large amounts of aluminum to get through to the second stage vanes. This slit in the thirteenth stage seal and the aluminum particles in the Stage 2 vane cooling air inlet (spoolie port) are shown in Figure 95. On future builds, this slit will be welded shut, and improved design will be incorporated on production parts.

Inner/Outer Fishmouth Seal - The location of the inner and outer fishmouth seals can be seen in Figure 82. Aluminum deposits were found along the aft face of the inner fishmouth seal. Wear patterns on the cylindrical area and bowing of the vertical flange indicated good contact with both the combustor and the nozzle forward flange. Wear patterns on the outer fishmouth seal appeared normal. Both the cylindrical and the radial portions of the seal are bowed.
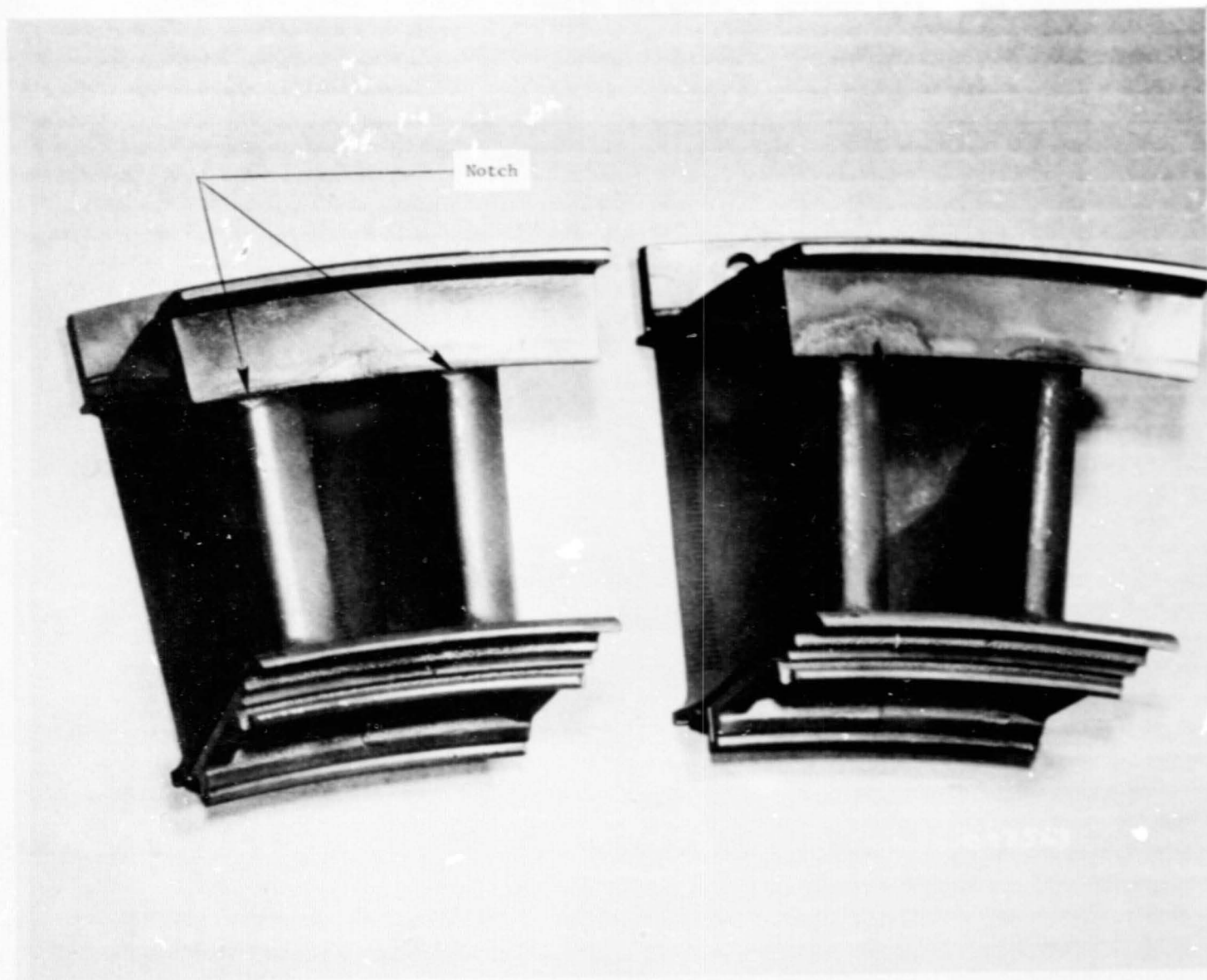
Notch

Figure 92. Typical Condition of Stage 2 Vanes After 1000 Cycles (Pressure Side).
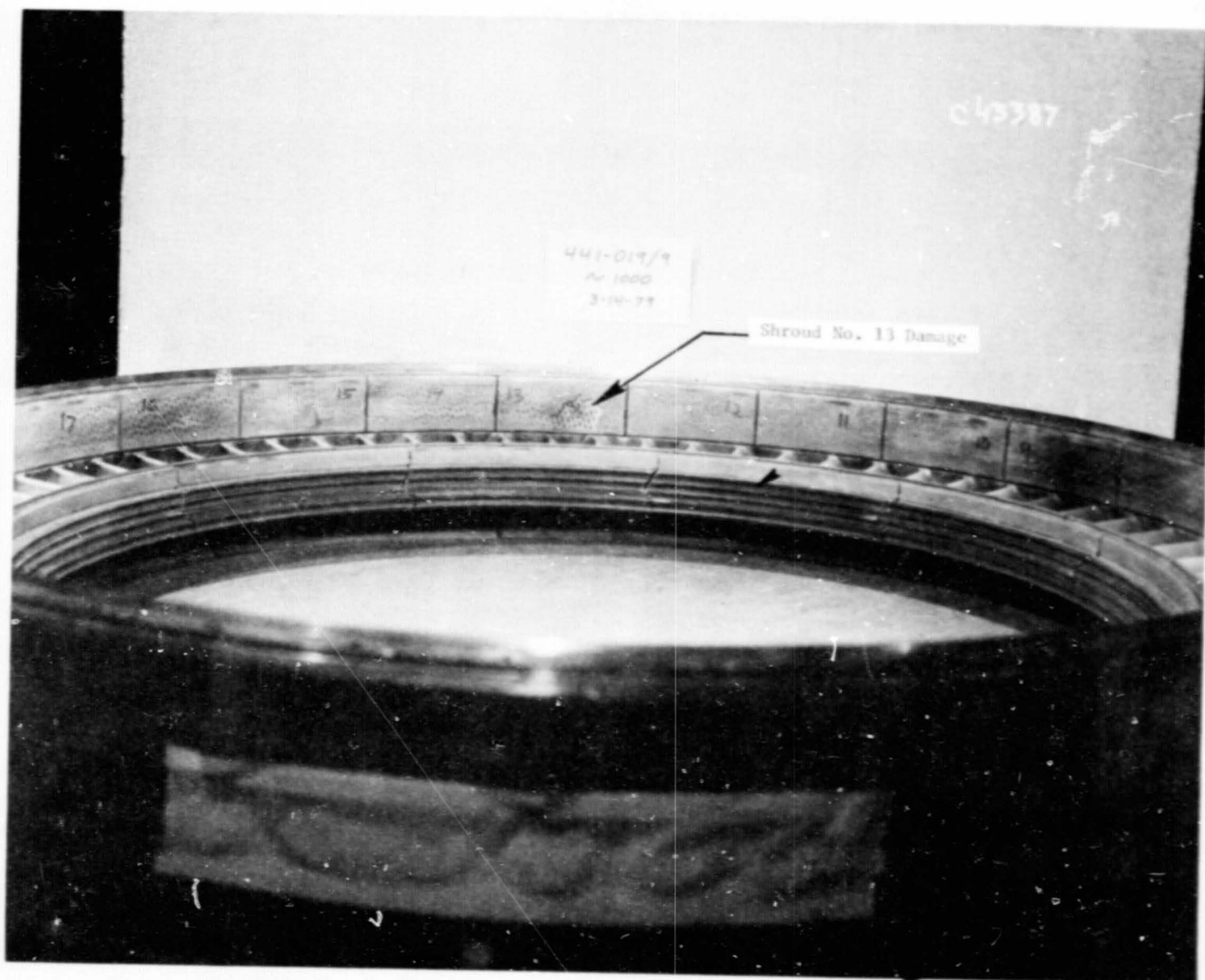
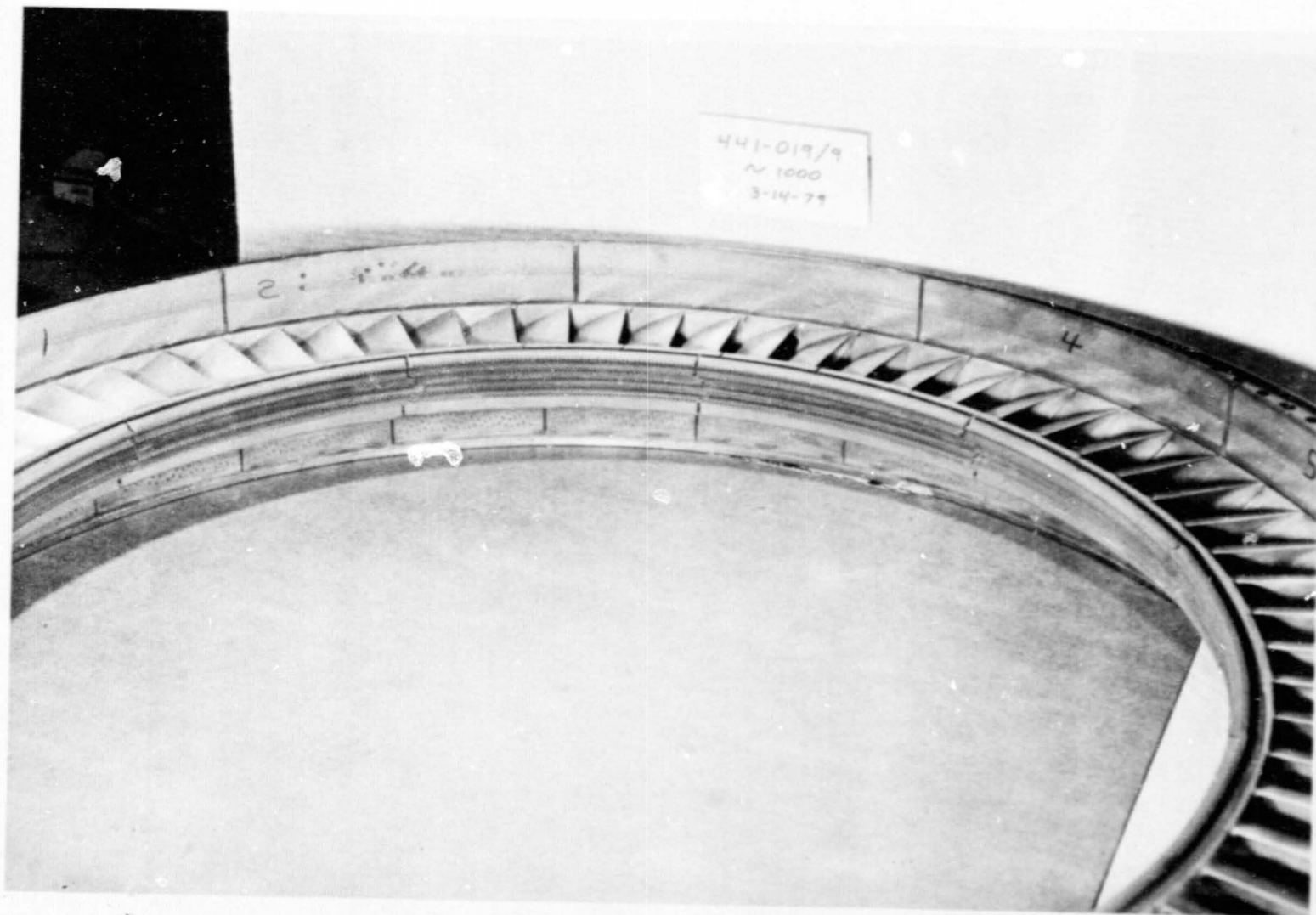Figure 93.   Stage 2 Nozzle Assembly and Stage 1 Shrouds After 1000 Cycles.

Figure 94.   Stage 2 Nozzle Assembly and Stage 2 Shrouds After 1000 Cycles.
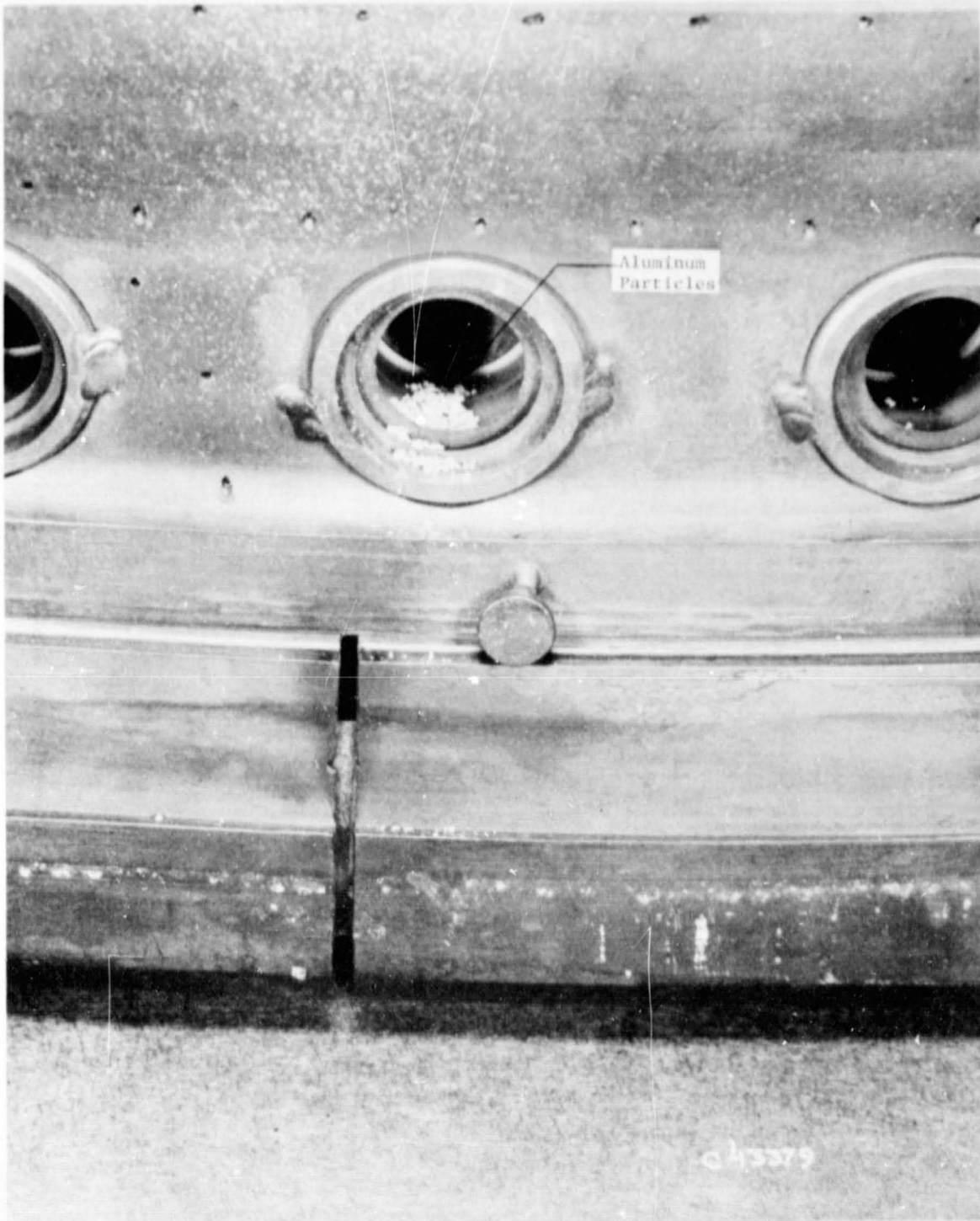
Figure 95. Thirteenth Stage Air Seal Slot After 1000 Cycles.

Inner/Outer Screen - The location of the inner and outer screens can be seen in Figure 82. A 7-inch long circumferential crack was found along the edge of the inner screen-to-flange weld as shown in Figure 96. This weld was of poor quality, as noted prior to buildup of the engine. Studies are underway to improve this joint by redesigning the joint configuration. In the installed position, the weld crack appeared tight, but aluminum was found in the Stage 1 vane inner platform holes during teardown. Some waviness of the screen flange was evident, as well as deposits of aluminum on its forward side. This might also account for aluminum passing the screen.

Two radial cracks were found in the outer screen aft sheetmetal ring. Both cracks appeared to start in the weld joint between the machined ring and the sheetmetal impingement plate vertical wall. One crack starts in the weld and terminates in a cooling hole in the last row of impingement holes. The radial seal riveted to the forward machined ring and extending from the outer band to the screen has 19 radial cracks approximately 6 mm (0.250 inch) long. Thermal gradients in the seal are the suspect cause. Design modification will be made if continued testing indicates these cracks are a problem. The screen is serviceable as-is.

Channel Spring - The channel spring, holding the inner fishmouth seal, can be seen in Figure 82. Light scuffing was noted on the contact surfaces of the springs; but otherwise, the springs were in excellent condition. Mating wear marks on the inner screen flange indicate no circumferential motion of the inner screen relative to the spring.

Channel Cover - The channel cover, shown in Figure 82, provides windage coverage for the wheelspace baffle bolt circle nuts. Some of the nut plate nuts appeared bound in the untorqued position but could be freed with a light blow. No other distress was noted.

Wheelspace Baffle - The wheelspace baffle, shown in Figure 82, discourages recirculation of flowpath gases into the cavity. This reduces the purge air required and parasitic losses. No difficulties were found with the basic baffle. However, two baffles drilled for pressure taps near the outer edge had radial cracks extending from the hole to the edge. These holes will not be included in the production design.

Thermal Shield (Stage 1 Vane) - Thirteen of 16 thermal shields (Figure 82) had radial cracks through their locating pin holes, as shown in Figure 97, and two shields had circumferential cracks above the bolt holes. There were two shields which rubbed the Stage 1 blade angel wings. In the first case, one-half of the lip was missing from the bolt holes outward and in the second case, a 32 mm (1.25 inch) length was rubbed through. A design solution for this problem has been implemented and tested in subsequent endurance tests. The design modification consisted of reducing the thermal stresses on the heat shields by making them half as long and adding damping by making the shields an interference fit with the underside of the Stage 1 vane.
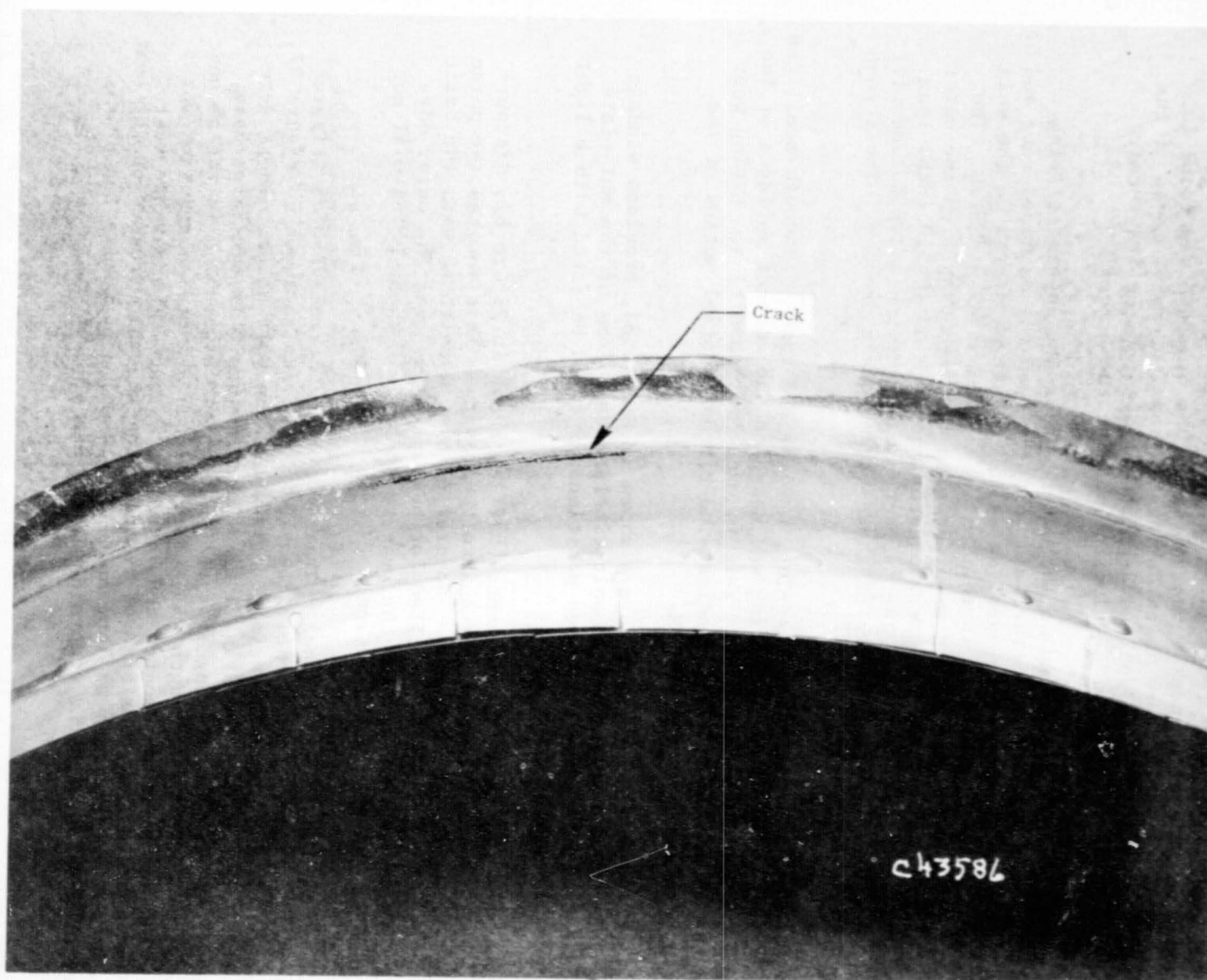
Crack

C43586

Figure 96.   Inner Screen Damage After 1000 Cycles.
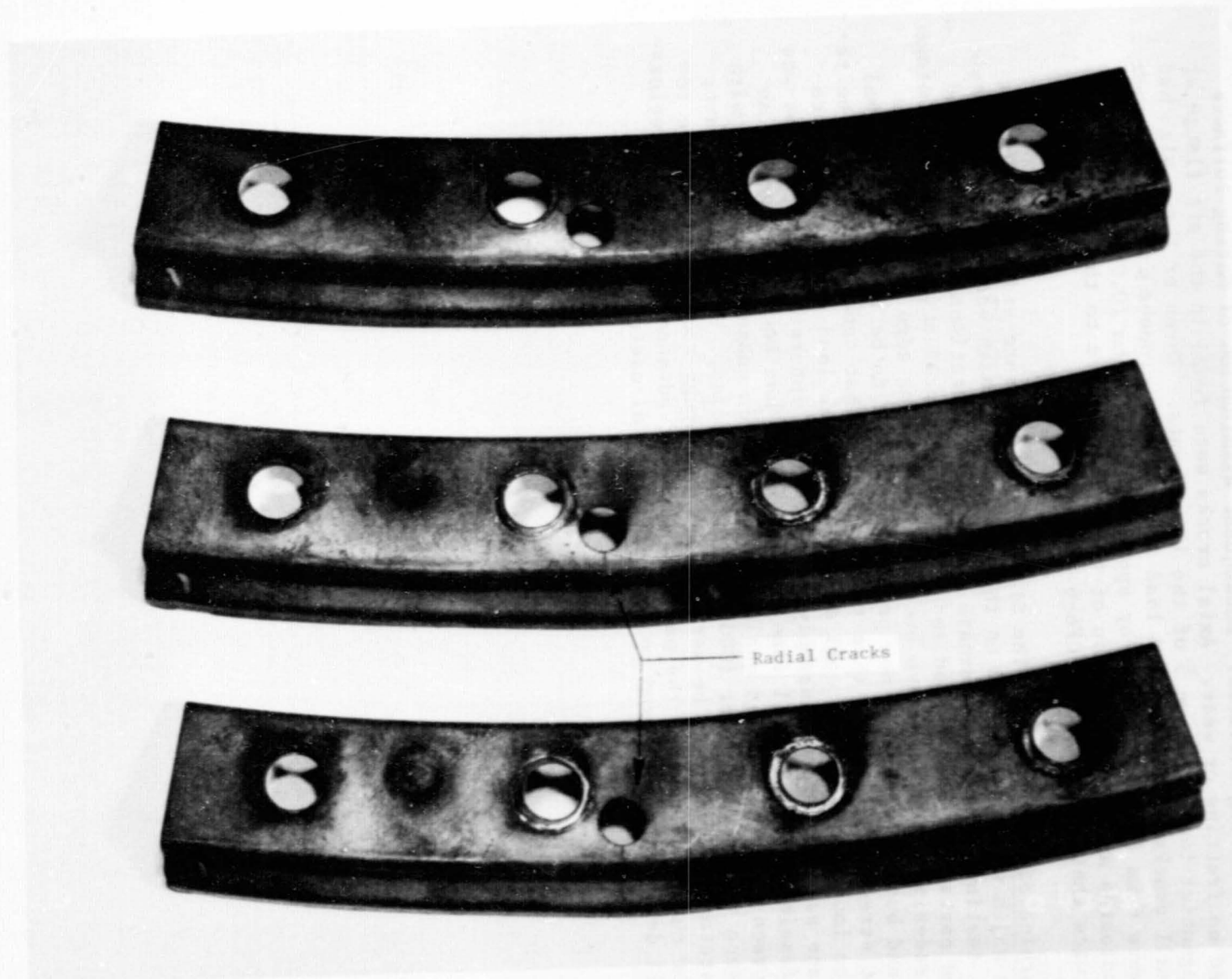
Radial Cracks

Figure 97. Stage 1 Vane Thermal Shield After 1000 Cycles.

Interstage Seals - Disassembly of the interstage seals (shown in Figure 82) from the Stage 2 vane segments required considerable force to overcome sliding friction, indicating that engine operation had not opened up clearances between mating surfaces. Subsequent examination of mating surfaces revealed no fretting or wear. Axial cracks were found in the aft flange at the tangential load stops on 5 of the 11 segments. Three of these also had very small cracks at the forward load stops. Wear grooves in the honeycomb seals were 6 mm (0.25 in.) wide by approximately 1.5 mm (0.060 in.) deep. This indicates an axial excursion of the seal relative to the rotor of at least twice that of a standard CF6-6 engine.

Turbine Stator Summary - The Stage 1 vane pressure side cracking is a problem which was not expected on these parts but which was addressed in subsequent testing. Work on alternate cooling configurations is complete and modified parts have been tested and introduced on production parts. The Stage 2 vane redesign appears to have overcome the leading edge cracking at the outer band but has generated new problems believed to be related to thermal gradient stresses. Although this test indicated that some changes will be required to improve interstage seal durability in the load stop areas and to facilitate assembly and disassembly, the boltless interstage seal concept was proven feasible. The Stage 1 vane thermal shield has been redesigned. An inner screen with an improved quality weld has been subsequently tested with no evidence of cracking after 1000 core engine cycles. Virtually all parts in the stator are judged to be serviceable. Although some parts will be removed for cutup and rework, the parts in the most advanced state of deterioration will deliberately be used to demonstrate total useful life.

140

9.0 ECONOMIC ASSESSMENT

The HPT aerodynamic performance improvement concept was evaluated by Douglas under Task 1 of this program (Reference 1) for a cruise specific fuel consumption improvement of 1.3%. The CF6 turbofan engine static back-to-back test demonstrated this performance improvement at cruise equivalent power for new engines.

The 1.3% reduction in cruise sfc results in the block fuel savings shown in Table V for the minimum fuel consumption mission. This is based on the data of Reference 1.

Table V. High Pressure Turbine Aerodynamic Performance Improvement Block Fuel Savings.

Aircraft	Range (km)	Δ Fuel	
		kg	%
DC-10-10	645	-103.4	-1.3
	1690	-215.0	-1.3
	3700	-449.5	-1.4

The estimated annual fuel savings per aircraft for the above block fuel savings are shown in Table VI.

Table VI. High Pressure Turbine Aerodynamic Performance Improvement-Estimated Annual Fuel Savings Per Aircraft.

Aircraft	Range (km)	Δ Fuel l/AC/Year
DC-10-10	645	276,000
	1690	381,800
	3700	426,000

The economic assessment for the assumed medium fuel price of 11.89¢/liter (45¢/gal) is summarized in Table VII. The increase in fuel cost to about double the above medium price 24¢/liter (90¢/gal) reduces the payback time to 0.105 year which makes this concept even more attractive.

141

Table VII. Economic Assessment of HP
            Turbine Aerodynamic Performance
            Improvement Concept.

(Medium Range, Medium Fuel Price,
  Minimum Fuel Analysis)

Aircraft	Payback Years	ROI %
DC-10-10	0.17	600

10.0 SUMMARY OF RESULTS

The high pressure turbine aerodynamic performance improvement concept has been evaluated in component tests and in engine ground tests. The main results of these tests are discussed below:

Component Tests

Stage 1 Vane Cascade Test - This test demonstrated that the fully cooled improved turbine Stage 1 vane has an aerodynamic efficiency equal to the fully cooled original production vane.

Stage 2 Vane Leading Edge Flow Evaluation - This test demonstrated that the improved design vane insert inlet area reduced the static pressure loss, resulting in a reduction of the radial pressure gradient within the inlet. Larger trailing edge holes are required to achieve the design flow split.

Stage 1 Vane Trailing Edge Test - This test demonstrated that the selected improved vane design of two walls promoted in the staggered matrix has 2.44 times the heat transfer promotion than all walls smooth. The selected design reduces trailing edge temperature by 16.7° C (30° F) with a temperature increase of only 5.6° C (10° F) in the promoted region.

Stage 2 Vane Leading Edge Test - The test showed that the improved design vane insert results in a 10% increase in Nusselt number in the leading edge region. This indicates an improvement in the cooling of the vane leading edge.

Stage 2 Vane Trailing Edge Pin Fin Test - This test demonstrated that the selected trailing edge pin fin geometry of the improved Stage 2 vane design increased the heat transfer coefficient by a factor of 3 over that of a smooth wall.

Blade Dynamic and Steady-State Strain Distribution - Resonant frequencies and nodal patterns were obtained for the Stage 1 and 2 improved design blades. Relative strain distributions were determined for all modes, giving the detailed distribution of stress in the blades. The steady-state strain distributions obtained showed no unusual effects for either Stage 1 or Stage 2. The magnitude of the end effects is within the realm of experience for blading of this type.

Blade Frequency and Amplitude as a Function of Damper Force - The results of the test indicate that the dampers will produce the desired effects relating to frequency gain and stress reduction. A gain of about 11% in the first-flex frequency was found for both Stage 1 and Stage 2 blades. The Stage 1 blade could not be driven at high amplitudes which was expected. The magnitude of the Stage 2 stress reduction was similar to that seen for the CF6-50 Stage 2 blade.

Turbine Disk Rim Stress Distribution Test

The stress concentration factors of the forward and aft rabbet fillets of the Stage 1 and Stage 2 turbine disk rims were determined from this test. The Stage 2 results are in good agreement with the two-dimensional analysis while the Stage 1 results show some differences.

Instrumented Engine Test

This test determined the operating characteristics of the improved (single shank) turbine, such as:

- Stage 1 Blade Vibratory Response
- Stage 2 Blade Vibratory Response
- Rotor Vibratory Response
- Stage 1 Blade Metal Temperatures
- Stage 2 Blade Metal Temperatures
- Rotor Spool Metal Temperatures
- Rotor Cooling Flow
- Stage 2 Nozzle Cooling Flow
- Interstage Cavity Temperatures
- Rotor and Stator Transient Temperatures
- Stator Structure Temperatures
- Stator Structure Transient Response

The results were used to conduct additional life and design analyses.

Endurance Test

The 1000 cycle core engine endurance test on engine 441-019 fulfilled the test objectives of subjecting the new turbine design to the equivalent of 2500-3500 hours of airline service. A number of problem areas were uncovered but, in general, the posttest condition of the turbine was excellent. In the areas where problems were uncovered, modifications have been defined and programs were put in place to procure hardware, perform analysis, and evaluate the modification effectiveness via additional engine and component testing.

No major design flaws were uncovered by the test which would hinder completion of the overall program on schedule. The 1000 cycle endurance test was successful in fulfilling all objectives in quickly identifying potential field problems. Basic integrity of the new turbine design was established.

Further Development

As a result of these tests and additional General Electric funded efforts, the development and certification of the improved (single shank) turbine were continued. Initial back-to-back engine tests of the original and the improved turbine demonstrated an improvement of 1.3% in cruise sfc and a 10° C reduction in exhaust gas temperature (EGT). An additional improvement of 0.3% in cruise sfc and 6° C on EGT is projected for long service engines.

The single shank turbine will be used in the advanced versions of the CF6-6 engine such as the CF6-6K and the CF6-32.

APPENDIX A

QUALITY ASSURANCE

INTRODUCTION

The quality program applied to this contract is a documented system throughout the design, manufacture, and repair, overhaul, and modification cycle for gas turbine aircraft engines. The quality system has been constructed to comply with military specifications MIL-Q-9858A, MIL-I-45208, and MIL-C-45662 and Federal Aviation Regulations FAR-145 and applicable portions of FAR-21.

The quality system and its implementation are defined by a complete set of procedures which has been coordinated with the DOD and FAA, and which has their concurrence. In addition, the quality system as described in the quality program for this contract has been coordinated with NASA-Lewis Research Center. The following is a brief synopsis of the system.

QUALITY SYSTEM

The quality system is documented by operating procedures which coordinate the quality-related activities in the functional areas of Engineering, Manufacturing, Materials, Purchasing, and Engine Programs. The quality system is a single-standard system wherein all product lines are controlled by the common quality system. The actions and activities associated with determination of quality are recorded, and documentation is available for review.

Inherent in the system is the assurance of conformance to the quality requirements. This includes the performance of required inspections and tests. In addition, the system provides change control requirements which assure that design changes are incorporated into manufacturing, procurement and quality documentation, and into the products.

Measuring devices used for product acceptance and instrumentation used to control, record, monitor, or indicate results of readings during inspection and test are initially inspected and calibrated and periodically are reverified or recalibrated at a prescribed frequency. Such calibration is performed by technicians against standards which are traceable to the National Bureau of Standards. The gages are identified by a control number and are on a recall schedule for reverification and calibration. The calibration function maintains a record of the location of each gage and the date it requires recalibration. Instructions implement the provisions of MIL-C-45662 and the appropriate FAR requirements.

Work sent to outside vendors is subject to quality plans which provide for control and appraisal to assure conformance to the technical requirements. Purchase orders issued to vendors contain a technical description of the work to be performed and instructions relative to quality requirements.

147

Engine parts are inspected to documented quality plans which define the characteristics to be inspected, the gates and tools to be used, the conditions under which the inspection is to be performed, the sampling plan, laboratory and special process testing, and the identification and record requirements.

Work instructions are issued for compliance by operators, inspectors, testers, and mechanics. Component part manufacture provides for laboratory overview of all special and critical processes, including qualification and certification of personnel, equipment, and processes.

When work is performed in accordance with work instructions, the operator/inspector records that the work has been performed. This is accomplished by the operator/inspector stamping or signing the operation sequence sheet to signify that the operation has been performed.

Various designs of stamps are used to indicate the inspection status of work in process and finished items. Performance or acceptance of special processes is indicated by distinctive stamps assigned specifically to personnel performing the process or inspection. Administration of the stamp system and the issuance of stamps are functions of the Quality Operation. The stamps are applied to the paperwork identifying or denoting the items requiring control. When stamping of hardware occurs, only laboratory approved ink is used to assure against damage.

The type and location of other part marking are specified by the design engineer on the drawing to assure effects do not compromise design requirements and part quality.

Control of part handling, storage and delivery is maintained through the entire cycle. Engines and assemblies are stored in special dollies and transportation carts. Finished assembled parts are stored so as to preclude damage and contamination, openings are covered, lines capped and protective covers applied as required.

Nonconforming hardware is controlled by a system of material review at the component source. Both a Quality representative and an Engineering representative provide the accept (use as-is or repair) decision. Nonconformances are documented including the disposition and corrective action if applicable to prevent recurrence.

The system provides for storage, retention for specified periods, and retrieval of nonconformance documentation. Documentation for components is filed in the area where the component is manufactured/inspected.

A buildup record and test log are maintained for the assembly, inspection, and test of each major component or engine. Component and engine testing is performed according to documented test instructions, test plans, and instrumentation plans. Test and instrumentation plans are submitted to NASA for approval prior to the testing.

Records essential to the economical and effective operation of the
quality program are maintained, reviewed, and used as a basis for action.
These records include inspection and test results, nonconforming material
findings, laboratory analysis, and receiving inspection.

APPENDIX B

REFERENCES

1. Fasching, W.A., "CF6 Jet Engine Performance Improvement Program - Task 1 Feasibility Analysis," NASA CR-159450, March 1979.

2. Kreith, F., PRINCIPLES OF HEAT TRANSFER, International Text Book Company, 1958.

150

APPENDIX C

SYMBOLS AND DEFINITIONS

A	Cross-sectional Area, m^2
AC	Aircraft
A_H	Heater Plate Surface Area, m^2
C_p	Specific Heat at Constant Pressure, $\dfrac{W\ hr}{kg\ ^\circ C}$
D_p	Pin Diameter, m
h	Heat Transfer Coefficient, $\dfrac{W}{m^2\ ^\circ C}$
I	Electrical Current, A
k	Conductivity, $\dfrac{W}{m^2\ ^\circ C/m}$
L_p	Pin Length/2, m
p	Pin Perimeter, m
P	Electrical Power Input, W
Pr	Prandtl Number $= \dfrac{C_p \mu}{k}$
P_T	Total Pressure, N/cm^2
Q_p	Total Pin Fin Heat Loss for Each Heater, W
R	Electrical Resistance, Ω
Re_D	Reynolds Number (based on diameter), $\dfrac{\rho\ V_e\ D}{\mu}$
T_A	Air Temperature, $^\circ C$
T/C	Thermocouple
T_H	Heat Plate Temperature, $^\circ C$
T_p	Pin Temperature, $^\circ C$
V_1	Local Velocity, m/sec
W_c	Cooling Airflow, % of Compressor Flow

ρ Density, kg/m^3

η_T Turbine Efficiency, %

μ Viscosity, $\dfrac{kg}{hr \, m}$